

**Evaluation of metallophthalocyanine functionalized  
photocatalytic asymmetric polymer membranes for  
pollution control and antimicrobial activity**

**A thesis submitted in fulfilment of the requirements  
for the degree of**

**DOCTOR OF PHILOSOPHY  
Of**

**Rhodes University  
By**

**Donovan Musizvinoda Chidyamurimi Mafukidze  
August 2020**

## **Dedication**

This work is dedicated to my family and the loving memory of my late grandmother  
Diana Kawonza.

## **Acknowledgements**

My sincere appreciation goes to my supervisor, Distinguished Prof Tebello Nyokong for giving the opportunity to be a student under her mentorship through-which she guided me with resilience and patience. I would like to thank Prof John Mack, Dr Jonathan Britton, Ms. Gail Cobus and Mr Francis Chindeka for their unwavering support and assistance throughout my studies. I also extend my gratitude to Shirley Pinchuck and Marvin Randall for their assistance with TEM and SEM at the Electron Microscopy Unit (EMU).

I would like to thank the past and present members of S22 research group, especially Dr Olawale L Osifeko, Dr Munyaradzi Shumba, Dr Edith Dube, Dr Balaji Babu, Dr Muthumuni Managa and Azole Sindelo for your assistance and support. I also acknowledge financial support by the National Research Foundation (NRF) South Africa and Sasol Inzalo Foundation, and support by the Chemistry Department of Rhodes University, all staff members and all the postgraduate students.

To my family, Ayanda Zulu, Dr Leo Mafuso, thank you for your prayers and being there, you've been an ever-present source of joy and support. Lastly, I give praise to God who made it all possible.

## Abstract

The conceptualisation of photosensitizing water treatment polymer membranes using phthalocyanine based photosensitizers is reported in this thesis. The key to successful preparation of stable photoactive polymer membranes was established as the covalent anchorage of the photosensitizer to a polymer, which was proven by singlet oxygen generation by the membranes without photosensitizer deterioration. Despite this limitation, the covalent linkage-incapable unsubstituted zinc (II) phthalocyanine (complex **2**) was applied as a nanoconjugate of graphene quantum dots (**2** $\pi$ (GQDs)). **2** $\pi$ (GQDs) was formed through  $\pi$ - $\pi$  stacking, and was then covalently anchored, as a proof of concept. This concept was also applied to 2-(4-carboxyphenoxy) phthalocyaninato zinc (II) (complex **3**) which is capable of covalent linkage but proved to deteriorate the efficiency of singlet oxygen formation with comparison to the covalent conjugates.

Singlet oxygen generation by functionalized polymer membranes rendered them photocatalytic in the degradation of organic pollutants and microorganisms in water. Organic pollutant degradation capability was exemplified by **2** $\pi$ (GQDs) and a porphyrin-phthalocyanine heterodiyad (complex **10**) functionalized membranes (**2** $\pi$ (GQDs)-memb and **10**-memb respectively), where a MPc loading of approximately 0.139  $\mu\text{mol MPc/g}$  of membrane was able to achieve a 4-chlorophenol degradation rate of  $3.77 \times 10^{-6} \text{ mol L}^{-1} \text{ min}^{-1}$  in a second order reaction with an initial 4-chlorophenol concentration of  $3.24 \times 10^{-4} \text{ mol L}^{-1}$  for **2** $\pi$ (GQDs)-memb as an example. Antibacterial studies against *S.aureus* using a quaternized MPc and conjugates of silver triangular nanoprisms with zinc (II) and indium (III) MPcs showed note-worthy improvements in photodynamic antimicrobial chemotherapy (PACT) activity in

comparison to the unquaternized MPc precursor, and the free zinc and indium MPcs respectively. Functionalization of polymer membranes with these higher activity photosensitizers translated to the formation of potentially superior biological fouling resistant membranes.

The use of porphyrin-phthalocyanine polynuclei arrays (complex **10**) in polymer membrane functionalization resulted in the use of a wider wavelength range (white light). The findings from this work as a whole, thus presents the potential applicability of phthalocyanine functionalized polymer membranes in water treatment technology.

# TABLE OF CONTENTS

## Contents

Dedication .....	ii
Acknowledgements .....	iii
Abstract .....	iv
TABLE OF CONTENTS .....	vi
List of abbreviations .....	x
List of symbols .....	xiii
CHAPTER 1 .....	1
Preamble .....	2
1. Introduction .....	3
1.1. Membrane technology and Polymer membranes .....	3
1.1.1. Membrane preparation: Nonsolvent induced phase inversion method (Loeb-Sourirajan technique) .....	3
1.1.2. Photocatalytic polymer membrane development .....	6
1.2. Phthalocyanines .....	7
1.2.1. Electronic absorption spectrum .....	8
1.2.2. Synthesis .....	9
1.2.3. Phthalocyanine-Porphyrin dyads .....	12
1.2.4. Photosensitization .....	14
1.2.5. Phthalocyanines used in this study .....	24
1.3. Nanoparticles .....	28
1.3.1. Graphene quantum dots (GQDs) .....	29
1.3.2. Silver triangular nanoprisms (AgTNPs) .....	30
1.4. Summary of aims and objectives .....	33
CHAPTER 2 .....	35
2. Experimental .....	36
2.1. Materials .....	36
2.1.1. General reagents and solvents .....	36
2.1.2. Reagents for polymer modification and membrane synthesis .....	36
2.1.3. Reagents for phthalocyanine and porphyrin synthesis .....	37
2.1.4. Reagents for nanoparticle synthesis .....	37
2.1.5. Reagents and materials for photodegradation and bacterial studies .....	37
2.2. Equipment .....	37
2.3. Synthesis .....	42

2.3.1.	Synthesis of metallophthalocyanines (MPcs) .....	42
2.3.2.	Synthesis of MPc-GQD conjugates .....	47
2.3.3.	Synthesis of AgTNPs (Scheme 3.5).....	48
2.3.4.	Synthesis of MPc-AgTNPs conjugates (Scheme 3.6).....	48
2.3.5.	Synthesis of functionalized polymers .....	49
2.3.6.	Synthesis of photosensitizer-polymer conjugates .....	52
2.3.7.	Synthesis of functionalized polymer membranes .....	56
2.4.	Photodegradation studies .....	58
2.5.	Light harvesting studies for 10-memb .....	59
2.6.	Procedures for photodynamic antimicrobial chemotherapy (PACT) studies..	60
2.6.1.	Bacterial culture and dilution optimization .....	60
2.6.2.	Photodynamic antimicrobial chemotherapy activity .....	61
2.6.3.	Statistical analysis .....	62
RESULTS AND DISCUSSIONS.....		63
Publications.....		64
CHAPTER 3.....		67
3.	Synthesis and characterization.....	68
3.1.	Metallophthalocyanines (MPcs) .....	68
3.1.1.	2(3),9(10),16(17),23(24)-Tetrakis-(4-carboxyphenoxy) phthalocyaninato indium (III) chloride (4b) .....	68
3.1.2.	2-(4-Carboxyphenoxy)-9(10),16(17),23(24)-tris-(dimethylamino) phthalocyaninato zinc (II) (5) and 2-(4-carboxyphenoxy)-9(10),16(17),23(24)-tris-(trimethylamino) phthalocyanine zinc (II) methyl sulfate (6) .....	72
3.1.3.	5-(4-aminophenyl)-10,15,20-triphenylporphyrin (8), 2-(4-carboxyphenoxy)-9(10),16(17),23(24)-trichlorophthalocyaninato zinc (II) (9) and 2-(4-[4-(10,15,20-triphenylporphyrin-5-yl)phenyl]-amidophenoxy)-9(10),16(17),23(24)-trichlorophthalocyaninato zinc (II) (10) .....	76
3.2.	Nanoparticles and their MPc conjugates.....	84
3.2.1.	Graphene quantum dots (GQDs) and MPc conjugates.....	84
3.2.2.	Silver triangular nanoprisms (AgTNPs) and MPc conjugates.....	95
3.3.	Functionalization of polymers .....	103
3.3.1.	(COOH)PAN .....	103
3.3.2.	(COOH)PS and a(NH <sub>2</sub> )PS .....	105
3.3.3.	b(NH <sub>2</sub> )PS .....	107
3.4.	Photosensitizer-polymer conjugates.....	109
3.4.1.	Amide conjugates .....	111
3.4.2.	10-PS (Buchwald-Hartwig coupling) .....	121

3.4.3. MPc loading .....	124
3.5. Polymer membranes .....	126
3.5.1. Physical appearance .....	127
3.5.2. SEM analysis .....	128
3.5.3. Solid-state UV-Vis analysis .....	132
3.6. Summary of chapter .....	136
CHAPTER 4.....	137
4. Photophysical and Photochemical Properties.....	138
4.1. Photophysical and photochemical parameters .....	138
4.1.1. Fluorescence quantum yield ( $\Phi_F$ ) and lifetime ( $\tau_F$ ) .....	138
4.1.2. Förster resonance energy transfer (FRET) .....	139
4.1.3. Triplet quantum yield ( $\Phi_T$ ) and lifetime ( $\tau_T$ ).....	140
4.1.4. Singlet oxygen quantum yield ( $\Phi_\Delta$ ) .....	141
4.2. Fluorescence properties .....	143
4.2.1. Fluorescence excitation and emission spectra .....	143
4.2.2. Fluorescence quantum yield ( $\Phi_F$ ) and lifetime ( $\tau_F$ ) .....	144
4.2.3. Förster resonance energy transfer (FRET) .....	150
4.3. Triplet quantum yields ( $\Phi_T$ ) and lifetimes ( $\tau_T$ ) .....	153
4.4. Singlet oxygen quantum yields ( $\Phi_\Delta$ ) .....	158
4.4.1. Singlet oxygen quantum yields in solution.....	158
4.4.2. Singlet oxygen quantum yields of membranes .....	162
4.5. Summary of chapter .....	165
CHAPTER 5.....	167
5. Photodegradation and Photodynamic Antimicrobial Chemotherapy (PACT) .....	168
5.1. Photocatalytic degradation of 4-chlorophenol (4-CP).....	168
5.1.1. UV-Vis spectral studies .....	168
5.1.2. Kinetics of 4-chlorophenol photooxidative degradation .....	172
5.1.3. Light harvesting studies of 10-memb .....	176
5.2. Photodynamic Antimicrobial Chemotherapy (PACT).....	179
5.2.1. Application of AgTNPs for enhanced PACT .....	179
5.2.2. Quaternization of MPcs for enhanced PACT activity .....	184
5.3. Summary of chapter .....	189
CHAPTER 6.....	191
6. Conclusions and Recommendations.....	192
6.1. General conclusions .....	192
6.2. Recommendations .....	194



<b>REFERENCES .....</b>	<b>195</b>
-------------------------	------------

## List of abbreviations

$^1\text{H}$ NMR	= Proton nuclear magnetic resonance
ADMA	= Tetrasodium $\alpha,\alpha$ -(anthracene-9,10-diyl) dimethylmalonate
AOPs	= Advanced oxidation processes
$\text{CDCl}_3$	= Deuterated chloroform
DBU	= 1,8-diazabicyclo[5.4.0]undec-7-ene
DCC	= Dicyclohexylcarbodiimide
DMF	= Dimethylformamide
DMS	= Dimethyl sulfate
DMSO	= Dimethyl sulfoxide
$\text{DMSO-d}_6$	= Deuterated dimethyl sulfoxide
DPBF	= Diphenylisobenzofuran
EDS	= Energy dispersive X-ray spectroscopy
FT-IR	= Fourier Transform Infrared
GQDs	= Graphene quantum dots
GSH	= Glutathione
HOMO	= Highest occupied molecular orbital
IC	= Internal conversion
IRF	= Instrument response function

ISC	= Intersystem crossing
LUMO	= Lowest unoccupied molecular orbital
MALDI	= Matrix–Assisted Laser Desorption/Ionization
MPc	= Metallophthalocyanine
MS	= Mass Spectrometer
Nd–YAG	= Neodymium–doped Yttrium Aluminum Garnet
NPs	= Nanoparticles
PACT	= Photodynamic antimicrobial chemotherapy
PBS	= Phosphate buffer saline
Pc	= Phthalocyanine
PDT	= Photodynamic therapy
PS	= Polystyrene
ROS	= Reactive oxygen species
SEM	= Scanning electron microscope
SPR	= Surface plasmon resonance
Std	= Standard
TCSPC	= Time-correlated single photon counting
TEM	= Transmission electron microscope
THF	= Tetrahydrofuran
TNPs	= Triangular nanoprisms

UV–Vis	= Ultraviolet–Visible
VR	= Vibrational relaxation
XPS	= X–ray Photoelectron Spectroscopy
XRD	= X–ray Diffractometer

## List of symbols

$\alpha$	= Non-peripheral position
$\beta$	= Peripheral position
$\varepsilon$	= Molar extinction coefficients
$\varepsilon_S$	= Singlet state molar extinction coefficients
$\varepsilon_T$	= Triplet state molar extinction coefficients
$\lambda$	= Wavelength
$\tau_F$	= Fluorescence lifetime
$\tau_T$	= Triplet lifetime
$\Phi_{ADMA}$	= Quantum yield of ADMA
$\Phi_F$	= Fluorescence quantum yield
$\Phi_T$	= Triplet quantum yield
$\Phi_\Delta$	= Singlet oxygen quantum yield
$\Delta A_S$	= Changes in the singlet state absorbance
$\Delta A_T$	= Changes in the triplet state absorbance
$Eff$	= FRET efficiency
$I_{abs}$	= Light intensity
$J$	= Förster overlap integral
$k_a$	= Rate constant for the reaction of ADMA with singlet oxygen
$k_d$	= Decay constant of singlet oxygen
$k_{obs}$	= Observed rate constant
$n$	= Refractive index
$r$	= Donor-acceptor distance
$R_0$	= Förster distance

$r_0$	= Initial rate
$S_{\Delta}$	= Fraction of triplet state quenched by molecular oxygen
$t$	= Time
$t_{1/2}$	= Half-life

# CHAPTER 1

### Preamble

This thesis introduces metallophthalocyanines (MPcs) as photocatalysts when embedded in asymmetric polymer membranes. The thesis focuses on 4-chlorophenol removal from water through MPc-mediated photocatalysis, as well as improved membrane biofouling resistance through photodynamic antimicrobial chemotherapy (PACT) activity. While achieving this, the work also explores various means of incorporation of MPcs into polymer membranes together with the photoactivity and photostability of the product membranes. MPcs are also employed in the presence of graphene quantum dots (GQDs) and silver triangular nanoprisms (AgTNPs).



## 1. Introduction

### 1.1. Membrane technology and Polymer membranes

The nature and structure, and ultimately properties of the membranes are incredibly diverse, and so are their applications. Porous membranes are of greatest interest whereby their core applications are as filters for various separation processes ranging from reverse osmosis, ultrafiltration, nanofiltration to gas separation [1–3]. The most popular membranes are polymer membranes due to their overall cost-effectiveness [4]. Applications of membrane technology has proven to give impressive results especially in waste water treatment where they have achieved log reduction values greater than 6.5 for viruses, protozoans and bacteria [5].

This study focuses on the flat-sheet asymmetric polymer membranes prepared using the nonsolvent induced phase inversion method which allows controlled tailoring of properties for the desired applications [2,6–8], hence their interest in this work.

#### 1.1.1. Membrane preparation: Nonsolvent induced phase inversion method (Loeb-Sourirajan technique)

Phase inversion is a controlled transformation process of a polymer solution which is initially a homogeneous liquid, to a solid state. Phase inversion polymer membrane preparation by immersion precipitation (nonsolvent induced phase invasion) was discovered by Sidney Loeb and Srinivasa Sourirajan [9]. It is the most popular method mainly for its simplicity and flexibility of the process parameters. This flexibility allows for the preparation of various membranes to suit the needs for specific applications. The process involves three steps which are; polymer solution preparation, solution casting and membrane precipitation (**Fig 1.1**).

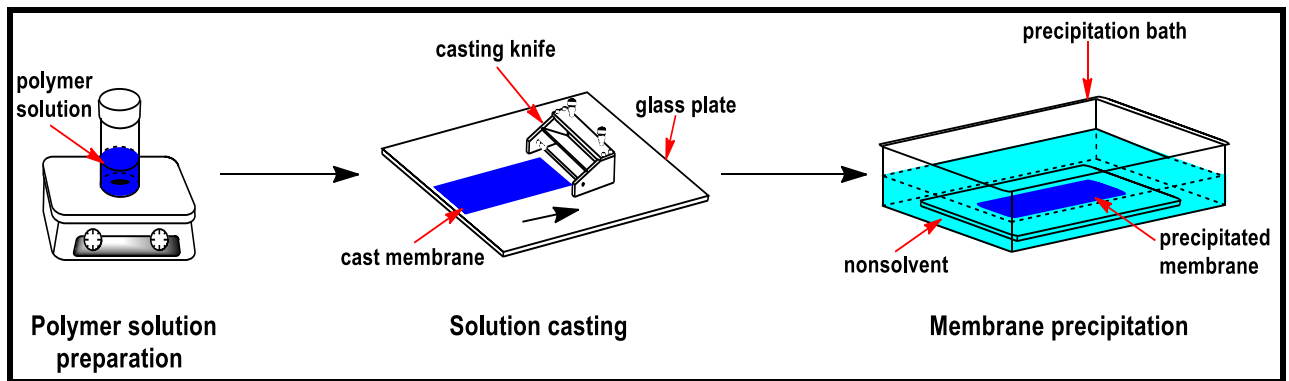


**Fig. 1.1:** Nonsolvent induced (Loeb-Sourirajan) phase invasion polymer membrane synthesis.

### Step 1: Polymer solution preparation

A suitable polymer or mixture of polymers, together with other additives (if any) are dispersed in an appropriate solvent and homogenized. Properties and structure of the product membrane depend on the choice of polymer, solvent, additives and polymer solution concentration [10]. Recent interest has been on the introduction of nanomaterial additives in polymer membrane matrices which has proven to enhance the formation of finger-like membrane morphologies with improved flux rates [11–14].

### Step 2: Membrane casting

At this step, the homogeneous polymer solution is spread on an even surface such as a glass plate, using a casting knife/ doctor's blade (**Fig. 1.1**). During this process, the desired dimensions of the membrane including the thickness are implemented.

### Step 3: Membrane precipitation

In the final step, the cast solution is immersed in a nonsolvent/ coagulation bath to precipitate out the product membrane. The nonsolvent is a solvent that is miscible with the polymer solution solvent but does not dissolve the polymer. The choice of nonsolvent, temperature of the bath and polymer solution additives determine the rate

of demixing (separation of solvent and polymer) and is critical to the overall membrane morphology [15–17]. The demixing process, is usually based on solvent -nonsolvent exchange rate during membrane precipitation and can either be instantaneous or delayed. In instantaneous demixing, fast solvent-nonsolvent exchange occurs immediately after cast immersion and results in membranes with a porous top layer (skin) and finger-like sublayer (bulk). On the other hand, with delayed demixing, slow solvent-nonsolvent exchange occurs and membranes with a dense less porous skin and sponge-like bulk morphologies are formed [6–8,18]. **Fig. 1.2** shows a schematic representation of the difference between asymmetric and symmetric phase inversion polymer membranes. This work focuses on asymmetric phase inversion membranes due to their high flux afforded by reduced flow resistance, and the general simplicity in their preparation [19].

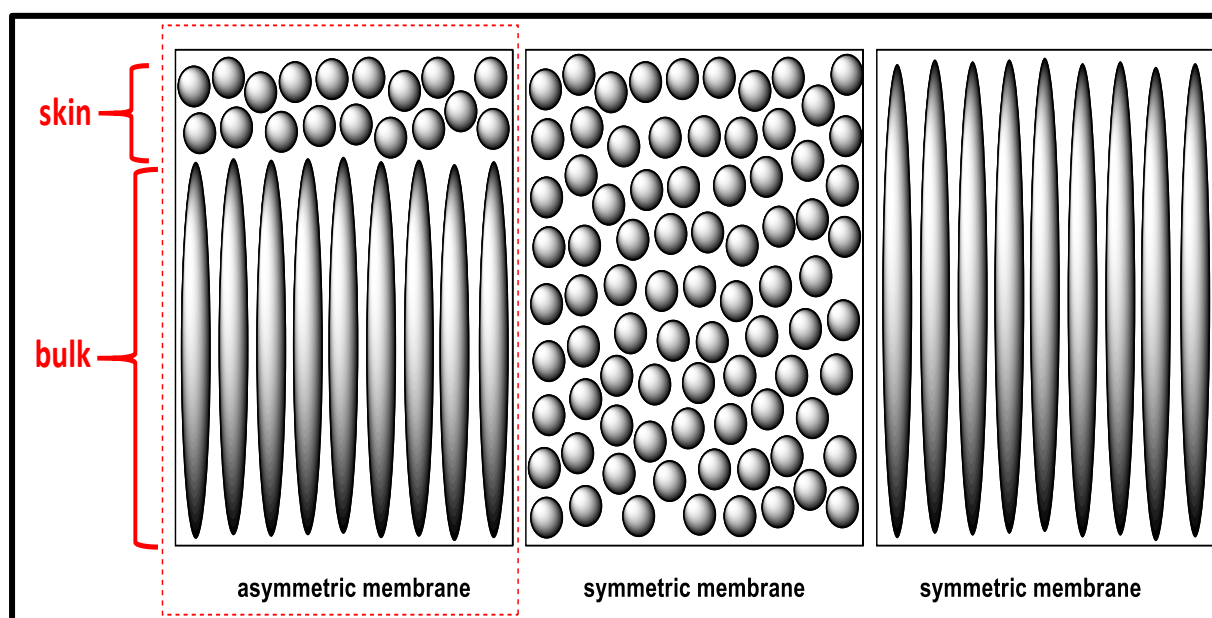


**Fig. 1.2:** Schematic representation of asymmetric and symmetric phase inversion polymer membranes.

### 1.1.2. Photocatalytic polymer membrane development

To improve water treatment efficiency, photocatalysts such as  $\text{TiO}_2$  have been introduced in membranes [20–23]. However, these membranes still have limitations which significantly challenge their upscale and commercialization.  $\text{TiO}_2$  nanoparticles respond to UV light where only less than 5 % of the sun's irradiation is available for use [24]. On the other hand, doped  $\text{TiO}_2$  nanoparticles responsive to visible light (400 - 700 nm) have been developed, but at the expense of the photocatalytic reaction efficiency. Also, there are concerns of possible photocatalyst leaching during application. The effective catalyst surface area is also reduced [13]. **Table 1.1** [25-29] shows some examples of photocatalytic polymer membranes containing  $\text{TiO}_2$  reported in literature.

**Table 1.1:** Examples of reported photocatalytic  $\text{TiO}_2$ -containing polymer membranes [25-29].

Polymer (% efficiency)	Pollutant in water	Reference
Polyamide ( $\pm 91$ %)	Methylene blue	[25]
Polyvinylidene fluoride Polycarbonate Polysulphone Polytetrafluoroethylene Polypropylene Polyacrylonitrile Polyethersulphone Cellulose acetate	-	[26]
Poly (vinylidene fluoride–trifluoro ethylene) ( $>99$ %)	Oil	[27]
Polyvinylidene fluoride ( $>60$ %)	Oil	[28]
polyvinylidene fluoride ( $>67$ %)	Aerobically treated palm oil mill effluent	[29]

The current study builds up on the concept of photocatalytic polymer membranes by attempting to eliminate the limitations of  $\text{TiO}_2$  immobilized polymer membranes. This will be achieved by introducing for the first time, metallophthalocyanines (MPcs) as possible superior photocatalysts responsive to visible light and can be chemically bound to the asymmetric phase inversion polymer membranes. In this study emphasis will be on the photoactivity and related properties of the MPc functionalized polymer membranes.

## 1.2. Phthalocyanines

Phthalocyanines (Pcs) are a family of porphyrinoid macrocyclic dye molecules that may be referred to as tetrabenzotetraazaporphyrins which are related to porphyrins (**Fig. 1.3**). These compounds have an extensive  $\pi$  conjugated system similar to porphyrins, which is further extended by the fused benzene rings. The fused benzene

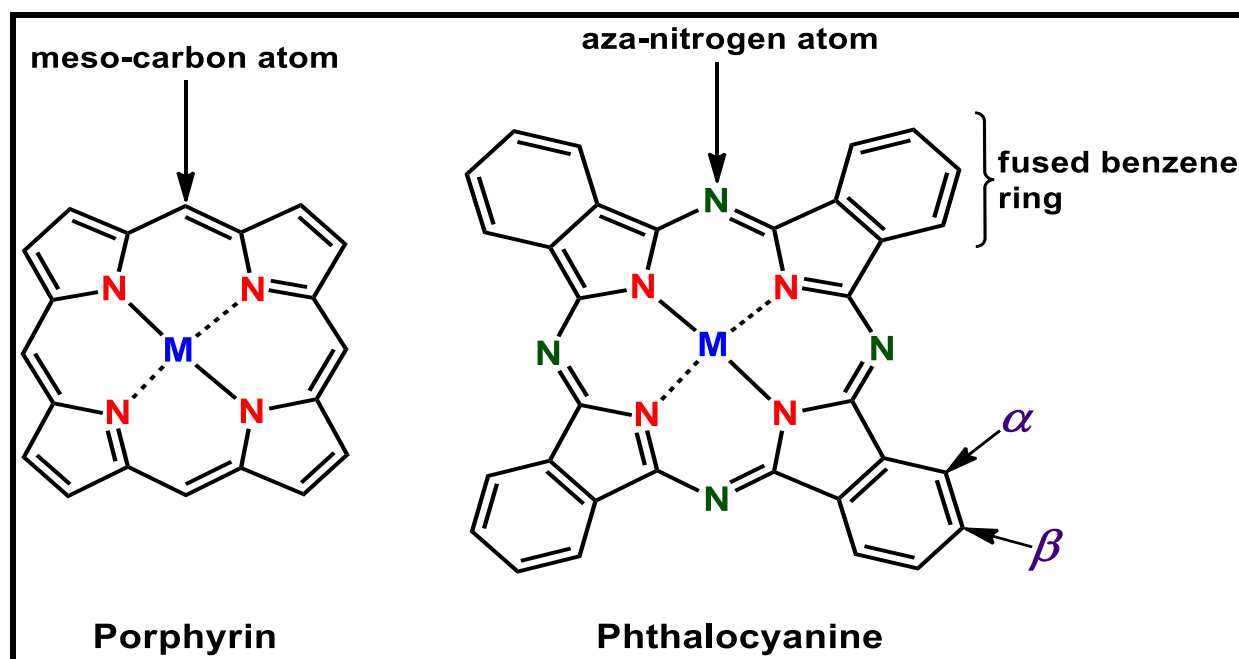


**Fig. 1.3:** General molecular structure of porphyrins and phthalocyanines.

rings also introduce substitutable hydrogen atoms at the  $\alpha$  (non-peripheral) and  $\beta$  (peripheral) positions (**Fig. 1.3**) which affords incredible variability in possible properties of the compounds. The central cavity of the molecules can accommodate various elements, mainly metals to form metallophthalocyanines (MPcs), which to a large extent give the compounds their distinct properties and possible applications [30–34].

Phthalocyanines are mainly characterised by their high chemical and thermal stability, but of most importance to the current work are their specific photophysicochemical properties which are due to the electronic transitions observed in these compounds. These properties include fluorescence and triplet quantum yields and lifetimes, but most importantly singlet oxygen generation.

### 1.2.1. Electronic absorption spectrum

The ground state electronic absorption spectra of MPcs are characterised by two main absorption bands, the more intense sharp Q-band and the less intense broad B-band (**Fig. 1.4**). The Q-band which is observed in the visible and near infrared regions of the electromagnetic spectrum is assigned to the  $\pi$ - $\pi^*$  transition between the ground state highest occupied molecular orbital (HOMO)  $a_{1u}$  to the lowest unoccupied molecular orbital (LUMO) degenerate  $e_g$ , according to Gouterman's four orbital model [35]. On the other hand, the B-band which is found in the ultraviolet region (usually between 300 and 400 nm) is due to the overlap of  $B_1$  and  $B_2$  bands, arising from the HOMO  $a_{2u}$  and  $b_{2u}$  to the LUMO  $e_g$ ,  $\pi$ - $\pi^*$  transitions, respectively (**Fig. 1.4**, insert), hence its observed broadness [36].

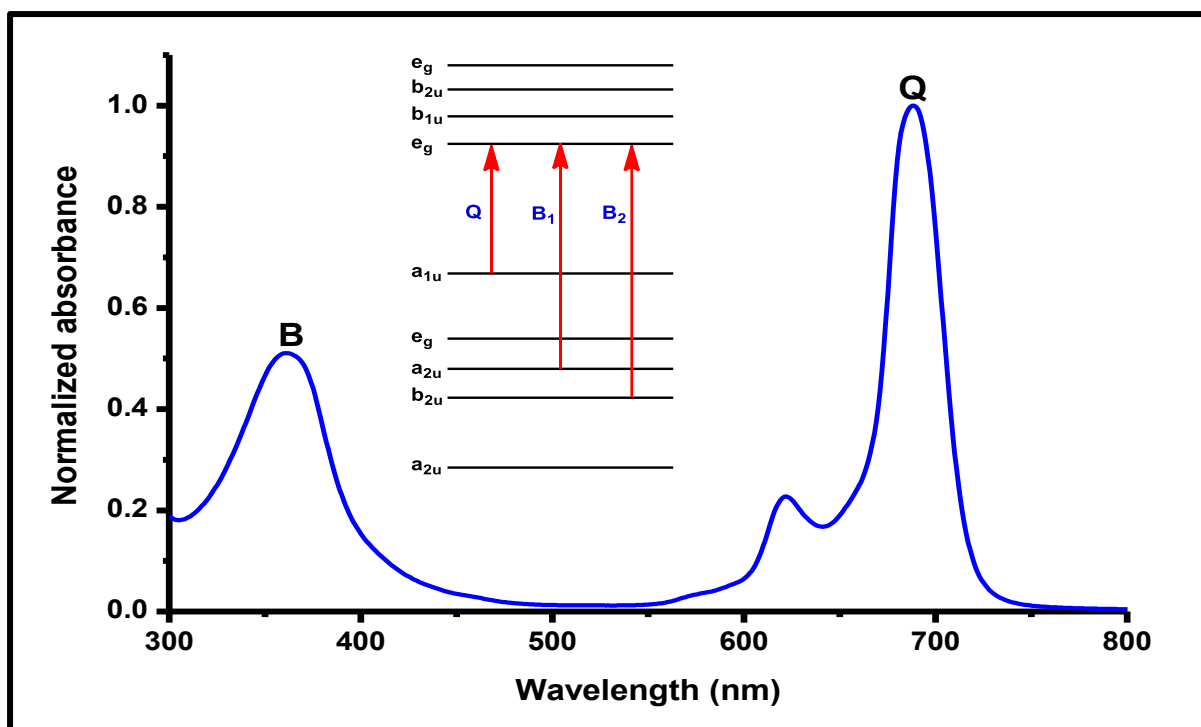
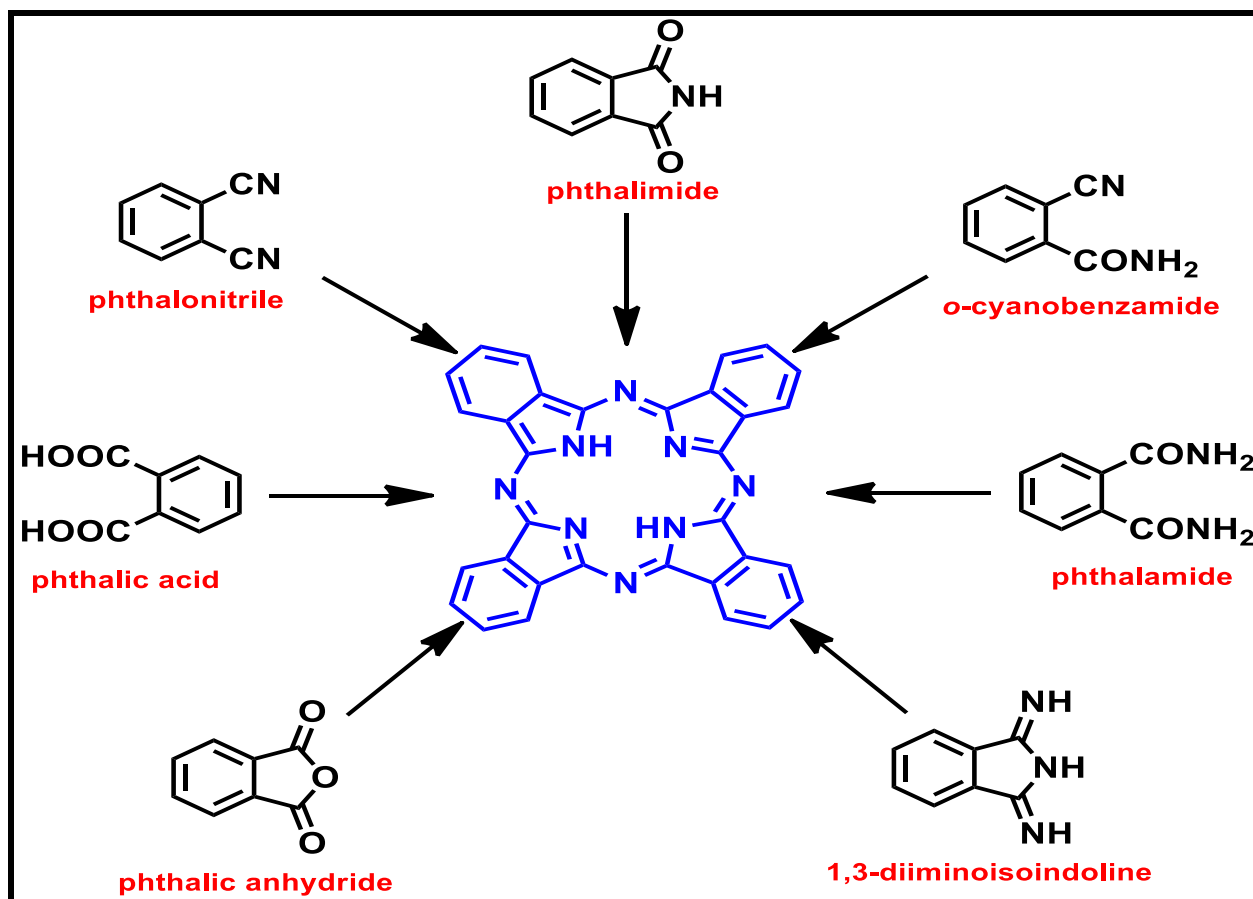


**Fig. 1.4:** Typical UV-Vis ground state electronic absorption spectrum of MPcs.

### 1.2.2. Synthesis

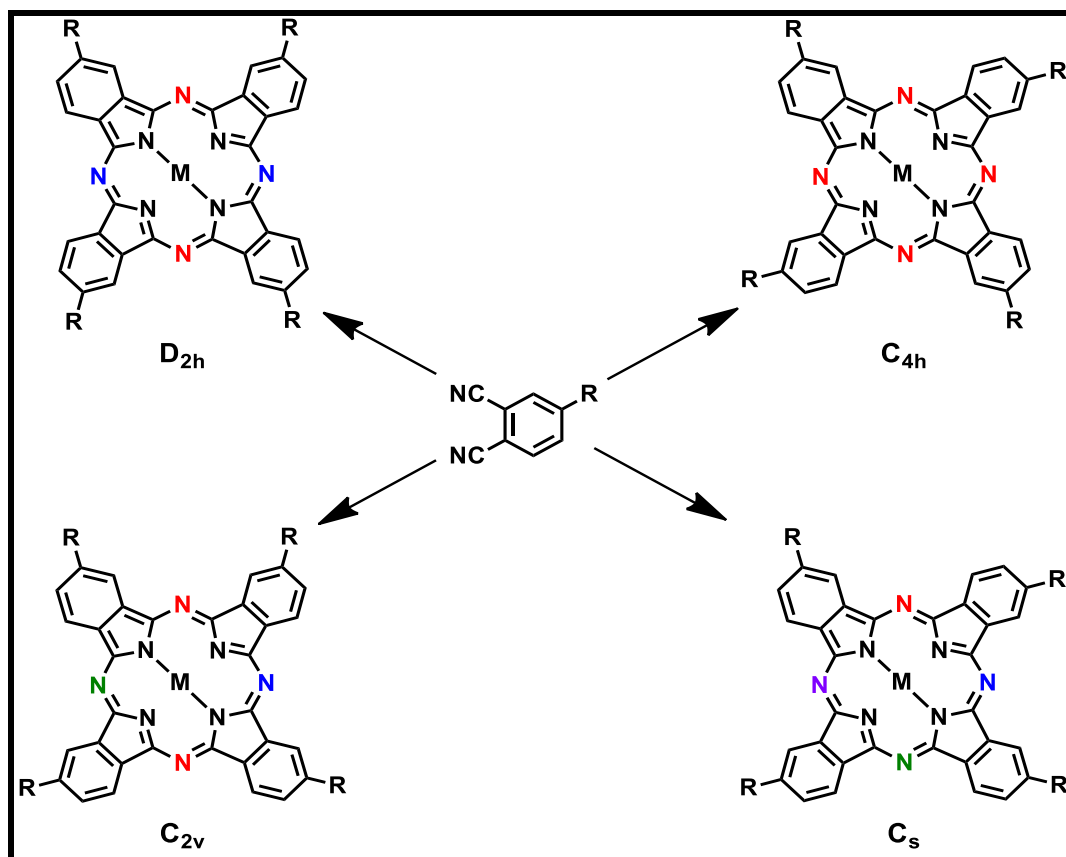
Phthalocyanine synthesis is achieved in several ways depending on the specific precursor available. **Scheme 1.1** summarizes the main precursors in Pc synthesis [37]. In general, synthesis involves refluxing the precursor in a high boiling point solvent in the presence of a metal salt (for MPcs), basic catalyst and usually an inert atmosphere. Other methods such as microwave synthesis and solvent free reactions have also been reported [37]. However, in this work synthesis was limited to the more popular conventional refluxing of phthalonitrile precursors. Substituted Pcs are usually synthesized from 4-nitrophthalonitrile and 3-nitrophthalonitrile precursors to give  $\beta$  and  $\alpha$ -substituted Pcs, respectively. Specially substituted Pcs can be obtained by modification of the phthalonitrile.



**Scheme 1.1:** Precursors for phthalocyanine synthesis.

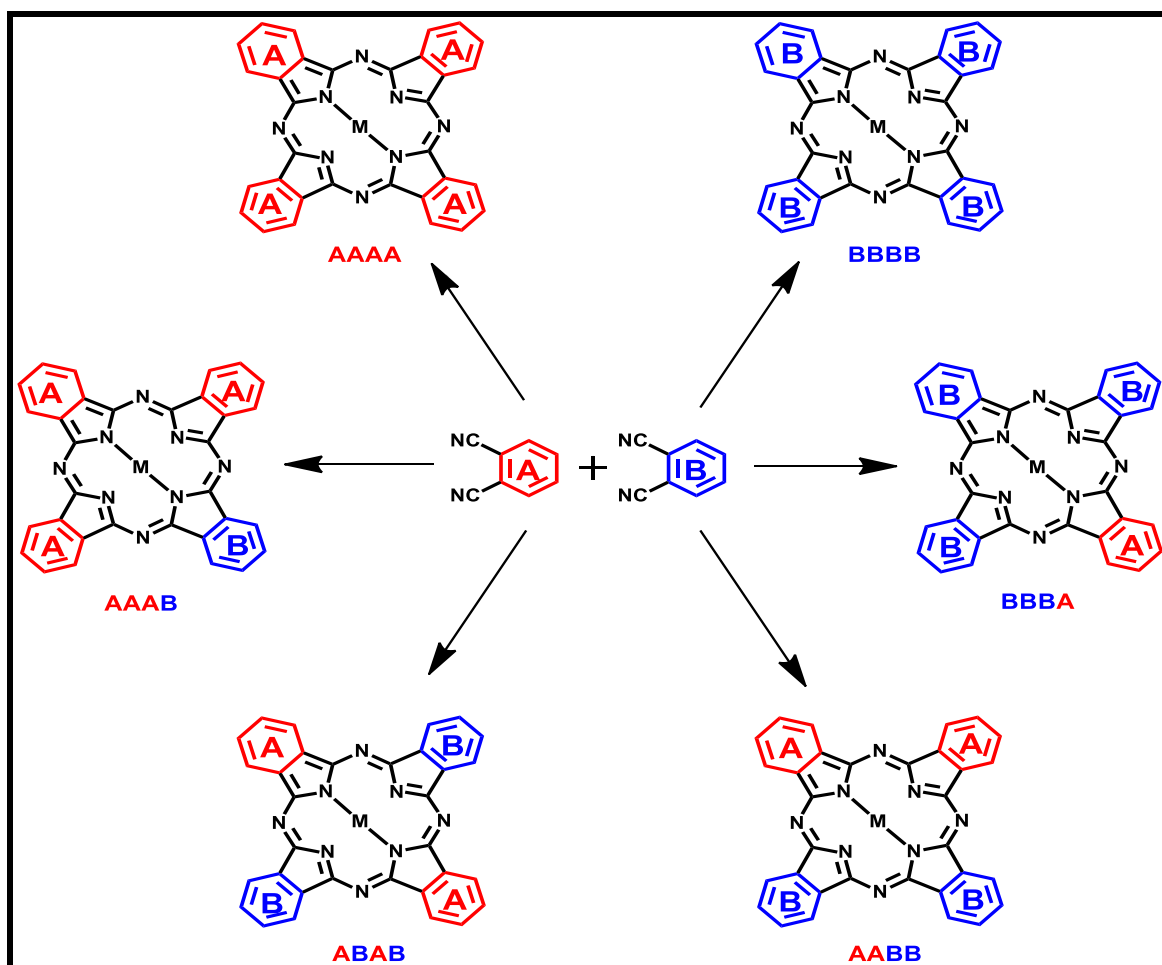
Cyclization of these mono-substituted phthalonitriles gives rise to mixtures of four constitutional isomers of tetra-substituted Pcs (**Scheme 1.2** using  $\beta$ -substituted MPcs as an example). On the other hand, cyclization of differently substituted phthalonitriles (mixed condensation) yields a mixture of six possible differently substituted MPcs (**Scheme 1.3**). This procedure is of significant importance in the synthesis of asymmetric (low symmetry) Pcs ( $A_3B$  or  $AB_3$ ). The desired compounds are then isolated by chromatography. Asymmetry in Pcs introduces macrocyclic distortions which have an effect on the Pc electronic states, giving rise to improved photophysical





**Scheme 1.2:** Constitutional isomers of symmetrical tetra- $\beta$ -substituted phthalocyanines.

properties [38]. Asymmetry is also important where specific directed conjugation of the Pc is required. In practice mixed condensation is carried out with a minimum ratio of 3:1 for the two differently substituted phthalonitriles to statistically enhance the probability of formation of the desired compound. Depending on the availability and reactivity of the phthalonitriles, higher ratios such as 10:1, may be employed to maximize the yields where  $A_3B$  or  $AB_3$  molecules are targeted. Other routes have also been developed to achieve asymmetrical Pcs, such as subphthalocyanine ring expansion and polymer-support based methods [38], but in this work statistical mixed condensation was applied.



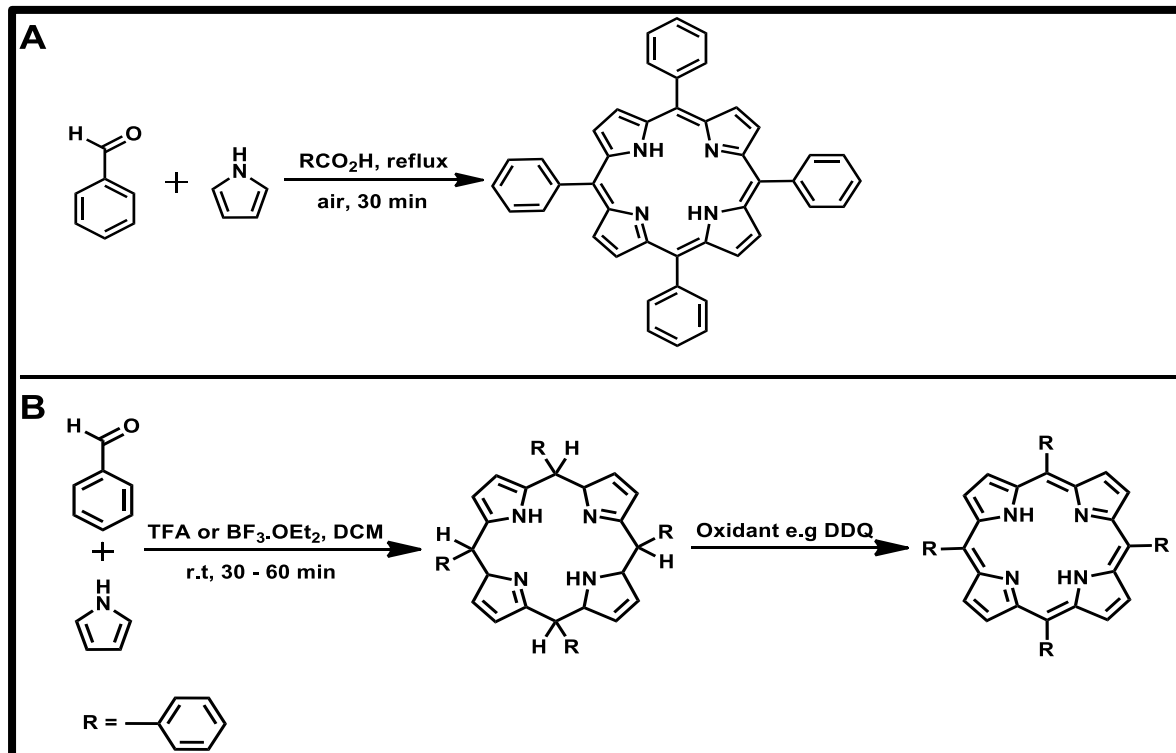
**Scheme 1.3:** Possible outcome phthalocyanines from a mixed condensation reaction.

### 1.2.3. Phthalocyanine-Porphyrin dyads

Phthalocyanine-Porphyrin dyads are heterocyclic dimers of Pcs and porphyrins. Although Pcs and porphyrins are structurally similar, the two have several significant differences. An example of such differences is that in their ground-state absorption spectra, which is to a large extent complementary where porphyrins have their characteristic absorption bands in the 400 – 650 nm region [39] unlike Pcs, and is of interest in this work. Coupling Pcs and porphyrins to form dyads thus combines their properties in the hybrids [40–42]. Formation of Pc-porphyrin dyads also has some new properties unique to the dimers and absent in their component macrocycles which have been studied in excited state dynamics and electrochemistry [41–46]. In this

thesis a novel Pc-porphyrin dyad is presented as a superior light harvesting photosensitizer for functionalization of polymer membranes. The application of Pc-porphyrin heterodyads in photocatalytic degradation of pollutants is also reported here for the first time.

Synthesis of Pc-Porphyrin dyads is strategized based on the synthesis of their Pc and porphyrin components [47]. The synthesis of Pcs has been discussed, and that of porphyrins is summarized in **Scheme 1.4** using tetraphenylporphyrin as an example. The Adler-Longo synthetic route (**Scheme 1.4 (A)**), which was used in this work, is mostly used with aldehydes that have functional groups that are not significantly sensitive to acidic conditions [48]. The Lindsey synthetic route (**Scheme 1.4 (B)**) on the other hand, allows the synthesis of porphyrins bearing acid sensitive functional groups [48]. For asymmetric porphyrins, synthesis is achieved by statistical



**Scheme 1.4:** Synthetic routes for tetraphenylporphyrin using (A) the Adler-Longo method, and (B) the Lindsey method.

condensation using two different aldehydes.

Two approaches can be employed in the synthesis of Pc-porphyrin heterodyads which are:

- i. Linking of the monomer macrocycles after separate synthesis.
- ii. Step-wise synthesis from a macrocyclic (Pc or porphyrin) precursor of one of the dyad component macrocycles (complementary to the precursor macrocycle).

Using both strategies, heterodyads with directly linked macrocycles, macrocycles with an extended conjugation linker and macrocycles with a discontinuous conjugation linker are possible [42–45,49]. However, separately synthesized monomer macrocycles may also be axially linked [41], which is not possible with the step-wise synthesis approach. Amide linkage of Pcs and porphyrins in the formation of dyads is reported in this thesis for the first time.

#### 1.2.4. Photosensitization

Photosensitization is based on the production of singlet oxygen and other reactive oxygen species (ROS). Oxygen exists in a triplet ground state ( $^3\Sigma_g^-$ ) with two unpaired electrons distributed in the highest occupied orbitals (**Table 1.2**) [50]. Excitation of molecular oxygen results in two possible singlet states,  $^1\Sigma_g^+$  (spin pairing electrons in different orbitals) and  $^1\Delta_g$  (both electrons are paired in a single orbital) (**Table 1.2**). Neither  $^1\Delta_g$  nor  $^1\Sigma_g^+$  has unpaired electrons, hence both are not radicals. In both  $^1\Delta_g$  and  $^1\Sigma_g^+$   $^1O_2$  forms, the spin restriction is removed such that the oxidizing ability is greatly increased [51]. The  $^1\Sigma_g^+$  form is however more reactive than the  $^1\Delta_g$  form resulting in a shorter lifetime. The  $^1\Sigma_g^+$  form rapidly decays to the  $^1\Delta_g$  form before chemical reactions can occur, hence reference to singlet oxygen in this thesis refers

**Table 1.2:** Different energy states of molecular oxygen.

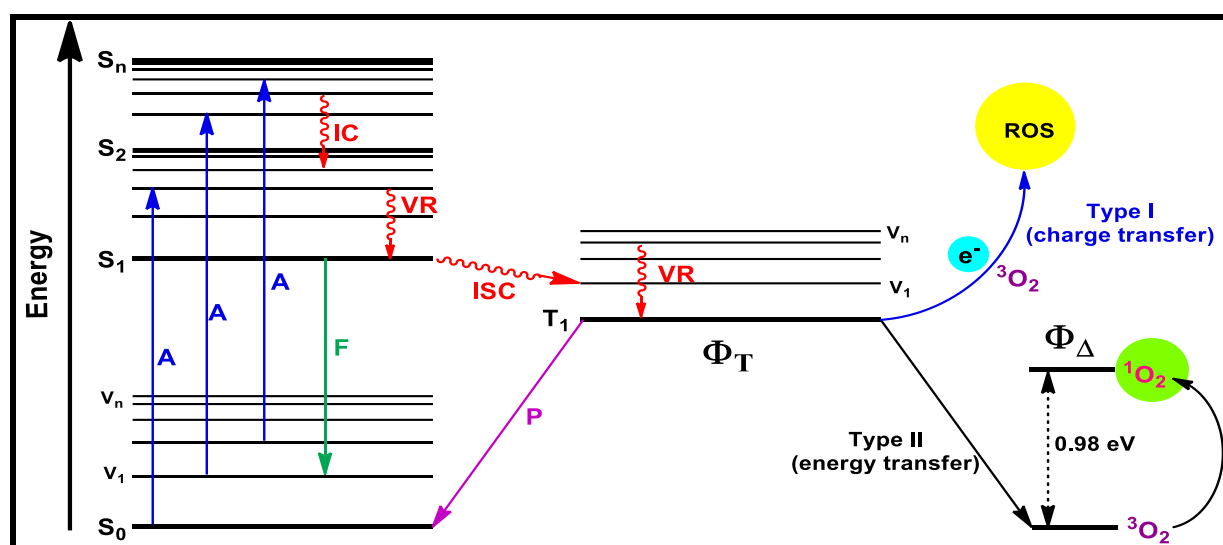
State of oxygen molecule	Highest orbital occupation	Energy above ground state
Ground state ( $^3\Sigma_g^-$ )	$\uparrow \quad \uparrow$	
First excited state ( $^1\Delta_g$ )	$\uparrow\downarrow \quad \text{---}$	22.4 kcal (0.98 eV)
Second excited state ( $^1\Sigma_g^+$ )	$\uparrow \quad \downarrow$	37.5 kcal (1,64 eV)

only to the  $^1\Delta_g$  form. It is also important to note that the lifetime of singlet oxygen depends on the nature of the solvent it is generated [52]. Singlet oxygen can be generated by chemical and physical methods. In chemical methods reactions of certain compounds with peroxides gives rise to singlet oxygen [51]. In physical methods singlet oxygen is generated either using photosensitizers following exposure to radiation of various wavelength or by microwave or radiofrequency discharge [53]. In this thesis, the focus will be on the photosensitizer mediated generation of singlet oxygen as a source of photocatalytic activity.

The mechanism of photocatalysis involves the excitation of a photosensitizer to the singlet excited state followed by intersystem crossing to the triplet excited state. From the triplet excited state, the photosensitizer may undergo redox reactions with its environment to give rise to reactive oxygen radicals (**Fig. 1.5**, Type I), or it may transfer its excitation energy to molecular oxygen to form singlet oxygen (**Fig. 1.5**, Type II). The key property of a photosensitizer for use in photocatalysis is hence sufficient population of triplet excited state molecules (high triplet quantum yields). The ability of various classes of compounds to populate the triplet excited state attracts their interest as potential photosensitizers, hence the interest in MPcs in this work. In the current work the most important property of interest is the generation of singlet oxygen. The excited singlet state of molecular oxygen lies 0.98 eV above its triplet ground state

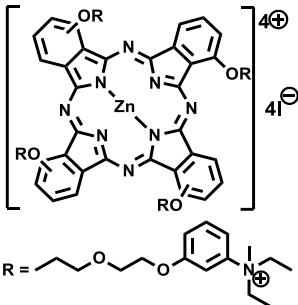
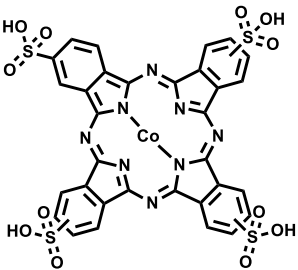
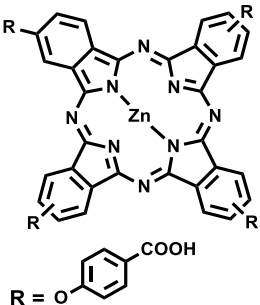
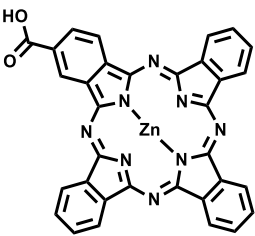
and hence the condition for single oxygen generation by MPcs is that their triplet excited state ( $T_1$ ) should be at least 0.98 eV [54] (**Fig. 1.5**).

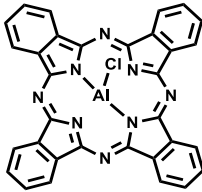
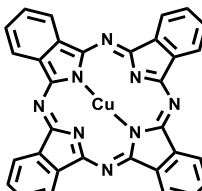
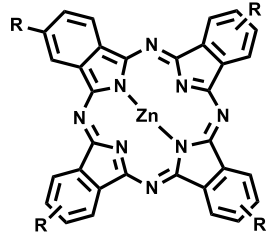
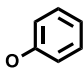
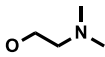
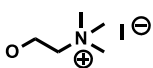
As the possible applications of MPcs continue to grow, so has the establishment of their application in water treatment related processes. The ability of MPcs to generate singlet oxygen and other reactive oxygen species makes them potential candidates as photosensitizers for photocatalytic degradation of pollutants and photodynamic antimicrobial chemotherapy (PACT). **Table 1.3** [55-72] gives some examples of reported MPc applications related to water treatment. As the table shows, there has been no studies on MPcs supported by non-solvent induced phase inversion polymer membranes, which are more stable compared to for example electrospun fibers.



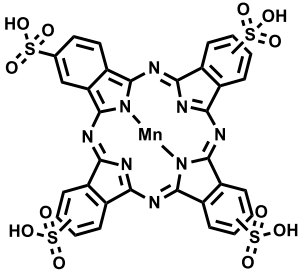
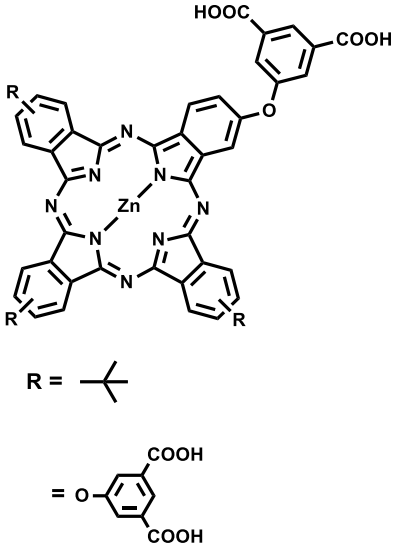
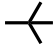
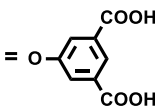
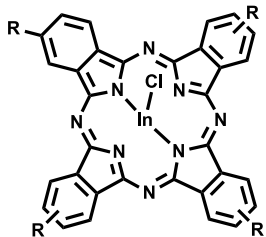
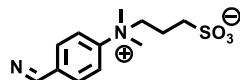
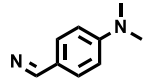
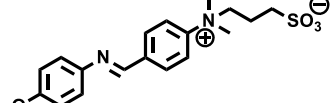
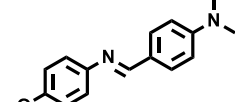
**Fig. 1.5:** Jablonski diagram showing the electronic transitions of a photosensitizer in the generation of singlet oxygen from triplet ground state molecular oxygen after irradiation with light. A = absorption; F = fluorescence; P = phosphorescence; IC = internal conversion; VR = vibrational relaxation; ISC = intersystem crossing;  $S_0$  = singlet ground state;  $S_1$  = first singlet excited state;  $S_n$  = nth singlet excited state;  $T_1$  = first triplet excited state;  $V_1$  = first vibrational energy level;  $V_n$  = nth vibrational energy level;  $^1O_2$  = singlet molecular oxygen;  $^3O_2$  = triplet molecular oxygen; ROS = reactive oxygen species.

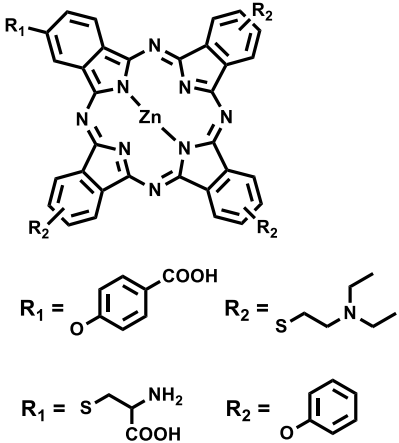
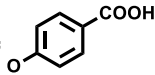
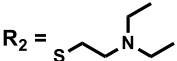
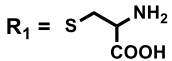
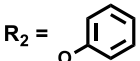
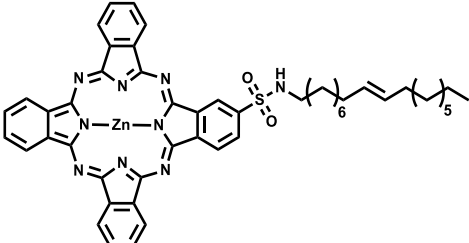
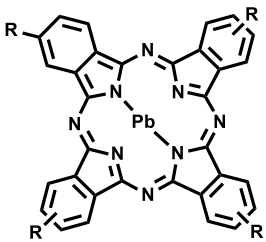
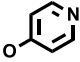
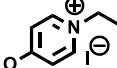
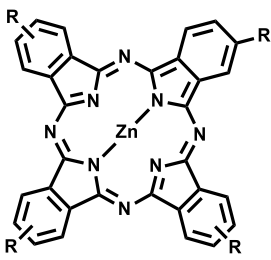
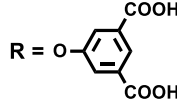
**Table 1.3:** Examples of phthalocyanine applications related to water treatment [55-72].

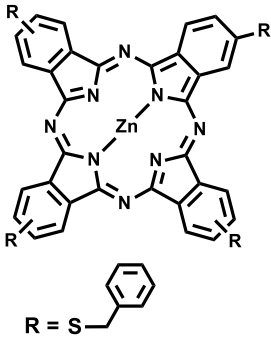
Phthalocyanine	Support/ Medium	Target of action/ Pollutant (Application)	Reference
	Titanium dioxide nanoparticles	Methylene orange and Cr (VI) ions  (Photodegradation)	[55]
	Titanium dioxide nanoparticles and MCM-41	4-chlorophenol and 2,4-dichlorophenol  (Photodegradation)	[56,57]
	Silica-coated gadolinium oxide nanoparticles	Orange G  (Photodegradation)	[58]
	Solution	<i>P.gingivalis</i> , <i>S.aureus</i> and <i>P.acnes</i>  (PACT)	[59,60]

	Bentonite clay, Solution	4-chlorophenol, 4-nitrophenol, 2,4-dichlorophenol, 2,4,6-trichlorophenol  <b>(Photodegradation)</b>  <i>P. aeruginosa</i> and <i>S. aureus</i>  <b>(PACT)</b>	[61,62]
	(Alumina)-zeolite-X	Cyanide  <b>(Photodegradation)</b>	[63]
 <p>R = NO<sub>2</sub></p>   	Mesoporous silica Al-MCM-41	Fenamiphos and pentachlorophenol  <b>(Photodegradation)</b>	[64]



	TiO <sub>2</sub> @SiO <sub>2</sub> hybrid nanoparticles	Rhodamine B and <i>o</i> -phenylenediamine  <b>(Photodegradation)</b>	[65]
 <p>R = </p> <p>= </p>	Cobalt ferrite nanoparticles embedded in electrospun fibers	Methyl Orange and Orange G  <b>(Photodegradation)</b>	[66]
 <p>R = </p> <p>= </p> <p>= </p> <p>= </p>	Silver-iron dimers (Ag-Fe <sub>3</sub> O <sub>4</sub> ) and silver-iron core shell (Ag@Fe <sub>3</sub> O <sub>4</sub> ) nanoparticles	<i>E. coli</i>  <b>(PACT)</b>	[67]

 <p> <math>R_1 = </math>  <math>R_2 = </math>  </p> <p> <math>R_1 = </math>  <math>R_2 = </math>  </p>	Polystyrene electrospun polymer fibers	<i>S.aureus</i>  (PACT)	[68]
	polyhydroxybutyrate polymer submicron fiber mat	<i>E.coli</i> and <i>E.faecalis</i>  (PACT)	[69]
 <p> <math>R = \text{PbTpyPc} = </math>  </p> <p> <math>\text{PbTepyPc} = </math>  </p>	Polystyrene electrospun nanofiber	<i>E.coli</i>  (PACT)	[70]
 <p> <math>R = </math>  </p>	Pd and Co nanoparticles decorated titania fibers	Methanol  (Photodegradation)	[71]

 <p>R = S-CH<sub>2</sub>-C<sub>6</sub>H<sub>5</sub></p>	Gold nanoparticles embedded in electrospun polystyrene fibers	4-Chlorophenol and Orange G  (Photodegradation)	[72]
--	---	---	------

#### 1.2.4.1. Photocatalytic degradation/ transformation of pollutants

Industrial activities such as production of dyes, pharmaceuticals, pesticides and plastics just to mention a few, give rise to organic by-products which easily find their way into the environment especially bodies of water [73–75]. These by-products may be toxic or not be completely biodegradable, hence posing a potential threat to the environment which nature cannot eliminate. Of particular concern are the chlorinated phenolic compounds in water since a number of elimination methods have proven to actually give rise to products that are more toxic than the starting compound [76–78]. In this regard, advanced oxidation processes (AOP) have hence gained popularity as cleaner and safer alternatives since only oxygen is used and toxic by-products are avoided [79].

The lucrative photocatalytic properties of Pcs and porphyrins has led to their applications in the development of AOP technologies with emphasis on catalyst recovery mechanisms, in which various materials have been applied as catalyst supports [57,61,63,64,80,81]. As an addition to existing technology, this thesis reports for the first time on the use of phthalocyanine-based photocatalyst functionalized asymmetric polymer membranes in the degradation of organic pollutants in water, and

their potential development as efficient solar radiation activated material. 4-Chlorophenol was used as a model chlorinated phenolic pollutant for the reasons stated above. As **Table 1.3** shows, Pcs have not been supported on polymer membranes for the degradation of phenols.

#### 1.2.4.2. Photodynamic antimicrobial chemotherapy (PACT)

Photodynamic antimicrobial chemotherapy (PACT) is an alternative microbial eradication strategy that uses a photosensitizer which is activated by light of a specific wavelength to give rise to reactive oxygen species which then destroy the microorganisms [82]. The establishment and continued research in this treatment modality has been motivated by the rapid evolutionary changes in microorganisms that is continuously giving rise to drug resistant pathogens [83,84]. Conjugation of MPcs to metallic nanoparticles encourages intersystem crossing to the triplet excited state [85], hence MPc-silver nanoparticle conjugates were applied in this work. **Table 1.3** gives examples of some MPcs and various MPc-nanoparticle conjugates reported in literature that have been used in PACT.

The effectiveness of PACT to the largest extent is dependent on the extent and efficiency of photosensitizer binding onto and/ or penetration into the microorganism [86]. This in turn depends on the nature of the microorganisms' cell wall structures (Gram (+) or Gram (-)) and the overall charge of the photosensitizer [87]. **Fig. 1.6** shows the generalized structures of Gram (+) and Gram (-) microorganism cell wall structures. Gram (+) cell wall structure such as that of *S.aureus*, consists of a single cell membrane which offers less resistance to penetration of photosensitizers into the cells and rupturing of the cell envelope as compared to the Gram (-) strains [88,89].

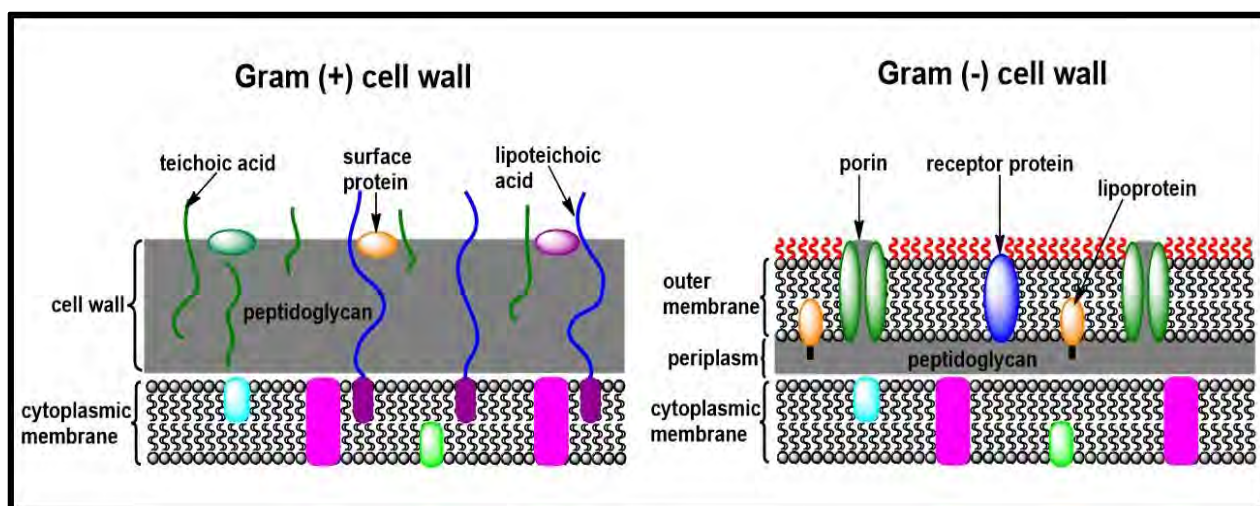


**Fig. 1.6:** Schematic structures of Gram (+) and Gram (-) bacteria cell walls.

Microorganisms generally have a negative surface charge, hence positive photosensitizers have less to no electrostatic resistance to approach and bind or penetrate the microorganisms' cell wall envelopes regardless of the cell wall structure (Gram (+) or Gram (-)). On the other hand, neutral and negative photosensitizers experience electrostatic based resistance to binding and penetration of microorganisms [86]. In this thesis antimicrobial studies were done using *S.aureus* (Gram (+) bacteria) as a model microorganism. *S.aureus* was chosen due to its recognition as a leading cause of infective endocarditis, bacteraemia, skin and soft tissue, osteoarticular, pleuropulmonary and device- related infections [90] and its reported drug resistance [83,84,91]. *S.aureus* was also chosen, as a Gram (+) microorganism, due to the sensitivity of Gram (-) microorganisms to sulfur content in their environment [92] which may influence experimental outcomes.

PACT was mainly established as an infection treatment modality [82,93], but in the current work, the principles of PACT were adopted to introduce antimicrobial activity in polymer membranes for enhanced water treatment and biofouling resistance. The examples in **Table 1.3** are representative of the various states and supports in which

MPcs have been used for PACT and it can be observed that no studies have been done using polymer membranes as photosensitizer supports, hence this is reported for the first time in this thesis. The application of a positive polymer membrane surface charge for biofouling resistance is also introduced and briefly evaluated for the first time here.

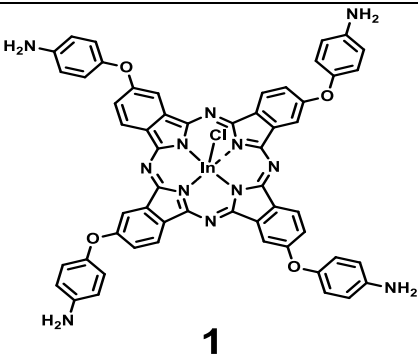
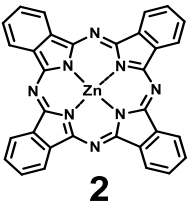
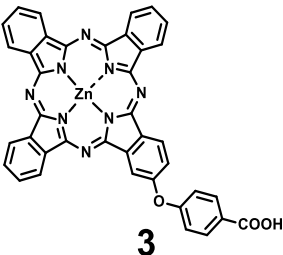
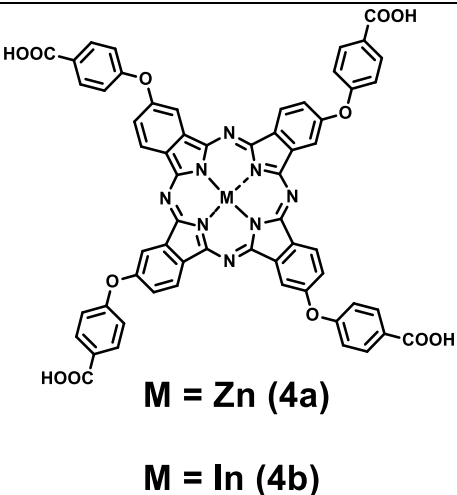
#### 1.2.5. Phthalocyanines used in this study

The structures and names of phthalocyanines used in this study are summarized in **Table 1.4**. Both symmetrical and asymmetrical phthalocyanines were synthesized with either zinc or indium as central metals. Zinc and indium were chosen as central metals because of their diamagnetic closed shell structures and their relatively heavy nuclei, which give MPcs favorable triplet and singlet oxygen quantum yields [94,95]. All substitutions on the phthalocyanines were peripheral. The choice of substituents was mainly motivated by the specific conjugation requirements for each molecule. In general, NH<sub>2</sub> and COOH functionalized substituents were used to allow for amide conjugation of the MPcs. Complexes **1**, **3** and **4a** have been reported [96-98], the rest of the complexes are new.

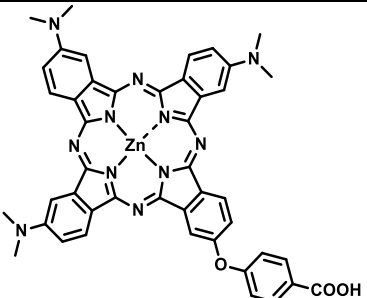
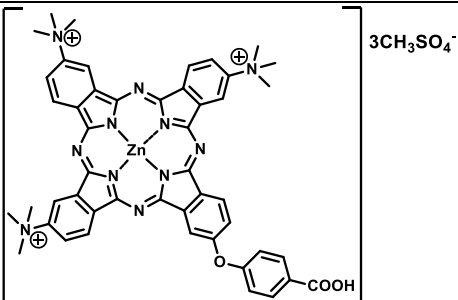
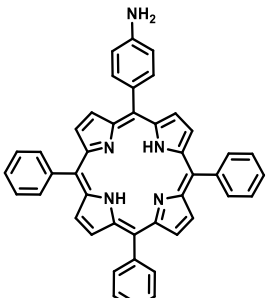
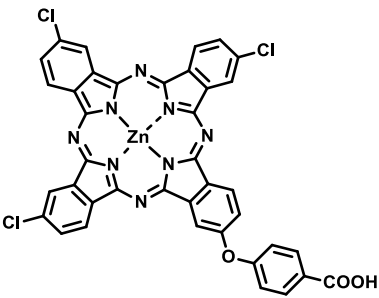
Where asymmetric molecules were used, choice of substituents was to allow the molecules to be conjugated to other material and also have additional functionality (complexes **5**, **6** and **9**). Dimethyl amino substituents in complex **5** were used to enable further modification of the molecule through quaternization to give complex **6**. Chloro substituents in complex **9** were used to possibly enhance intersystem crossing to the triplet state in the MPc through spin orbit coupling (heavy atom effect) [95], but most importantly to enable further conjugation of complex **10** to the polymer. Complex **7** was obtained as an intermediate that was not isolated and hence will not be discussed

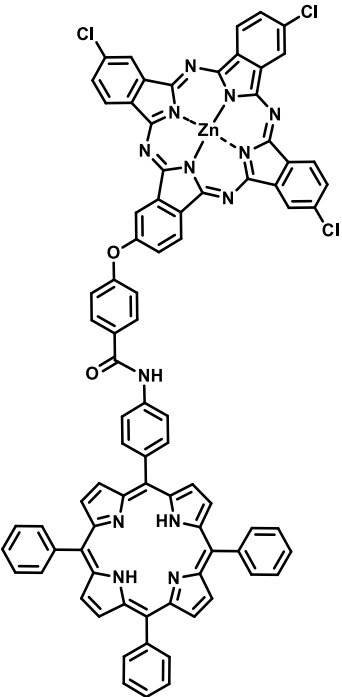
in this thesis. Complexes **2**, **3** and **4a** will be compared for effect of symmetry and substitution, while complexes **1** and **4b** will be compared for variation in substituents. Complexes **5**, **6** and **9** will also be compared for variation in substituents while complexes **5** and **6** will be compared for the effect of quaternization. Complexes **8** and **9** were used to form complex **10** which was used for enhanced light harvesting.

**Table 1.4:** Phthalocyanines used in this study.

Complex structure	Nanoparticles used [Conjugates]	Complex name (Application)
	-	2(3),9(10),16(17),23(24)-tetrakis-(4-aminophenoxy) phthalocyaninato indium (III) chloride [96]  <b>(Photophysics)</b>
	Graphene quantum dots (GQDs) [2 $\pi$ (GQDs)]	Zinc (II) phthalocyanine (ZnPc) [purchased]  <b>(Photophysics and Photodegradation)</b>
	Graphene quantum dots (GQDs) [3 $\pi$ (GQDs) and 3(GQDs)]	2-(4-carboxyphenoxy) phthalocyaninato zinc (II) [97]  <b>(Photophysics)</b>
	Silver triangular nanoprisms (AgTNPs) [4a(AgTNPs) and 4b(AgTNPs)]	2(3),9(10),16(17),23(24)-tetrakis-(4-carboxyphenoxy) phthalocyaninato zinc (II) [98]  2(3),9(10),16(17),23(24)-tetrakis-(4-carboxyphenoxy) phthalocyaninato indium (III) chloride <b>(New)</b>  <b>(Photophysics and PACT)</b>



 <p style="text-align: center;"><b>5</b></p>	-	<p>2-(4-carboxyphenoxy)-9(10), 16(17), 23(24)-tris- (dimethylamino)phthalocyaninato zinc (II) <b>(New)</b></p> <p><b>(Photophysics and PACT)</b></p>
 <p style="text-align: center;"><b>6</b></p>	-	<p>2-(4-carboxyphenoxy)-9(10), 16(17), 23(24)- tris(trimethylamino) phthalocyanine zinc (II) methyl sulfate <b>(New)</b></p> <p><b>(Photophysics and PACT)</b></p>
 <p style="text-align: center;"><b>8</b></p>	-	<p>5-(4-aminophenyl)-10,15,20- triphenylporphyrin <b>(New)</b></p> <p><b>(Photophysics)</b></p>
 <p style="text-align: center;"><b>9</b></p>	-	<p>2-(4-carboxyphenoxy)-9(10), 16(17), 23(24)- trichlorophthalocyaninato zinc (II) <b>(New)</b></p> <p><b>(Photophysics)</b></p>

 <p style="text-align: center;"><b>10</b></p>	-	<p>2-(4-[4-(10,15,20-triphenylporphin-5-yl)phenyl]-amidophenoxy)-9(10), 16(17), 23(24)-trichlorophthalocyaninato zinc (II) <b>(New)</b></p> <p><b>(Photophysics and Photodegradation)</b></p>
--	---	---

### 1.3. Nanoparticles

Nanoparticles, by definition are particulate material which have dimensions in the range 1-100 nm, but there are some exceptions where the dimensions extend beyond 100 nm [99]. The size range limit of the definition represents the state where most materials exhibit phenomenal properties different from those of the bulk material (upper limit of the range) and those of atomic or molecular entities (lower limit of the range), and are observed to be size dependent [100]. Nanoparticle properties differ from one particle to the next mainly based on composition, size and shape [99]. In this study two types of nanoparticles were strategically employed, namely graphene quantum dots and silver triangular nanoprisms together with MPcs for organic pollutant degradation and enhanced PACT activity, respectively.

### 1.3.1. Graphene quantum dots (GQDs)

Graphene quantum dots can be described in the most modest way as single layers to tens of layers of graphene sheets with characteristic cross-section dimensions less than 30 nm [101–105]. These nanoparticles have a fairly flat  $\pi$  electron rich general graphitic carbon assembly which may be decorated with various functional groups including incorporation of heteroatoms in the honeycomb carbon atom network. The  $\pi$  electron rich structure gives GQDs good  $\pi$ - $\pi$  interaction capability with other  $\pi$  electron rich materials. This attribute of GQDs has drawn attention to their potential application in sensing systems [101,106–108] and may also pave the way for other conceivable applications. Incorporation of various heteroatoms in the graphitic structure together with adjusting nanoparticle size, modulate GQDs properties. The remarkable properties of GQDs which include low toxicity, chemical and thermal stability, stable photoluminescence, a well-defined quantum confinement effect, and many more have attracted attention to their potential application in electronics, imaging, biological systems and environmental applications just to mention a few [101–106,108–111].

GQDs are generally synthesized using two strategies namely, top-down and bottom-up approaches. Top-down methods involve the breakdown of large graphene-like material such as graphene, carbon nanotubes, fullerenes and natural coals, into nanosized structures characteristic of GQDs [103,112,113]. The break-down is achieved by subjecting the precursor materials to processes such as acid oxidation and exfoliation, hydrothermal and solvothermal processes, microwave reactions and electrochemical oxidation. On the other hand the bottom-up methods involve hydrothermal or solvothermal (autoclave or microwave) reactions and pyrolysis of

carbon source molecular precursors [112,113]. Introduction of heteroatoms can be achieved post GQDs synthesis or in-situ during synthesis in both top-down and bottom-up approaches [103,113]. In this work the bottom-up autoclave hydrothermal reaction of citric acid and polyethylenimine (PEI) was applied to achieve amine functionalized GQDs.

In the current study, focus and interest is on the  $\pi$ - $\pi$  interaction abilities of GQDs with MPcs. The objective for the use of GQDs to be more specific in this work, was to eliminate the requirement for specific functional groups on MPcs for them to be applicable in polymer membrane functionalization. Other graphitic nanomaterials such as carbon nanotubes and graphene oxide have been incorporated into polymer membranes [12], but incorporation of GQDs or their conjugates with MPcs is reported in this thesis for the first time. Enhancement of MPc triplet and singlet oxygen quantum yields following conjugation to GQDs has been reported before [114,115], and would be applicable in the current study. GQDs linked to MPcs have been reported before for applications in sensing [107], nonlinear optics [114] and drug delivery [116], just to mention a few. However, as noted in **Table 1.3**, no reports have yet been made on the application of MPc-GQDs nanoconjugates in water treatment or pollution control, hence this is reported here for the first time.

### 1.3.2. Silver triangular nanoprisms (AgTNPs)

Silver triangular nanoprisms or silver nanoplates, are nanosized three-dimensional triangle (normally equilateral) shaped silver nanoparticles. The thickness of these nanoplates is usually a distinctly small fraction of the triangle edge length, which is the main size characterization of these nanoparticles. These nanoparticles are characterized by their distinct spectroscopic properties, especially their absorption

spectrum which consists of three surface plasmon resonance (SPR) bands. The three bands correspond to various modes of plasmon excitation of triangular nanoplates [117]. The two main bands, a less intense sharp peak around 335 nm (**Fig. 1.7, a**) and a broader more intense peak from about 400 nm to over 1000 nm depending on nanoparticle size (**Fig. 1.7, c**), are due to the out-of-plane quadrupole resonance and in-plane dipole resonance, respectively. The third band appears between the two main peaks (usually as a shoulder) and is attributed to the in-plane quadrupole resonance of the nanoplates (**Fig. 1.7, b**). These nanoparticles are water soluble when bare, but solubility may vary upon capping. AgTNPs, like silver nanospheres, are well recognized for their antimicrobial properties, but are reported to be more active than the spheres, which has been attributed to higher percentages of high-atom-density facets such as {111} in these nanoparticles [118,119].

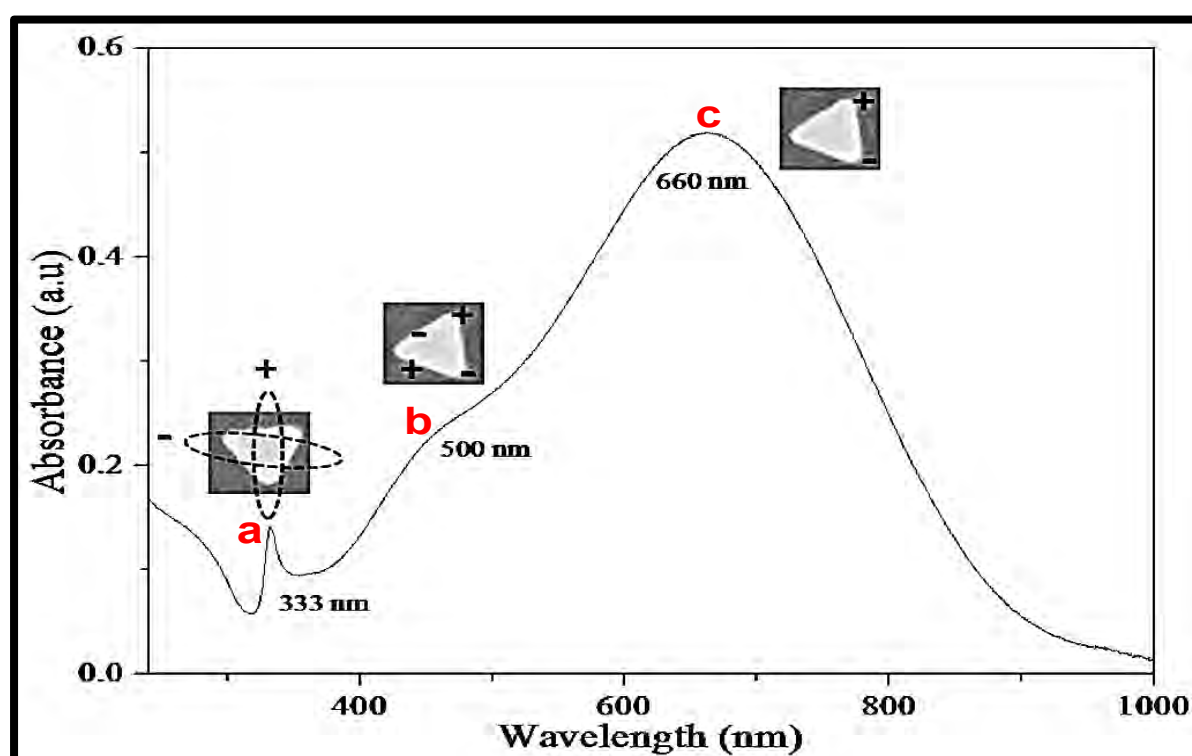


**Fig. 1.7:** UV-Vis spectrum of AgTNPs showing the characteristic SPR bands adapted from Bakar *et al* [117].

There are generally two strategies for the synthesis of AgTNPs namely, thermal and photochemical methods [120]. In the photochemical methods, light of specific wavelength is used to selectively excite the plasmon of nanoprisms precursors resulting in the formation of tailored nanoparticles. The relevance of this strategy is mainly observed in the significant control of the size and shape of the synthesized nanoparticles [121]. On the other hand, thermal methods involve gradual conversion of colloidal nanoparticles into the desired triangular nanoprisms. Most reported thermal methods are quick (less than 20 min) one-pot synthesis at room temperature without the use of special equipment, but lack the ability to control the size and thickness of the particles [120,122]. However, research on these methods is still in progress and some synthetic routes that enable control of edge length and thickness have been developed [120]. In the current study size specificity was not a strict requirement although relatively large nanoparticles were targeted, and hence a thermal method was applied for convenience.

AgTNPs were used to introduce light independent antimicrobial activity (for which they are superior to spheres [118,119]) of the functionalized polymer membranes in addition to enhancement of MPc triplet properties, loading and dispersity in the membranes. This is the first time that AgTNPs have been used to functionalize water treatment polymer membranes, especially as part of a photocatalyst.

## 1.4. Summary of aims and objectives

### Aim

To introduce, evaluate and validate phthalocyanine photoactivation of nonsolvent induced phase invasion asymmetric polymer membranes for pollution control and antimicrobial activity in water.

### Specific objectives

1. To identify and select polymers to use in the study.
2. To establish parameters for preparation of satisfactorily structured asymmetric polymer membranes by nonsolvent induced phase invasion.
3. To establish strategies of introducing MPcs as stable photosensitizers in asymmetric polymer membranes.
4. To design, synthesize and characterize novel MPcs for polymer membrane functionalization.
5. To characterize the photoactive polymer membranes and quantify their photoactivity by determining their singlet oxygen quantum yields.
6. To synthesize and characterize graphene quantum dots and silver triangular nanoprisms, their conjugates to MPcs and their corresponding functionalized polymer membranes.
7. To investigate and evaluate the possible antimicrobial activity enhancements of photoactive polymer membranes by incorporation of silver triangular nanoparticles and quaternized MPcs.
8. To investigate the organic pollutant photodegradation potential of MPc functionalized polymer membranes by studying their photodegradation kinetics of 4-chlorophenol as a model organic pollutant.

9. To synthesize, characterize and evaluate a MPc-porphyrin heterodyad as a potential efficient solar harvesting photosensitizer for potentially applicable polymer membrane functionalization.



# CHAPTER 2

## 2. Experimental

### 2.1. Materials

#### 2.1.1. General reagents and solvents

Methanol, ethanol, tetrahydrofuran (THF), acetone, ethyl acetate (EtOAc), diethyl ether, dimethyl sulfoxide (DMSO), cyclohexane, acetonitrile, deuterium oxide ( $D_2O$ ) and deuterated DMSO ( $DMSO-d_6$ ) were obtained from Merck. 1,3-Diphenylisobenzofuran (DPBF), anthracene-9,10-bismethylmalonate (ADMA), 9,10-dimethylantracene (DMA), anhydrous dimethylformamide (DMF), *N*-(3-dimethylaminopropyl)-*N'*-ethylcarbodiimide hydrochloride (EDC), *N*-hydroxysuccinimide (NHS), *N,N'*-dicyclohexylcarbodiimide (DCC), zinc (II) phthalocyanine (ZnPc), zinc (II) tetraphenylporphyrin (ZnTTP) and deuterated chloroform ( $CDCl_3$ ) were obtained from Sigma Aldrich. Hydrochloric acid, chloroform and Rose Bengal (RB) were purchased from Minema, B & M Scientific and Fluka respectively. ClAlPcSmix containing a mixture of differently sulfonated Pc derivatives was synthesized as reported before [123], and used as a singlet oxygen reference standard in water.

#### 2.1.2. Reagents for polymer modification and membrane synthesis

Unfunctionalized polyacrylonitrile (PAN, MW = 150 000 Da), unfunctionalized polystyrene (PS, MW = 192 000 Da), hydroxymethyl-polystyrene ((HOMe)PS, 200-500 mesh, 1.1 mmol/g loading), chromium trioxide and hydrazine monohydrate were obtained from Sigma Aldrich. Nitric acid (55 %) and stannous chloride dihydrate were purchased from Saarchem. Sulphuric acid (98 %) was obtained from Merck.

### 2.1.3. Reagents for phthalocyanine and porphyrin synthesis

Zinc (II) acetate dihydrate, indium (III) chloride, *n*-pentanol, dimethylamino ethanol (DMAE), 1,2,4-trichlorobenzene (TCB), tetrakis(triphenylphosphine)palladium(0) (Pd(PPh<sub>3</sub>)<sub>4</sub>), pyrrole, 1,4-dioxane, benzaldehyde, propionic acid, dimethyl sulfate (DMS) and potassium *tert*-butoxide (KOtBu) were obtained from Sigma Aldrich. 1,8-Diazabicycloundec-7-ene (DBU) was purchased from Merck.

### 2.1.4. Reagents for nanoparticle synthesis

Silver nitrate, sodium borohydride, sodium citrate, poly(sodium 4-styrenesulfonate) (PSSS, MW = 1 000 000 Da) and glutathione were obtained from Sigma Aldrich. Hydrogen peroxide was purchased from Merck.

### 2.1.5. Reagents and materials for photodegradation and bacterial studies

4-Chlorophenol (4-CP) was purchased from Fluka. The bacteriological BBL Muller Hinton broth and nutrient agar were obtained from Merck. *S.aureus* (ATCC 25923) was bought from Davies Diagnostics, South Africa. Phosphate buffer saline (10 mM PBS) pH 7.4 (for bacterial studies) or pH 11.0 (for 4-CP degradation studies) was prepared using appropriate amounts of Na<sub>2</sub>HPO<sub>4</sub> and NaOH in ultra-pure water from either a Milli-Q Water system (Millipore Corp, Bedford, MA, USA) or ultra-pure Type II water obtained from Elga PURELAB chorus 2 (RO/DI) system.

## 2.2. Equipment

- i. Ultraviolet–visible spectra (UV–Vis) for solutions were recorded on a Shimadzu UV–Vis 2550 spectrophotometer.
- ii. UV–Vis spectra for solid samples were obtained from a Perkin Elmer Lambda 950 UV–Vis NIR spectrophotometer where reflectance measurements were

converted into equivalent absorption spectra using the reflectance of holmium as a reference.

- iii. Excitation and emission spectra were recorded on a Varian Eclipse spectrofluorimeter.
- iv. Fluorescence lifetimes were measured using time correlated single photon counting (TCSPC) setup (PicoQuant FluoTime 300), **Fig. 2.1**. The excitation sources were diode lasers (LDH-P-670 (for Pc) driven by PDL 800-B, 670 nm, 20 MHz repetition rate, 44 ps pulse width, PicoQuant GmbH). LDH-P-375 driven by PDL 800-B, 670 nm, 20 MHz repetition rate, 44 ps pulse width was used for exciting at a wavelength where GQDs absorbed, while an LDH-P-485 driven by PDL 800-B, 670 nm, with a 10 MHz repetition rate, 88 ps pulse width was applied

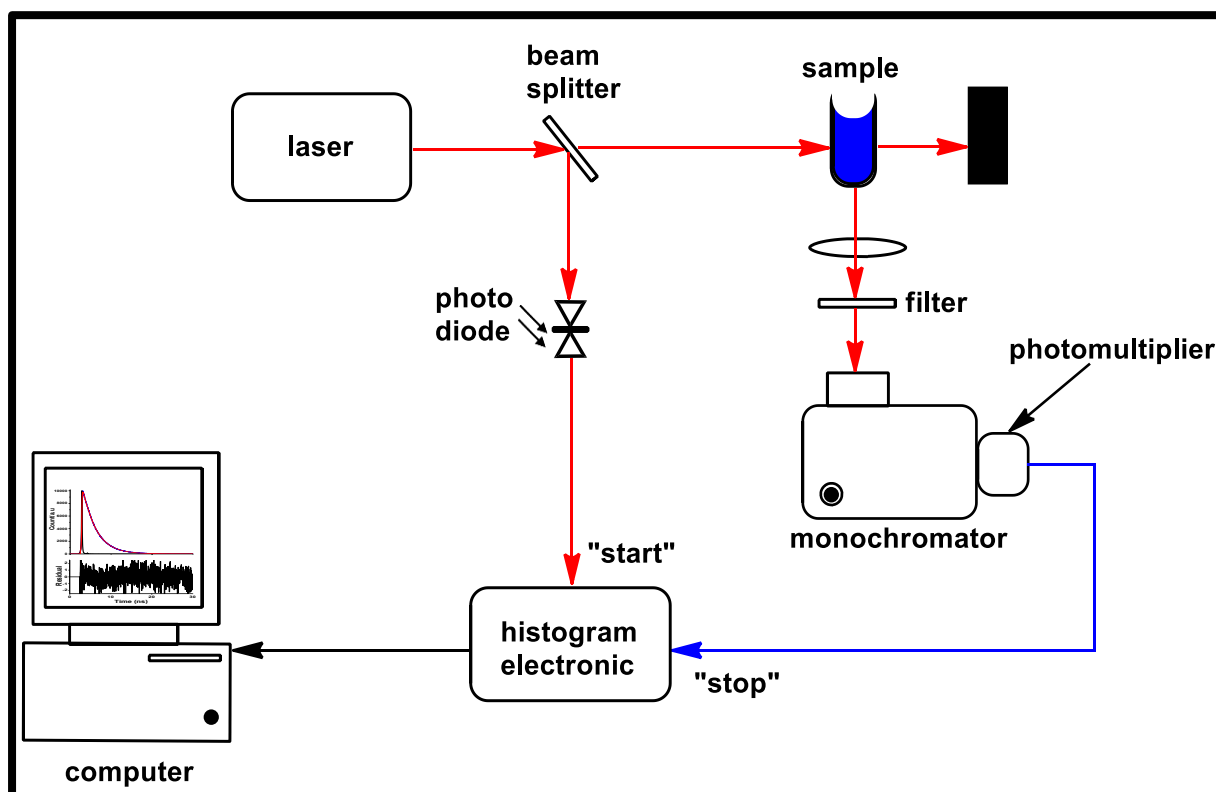


**Fig. 2.1:** Schematic diagram of the TCSPC setup.

where the porphyrin absorbed. The response function of the system, which was measured with a scattering LUDOX (HS-40) colloidal silica (DuPont), had a full width at half-maximum (FWHM) of 300 ps. The luminescence decay curve was measured at the maximum of the emission peak and the lifetime was obtained by deconvolution of the decay curve using the FluoFit Software program (PicoQuant GmbH, Germany). The errors of the decay times were estimated using the support plane approach.

- v. A laser flash photolysis system consisting of an LP980 spectrometer (Edinburgh Instruments) with a PMT-LP detector and an ICCD camera (Andor DH320T-25F03) was used to determine triplet quantum yields. **Fig. 2.2** shows the laser flash photolysis system schematic setup. The signal from a PMT detector was recorded on a Tektronix TDS3012C digital storage oscilloscope. The excitation pulses were produced using a tuneable laser system consisting

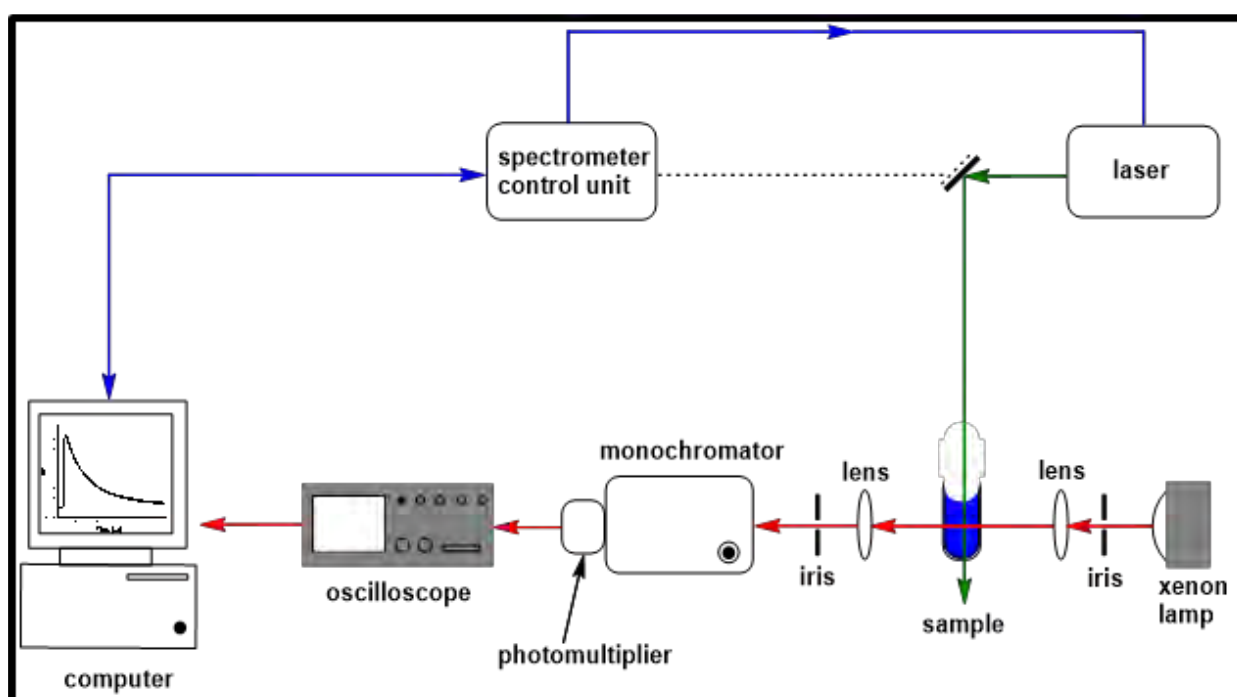


**Fig. 2.2:** Schematic diagram of the laser flash photolysis setup.

of an Nd:YAG laser (355 nm, 135 mJ/4-6 ns) pumping an optical parametric oscillator (OPO, 30 mJ/3-5 ns) with a wavelength range of 420 - 2300 nm (NT-342B, Ekspla). Exponential fitting of the kinetic curves using OriginPro 8 software gave the triplet lifetimes.

- vi. Low speed centrifugation (up to 4000 rpm) during purification of metallophthalocyanines, modified polymers and photosensitizer-polymer conjugates was achieved using an Eppendorf Centrifuge 5810.
- vii. High speed centrifugation (up to 20000 rpm) during concentration and purification of nanoparticles and their conjugates with metallophthalocyanines was achieved using a Beckman Coulter Allegra 64R Centrifuge.
- viii. A Berghof (Germany) High Pressure Laboratory Reactor (highpreactor) BR-300, V.3.0 equipped with PT-100 temperature and pressure sensors, BTC-300 Temperature regulator and manometer and PTFE lining was used for hydrothermal syntheses.
- ix. Proton nuclear magnetic resonance ( $^1\text{H}$  NMR) spectra were recorded on a Bruker AVANCE II 600 MHz NMR spectrometer.
- x. Mass spectral data were collected with a Bruker AutoFLEX III Smartbeam TOF/TOF Mass spectrometer, using  $\alpha$ -cyano-4-hydrocinnamic acid as the MALDI matrix.
- xi. The thermal decomposition profiles of the synthesized material were obtained using a Perkin Elmer TGA 8000 Thermogravimetric Analyzer over a temperature range of 50–800 °C while purging with nitrogen.
- xii. Raman data was collected using a Bruker Vertex 70-Ram II Raman spectrometer equipped with a 1064 nm Nd:YAG laser and liquid nitrogen cooled germanium detector.

- xiii. Infra-red spectra were collected on a Bruker Alpha model FT-IR Spectrometer with platinum-ATR.
- xiv. X-ray photoelectron spectroscopy (XPS) was done using a Kratos Axis Ultra DLD, using an Al (monochromatic) anode, equipped with charge neutralizer and the operating pressure kept below  $5 \times 10^{-9}$  Torr. For wide/survey XPS scans, the following parameters were used: emission current was kept at 5 mA and the anode voltage at 15 kV. The resolution used to acquire wide/survey scans was at 80 eV pass energy using a hybrid lens in the slot mode. For high resolution scans, the resolution was changed to 40 eV pass energy in the slot mode. Curve fitting was performed using Gaussian-Lorentzian peak shape after performing a linear background correction.
- xv. X-ray powder diffraction patterns were recorded on a Bruker D8 Discover equipped with a Lynx Eye detector, using Cu-K $\alpha$  radiation ( $\lambda = 1.5405 \text{ \AA}$ , nickel filter). Data were collected in the scan range of  $2\theta = 10^\circ$  to  $100^\circ$ , scanning at  $1^\circ \text{ min}^{-1}$  with a filter time constant of 2.5 s per step and a slit width of 6.0 mm.
- xvi. Irradiation at 680 and 690 nm wavelengths was achieved using a Modulight ML7710- 680/690-RHO 2 channel laser system equipped with a cylindrical irradiation chamber, an integrated calibration module and a foot/ hand switch pedal.
- xvii. The sterilization and autoclaving of nutrient broth, nutrient agar and phosphate buffer as well as various apparatus for PACT studies was done using an Autoclave RAU-530D.
- xviii. The homogenization of the bacteria suspension was done using PRO VSM-3 Lab plus Vortex mixer.
- xix. The evaluation of the colony forming units (CFU/mL) during bacterial studies was done using a Scan 500 automatic colour colony counter.

- xx. The optical density of the bacteria culture was determined using the LEDETECT 96 from LABXIM PRODUCTS.
- xxi. The incubation processes for the photodynamic antimicrobial chemotherapy was done using a thermostatic oven.
- xxii. The harvesting of the bacteria cells after culture was achieved by centrifugation using a HERMLE Z233M-2 centrifuge.
- xxiii. Transmission electron microscope (TEM) micrographs were obtained using a Zeiss Libra 120 TEM operating at 80 kV. iTEM and ImageJ software were used for TEM microgram processing.
- xxiv. Scanning electron microscope (SEM) images were obtained using a JOEL JSM 840 scanning electron microscope.
- xxv. Energy dispersive X-ray spectroscopy (EDS) was done on an INCA PENTA FET coupled to the VAGA TESCAME using 20 kV accelerating voltage.
- xxvi. Light intensity was measured with a POWER MAX 5100 (Molelectron Detector Inc.) power meter.

### 2.3. Synthesis

#### 2.3.1. Synthesis of metallophthalocyanines (MPcs)

Six pophyrinoid complexes are reported here for the first time and the details of their synthesis are given in this section of the thesis. All the precursors (phthalonitriles or aldehydes) were either purchased or synthesized according to already reported procedures. The reported precursors are 4-(3,4-dicyanophenoxy)benzoic acid (i) [124], 4-(dimethylamino)phthalonitrile (ii) [125], 4-aminobenzaldehyde (iii) [126] and 4-chlorophthalonitrile (iv) [127]. The details for the synthesis of known MPcs 2(3),9(10),16(17),23(24)-tetrakis-(4-aminophenoxy)phthalocyaninato indium (III)



chloride (1) [96], 2-(4-carboxyphenoxy)phthalocyaninato zinc (II) (3) [97], 2(3),9(10),16(17),23(24)-tetrakis-(4-carboxyphenoxy)phthalocyaninato zinc (II) (4a) [98] are as given in literature.

#### 2.3.1.1. Synthesis of 2(3),9(10),16(17),23(24)-tetrakis-(4-carboxyphenoxy)phthalocyaninato indium (III) chloride (4b) (Scheme 3.1)

Complex **4b** was synthesized by refluxing 4-(3,4-dicyanophenoxy)benzoic acid (i) (250 mg, 0.947 mmol) and indium chloride (200 mg, 0.904 mmol) in 3.0 mL dry *n*-pentanol under inert atmosphere in the presence of DBU (0.1 mL), for 6 h. After cooling to room temperature, the product was precipitated out of solution using acetone. The product was then collected and washed several times by centrifugation successively using acetone, water, methanol and then once with diethyl ether. The pure product was then air dried. Yield: 134 mg (44%). UV/Vis (DMSO):  $\lambda_{\max}$  nm (log  $\epsilon$ ): 361 (4.85), 622 (4.50), 687 (5.16). IR [(ATR)  $\nu_{\max}/\text{cm}^{-1}$ ]: 3272 (O–H), 3064 (Ar–H), 1701 (C=O), 1228 (C–O–C).  $^1\text{H}$  NMR (600 MHz, DMSO- $d_6$ ):  $\delta$ , ppm; 12.81 (s, 4H, COOH), 8.33–9.45 (2br, 8H, Ar–H), 8.07–8.23 (2br (overlapping), 8H, Ar–H), 7.79–7.97 (br, 4H, Ar–H), 7.39–7.57 (2br (overlapping), 8H, Ar–H). MS (MALDI-MS)  $m/z$ : calcd. 1206.1; found: 1206.9  $[\text{M}]^+$  and 1171.4  $[\text{M} - \text{Cl}]^+$ . Anal. calcd. for  $\text{C}_{60}\text{H}_{32}\text{ClInN}_8\text{O}_{12}$ : C (59.69), H (2.67), N (9.28 %); found: C (58.92), H (2.87), N 9.01%.

#### 2.3.1.2. Synthesis of 2-(4-carboxyphenoxy)-9(10), 16(17), 23(24)-tris-(dimethylamino)phthalocyaninato zinc (II) (5) (Scheme 3.2)

Complex **5** was synthesized by a mixed condensation reaction of 4-(3,4-dicyanophenoxy)benzoic acid (i) (70 mg, 0.26 mmol), 4-(dimethylamino)phthalonitrile (ii) (454 mg, 2.65 mmol) and zinc(II) acetate dihydrate (400 mg, 1.82 mmol) in 4 mL DMF/DMAE (1:1, v:v) solvent mixture, in the presence of DBU (0.5 mL) under an inert

atmosphere for 12 h after pre-reaction homogenization of the reaction mixture to favor formation of the desired compound. The MPc mixture was preliminarily purified by successively washing with a water:methanol (1:1, v:v) mixture by centrifugation. The sample was then air dried. Complex **5** was then isolated from the mixture by column chromatography using a 9:1 chloroform: methanol solvent system. Yield: 96 mg (44%). UV/Vis (DMSO):  $\lambda_{\max}$  nm (log  $\epsilon$ ): 360 (4.59), 652 (4.26), 725 (4.81). IR [(ATR)  $\nu_{\max}/\text{cm}^{-1}$ ]: 3347 (O–H), 3055 (Ar–H), 2916 and 2847 (C–H stretch), 1701 (C=O), 1499 (C–H bend), 1225 (C–O–C).  $^1\text{H}$  NMR (600MHz, DMSO- $d_6$ ):  $\delta$ , ppm; 7.60 (d, 4H, Ar–H,  $J = 1.8$  Hz), 7.55 (dd, 4H, Ar–H,  $J = 8.4, 1.8$  Hz), 7.33 (d, 4H, Ar–H,  $J = 8.4$  Hz), 7.15 (s, 4H, Ar–H), 3.40 (s, 18H,  $-\text{CH}_3$ ). MS (MALDI-MS)  $m/z$ : calcd. 841.2; found: 841.4  $[\text{M}]^+$ . Anal. calcd. for  $\text{C}_{45}\text{H}_{35}\text{N}_{11}\text{O}_3\text{Zn}$ : C (64.10), H (4.18), N (18.27 %); found: C (63.87), H (4.31), N (18.13 %).

### 2.3.1.3. Synthesis of 2-(4-carboxyphenoxy)-9(10), 16(17), 23(24)-tris(trimethylamino) phthalocyanine zinc (II) methyl sulfate (**6**) (Scheme 3.2)

Complex **6** was synthesized by quaternization of the dimethyl amino substituents of complex **5** as follows: complex **5** (50 mg, 0.059 mmol) was dispersed in 3 mL DMF and DMS (1 mL, excess) was then added followed by refluxing for 2 h. The reaction mixture was allowed to cool to room temperature and the product was precipitated out of solution using a 1:1 (v:v) acetone-methanol mixture. The product was collected and washed twice with acetonitrile and then several times with acetone by centrifugation. The product was then air dried. Yield: 59 mg (82%). UV/Vis (DMSO):  $\lambda_{\max}$  nm (log  $\epsilon$ ): 333 (4.60), 607 (4.37), 672 (5.12). IR [(ATR)  $\nu_{\max}/\text{cm}^{-1}$ ]: 3395 (O–H), 3038 (Ar–H), 2919 and 2848 (C–H stretch), 1690 (C=O), 1487 (C–H bend), 1228 (C–O–C).  $^1\text{H}$  NMR (600MHz,  $\text{D}_2\text{O}$ ):  $\delta$ , ppm; 8.30 (d, 4H, Ar–H,  $J = 2.4$  Hz), 8.25 (dd, 4H, Ar–H,  $J = 8.4, 2.4$  Hz), 8.04 (d, 4H, Ar–H,  $J = 8.4$  Hz), 7.85 (s, 4H, Ar–H), 3.76 (s, 9H,  $-\text{CH}_3$ ), 3.68

(s, 27H,  $-\text{CH}_3$ ). Anal. calcd. for  $\text{C}_{51}\text{H}_{53}\text{N}_{11}\text{O}_{15}\text{S}_3\text{Zn}$ : C (50.14), H (4.37), N (12.61), S (7.87 %); found: C (50.53), H (4.25), N (12.13), S (7.98 %).

#### 2.3.1.4. Synthesis of 5-(4-aminophenyl)-10,15,20-triphenylporphyrin (**8**) (Scheme 3.3 (A))

Complex **8** was synthesized by heating 4-aminobenzaldehyde (**iii**) (0.3 g, 2.5 mmol) and benzaldehyde (**v**) (2.53 mL, 24.8 mmol) in 80 mL of propionic acid to the reflux temperature followed by dropwise addition of 1.89 mL (27.3 mmol) of pyrrole (**vi**) in 20 mL of propionic acid. After complete addition of pyrrole, the reaction was then allowed to reflux for a further 3 h. After 3 h the solvent was evaporated to give a solid crude product mixture containing complex **7**. The crude mixture (3.9 g) was then dissolved in 49.5 mL of 1,4-dioxane to which 5.5 mL of 4 N NaOH in methanol was added and the reaction mixture heated to 80 °C for 24 h. After 24 h the solvent was evaporated and the target product (complex **8**) was isolated from the product mixture by column chromatography using silica gel, eluting with a 3:7 (v/v) EtOAc:cyclohexane solvent system. Yield: 426 mg (27 %). UV/Vis (DMSO):  $\lambda_{\text{max}}$  nm (log  $\epsilon$ ): 420 (5.57), 518 (4.36), 558 (4.20), 592 (3.96), 651 (3.97). IR [(ATR)  $\nu_{\text{max}}/\text{cm}^{-1}$ ]: 3446 and 3353 ( $-\text{NH}_2$ ), 3034 (Ar-H), 1617 (C=N), 1595 (C=C).  $^1\text{H}$  NMR (600MHz,  $\text{CDCl}_3$ ):  $\delta$ , ppm; 9.01 (d, 2H, Ar-H,  $J = 4.2$  Hz), 8.91 (s, 6H, Ar-H), 8.29 (d, 6H, Ar-H,  $J = 6.6$  Hz), 8.04 (d, 2H, Ar-H,  $J = 8.4$  Hz), 7.84 - 7.78 (m, 9H, Ar-H), 7.05 (d, 2H, Ar-H,  $J = 7.8$  Hz), 3.97 (s, 2H,  $\text{NH}_2$ ), -2.65 (s, 2H, NH). MS (MALDI-MS)  $m/z$ : calcd. 629.3; found: 630.3 [ $\text{M} + \text{H}^+$ ]. Anal. calcd. for  $\text{C}_{44}\text{H}_{31}\text{N}_5$ : C (83.92), H (4.96), N (11.12 %); found: C (83.74), H (4.87), N (11.22 %).

### 2.3.1.5. Synthesis of 2-(4-carboxyphenoxy)-9(10), 16(17), 23(24)-trichlorophthalocyaninato zinc (II) (9) (Scheme 3.3 (B))

Complex **9** was synthesized by mixed condensation of 4-(3,4-dicyanophenoxy)benzoic acid (**i**) (70.0 mg, 0.26 mmol) and 4-chlorophthalonitrile (**iv**) (430.7 mg, 2.65 mmol) in 8 mL TCB, in the presence of zinc (II) acetate (486.2 mg, 2.65 mmol) and DBU (0.5 mL) under an inert atmosphere for 12 h. The MPc mixture was purified by successive washing by centrifugation using a water:methanol (1:1, v:v) mixture. The sample was then air dried. Isolation of complex **9** was then achieved by column chromatography using silica gel, eluting with a 1:2 (v/v) THF:cyclohexane solvent system. Yield: 91 mg (43%). UV/Vis (DMSO):  $\lambda_{\text{max}}$  nm (log  $\epsilon$ ): 350 (5.20), 610 (4.81), 675 (5.36). IR [(ATR)  $\nu_{\text{max}}$ /cm<sup>-1</sup>]: 3427 (O–H), 3062 (Ar–H), 1690 (C=O), 1230 (C–O–C), 740 (C–Cl). <sup>1</sup>H NMR (600MHz, DMSO-d<sub>6</sub>):  $\delta$ , ppm; 11.56 (s, 1H, COOH), 7.62 (d, 4H, Ar–H,  $J$  = 2.4 Hz), 7.52 (dd, 4H, Ar–H,  $J$  = 8.4, 1.8 Hz), 7.31 (d, 4H, Ar–H,  $J$  = 8.4 Hz), 7.15 (s, 4H, Ar–H). MS (MALDI-MS)  $m/z$ : calcd. 818.0; found: 818.2 [M]<sup>+</sup>. Anal. calcd. for C<sub>39</sub>H<sub>17</sub>Cl<sub>3</sub>N<sub>8</sub>O<sub>3</sub>Zn: C (57.31), H (2.10), N (13.71 %); found: C (57.16), H (2.31), N (13.47 %).

### 2.3.1.6. Synthesis of 2-(4-[4-(10,15,20-triphenylporphin-5-yl)phenyl]-amidophenoxy)-9(10), 16(17), 23(24)-trichlorophthalocyaninato zinc (II) (10) (Scheme 3.3 (C))

The synthesis of complex **10** was achieved by the amide coupling of complexes **8** and **9** as follows: Complex **8** (28 mg, 0.045 mmol), complex **9** (31 mg, 0.038 mmol), DCC (10 mg, 0.048 mmol) were dissolved in 3 mL of chloroform and stirred at room temperature for 48 h. After 48 h, the reaction mixture was dried in air and the pure product isolated by column chromatography using silica gel, eluting with a 7:3 (v/v) cyclohexane: EtOAc solvent system. Yield: 35 mg (64%). UV/Vis (DMSO):  $\lambda_{\text{max}}$  nm

(log  $\epsilon$ ): 346 (5.13), 418 (5.53), 515 (4.24), 552 (4.09), 608 (4.68), 673 (5.38). IR [(ATR)  $\nu_{\text{max}}/\text{cm}^{-1}$ ]: 3315 (N–H), 3032 (Ar–H), 1643 (C=O), 1568 (C=C), 1240 (C–O–C), 795 (C–Cl).  $^1\text{H}$  NMR (600MHz,  $\text{CDCl}_3$ ):  $\delta$ , ppm; 9.58 (s, 1H, CONH), 9.04 (d, 2H, (Por) Ar–H,  $J = 4.2$  Hz), 8.93 (s, 6H, (Por) Ar–H), 8.31 (d, 6H, (Por) Ar–H,  $J = 6.6$  Hz), 8.05 (d, 2H, (Por) Ar–H,  $J = 8.4$  Hz), 7.86 - 7.80 (m, (Por) 9H, Ar–H), 7.60 (d, 4H, (Pc) Ar–H,  $J = 1.8$  Hz), 7.55 (dd, 4H, (Pc) Ar–H,  $J = 8.4, 1.8$  Hz), 7.33 (d, 4H, (Pc) Ar–H,  $J = 8.4$  Hz), 7.15 (s, 4H, (Pc) Ar–H), 7.08 (d, 2H, (Por) Ar–H,  $J = 7.8$  Hz), -2.63 (s, 2H, (Por) NH). MS (MALDI-MS)  $m/z$ : calcd. 1427.2; found: 1429.1  $[\text{M} + 2\text{H}^+]$ . Anal. calcd. for  $\text{C}_{83}\text{H}_{46}\text{Cl}_3\text{N}_{13}\text{O}_2\text{Zn}$ : C (69.76), H (3.24), N (12.74 %); found: C (69.57), H (3.51), N (12.43 %).

### 2.3.2. Synthesis of MPc-GQD conjugates

The GQDs were prepared from polyethylenimine as the  $-\text{NH}_2$  source, as reported in literature [128], hence their synthesis is not reported here. Two batches (different instances) of  $-\text{NH}_2$  functionalized GQDs were synthesized, one for conjugation to complex **2** and the other for conjugation to complex **3**. Conjugation of MPcs was either by  $\pi$ - $\pi$  stacking where conjugates will be denoted as **MPc** $\pi$ (GQDs), or by covalent linkage.

#### 2.3.2.1. Synthesis of $\pi$ - $\pi$ conjugates (Scheme 3.4 (A))

Complex **2** was conjugated to  $-\text{NH}_2$  functionalized GQDs via  $\pi$ - $\pi$  stacking using a previously reported procedure [106,109] to form **2** $\pi$ (GQDs). Briefly: GQDs (75.0 mg in 1 mL water) and complex **2** (100.0 mg, 0.17 mmol) were dispersed in 2.0 mL dry DMF and sonicated for 16 h. The mixture was then stirred at room temperature for 48 h followed by successive washing with ethanol, deionized water, and then with 1:1 (v:v), THF:ethanol mixture by centrifugation. The product (**2** $\pi$ (GQDs)) was finally washed with diethyl ether and air dried. Nanoconjugate **3** $\pi$ (GQDs) was also

synthesized using the same procedure but using 24 mg GQDs and 32 mg (0.045 mmol) of complex **3**.

#### 2.3.2.2. Synthesis of covalent conjugate (Scheme 3.4 (B))

In the synthesis of **3**(GQDs) conjugate, complex **3** (24.2 mg, 0.034 mmol) and DCC (14.0 mg, 0.068 mmol) were dispersed in 2.0 mL dry DMF, and the mixture was stirred at room temperature for 48 h. After 48 h, 18 mg of GQDs in 1.5 mL of 1:2 (v:v), water:DMF was added and the reaction allowed to proceed for 72 h. The product was then collected and successively washed with deionized water, ethyl acetate and then with 1:1 (v:v), THF:ethanol mixture, by centrifugation. The product was then air dried.

#### 2.3.3. Synthesis of AgTNPs (Scheme 3.5)

The AgTNPs were synthesized according to literature [120] with modifications as follows: silver nitrate (50 mM, 2.4 mL), sodium citrate (75 mM, 23.5 mL), hydrogen peroxide (30 wt %, 2.8 mL) and PSSS (2 wt %, 5.0 mL) were added to distilled water (1.14 L) while stirring vigorously. Freshly prepared 100 mM sodium borohydride (11.8 mL) was finally injected into the reaction mixture and the stirring continued until the solution turned blue. The solution was then concentrated by high speed centrifugation to about 100.0 mL followed by addition of glutathione (130 mM, 5.0 mL) and stirring at room temperature for 12 h. The glutathione (GSH) capped nanoprisms were then obtained as a solid by centrifugation and washed with ethanol and THF, also by centrifugation. The pure product (GSH capped AgTNPs) was then dried under reduced pressure.

#### 2.3.4. Synthesis of MPc-AgTNPs conjugates (Scheme 3.6)

AgTNPs were conjugated to complexes **4a** and **4b** via an amide bond. In the procedure, the MPc (**4a** (35 mg, 0.031 mmol) or **4b** (40 mg, 0.033 mmol)) and DCC

(40 mg, 0.19 mmol) were dispersed in 3.0 mL of dry DMF and stirred at room temperature for 24 h. After 24 h, AgTNPs (10 mg) were added to the reaction mixtures which were allowed to react at room temperature for 72 h. After 72 h the reaction mixtures were added to 100.0 mL of methanol. The products were then collected by centrifugation and washed with THF, also by centrifugation. The pure products were then air dried, to give **4a**(AgTNPs) and **4b**(AgTNPs)

### 2.3.5. Synthesis of functionalized polymers

The use of polyacrylonitrile (PAN) and polystyrene (PS) in polymer membrane fabrication has been reported before [8,9,69,129–131], hence these polymers were selected as candidate polymers for use in this work. In preliminary experiments using complex **1**, leaching of the MPc from the membranes was observed when the complex was simply mixed with the polymer in solution (without prior conjugation) before membrane casting. Henceforth to prevent this, photosensitizers were thus covalently conjugated to polymer anchors before the formation of the membranes. Data from the discontinued efforts with the leaching membranes will not be presented or discussed in this thesis. To allow for photosensitizer conjugation, polymer anchors required availability of functional groups complimentary to those on the photosensitizers for the formation of covalent linkages. In this work photosensitisers were functionalised with either carboxylic groups ( $-\text{COOH}$ ) or amine groups ( $-\text{NH}_2$ ) hence amide linkage was targeted. Since polyacrylonitrile (PAN) and polystyrene (PS) polymers were to be used in the membrane synthesis, their corresponding derivatives were expected to be the most compatible anchor polymers and were hence obtained by introducing either  $-\text{COOH}$  or  $-\text{NH}_2$  groups in the polymers. Two forms of the  $-\text{NH}_2$  functionalized PS (**a**( $\text{NH}_2$ )PS and **b**( $\text{NH}_2$ )PS) polymers were prepared due to the limited availability of (HOME)PS for further synthesis of the initial **a**( $\text{NH}_2$ )PS form.

**2.3.5.1. Synthesis of (COOH)PAN (Scheme 3.7)**

(COOH)PAN was prepared by partial conversion of the nitrile groups of polyacrylonitrile (PAN) to carboxylic groups as follows: Unfunctionalized PAN (5.0 g) was refluxed in 100 mL of 4.1 M HCl for 4 h. The reaction mixture was then diluted with 800 mL of deionized water. The product was filtered off and washed with deionized water followed by air drying.

**2.3.5.2. Synthesis of (COOH)PS (Scheme 3.8)**

(COOH)PS was prepared by oxidation of the primary alcohol groups of hydroxymethyl-polystyrene ((HOMe)PS) to the carboxylic acid as follows: Chromium trioxide (2.0 g, 20 mmol) was added to a 100 mL round bottomed flask and dissolved by addition of 5 mL of 1 M H<sub>2</sub>SO<sub>4</sub>. Concentrated (98%) H<sub>2</sub>SO<sub>4</sub> (5 mL) was then added slowly under cooling (in an ice bath) and magnetic stirring. (HOMe)PS (0.5 g) was added and the mixture refluxed for 1 h. The reaction mixture was then added to 500 mL of deionized water and the product allowed to settle for about 2 h. The precipitated product was washed and collected by centrifugation. The final product ((COOH)PS) then was air dried.

**2.3.5.3. Synthesis of amino functionalized polystyrene a(NH<sub>2</sub>)PS (Scheme 3.8)**

a(NH<sub>2</sub>)PS was synthesized by modifying (COOH)PS using hydrazine. In the synthesis, (COOH)PS (100 mg) was activated using DCC (50 mg, 0.242 mmol) for 48 h at room temperature in 2 mL of dry DMF. After 48 h, hydrazine (0.5 mL, 15.9 mmol) was added to the reaction mixture and allowed to react for 72 h. After 72 h the reaction mixture was precipitated and washed with acetone several times by centrifugation and air dried.



#### 2.3.5.4. Synthesis of amino functionalized polystyrene b(NH<sub>2</sub>)PS (Scheme 3.9)

Firstly (NO<sub>2</sub>)PS was synthesized from commercially available unfunctionalized polystyrene by partial nitration of the benzene ring moieties of the polymer. Unfunctionalized polystyrene beads were first fluffed as follows: Unfunctionalized polystyrene beads (6 g) were dissolved in 20 mL dry DMF and stirred for 3 h. The solution was then added dropwise to a vigorously stirred 500 mL of water and allowed to stir for 30 min at room temperature followed by filtration. The solid was dispersed in methanol and stirred for 30 min, filtered and then dried under reduced pressure for 12 h.

To nitrate, concentrated HNO<sub>3</sub> (3 mL) was slowly added to 18 mL of concentrated H<sub>2</sub>SO<sub>4</sub> cooled using an ice bath. After 10 min the mixture was carefully diluted with 6 mL of deionized water. The fluffy PS (1.5 g) was then quickly added and the temperature allowed to slowly rise to room temperature. The suspension was then stirred at room temperature for 12 h. After 12 h the suspension was poured on ice water and the product ((NO<sub>2</sub>)PS) was isolated by filtration. The solid product was then washed thrice with water and dried under reduced pressure.

b(NH<sub>2</sub>)PS was synthesized by the reduction of (NO<sub>2</sub>)PS using stannous chloride. In the procedure, 1 g of (NO<sub>2</sub>)PS and 5 g (22.2 mmol) of stannous chloride dihydrate were dispersed in 25 mL of absolute ethanol, and refluxed while stirring for 3 h under inert atmosphere. The reaction mixture was cooled to room temperature and added to 400 mL of a 2 M NaOH solution followed by stirring for 30 min at 80 °C. The solid was then filtered off under reduced pressure and washed first with 2 M NaOH, then with copious amounts of water and once with methanol. The product was then dried under reduced pressure.

### 2.3.6. Synthesis of photosensitizer-polymer conjugates

As previously mentioned, photosensitizers need to be covalently linked to a polymer anchor prior to membrane synthesis to prevent leaching of the photosensitizers. The procedures for the covalent linkage of photosensitizers to functionalized polymers are given in the following sections.

#### 2.3.6.1. Synthesis of 1-PAN (Scheme 3.10)

(COOH)PAN (0.50 g) was stirred in 10 mL of dry DMF until a homogenous mixture was obtained. This was followed by addition of EDC (0.027 g, 0.14 mmol) and NHS (0.032 g, 0.28 mmol), each in 0.10 mL DMF. The mixture was stirred for 6 h before complex **1** (0.10 g, 0.092 mmol) dissolved in 6.0 mL of DMF was added to the reaction mixture. The mixture was stirred for 15 h and then added dropwise to 800 mL of vigorously stirred deionized water. The stirring was continued for a further 2 h after complete addition to the water. The conjugate was then allowed to settle, and the bulk of the supernatant decanted. The conjugate was collected and washed with deionized water and methanol successively by centrifugation until complex **1** (sparingly soluble in methanol) spectral bands were not present in the UV-Vis spectrum of the methanol supernatant. The conjugate (**1**-PAN) was then air dried.

#### 2.3.6.2. Synthesis of amide MPc-PS conjugates

The conjugates **1**-PS, **2** $\pi$ (GQDs)-PS, **3**-PS, **3**(GQDs)-PS, **3** $\pi$ (GQDs)-PS, **4a**-PS, **4a**(AgTNPs)-PS, **4b**-PS, **4b**(AgTNPs), **5**-PS and **6**-PS were prepared by amide coupling of the photosensitizers (MPc or MPc nanoconjugate) with either (COOH)PS, a(NH<sub>2</sub>)PS or b(NH<sub>2</sub>)PS. Coupling was achieved by using either DCC (**3**-PS, **3**(GQDs)-PS, **3** $\pi$ (GQDs)-PS, **4a**-PS, **4a**(AgTNPs)-PS, **4b**-PS and **4b**(AgTNPs)-PS) or EDC-NHS (**1**-PS, **5**-PS and **6**-PS) coupling agents or thionyl chloride (**2** $\pi$ (GQDs)-PS) to facilitate the reaction. The different coupling agents (DCC, EDC-NHS and thionyl

chloride) were used for the conjugation reactions, but only the procedures that gave best results are described for each coupling reaction.

#### 2.3.6.2.1. DCC/ EDC-NHS facilitated conjugation (Schemes 3.10 – 3.13)

**Table 2.1** summarizes the specific details for each DCC/ EDC-NHS facilitated PS conjugation reaction. The general procedure for the conjugate syntheses is as follows: The –COOH bearing reactant (functionalized polymer or photosensitizer) and the coupling agent were dispersed in dry solvent and homogenized at room temperature by magnetic stirring for 6 – 48 h. This was followed by the addition of the –NH<sub>2</sub> bearing reactant (functionalized polymer or photosensitizer) and the mixture was allowed to react for 15 – 72 h. For conjugates **5-PS** and **6-PS**, both functionalized polymer and photosensitizer were added to the reaction at the same time (beginning of reaction) and the activation of the –COOH group was done in situ. After 15 – 72 h the reaction mixtures were added dropwise to 200 – 800 mL of vigorously stirred deionized water for EDC-NHS reactions or methanol for DCC reactions (**Schemes 3.10, 3.11(B), 3.12 and 3.13**). After complete addition of the reaction mixture, stirring was continued for an additional 30 min – 2 h before allowing the conjugate to settle and decanting the bulk of the supernatant. The conjugates were then collected by centrifugation and washed successively with water and methanol also by centrifugation until photosensitizer bands were not present in the UV-Vis spectra of the methanol supernatant. The conjugates were then air dried.

**Table 2.1:** Summary of the specific synthesis parameters for the DCC/ EDC-NHS photosensitizer-PS amide conjugates.

Conjugate	Photosensitizer (mg)	Polymer (mg)	Coupling agent (mg)	Solvent (DMF) (mL)	Duration (h)
<b>1-PS</b>	60	(COOH)PS (120)	EDC (100), NHS (100)	13 + 2	6 + 15
<b>3-PS</b>	20	a(NH <sub>2</sub> )PS (50)	DCC (15)	2	48 + 72
<b>3<math>\pi</math>(GQDs)-PS and 3(GQDs)-PS</b>	15	(COOH)PS (100)	DCC (50)	2 + 3	48 + 72
<b>4a-PS</b>	45	a(NH <sub>2</sub> )PS (100)	DCC (60)	2	24 + 72
<b>4b-PS</b>	50	a(NH <sub>2</sub> )PS (100)	DCC (60)	2	24 + 72
<b>4a(AgTNPs)-PS and 4b(AgTNPs)-PS</b>	15	a(NH <sub>2</sub> )PS (50)	DCC (40)	2	24 + 72
<b>5-PS and 6-PS</b>	7.5	b(NH <sub>2</sub> )PS (250)	EDC (10), NHS (10)	5	48

#### 2.3.6.2.2. Thionyl chloride facilitated conjugation (Synthesis of $2\pi$ (GQDs)-PS) (Scheme 3.11 (A))

(COOH)PS (200 mg) was dispersed in 2.0 mL of dry DMF, degassed by vacuum and placed under argon. Thionyl chloride (0.25 mL, 3.45 mmol) was injected into the reaction mixture which was stirred for 24 h at room temperature. Then, a solution of  $2\pi$ (GQDs) (15.0 mg) in dry DMF (1.5 mL) was injected into the reaction mixture followed by continuous stirring for 72 h. The reaction was then quenched by addition of 10 mL of deionized water. The product ( $2\pi$ (GQDs)-PS) was then collected and washed by centrifugation using deionized water and then a DMSO:THF (2:3) solvent mixture. The product was washed once with diethyl ether and then air-dried.

#### 2.3.6.3. Synthesis of 10-PS (Scheme 3.14)

10-PS was synthesized by the Buchwald-Hartwig cross-coupling of complex **10** and b(NH<sub>2</sub>)PS. Complex **10** (7.5 mg, 5.2  $\mu$ mol) and b(NH<sub>2</sub>)PS (250 mg) were dispersed in 5 mL dry 1,4-dioxane in a dry round bottomed flask and argon bubbled through the dispersion for 10 min while gently stirring the mixture. The atmosphere above the solvent was then saturated with argon and the vessel fitted with a condenser sealed with a septum. Tetrakis(triphenylphosphine)palladium(0) (1.6 mg, 1.4  $\mu$ mol) and KOtBu (1.2 mg, 10.5  $\mu$ mol) were then carefully and quickly added to the sealed reaction vessel while ensuring inert atmospheric conditions. The reaction mixture was then heated to 100 °C and the temperature maintained for 24 h. After 24 h, the reaction was allowed to cool to room temperature and added dropwise to 200 mL of vigorously stirred ethanol. After complete addition the mixture was stirred for a further 30 min before decanting the solvent. The residue was dispersed in ethyl acetate (200 mL) and vigorously stirred for 30 min before decanting the solvent. The conjugate was then washed by centrifugation using ethyl acetate until the UV-Vis spectral bands of

complex **10** were absent in the supernatant. The product conjugate was rinsed with methanol, collected by filtration and then air dried.

### 2.3.7. Synthesis of functionalized polymer membranes

The functionalized polymer membranes were prepared by dispersing a photosensitizer-polymer conjugate and a corresponding unfunctionalized polymer (PAN or PS) in dry DMF and homogenizing the mixture by stirring for at least 12 h at room temperature. The polymer solution (0.60 mL) was then cast on 76 x 26 mm glass slides and immediately added to a precipitation bath to give the photosensitizer functionalized membranes. The functionalized membranes were then soaked in ethanol overnight and then air dried before characterization and application. Unfunctionalized membranes were also prepared in the same way, but only using unfunctionalized polymer for the total polymeric composition. **Table 2.2** summarizes the names and specific preparation parameters for the synthesized membranes.

**Table 2.2:** Summary of specific preparation parameters for the synthesized membranes

Membrane	Photosensitizer-polymer conjugate (mg)	Unmodified polymer (mg)	Solvent (DMF) (mL)	Nonsolvent (v:v, 200 mL)
PAN-memb	(COOH)PAN (25)	PAN (480)	3.70	H <sub>2</sub> O
1-PAN-memb	1-PAN (25)	PAN (480)	3.70	H <sub>2</sub> O
PS-memb	(COOH)PS (12)	PS (490)	2.50	MeOH
1-PS-memb	1-PS (12)	PS (490)	2.50	MeOH
2 $\pi$ (GQDs)-memb	2 $\pi$ (GQDs)-PS (11.4)	PS (491.9)	2.12	MeOH
3-memb	3-PS (22.8)	PS (480.5)	2.12	MeOH
3(GQDs)-memb	3(GQDs)-PS (22.8)	PS (480.5)	2.12	MeOH
3 $\pi$ (GQDs)-memb	3 $\pi$ (GQDs)-PS (22.8)	PS (480.5)	2.12	MeOH
4a-memb	4a-PS (22.8)	PS (480.5)	2.12	MeOH
4a(AgTNPs)-memb	4a(AgTNPs)-PS (22.8)	PS (480.5)	2.12	MeOH
4b-memb	4b-PS (22.8)	PS (480.5)	2.12	MeOH

<b>4b(AgTNPs)-memb</b>	<b>4b(AgTNPs)-PS</b> (22.8)	PS (480.5)	2.12	MeOH
<b>5-memb</b>	<b>5-PS</b> (50)	PS (600)	2.20	MeOH:H <sub>2</sub> O (2:1)
<b>6-memb</b>	<b>6-PS</b> (50)	PS (600)	2.20	MeOH:H <sub>2</sub> O (2:1)
<b>10-memb</b>	<b>10-PS</b> (50)	PS (600)	2.20	MeOH:H <sub>2</sub> O (2:1)

Note: Polymers are only indicated for **1**-PAN-memb, PAN-memb, **1**-PS-memb and PS-memb to distinguish between these compared membranes, but the rest of the membranes are PS hence not specified.

#### 2.4. Photodegradation studies

Photocatalytic properties of functionalized polymer membranes were investigated by studying their degradation of 4-chlorophenol (4-CP) at various concentrations in pH 11 phosphate buffer solution using **2π**(GQDs)-memb and deionized water using **10**-memb in representative photodegradation studies. For studies using **2π**(GQDs)-memb, 4-CP solutions of concentrations  $2.17 \times 10^{-4}$  M,  $2.89 \times 10^{-4}$  M and  $3.24 \times 10^{-4}$  M were employed, while  $3.10 \times 10^{-5}$  M,  $6.74 \times 10^{-5}$  M and  $1.02 \times 10^{-4}$  M were used for **10**-memb. For each concentration, a fixed volume of solution was irradiated with laser light of appropriate wavelength (680 nm for **2π**(GQDs)-memb, and 515 and 690 nm for **10**-memb) in the presence of a functionalized polymer membrane in a sealed vessel at constant time intervals. The photocatalytic activity studies for **10**-memb were



carried out separately at 515 nm and 690 nm where the component complexes of the photosensitizer complementarily absorb while 680 nm for  $2\pi(\text{GQDs})\text{-memb}$  targeted the MPc Q-band. The change in concentration after each irradiation was monitored using UV–Vis spectroscopy by noting the decrease in the 4-CP absorption band at 244 nm in pH 11 buffer solution ( $2\pi(\text{GQDs})\text{-memb}$ ) or at 225 nm in deionized water (**10**-memb). A pH of 11 was used in the studies to optimise singlet oxygen generation during assessment of the photocatalytic activity of the functionalized membranes as a proof of concept. On the other hand, deionized water was also used to enable assessment of membrane photoactivity without positive or negative influence of pH. To account for adsorption of the 4-CP onto the polymer membranes, the membranes were soaked in the 4-CP solutions and kept in the dark for approximately 30 mins to allow adsorption equilibrium to be reached before initial UV-Vis absorption spectra were recorded prior to irradiation. Also, after each irradiation cycle, the solutions were homogenized, and the UV-Vis spectra recorded multiple times until they were stable and reproducible.

## 2.5. Light harvesting studies for **10**-memb

The light harvesting studies for **10**-memb were carried out by monitoring the rates of 4-CP degradation after irradiation with light from different sections of the electromagnetic spectrum with comparison to white light of the same intensity. The light source was a general electric quartz line lamp with adjustable voltage for variation of light intensity, which was monitored by the power meter described in section 2.2. In the procedure, the **10**-memb ( $0.8 \times 3.8$  cm) was secured in a cuvette with a tight-fitting lid. A 4-CP solution in deionized water (1.5 mL,  $1.02 \times 10^{-4}$  M) was added to the cuvette in the dark and the membrane irradiated with white light at 1 min cycles while the decrease in 4-CP absorbance at 225 nm was monitored by UV-Vis spectroscopy at

20 °C. The process was then repeated in the presence of a purple, red and green coloured glass as light filters to give exclusive light irradiation for different regions of the electromagnetic spectrum. The rate of 4-CP degradation was then compared on a plot of change in 4-CP concentration against time.

## **2.6. Procedures for photodynamic antimicrobial chemotherapy (PACT) studies**

PACT studies in this work were carried out using the colony count method (including for membranes). Photosensitizers **4a**, **4a**(AgTNP), **4b**, **4b**(AgTNP), **5** and **6**, and the functionalized membranes **4a**-memb, **4a**(AgTNP)-memb, **4b**-memb, **4b**(AgTNP)-memb, **5**-memb and **6**-memb were employed as examples. The study was achieved in two steps, namely bacterial culture and dilution optimization followed by photodynamic antimicrobial chemotherapy activity experiments.

### **2.6.1. Bacterial culture and dilution optimization**

A few crystal fragments of *S.aureus* lyophilized pellet were dispersed in 6 mL of nutrient broth and aerobically incubated at 37 °C while agitating on a rotary shaker (~200 rpm) to mid logarithmic phase (absorbance ~0.6 at 620 nm). The bacterial cells were then harvested by centrifugation of the broth culture at 3000 rpm for 15 min and washed twice with 10 mM of PBS and re-suspended in 1 mL of PBS. The cell solution was then diluted to 100 mL in PBS (dilution of  $10^{-2}$ ) to give the working stock bacterial cell solution.

Dilutions ranging from  $10^{-3}$  to  $10^{-8}$  obtained by serial dilution of the bacterial stock solution were inoculated (100  $\mu$ L of bacterial solution) on agar plates in triplicates and incubated at 37 °C for 20 h before colony counting. A dilution corresponding to the highest dilution giving a colony count of approximately 300 colonies was selected as

the optimum dilution for further studies. The optimum dilution was observed to be  $10^{-6}$  corresponding to  $\approx 10^9$  CFU/mL.

### 2.6.2. Photodynamic antimicrobial chemotherapy activity

For the photosensitizer concentration experiments, bacterial suspensions of  $10^{-6}$  dilution with varying photosensitizer concentrations in 2 % DMSO in PBS solutions (6 mL) were aseptically prepared in Pyrex brand culture tubes (13 × 100 mm) and incubated in an oven equipped with a shaker for 30 min in the dark at 37 °C. After incubation, 100 µL of the suspensions were immediately inoculated onto agar plates (0 min irradiation) and incubated while avoiding exposure to light and keeping the suspensions in the culture tubes covered with aluminium foil. The suspensions remaining in the culture tubes were then equally divided and added to two separate 24 well plates where one was irradiated using the set-up described above at the photosensitizer Q-band absorption for 60 min while the other was kept in the dark for the same period. After irradiation, 100 µL of the samples were aseptically inoculated on agar plates and the plates were incubated inverted at 37 °C overnight for 20 h before colony counting. Samples kept in the dark were processed in the same way as the irradiated samples. All inoculations were done in triplicates.

For each study, a concentration was selected for time-correlated experiments where compounds could be compared, which corresponded to the lowest studied concentration value showing the highest activity with the least dark toxicity. The selected photosensitizer concentrations were prepared and treated as described above, but inoculations onto agar plates was done periodically after successive 15 min irradiations until 60 or 75 min. Samples kept in the dark were also similarly inoculated. In the studies control treatments were as follows:

- (1) bacterial suspension without photosensitizer but irradiated;

(2) only bacterial suspension (no photosensitizer, no irradiation).

For the experiments using the membranes, the stock bacterial solution (dilution  $10^{-2}$ ) was inoculated (100  $\mu$ L) and approximately equal samples of the membranes cut into squares, were pasted on the inoculated agar plates. The plates were then irradiated at varying time intervals in 15 min increments up to 60 min. The plates were then incubated as described above and the activity of the membranes monitored after 20 h by their ability to inhibit colony formation on the agar in the area in direct contact with the membranes. Corresponding membrane samples were also similarly prepared and kept in the dark instead of irradiation, for dark toxicity assessment. Experiments were done in triplicates of membrane samples. Control treatments were as follows:

- (1) irradiated bacterial suspension inoculation in the presence of unfunctionalized polymer membrane;
- (2) inoculation of only bacterial suspension (no polymer membrane, no irradiation);
- (3) inoculation of only bacterial suspension (no polymer membrane, with irradiation).

### 2.6.3. Statistical analysis

The experimentally obtained data was statistically analysed. For each set of conditions, the experiments were done in triplicates and the statistical significance of the results for each photosensitizer were verified using the 1 tail type 3 t-test with  $\alpha$  set at 0.05.

## **RESULTS AND DISCUSSIONS**

### **3. Synthesis and characterization**

### **4. Photophysical and photochemical properties**

### **5. Photodegradation and Photodynamic Antimicrobial Chemotherapy (PACT)**

## Publications

The results discussed in the following chapters have been presented in the journal articles below that have been published or submitted for publication to peer-reviewed journals. Also, these articles have not been referenced in this thesis.

1. **D.M. Mafukidze**, P. Mashazi, T. Nyokong, Synthesis and singlet oxygen production by a phthalocyanine when embedded in asymmetric polymer membranes, *Polymer (Guildf)*. 105 (2016) 203–213.
2. **D.M. Mafukidze**, T. Nyokong, Graphene quantum dot-phthalocyanine polystyrene conjugate embedded in asymmetric polymer membranes for photocatalytic oxidation of 4-chlorophenol, *J. Coord. Chem.* 70 (2017) 3598–3618.
3. **D.M. Mafukidze**, T. Nyokong, A comparative study of the singlet oxygen generation capability of a zinc phthalocyanine linked to graphene quantum dots through  $\pi$ - $\pi$  stacking and covalent conjugation when embedded in asymmetric polymer membranes, *J. Mol. Struct.* 1180 (2019) 307–317.
4. **D.M. Mafukidze**, A. Sindelo, T. Nyokong, Spectroscopic characterization and photodynamic antimicrobial chemotherapy of phthalocyanine-silver triangular nanoprism conjugates when supported on asymmetric polymer membranes, *Spectrochim. Acta - Part A Mol. Biomol. Spectrosc.* 219 (2019) 333–345.
5. **D.M. Mafukidze**, T. Nyokong, Photodynamic antimicrobial chemotherapy of a dimethylamino-functionalized asymmetric zinc (II) phthalocyanine and its quaternized derivative against *Staphylococcus aureus* when supported on asymmetric polystyrene polymer membranes, *React. Funct. Polym.* 154 (2020) 104634.

6. **D.M. Mafukidze**, T. Nyokong, Photocatalytic and solar radiation harvesting potential of a free-base porphyrin-zinc (II) phthalocyanine heterodyad functionalized polystyrene polymer membrane for the degradation of 4-chlorophenol, J. Photochem. Photobiol. A: Chem. **Submitted**

#### **Additional publications not directly related to this thesis**

1. M. Managa, B.P. Ngoy, **D. Mafukidze**, J. Britton, T. Nyokong, Photophysical studies of meso-tetrakis(4-nitrophenyl) and meso-tetrakis(4-sulfophenyl) gallium porphyrins loaded into Pluronic F127 polymeric micelles, J. Photochem. Photobiol. A Chem. 348 (2017) 179–187.
2. M. Managa, B. Pitchou Ngoy, **D. Mafukidze**, T. Nyokong, Incorporation of metal free and Ga 5,10,15,20-tetrakis(4-bromophenyl) porphyrin into Pluronic F127-folic acid micelles, J. Lumin. 194 (2018) 739–746.
3. L.C. Nene, M.E. Managa, D.O. Oluwole, **D.M. Mafukidze**, A. Sindelo, T. Nyokong, The photo-physicochemical properties and in vitro photodynamic therapy activity of differently substituted-zinc (II)-phthalocyanines and graphene quantum dots conjugates on MCF7 breast cancer cell line, Inorganica Chim. Acta. 488 (2019) 304–311.
4. P. Sen, A. Sindelo, **D.M. Mafukidze**, T. Nyokong, Synthesis and photophysicochemical properties of novel axially di-substituted silicon (IV) phthalocyanines and their photodynamic antimicrobial chemotherapy (PACT) activity against *Staphylococcus aureus*, Synth. Met. 258 (2019) 116203.
5. B. Jones, J. Britton, **D. Mafukidze**, T. Nyokong, Photodegradation of 4-chlorophenol using Zn and In phthalocyanines substituted with pyrrole without

hetero atoms linkers and supported on polyacrylonitrile electrospun fibres, Polyhedron. 178 (2019) 114329.

6. B. Jones, **D. Mafukidze**, T. Nyokong, Fabrication of electrospun fibers from a porphyrin linked to polyacrylonitrile polymer for photocatalytic transformation of phenols, J. Mol. Struct. 1213 (2020) 128191.



# CHAPTER 3

### 3. Synthesis and characterization

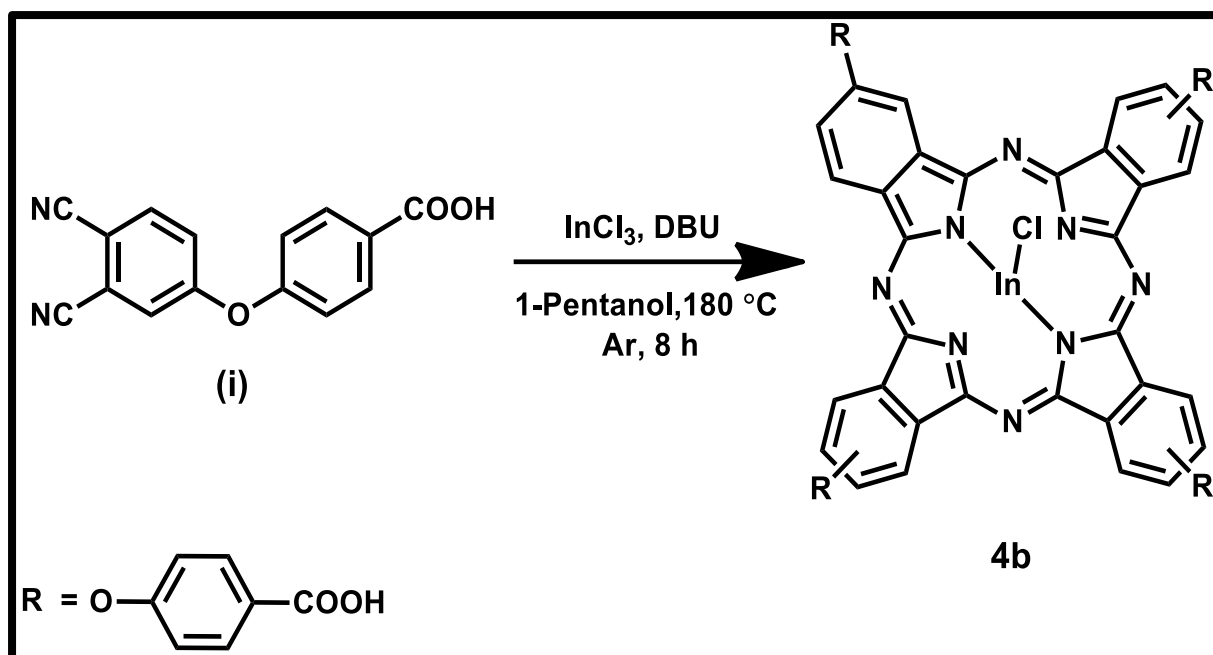
This chapter gives details of the synthesis and characterization of the MPcs, nanoparticles (NPs), MPc-NPs conjugates, functionalized polymers, photosensitizer-polymer conjugates and photosensitizer functionalized polymer membranes.

#### 3.1. Metallophthalocyanines (MPcs)

The complexes **1**, **3** and **4a** have been previously reported [96–98] and their characterization will thus not be discussed in this work. Only the characterization of new complexes **4b**, **5**, **6**, **8**, **9** and **10** will be discussed in detail in the following subsections. Although complex **8** is not a Pc, but instead a porphyrin, it is also discussed in this section since it is a porphyrinoid complex (similar to Pcs) intermediate in the synthesis of complex **10**. Also, complex **7** is omitted in the discussions since it was an intermediate that was not isolated.

##### 3.1.1. 2(3),9(10),16(17),23(24)-Tetrakis-(4-carboxyphenoxy) phthalocyaninato indium (III) chloride (**4b**)

Complex **4b** was synthesized by cyclocondensation of 4-(3,4-dicyanophenoxy) benzoic acid (**i**) in the presence of indium (III) chloride and a catalytic amount of DBU in dry *n*-pentanol under inert atmosphere (**Scheme 3.1**). The FT-IR spectrum for complex **4b** (**Fig. 3.1** insert (**a**)), shows the expected functional groups, carboxylic O–H at 3272 cm<sup>-1</sup>, aromatic C–H at 3064 cm<sup>-1</sup>, carboxylic C=O at 1701 cm<sup>-1</sup> and the ether C–O–C at 1228 cm<sup>-1</sup>, as the key peaks of interest. The mass spectrum (**Fig. 3.1**, insert (**b**)) shows two peaks where the main peak at 1206.9 corresponds to [M]<sup>+</sup>, while the minor peak at 1171.4 corresponds to [M-Cl]<sup>+</sup>. Elemental analysis values corresponded with expected values and also suggested purity of the complex. The <sup>1</sup>H NMR spectrum (not shown) consisted of the expected downfield carboxylic acid singlet signal at



**Scheme 3.1:** Synthetic route for complex **4b**.

12.81 ppm that integrated to 4 protons, and the aromatic signals for the MPc macrocycle and aromatic substituents which appeared between 7.39 and 9.45 ppm integrating to 28 protons, hence all expected protons were accounted for. The UV-Vis spectra of complex **4b** shows the characteristic MPc Q-band at 687 nm and B-band at 361 nm (**Fig. 3.1**). The Q-band is red shifted compared to that of the ZnPc derivative (complex **4a**) [98] (**Table 3.1**) due to the presence of the indium (III) ion, with a relatively bigger atomic radius than the zinc (II) which results in reduced planarity [132]. The presence of an axial ligand may also have contributed to the observed red shifted UV-Vis spectrum as has been reported for porphyrins [133].

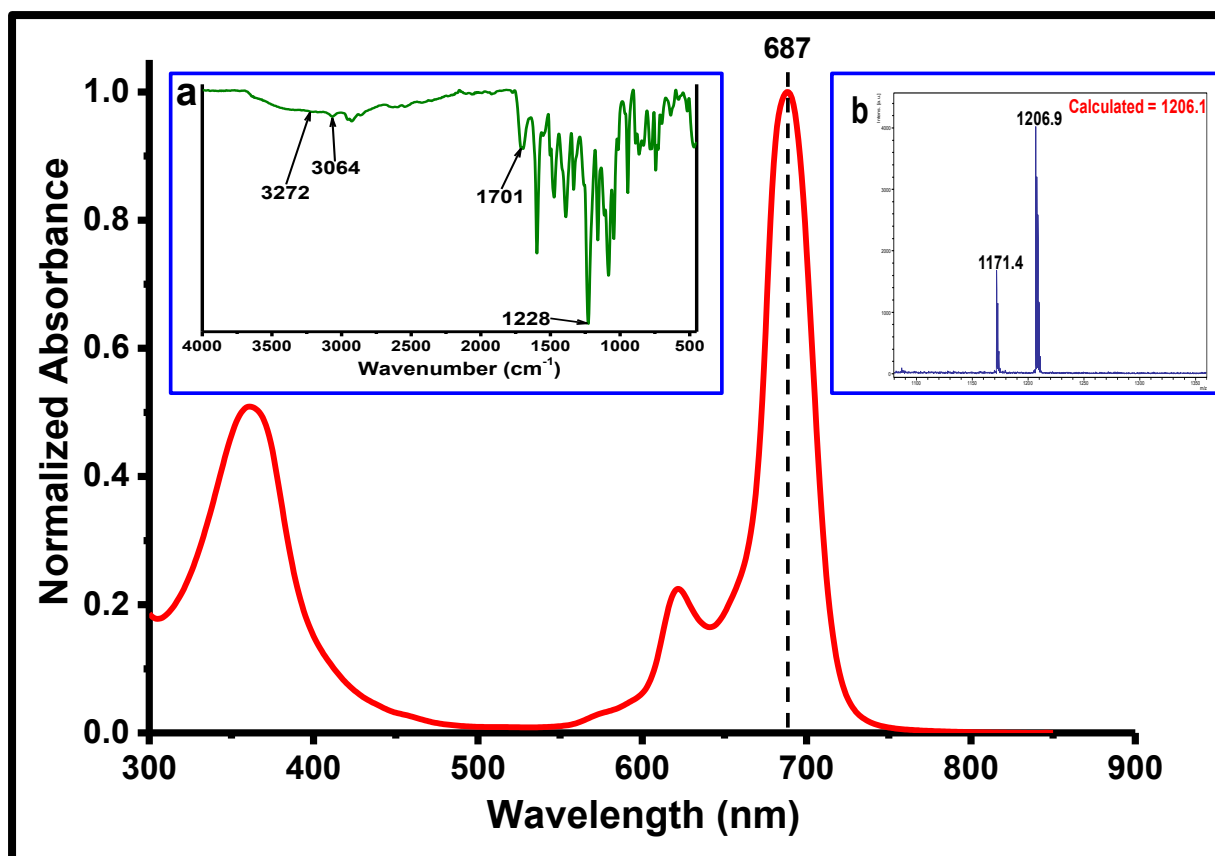


**Fig. 3.1:** UV-Vis spectrum in DMSO solution, FT-IR spectrum (insert **(a)**) and the MS (MALDI-TOF) (insert **(b)**) for complex **4b**.

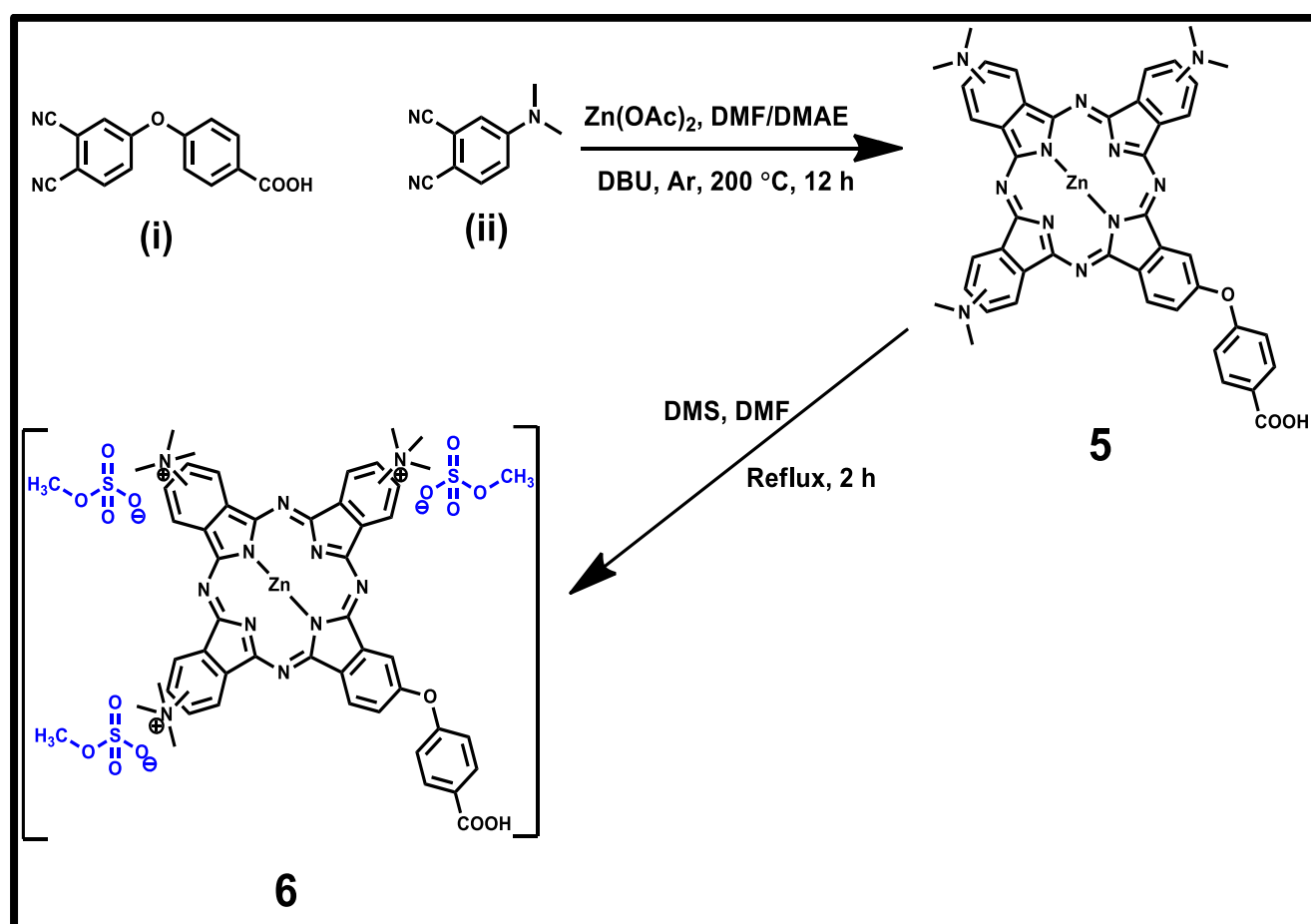
**Table 3.1:** Summary of the  $\lambda_{\max}$  values for the photosensitizers used in this work, in DMSO unless specified.

Photosensitizer	$\lambda_{\max}$ (nm)
<b>1</b>	698
<b>2</b>	672
<b>GQD</b> (first batch)	359 <sup>a</sup>
<b>2<math>\pi</math>(GQDs)</b>	672
<b>3</b>	674
<b>GQDs</b> (second batch)	350 <sup>a</sup>
<b>3<math>\pi</math>(GQDs)</b>	675
<b>3(GQDs)</b>	676
<b>AgTNPs</b>	702 <sup>a</sup>
<b>4a</b>	679
<b>4a(AgTNPs)</b>	679
<b>4b</b>	687
<b>4b(AgTNPs)</b>	693
<b>5</b>	725
<b>6</b>	672
<b>8</b>	420 <sup>b</sup>
<b>9</b>	675
<b>10</b>	418 <sup>b</sup>
	673

<sup>a</sup> Values in water. <sup>b</sup> Porphyrin Soret band absorption otherwise the rest are MPc Q-band absorptions.

**3.1.2. 2-(4-Carboxyphenoxy)-9(10),16(17),23(24)-tris-(dimethylamino) phthalocyaninato zinc (II) (5) and 2-(4-carboxyphenoxy)-9(10),16(17),23(24)-tris-(trimethylamino) phthalocyanine zinc (II) methyl sulfate (6)**

Complex **5** was synthesized by statistical condensation of 4-(3,4-dicyanophenoxy)benzoic acid (i) and 4-(dimethylamino)phthalonitrile (ii) in the presence of zinc(II) acetate and catalytic amounts of DBU in DMF/DMAE (1:1, v:v) solvent mixture (**Scheme 3.2**). The asymmetric complex was obtained after extensive chromatography separation. Complex **5** was then quaternized using dimethyl sulfate (DMS) to form complex **6**.



**Scheme 3.2:** Synthetic route for complexes **5** and **6**.

The FT-IR spectra for complexes **5** and **6** (**Fig. 3.2**) are almost identical since no new functional groups were either introduced or eliminated upon conversion from complex **5** to **6**. The two spectra mainly differ slightly in the fingerprint region (**Fig. 3.2**, highlighted in yellow) as would be expected for different compounds regardless of their similarities. Both complexes exhibit the expected peaks for –OH carboxylic acid stretching (3347 (**5**), 3395 (**6**)), aromatic C–H stretching (3055 (**5**), 3038 (**6**)), aliphatic C–H stretching (2916 and 2847 (**5**), 2919 and 2848 (**6**)), carboxylic C=O stretching (1701 (**5**), 1690 (**2**)), C–H bending (1499 (**5**), 1487(**6**)) and C–O–C bending vibrations (1225 (**5**), 1228 (**6**)). The mass spectrum for complex **5** (not shown) gave an  $m/z$  peak at 841.4 which corresponds to  $[M]^+$ . The mass spectrum for complex **6** could not be obtained possibly due to cleavage of the groups with no molecular ion peaks which has been reported before [134]. The elemental analysis values obtained corresponded with the expected values which suggested compound purity.

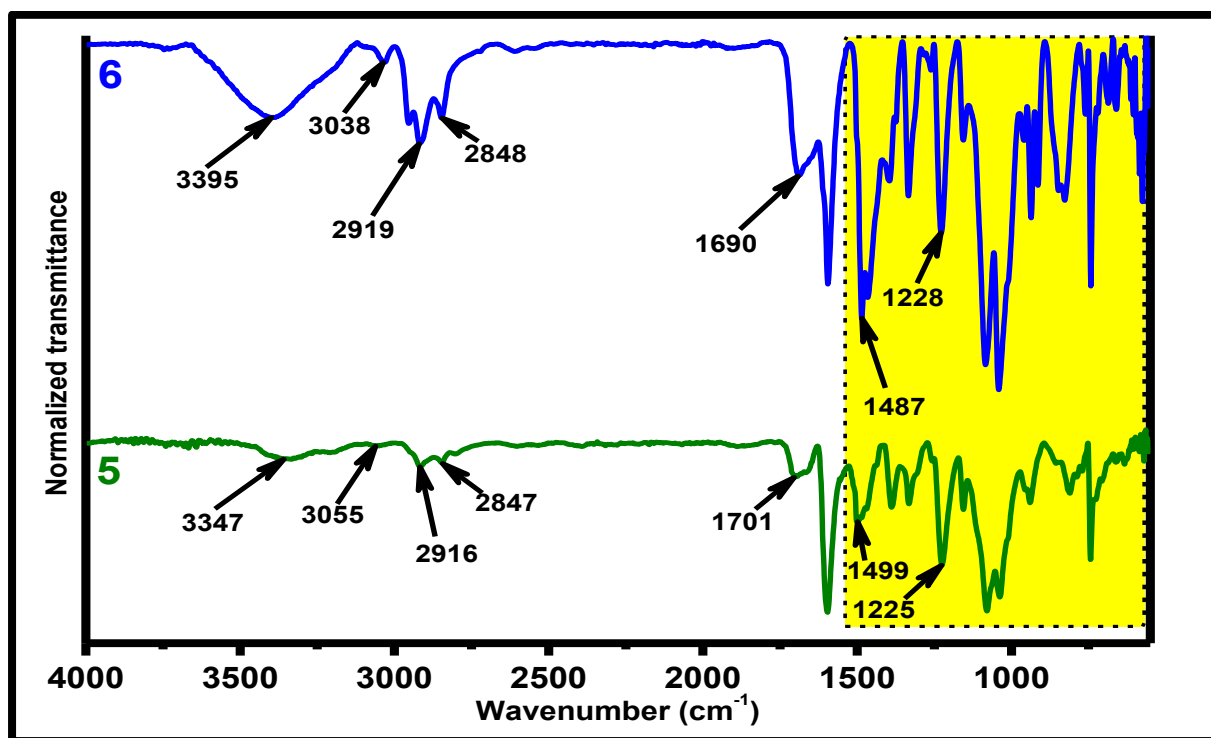


**Fig. 3.2:** FT-IR spectra for complexes **5** and **6**.

The  $^1\text{H}$  NMR spectrum of complex **5** (**Fig. 3.3(A)**) shows signals that integrate to give the expected number of protons in the expected regions. A singlet attributed to the dimethyl amine  $-\text{CH}_3$  protons is observed at 3.40 ppm and integrates to 18 protons while peaks in the aromatic region (7.15 – 7.60 ppm) integrate to the expected 16 aromatic protons of the MPc. The carboxylic proton signal is not observed due to deprotonation. The  $^1\text{H}$  NMR spectrum for complex **6** (**Fig. 3.3(B)**) is relatively similar to that of complex **5**, but the signals are shifted downfield and the amine  $-\text{CH}_3$  singlet integrates to 27 protons confirming successful quaternization of complex **5**. An additional singlet peak is also observed downfield next to the amine  $-\text{CH}_3$  singlet, which integrates to 9 protons and is attributed to the methyl sulfate counter ion.

**Fig. 3.4** shows the normalized UV-Vis spectra for complexes **5** and **6** in DMSO and 2 % DMSO in PBS (used for PACT). In DMSO, the spectra of both complexes exhibit the characteristic MPc bands (Q, vibronic and B-bands). Complex **5** is observed to have a Q-band that is relatively broad and red shifted with  $\lambda_{\text{max}}$  at 725 nm, **Table 3.1**. Such red shifted spectra have been reported before for amine derivative with substituents directly attached to the Pc macrocycle [135–137]. The spectrum also has a broad charge transfer band at about 476 nm. On the other hand, complex **6** is observed to have a sharper Q-band that is blue shifted ( $\lambda_{\text{max}} = 672$  nm), **Table 3.1**. The transformation of complex **5** to **6** is also accompanied by the disappearance of the charge transfer band in the UV-Vis spectra, which also indicated completion of quaternization during synthesis. These observations after conversion of complex **5** to **6** suggest that the red shifted Q-band and the presence of a charge transfer band are related to the availability of the lone pairs of electrons on the dimethyl amino substituents' nitrogen atoms. The UV-Vis spectra for both complexes in 2 % DMSO in PBS (used for bacterial studies) solution show significant aggregation of the



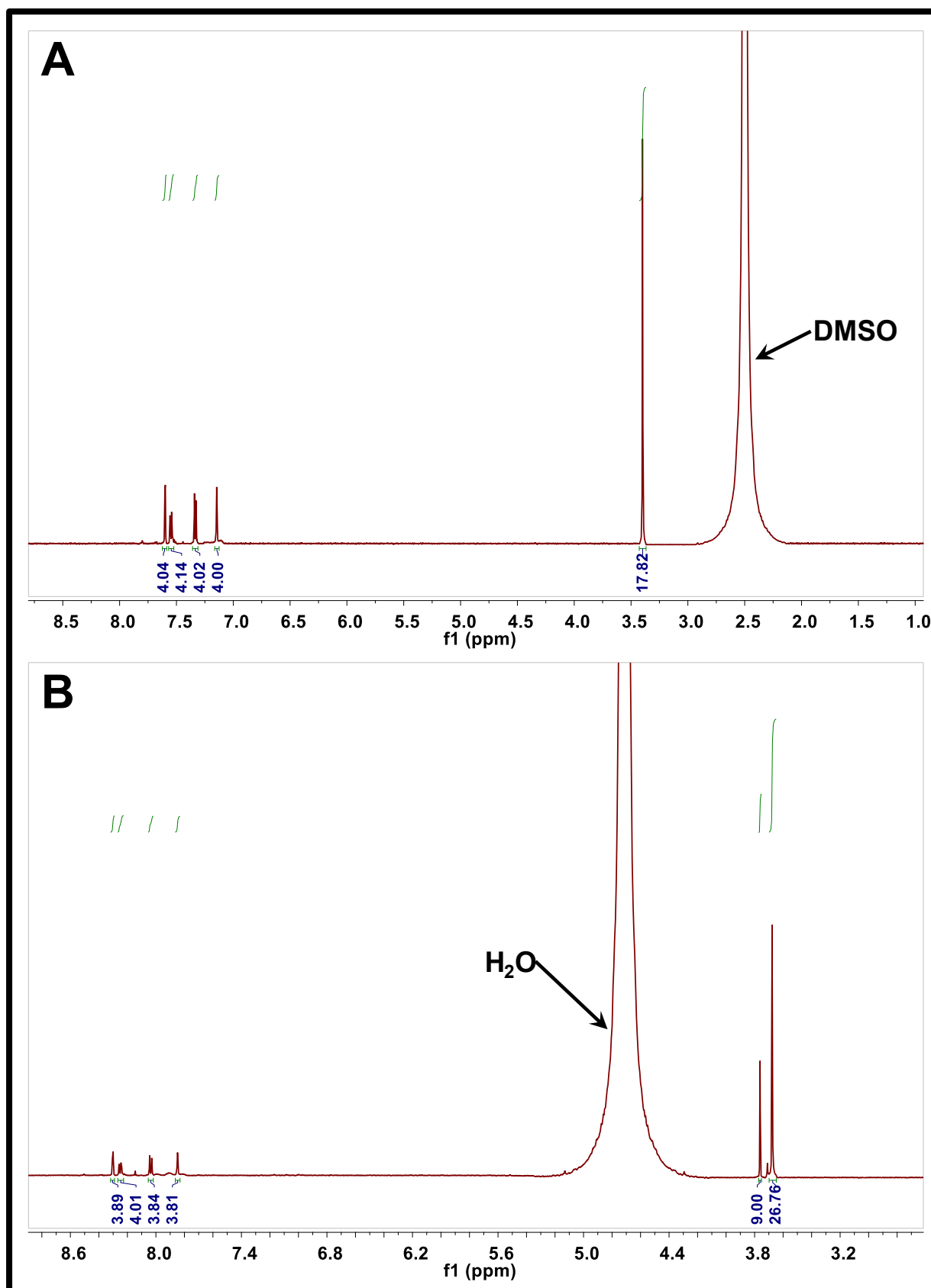
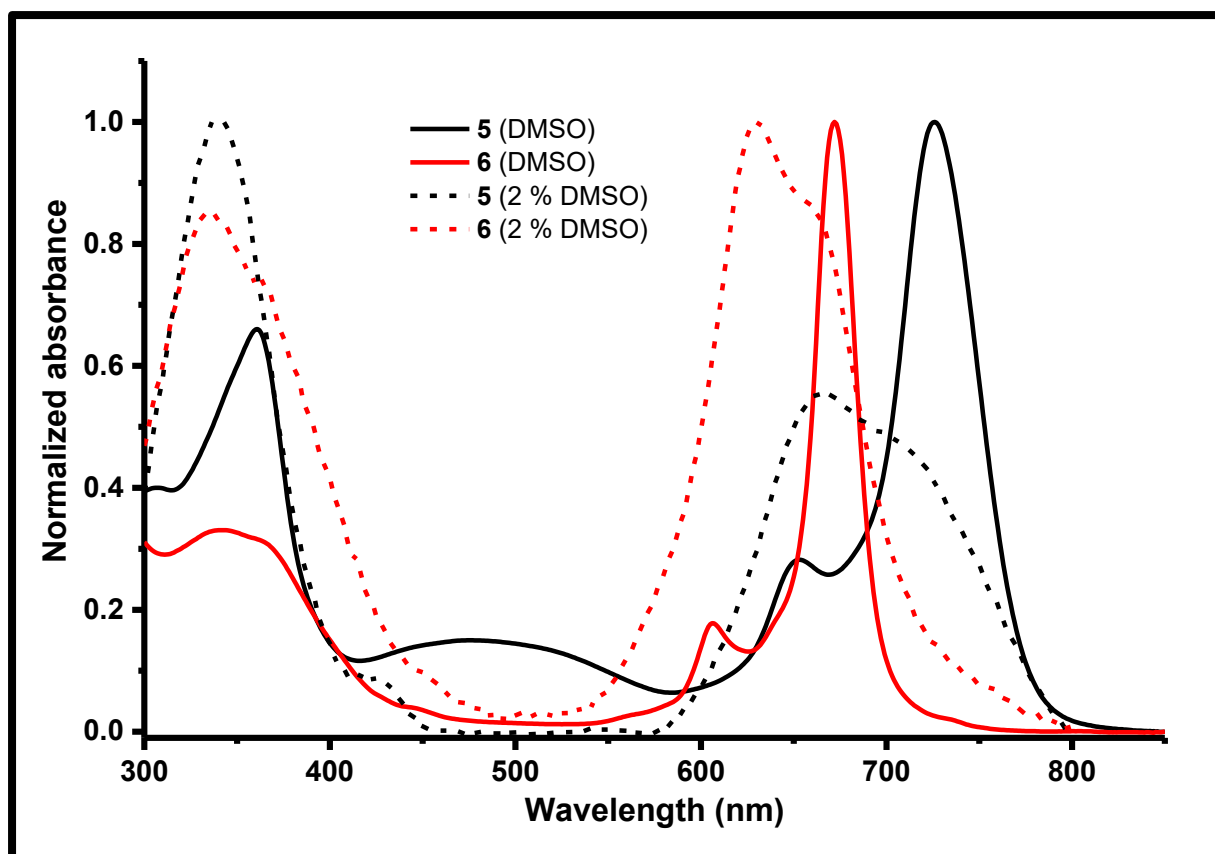


Fig. 3.3: NMR spectra for complexes **5** (A) and **6** (B).



**Fig. 3.4:** UV-Vis spectra for complexes **5** and **6** in DMSO and in 2 % DMSO in PBS solutions.

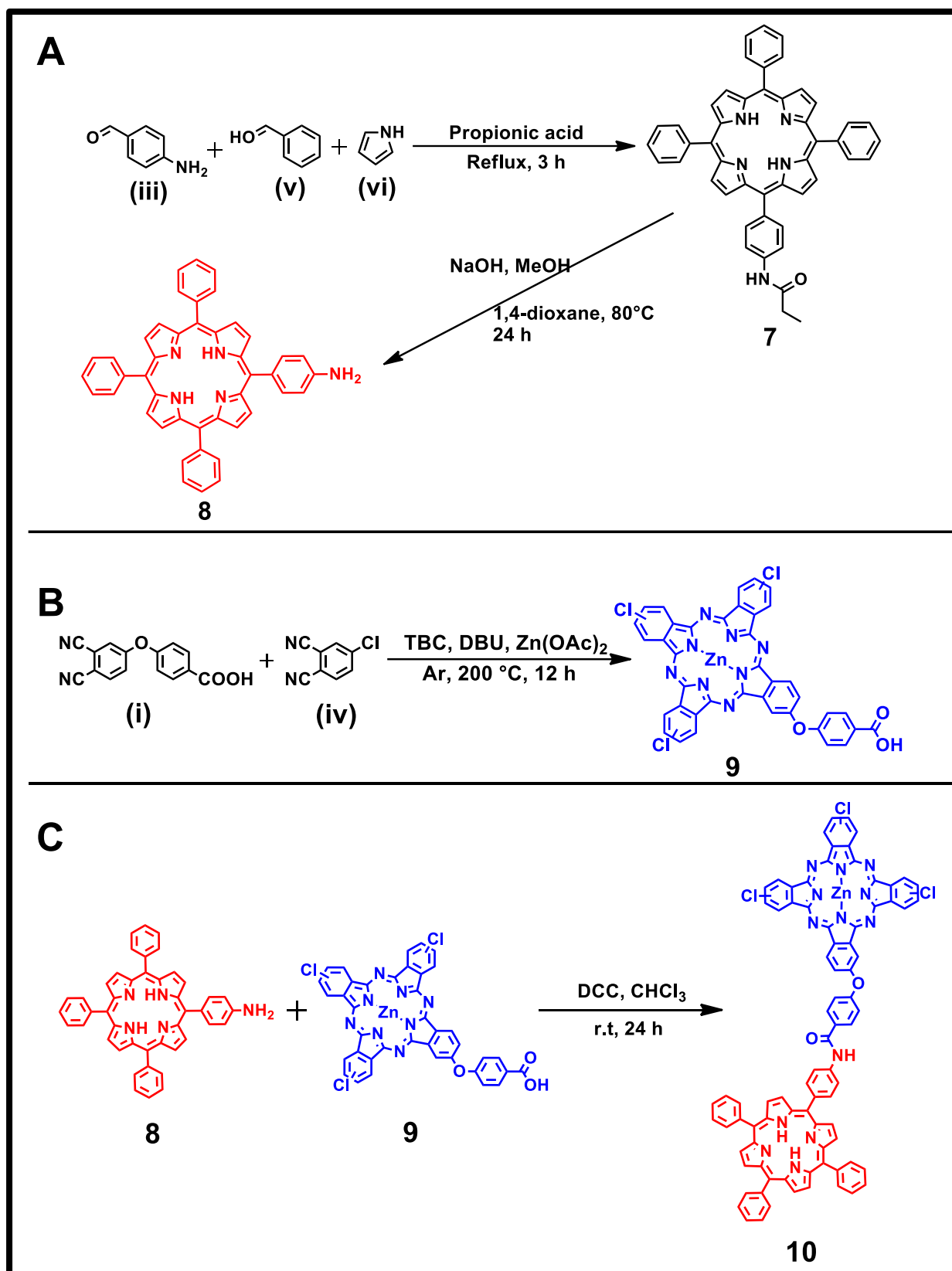
complexes. The aggregate peak is more prominent than the monomer peak which is typical of H-aggregation [138,139]. Complex **6** is readily soluble in aqueous solution (without the 2% DMSO) but is aggregated as observed in the spectrum of the complex in 2% DMSO (**Fig. 3.4**).

### 3.1.3. 5-(4-aminophenyl)-10,15,20-triphenylporphyrin (**8**), 2-(4-carboxyphenoxy)-9(10),16(17),23(24)-trichlorophthalocyaninato zinc (II) (**9**) and 2-(4-[4-(10,15,20-triphenylporphyrin-5-yl)phenyl]-amidophenoxy)-9(10),16(17),23(24)-trichlorophthalocyaninato zinc (II) (**10**)

The design of complexes **8** and **9** was based on foresight to their roles in the synthesis of complex **10** (**Scheme 3.3**), it's subsequent conjugation to b(NH<sub>2</sub>)PS and their roles

in the photosensitized polymer membrane. Complex **8** was designed to be asymmetric with one primary amine group for conjugation to complex **9** for the formation of complex **10**, while the three phenyl substituents ensured no interference with subsequent reactions including quenching of the photophysical properties. The free-base design was expected to avail the maximum number of Q-bands for maximum absorption wavelength coverage. On the other hand, complex **9** was also asymmetric with one carboxylic acid functional group to allow only linkage to one porphyrin molecule via amide bonding. Metalation with zinc and peripheral –Cl substituents were selected to facilitate and enhance intersystem crossing to the triplet excited state and minimise fluorescence, thus bottlenecking the energy loss via fluorescence from complex **10** after intramolecular energy transfer processes. The second and more specific function of the –Cl substituents was to allow for the subsequent conjugation of complex **10** to b(NH<sub>2</sub>)PS via Buchwald-Hartwig cross coupling.

Complex **8** was synthesized by slow addition of pyrrole (**vi**) to a refluxing mixture of benzaldehyde (**v**) and 4-aminobenzaldehyde (**iii**) in propionic acid (**Scheme 3.3 (A)**), while complex **9** was synthesized using a similar procedure as complex **5** using 4-chlorophthalonitrile (**iv**) and 4-(3,4-dicyanophenoxy)benzoic acid (**i**) as precursors and TCB as the solvent (**Scheme 3.3 (B)**). In the synthesis of complexes **8** and **9**, product yields were maximized by employing relatively large ratios (>1:9) of the precursor molecules (aldehyde or phthalonitrile) with comparison to the 1:3 in the formula. Amide linkage of complexes **8** and **9** to form complex **10** was achieved using DCC. In routine mass spectral analysis following the porphyrin reaction workup, a dominant peak of the amide porphyrin (complex **7**) at 685.1 Daltons was observed at the expense of the desired primary amine functionalized complex **8**. This suggested that the high



**Scheme 3.3:** Synthetic route for complexes **8** (A), **9** (B) and **10** (C).

temperature of the reaction and the excess of propionic acid were sufficient conditions to encourage and enable condensation of either 4-aminobenzaldehyde or the formed complex **8** with propionic acid resulting in formation of complex **7**. Hydrolysis of the crude mixture converted complex **7** to complex **8** with high efficiency (100 % based on mass spectrometry alone) which was consistent with the applied procedure [140]. Confirmations of complex **8** formation and isolation were made using mass spectroscopy, NMR and elemental analysis. Since complex **7** was obtained as an unexpected intermediate, it was not isolated from the crude product mixture to minimize synthesis steps and target compound loss in yield. Strategically, isolation of complex **8** was also expected to be simpler than isolation of complex **7**.

The specific route used for the synthesis of complex **10** was selected since it involved the least complications to achieve the desired compound. Other possible synthesis routes would involve the synthesis of either an aldehyde-functionalized Pc or a phthalonitrile-functionalized porphyrin precursor molecule. However synthesis of the complex using the Pc precursor would give rise to a completely metal-free complex whose component chromophores would be difficult to selectively metalate, since MPcs demetallate under elevated temperatures in acidic environments (reflux in propionic acid) [31]. On the other hand, synthesis using the porphyrin precursor would give a dually metalated complex whose component chromophores would also be difficult to selectively demetallate [44].

**Fig. 3.5** shows the FT-IR spectra for complexes **8**, **9** and **10**. Two primary amine stretching vibrations at 3446 and 3353  $\text{cm}^{-1}$  in the spectrum of complex **8** confirmed the presence of the  $-\text{NH}_2$  functional group. The  $-\text{OH}$  stretching vibration at 3427  $\text{cm}^{-1}$  and the  $\text{C}=\text{O}$  stretching vibration at 1690  $\text{cm}^{-1}$  in the spectrum of complex **9** confirmed

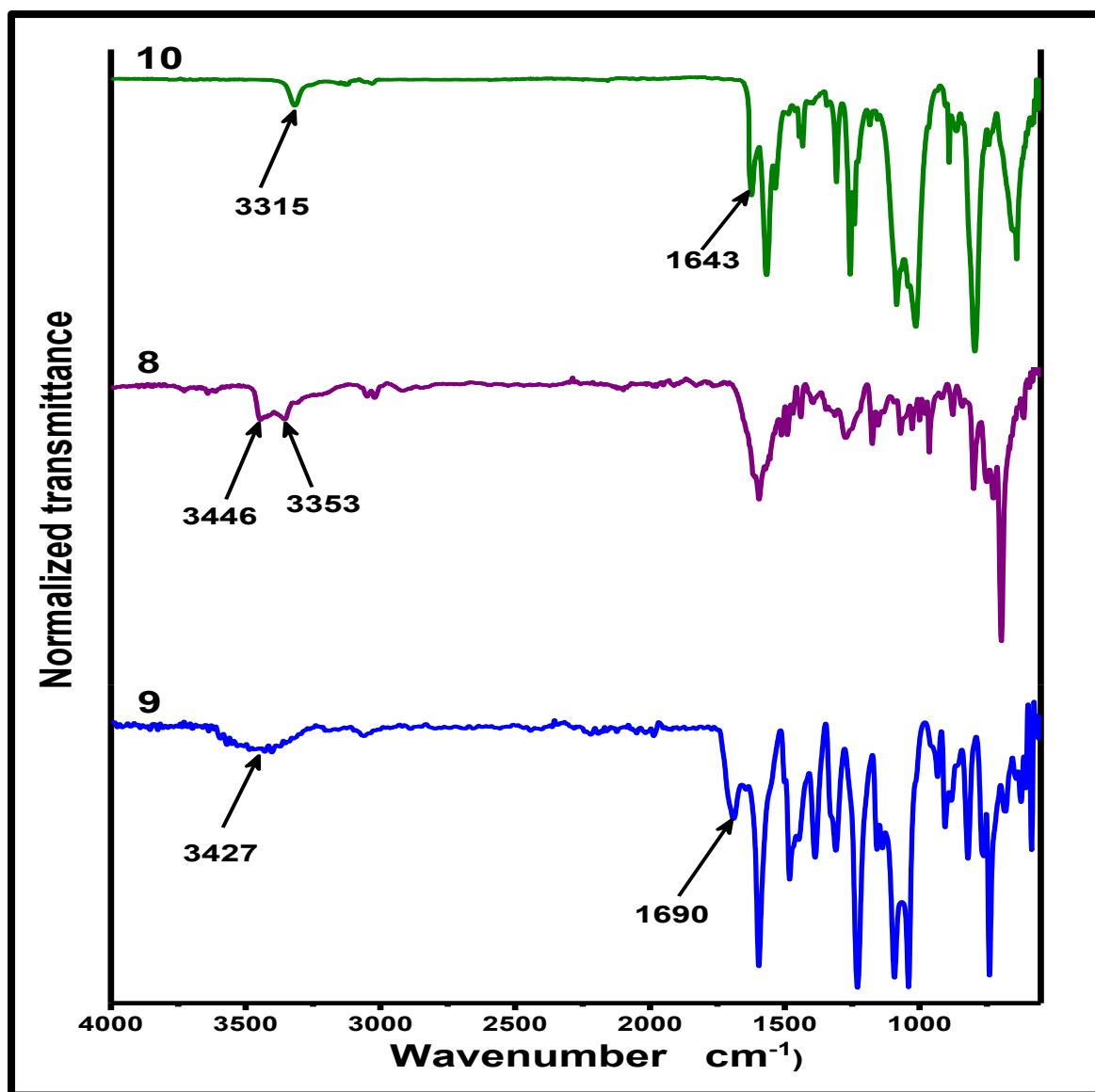


**Fig. 3.5:** FT-IR spectra for complexes **8**, **9** and **10**.

the presence of the carboxylic acid group, which together with the porphyrin  $\text{-NH}_2$  group in complex **8** were crucial for the subsequent formation of complex **10**. The shift and collapse of the two amine stretches at 3446 and 3353  $\text{cm}^{-1}$  in complex **8** to a single amide stretch at 3315 together with the shift in the carboxylic carbonyl peak of complex **9** at 1690  $\text{cm}^{-1}$  to the amide carbonyl at 1643  $\text{cm}^{-1}$  in the FT-IR spectrum for complex **10** (Fig. 3.5), strongly suggests successful linking of the chromophores.

Single peaks in the mass spectra for complexes **8**, **9** and **10** (**Fig. 3.6 (A-C)**, inserts) which correspond to the molecular ion ( $[M]^+$ ) peaks, and elemental analysis results which corresponded to the expected values for the three complexes, suggest successful isolation of complexes **8** and **9** from the crude reaction mixtures, and formation of complex **10**.

The  $^1\text{H}$  NMR spectrum for complex **8** (**Fig. 3.6 (A)**) exhibits signals which in total account for all the expected 31 protons. The signal distribution is 27 protons in the aromatic region, a singlet integrating to 2 protons at 3.97 ppm attributed to the  $-\text{NH}_2$  protons and another 2-proton singlet at -2.65 ppm which is attributed to the free-base inner core protons.  $^1\text{H}$  NMR results for complex **8** are consistent with the other characterizations and strongly suggest the successful isolation of the desired compound.  $^1\text{H}$  NMR spectrum for complex **9** is less complex, only consisting of aromatic protons integrating to 16 protons, which were attributed to the Pc macrocycle and substituent benzene ring protons, and a singlet at 11.56 ppm attributed to the carboxylic acid group proton. In total, the protons in the  $^1\text{H}$  NMR spectrum for complex **9** (**Fig. 3.6 (B)**) corresponds to the expected number which suggests successful isolation of the complex and supports the above results from other characterizations. For complex **10**, the  $^1\text{H}$  NMR spectrum integrates to the expected number of protons (**Fig. 3.6 (C)**). Also, the observation of the two proton signal at -2.63 ppm confirms the existence of the metal-free component [141]. The disappearance of the two proton primary amine signal at 3.97 ppm in the spectrum for complex **8** (**Fig. 3.6 (B)**) is accompanied by the appearance of an amide proton signal at 9.58 ppm that integrates to one proton in the spectrum for complex **10** (**Fig. 3.6 (C)**), which gives indication of successful linking of the chromophores.

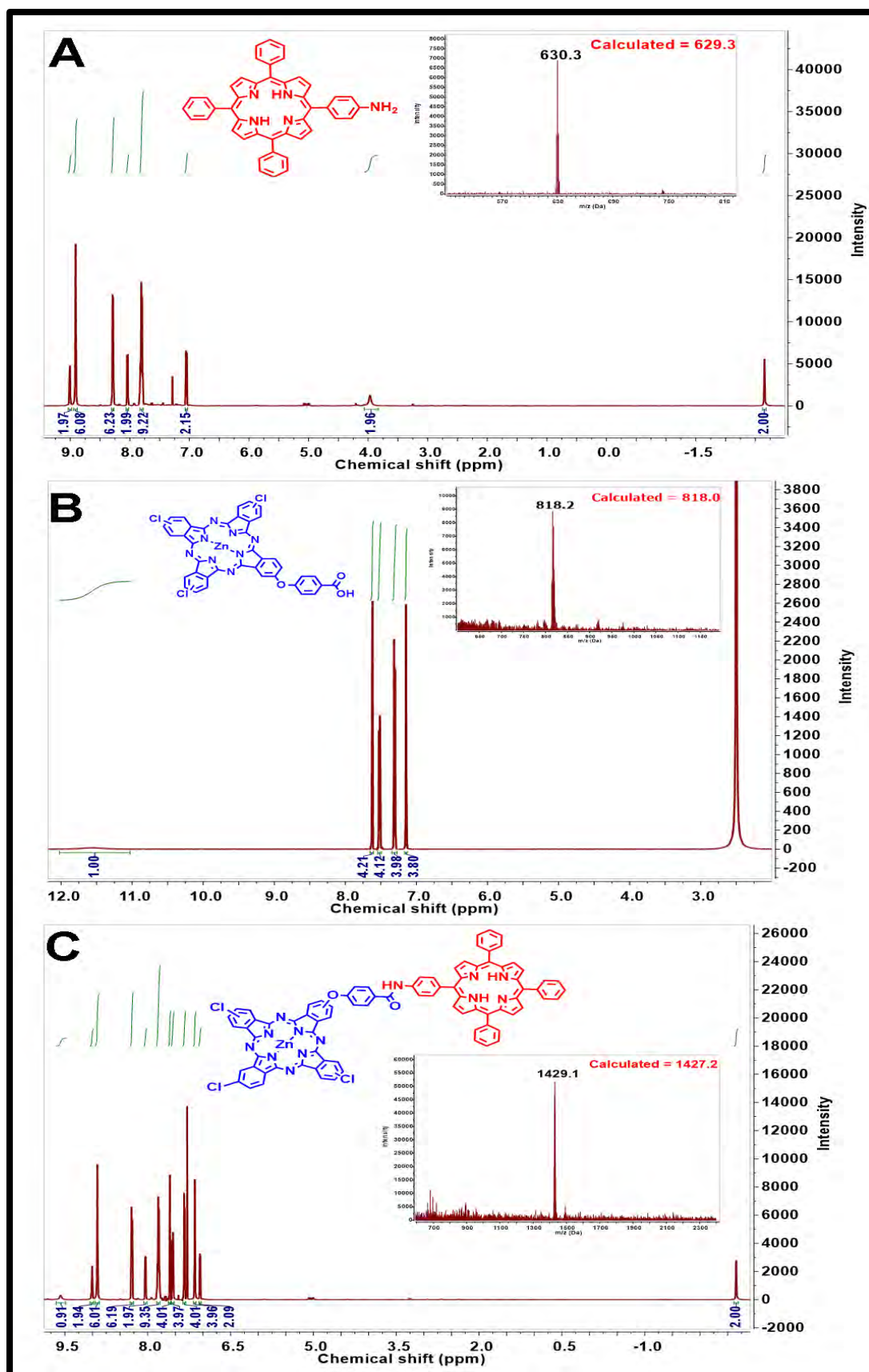
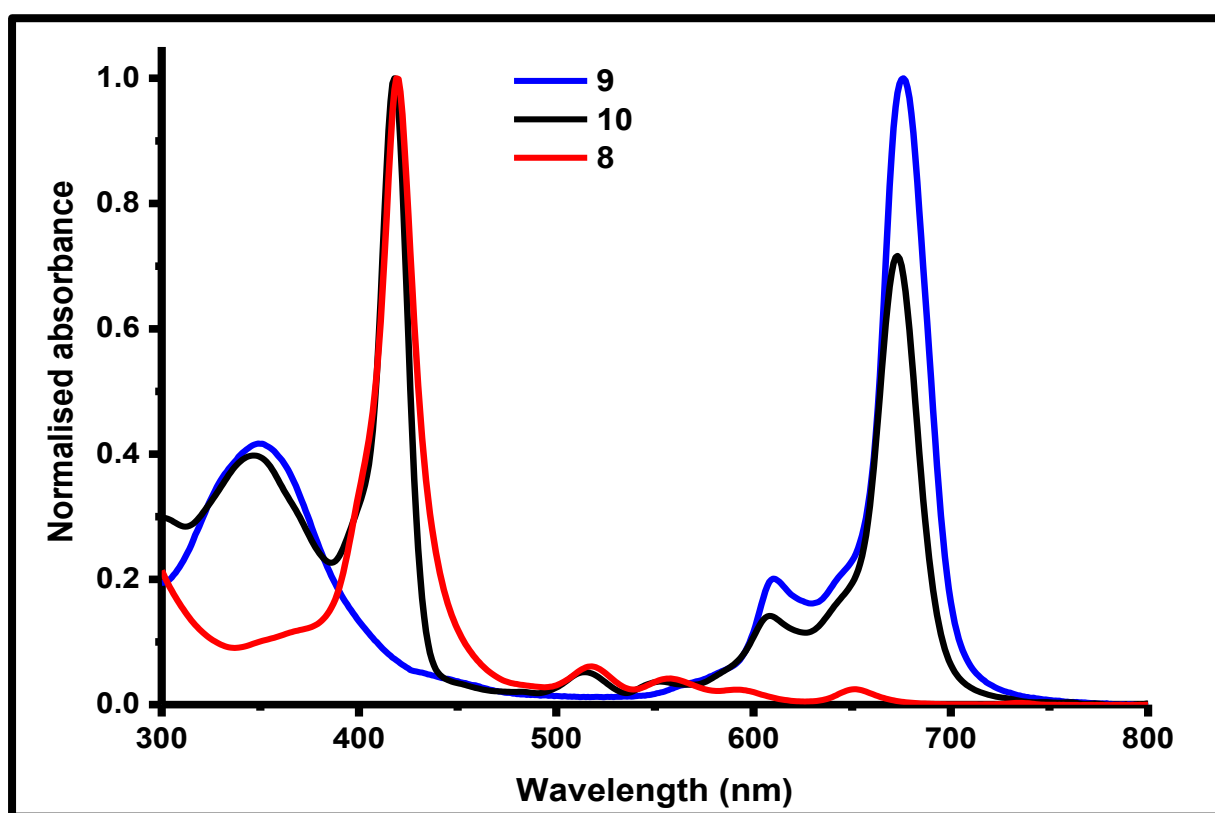


Fig. 3.6: NMR and MS (MALDI-TOF) (inserts) of complexes **8** (A), **9** (B) and **10** (C).



The ground state UV-Vis absorption spectra for complexes **8**, **9** and **10** are shown in **Fig. 3.7**. The spectrum for complex **8** exhibits an intense Soret band at 420 nm and four low intensity lower energy Q-bands which are characteristic of free-base porphyrins [35]. The UV-Vis spectrum for complex **9** on the other hand, exhibits a high energy broad relatively low intensity B-band at 350 nm and an intense narrow single peak energetically lower Q-band at 675 nm which is characteristic of zinc (II) metalated phthalocyanines [132,142–145]. The negligible shift in the porphyrin Soret and visible Q-bands for complex **10** (**Fig. 3.7**), suggests that the porphyrin component chromophore is still metal free. A shift of the Soret band to the red usually occurs on metalating [39]. The four Q bands are however not clear in the spectrum for complex **10**. On the other hand, the single unsplit Q-band for the MPc component (**Fig. 3.7**) suggests that the MPc component chromophore is metalated.



**Fig. 3.7:** Ground-state UV-Vis spectra for complexes **8**, **9** and **10** in DMSO solution.

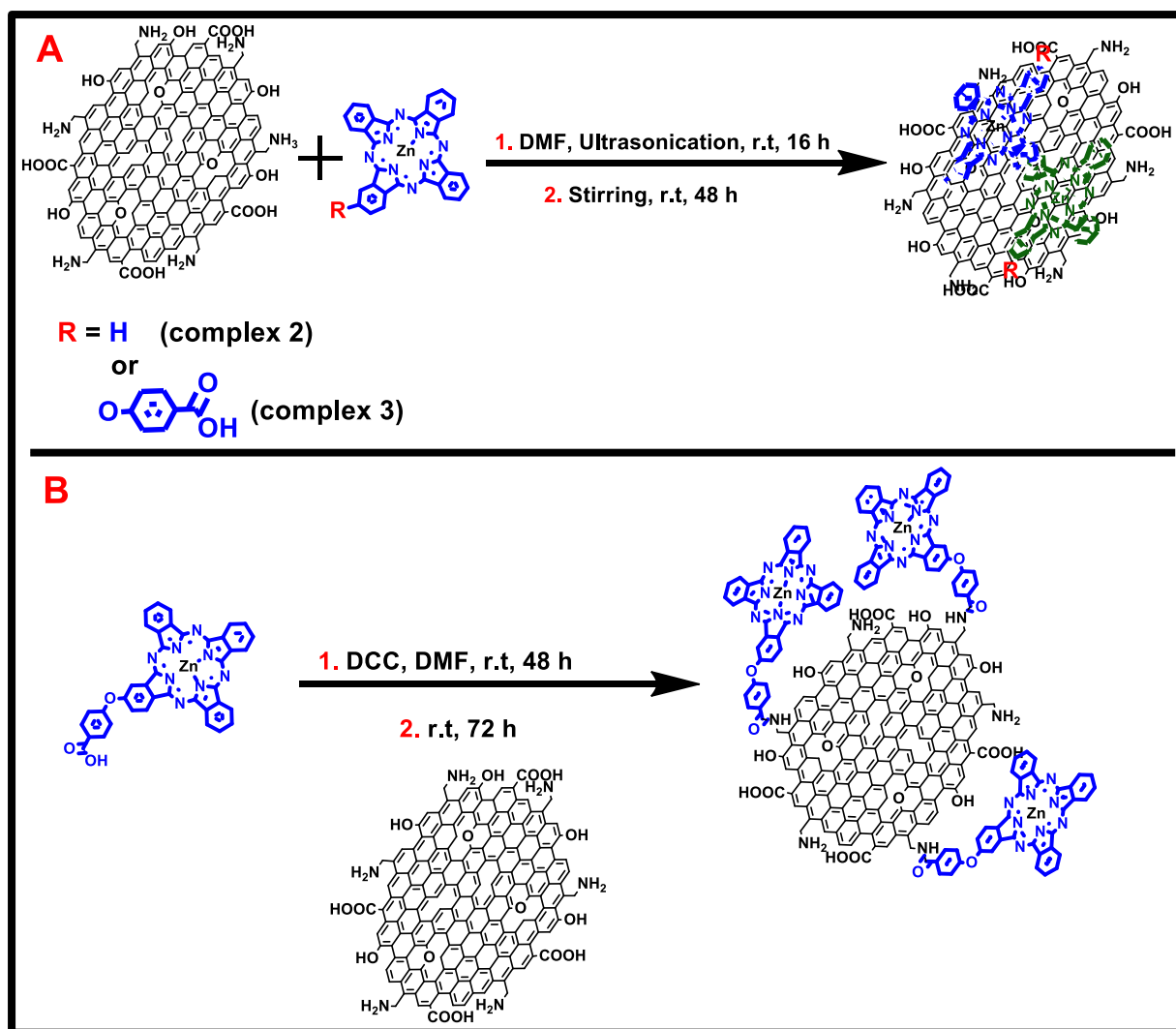
### 3.2. Nanoparticles and their MPc conjugates

This section outlines the synthesis and characterisation of the nanoparticles and their MPc conjugates used in this work. MPcs were linked to GQDs either by  $\pi$ - $\pi$  stacking (for complexes **2** and **3**) or by amide bonding between the  $-\text{COOH}$  of complex **3** and the  $-\text{NH}_2$  of the GQDs. Linkage to AgTNPs was achieved only by amide bonding of the  $-\text{COOH}$  of complexes **4a** and **4b** with the  $-\text{NH}_2$  of the GSH capping of the AgTNPs.

#### 3.2.1. Graphene quantum dots (GQDs) and MPc conjugates

##### 3.2.1.1. Synthesis

GQDs used in this work were synthesized using the hydrothermal method according to literature specifications [128] in two batches for the separate conjugation to complexes **2** and **3** (reasons provided in chapter 2). In the synthesis of the  $\pi$ - $\pi$  stacked conjugates (**Scheme 3.4 (A)**), small volumes of solvent and extended sonication periods were used in order to maximize MPc-GQDs contact and enhance possible  $\pi$ - $\pi$  interactions. Washing steps were carried out to ensure removal of unbound GQDs, MPcs and any possible MPc  $\pi$ - $\pi$  aggregates. The larger surface area and  $\pi$  electron system of GQDs supported the more stable geometric arrangement of  $\pi$ - $\pi$  interacting species [146] which favoured the MPcs binding onto the quantum dots rather than themselves. On the other hand, synthesis of **3**(GQDs) was achieved by DCC facilitated amide coupling of complex **3** with the GQDs (**Scheme 3.4 (B)**).



**Scheme 3.4:** Synthetic route for (A)  $2\pi$ (GQDs) and  $3\pi$ (GQDs), and (B)  $3$ (GQDs).

### 3.2.1.2. TEM

**Fig. 3.8** shows the TEM images and corresponding size distribution histograms for the second batch of GQDs and their complex **3** conjugates as representatives for the MPC-GQDs conjugates. The GQDs and conjugates were monodispersed, and the average size of the nanomaterials increased after conjugate formation from 14 nm for GQDs to 24 and 21 nm for  $3\pi$ (GQDs) and  $3$ (GQDs) respectively (**Table 3.2**). Gaussian distribution is also observed to improve following conjugate formation. These two

observations may be attributed to further purification processes for the conjugates compared to GQDs. The GQDs from the first batch (TEM not shown) were also monodispersed with size ranges between 1–6 nm with an average at approximately 2.0 nm. Similarly, the corresponding conjugate,  $2\pi$ (GQDs) was also monodispersed with a size range between 2–5 nm and an average of about 3.4 nm (Table 3.2).

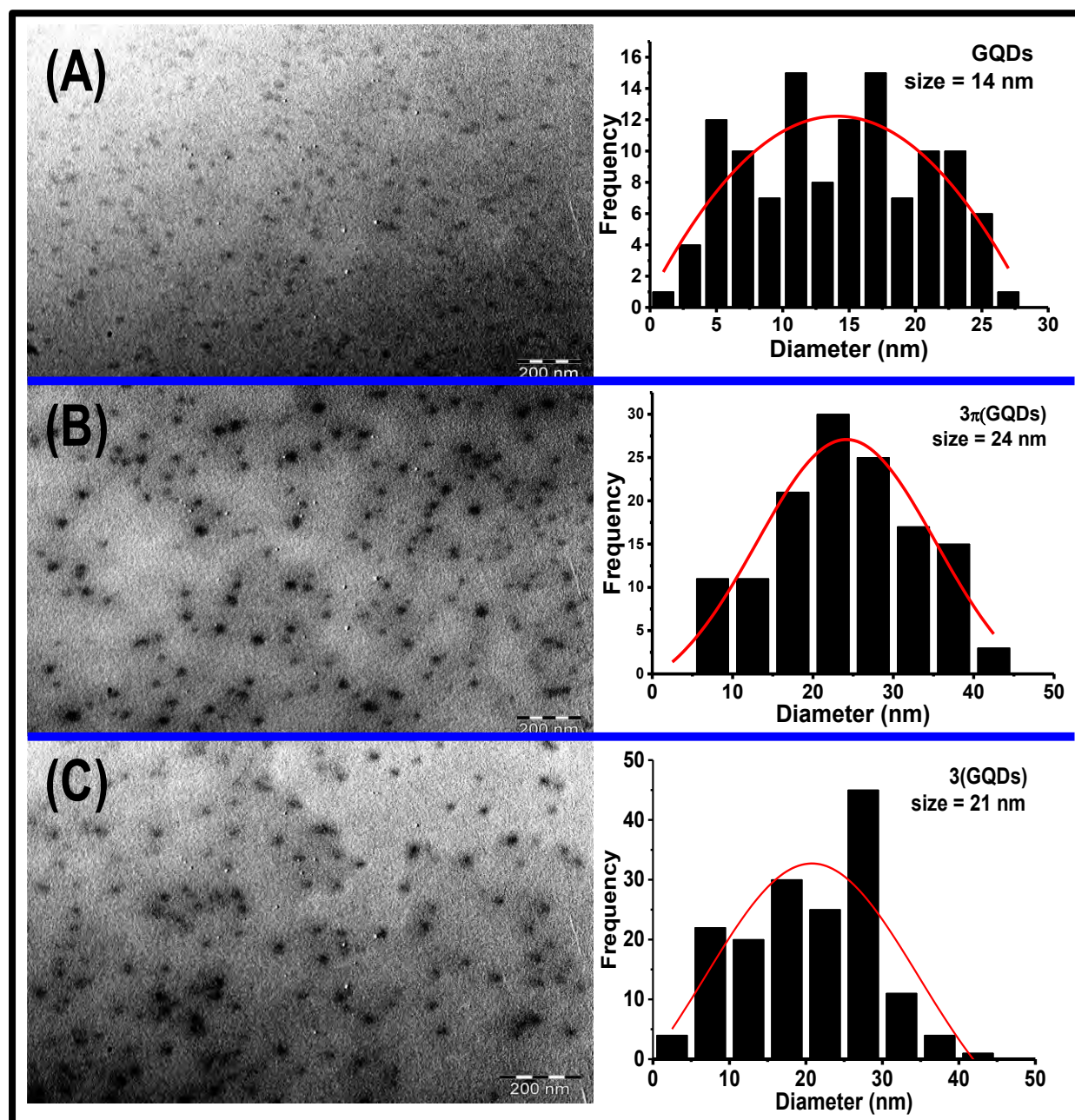


**Fig. 3.8:** TEM micrographs and size distribution histograms for (A) GQDs, (B)  $3\pi$ (GQDs) and (C)  $3$ (GQDs).

**Table 3.2:** Summary of the NPs and MPc(NPs) conjugate average sizes (from TEM), MPc loading values and D/G ratios.

Sample	Average size (nm) (TEM)	Loading (mg MPc/ mg MPc(NPs))	D/G Ratio (Raman)
GQDs (first batch)	2.0	–	0.09
2 $\pi$ (GQDs)	3.4	0.67	0.38
GQDs (second batch)	14	–	0.05
3 $\pi$ (GQDs)	24	0.40	0.38
3(GQDs)	21	0.14	0.30
AgTNPs	26	–	–
4a(AgTNPs)	28	0.35	–
4b(AgTNPs)	27	0.59	–

### 3.2.1.3. FT-IR

The FT-IR spectra of 3 $\pi$ (GQDs) and 3(GQDs) together with their precursors (complex **3** and GQDs) are shown in **Fig. 3.9**, as examples for the MPc-GQDs conjugates. Both complex **3** and GQDs possess the –COOH group which is indicated by the carbonyl stretching vibrations at 1714 and 1692 cm<sup>-1</sup> respectively, together with the hydroxyl stretching vibrations in the region between 3300 and 3600 cm<sup>-1</sup> (highlighted in **Fig. 3.9**) for both materials. Upon conjugation carbonyl shoulders around 1698 and 1693 cm<sup>-1</sup> are observed in the spectra for 3 $\pi$ (GQDs) and 3(GQDs) respectively, which may be attributed to possible successful conjugation. The disappearance of complex **3**'s

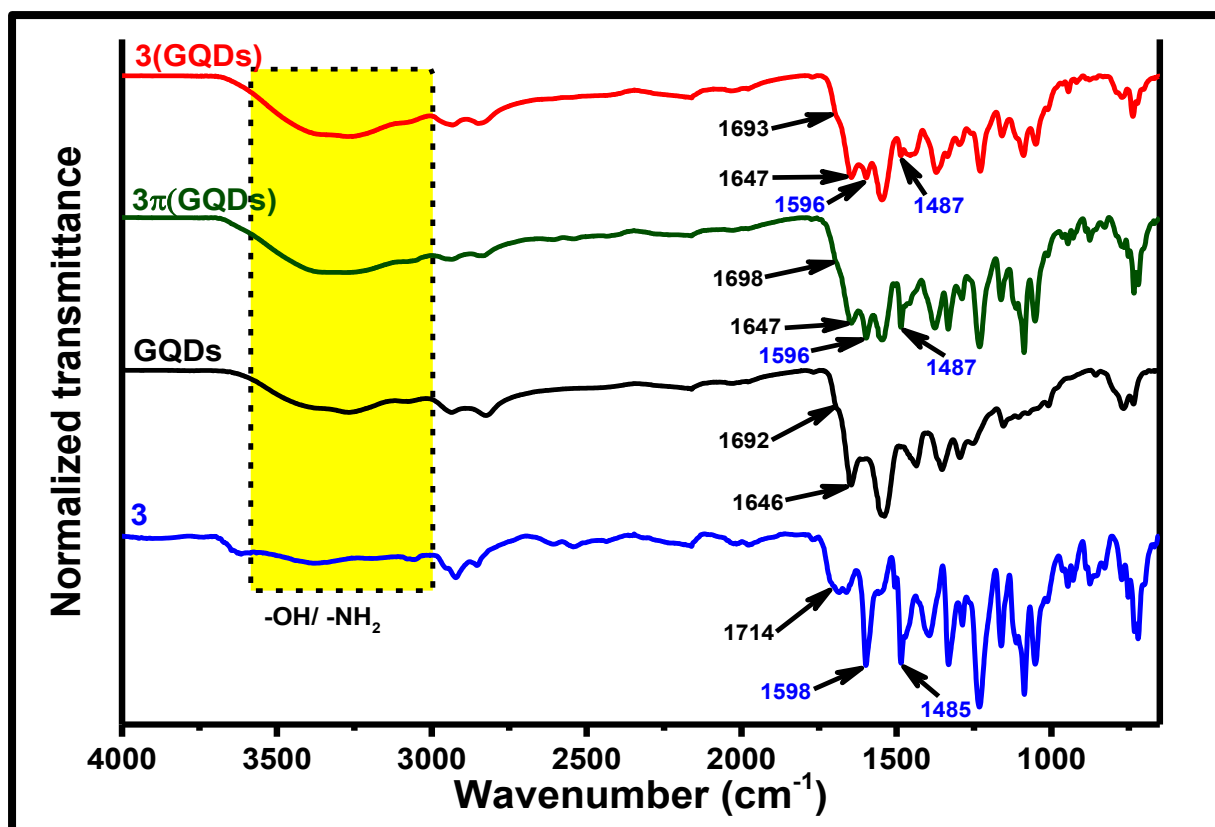


Fig. 3.9: FT-IR spectra for GQDs, complex **3**,  $3\pi(\text{GQDs})$  and  $3(\text{GQDs})$ .

C=O stretching vibration in  $3(\text{GQDs})$  is attributed to conversion of the carboxylic carbonyl to an amide carbonyl which overlaps with the GQDs spectral bands and is hence masked. On the other hand, a shift of the carboxylic carbonyl stretching vibration shoulder from  $1692\text{ cm}^{-1}$  in GQDs to  $1698\text{ cm}^{-1}$  in  $3\pi(\text{GQDs})$ , is attributed to the influence of the complex **3** –COOH groups which are available in the conjugate.

The presence of the complex **3** vibration peaks at  $1598$  and  $1485\text{ cm}^{-1}$  (as tracer peaks) in the conjugates confirms the presence of the MPc as an integration in the GQDs. These peaks are at  $1596$  and  $1487\text{ cm}^{-1}$  in the conjugates. The relative intensities of these tracer peaks also suggest a higher MPc loading in  $3\pi(\text{GQDs})$  than  $3(\text{GQDs})$  which is consistent with the observed loading values (Table 3.2) to be

discussed below. Retention of bands in the highlighted region in **Fig. 3.9** suggests the presence of available –OH, –NH<sub>2</sub> or –COOH groups in the conjugates for possible further conjugation to (COOH)PS.

### 3.2.1.4. Raman

Graphene quantum dots have two characteristic Raman peaks; the G band (sp<sup>2</sup>) tangential mode and D-disorder band (sp<sup>3</sup>) breathing mode. The Raman spectrum for the GQDs from the first batch shows characteristic G and D bands at 1594 and 1283 cm<sup>-1</sup>, respectively (**Fig. 3.10 (A)**), while those for the second batch are observed at 1454 and 1298 cm<sup>-1</sup> respectively (**Fig. 3.10 (C)**). The presence of defects on GQDs is quantified by the ratio of the intensity of the D over G band (D/G) and the values for the synthesized GQDs and their corresponding MPc conjugates are summarized in **Table 3.2**. The spectra for the MPcs consist of one distinct band (at 1506 cm<sup>-1</sup> for complex **2** and 1422 cm<sup>-1</sup> for complex **3**) assigned as the  $\nu_3$  vibrational mode (asymmetric stretch) coupled to the vibronic band electronic transition [147]. The Raman spectrum for 2 $\pi$ (GQDs) (D/G ratio of 0.38) shows a band in the region where the complex **2** band was observed. The peak could be that of complex **2** due to a high loading in 2 $\pi$ (GQDs) (**Table 3.2**) or a shifted G band of the GQDs. The increase in D/G ratio following 2 $\pi$ (GQDs) formation suggests a decrease in the average size of the sp<sup>2</sup> domains of the GQDs. For both 3 $\pi$ (GQDs) (D/G ratio of 0.38) and 3(GQDs) (D/G ratio of 0.30) there is a shift of both D and G bands to higher wavenumbers together with an increase in the D/G ratio after conjugation (**Table 3.2**). A greater D/G ratio in 3 $\pi$ (GQDs) than in 3(GQDs) may be related to the position of the MPcs in the conjugates where in the former, MPcs were expected mostly on the GQDs surfaces, and on the edges for the latter. Observed shifts in bands also suggest conjugation.



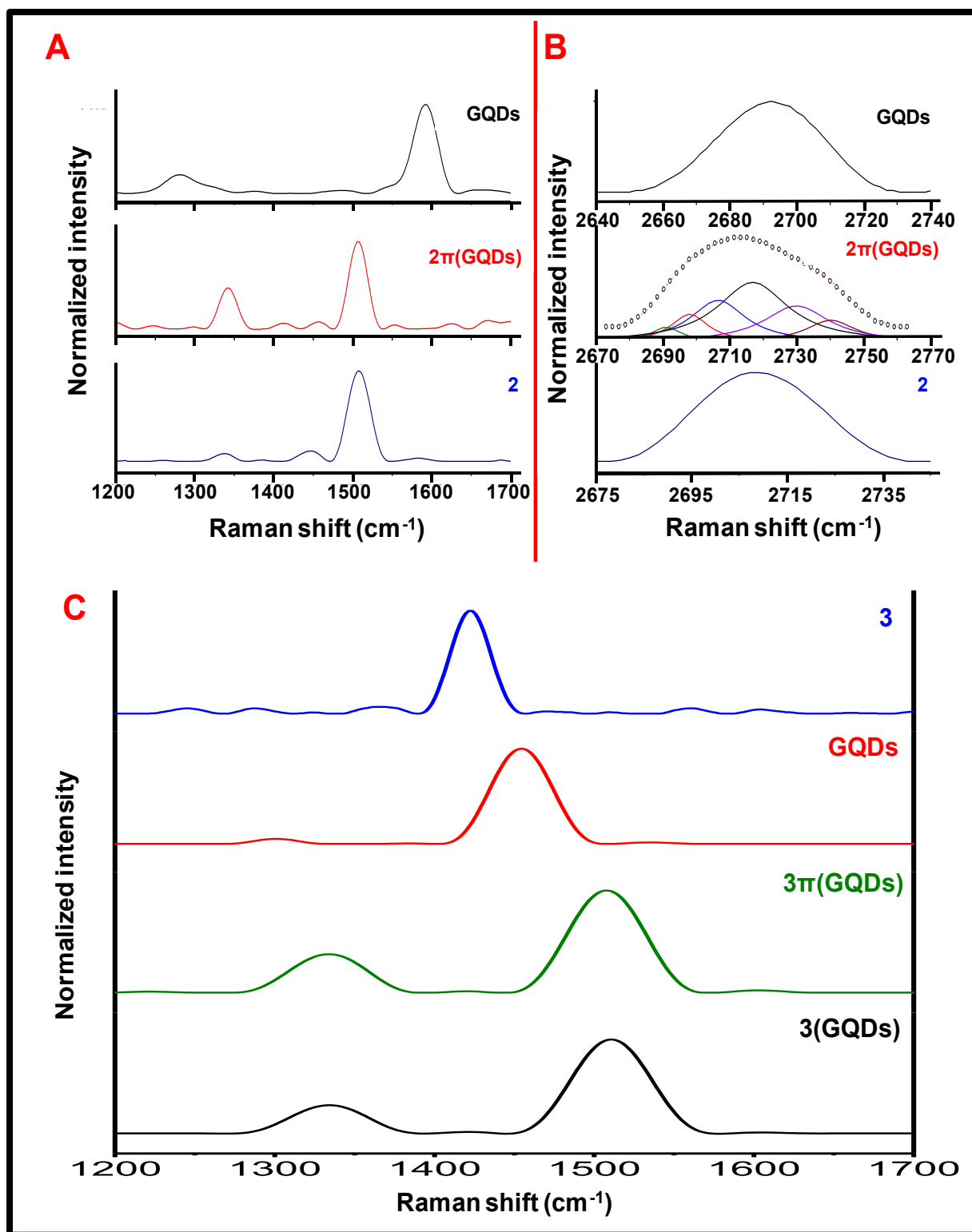


**Fig. 3.10:** FT-Raman spectra for (A) D and G band spectral region and (B) G' band spectral region for GQDs from first batch, complex **2** and  $2\pi(\text{GQDs})$ , and (C) D and G band spectral region for GQDs from second batch, complex **3**,  $3\pi(\text{GQDs})$  and  $3(\text{GQDs})$ .



**Fig. 3.10 (B)** shows the G' band spectral region of complex **2**, GQDs and  $2\pi$ (GQDs) as an example. The G' band of complex **2** and GQDs are relatively symmetrical peaks which can each be satisfactorily fitted with one Lorentzian curve and suggest the absence of interlayer interactions between the GQD units [148] or intermolecular interactions between complex **2** molecules. On the other hand, the G' band of  $2\pi$ (GQDs) showed low asymmetry with no obvious shoulders, which is similar to graphene films dominated by Bernal (ABA) stacking order [148,149]. This together with satisfactory fitting of the band with six Lorentzian curves suggest a trilayer arrangement in the conjugate [148]. Similar deconvolution of the G' band of  $3\pi$ (GQDs) (not shown) gave results that also suggest a trilayer arrangement in the conjugate. On the other hand, **3**(GQDs) had a symmetrical G' band (figure not shown) similar to the GQDs alone, which may be attributed to the conjugation occurring on the edges of the GQDs, thus they retain their layered structure in the conjugate.

#### 3.2.1.5. XRD

The XRD diffractogram of GQDs from the first batch (**Fig. 3.11 (A)**) shows a broad band with a maximum at approximately  $2\theta = 42^\circ$  and shoulder at  $2\theta = 30^\circ$ , while that of the GQDs from the second batch consist of a broad band with a maximum at  $2\theta = 20^\circ$  (**Fig. 3.11 (B)**). The broad bands indicate the amorphous nature of the GQDs. The diffractogram for complex **2** (**Fig. 3.11 (A)**) is composed of sharp peaks characteristic of a crystalline material which has been reported [150–152] and are consistent with the standard International Centre for Diffraction Data (ICDD) card number: 39-1882 [150]. The conjugate diffractogram is observed to be similar to that of complex **2** with slight changes in relative peak intensities and the presence of some broad bands around  $2\theta = 17^\circ$  and  $2\theta = 63^\circ$ , which suggests introduction of amorphous character in the previously crystalline complex **2**.

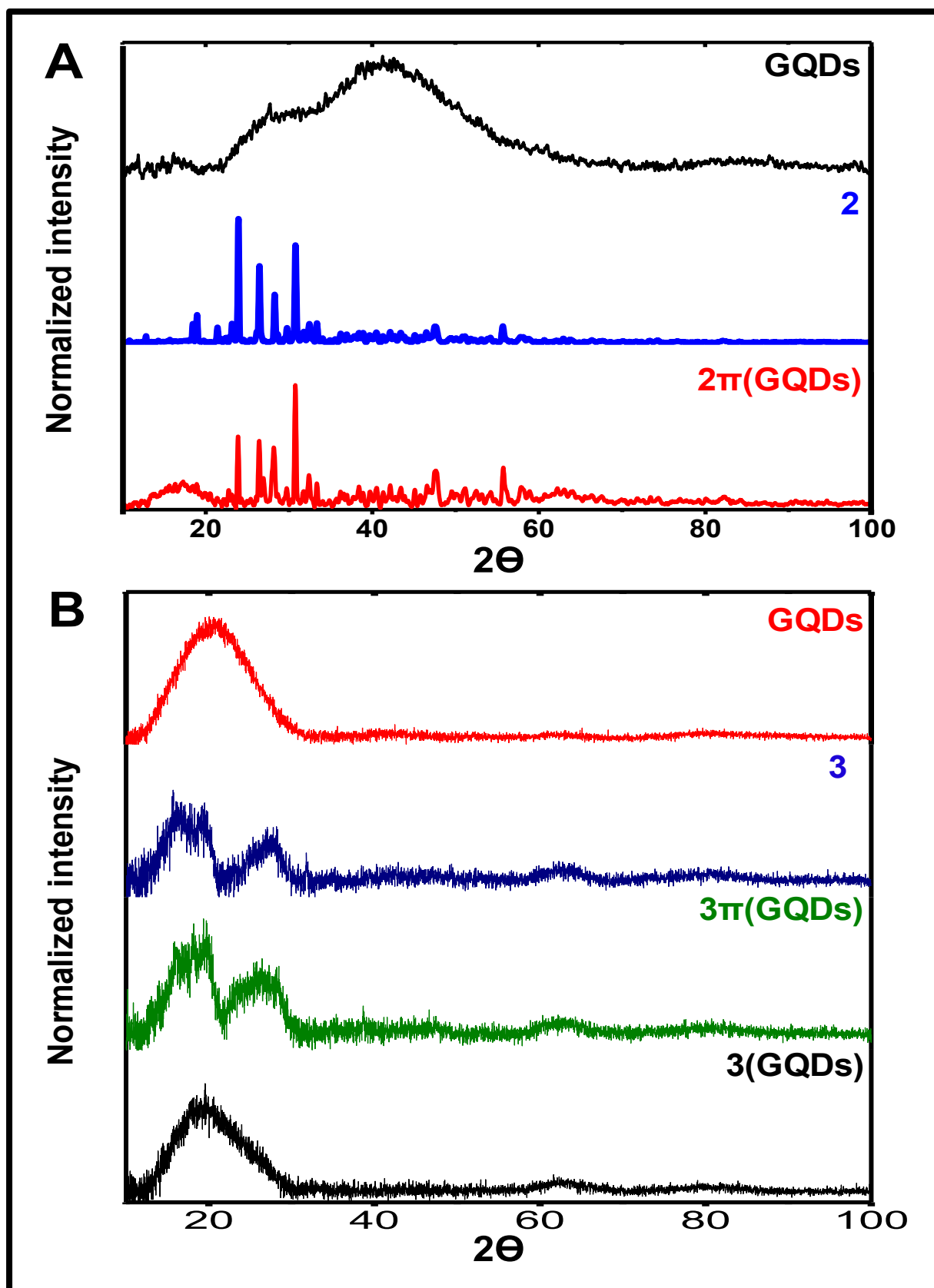


**Fig. 3.11:** Powder-XRD diffractograms for (A) GQDs from first batch, complex 2 and 2π(GQDs), and (B) GQDs from second batch, complex 3, 3π(GQDs) and 3(GQDs).

On the other hand, the diffractogram for complex **3** proves it to be amorphous (**Fig. 3.11 (B)**) possibly due to the carboxyphenoxy substituent which may hinder close packing of molecules and crystal formation in the solid state. The diffractograms of the conjugates for complex **3** are significantly different, but each closely resembling that of one of the components (GQDs or complex **3**). The diffractogram for **3** $\pi$ (GQDs) resembles that for complex **3** while the diffractogram for **3**(GQDs) resembles that of the GQDs. This observation may be attributed to the MPc loading and distribution on the GQDs. In **3** $\pi$ (GQDs) the MPcs were expected to cover the surfaces of the GQDs. This together with the higher loading (at 0.40 mg MPc/mg MPc(GQDs) to be discussed below) could have resulted in the conjugate exhibiting mostly the MPc properties. On the other hand, the diffractogram for **3**(GQDs) may be attributed to the lower MPc loading and conjugation of the MPcs on the GQDs edges where they may have given the effect of peripheral extensions.

### 3.2.1.6. UV-Vis

The UV–Vis spectrum for the GQDs (**Fig. 3.12**) shows an absorption band with  $\lambda_{\text{max}}$  at 359 nm for the first batch (**Fig. 3.12 (A)**) and 350 nm for the second batch (**Fig. 3.12 (B)**) in water (**Table 3.1**), which is associated with the  $n\text{--}\pi^*$  transition of C=O groups [128]. The variation in the  $\lambda_{\text{max}}$  values for the two batches may be attributed to the difference in the C=O group density in the GQDs as a result of their difference in size. The UV–Vis spectra for complex **2** and **2** $\pi$ (GQDs) (**Fig. 3.12 (A)**) are almost identical with no shifts in the Q-band. A similar observation was also made for complex **3** in both **3** $\pi$ (GQDs) and **3**(GQDs) (**Fig. 3.12 (B)**), with no significant shifts. Thus, for all MPc-GQDs conjugates there is no spectroscopic evidence of MPc-MPc  $\pi\text{--}\pi$  interactions (aggregation) in **Fig. 3.12** since aggregation in phthalocyanines is judged by splitting or broadening of the Q bands as a result of coplanar association of Pc rings

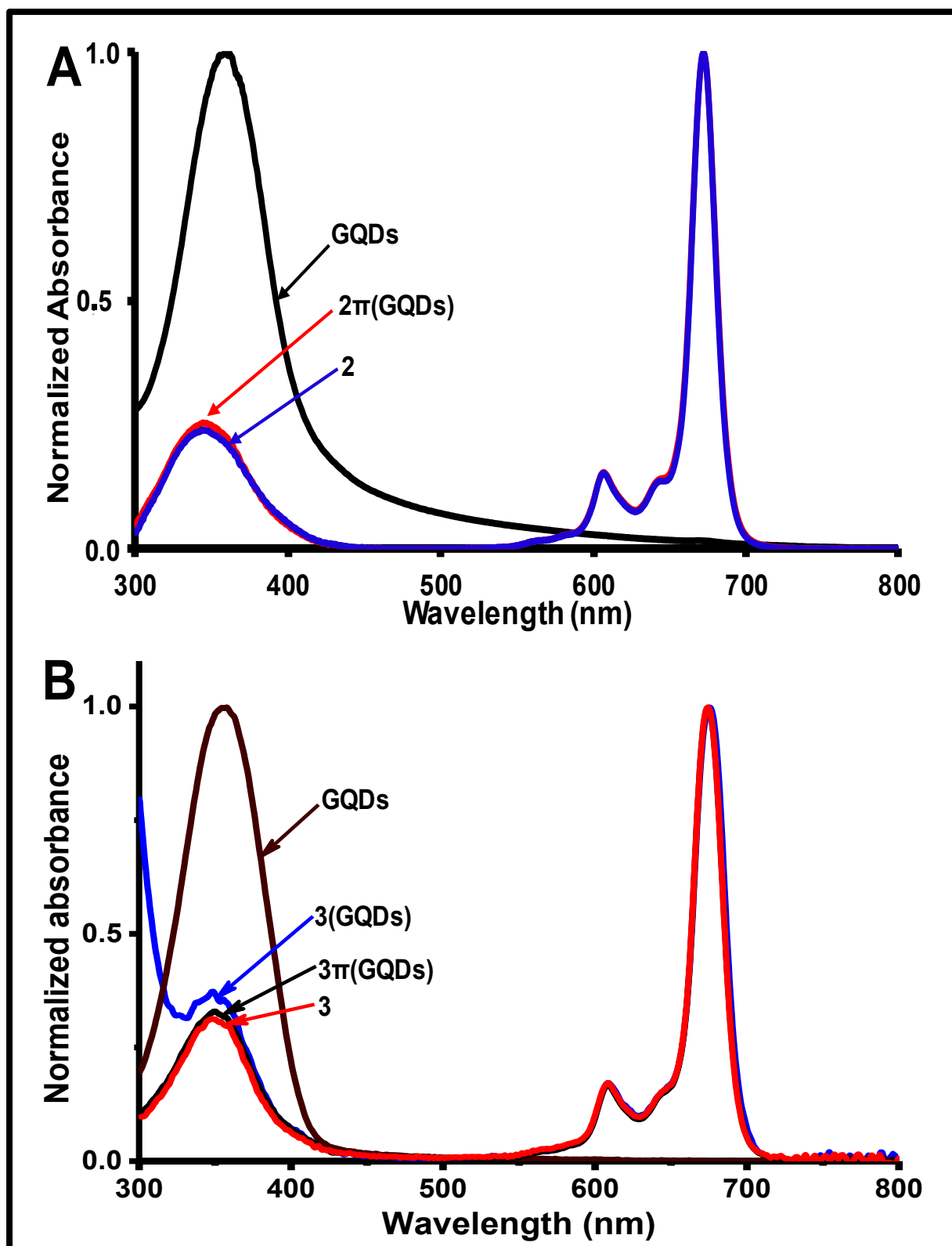


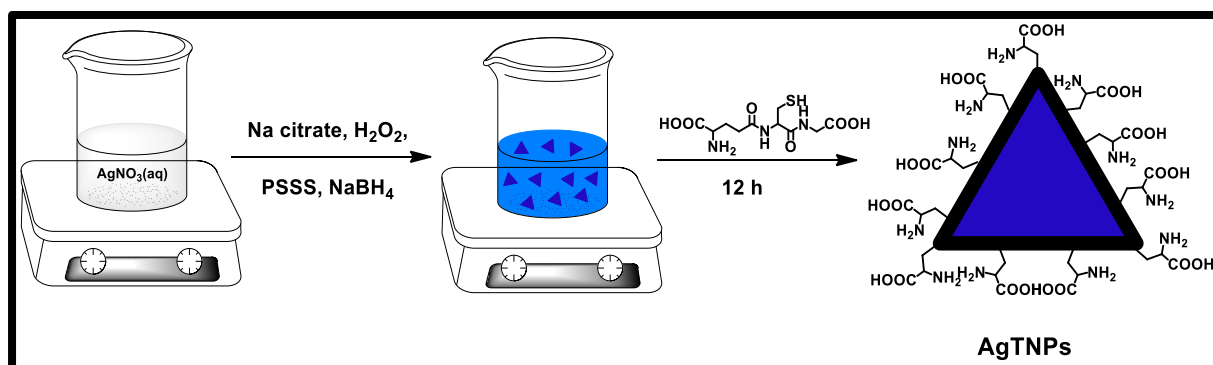
**Fig. 3.12:** Ground state UV-Vis absorption spectra for (A) complex **2** and  $2\pi(\text{GQDs})$  in DMSO, and GQDs in water, and (B) complex **3**,  $3\pi(\text{GQDs})$  and  $3(\text{GQDs})$  in DMSO, and GQDs in water.

progressing from monomers leading to aggregates [153]. This also confirms that the conjugates are formed between the GQDs and MPc complexes, not between two MPc molecules especially when considering  $2\pi$ (GQDs) and  $3\pi$ (GQDs). Since there is no spectroscopic evidence of MPc aggregation in the conjugates ( $2\pi$ (GQDs),  $3\pi$ (GQDs) and  $3$ (GQDs)), and the GQDs characteristic absorption bands do not overlap with the Q-bands of the corresponding MPcs, the loading of the complexes in the conjugates was determined spectroscopically using UV-Vis spectra as reported before [154]. The MPc loading values in the conjugates are summarized in **Table 3.2**, where  $2\pi$ (GQDs) is highest followed by  $3\pi$ (GQDs) and then  $3$ (GQDs).

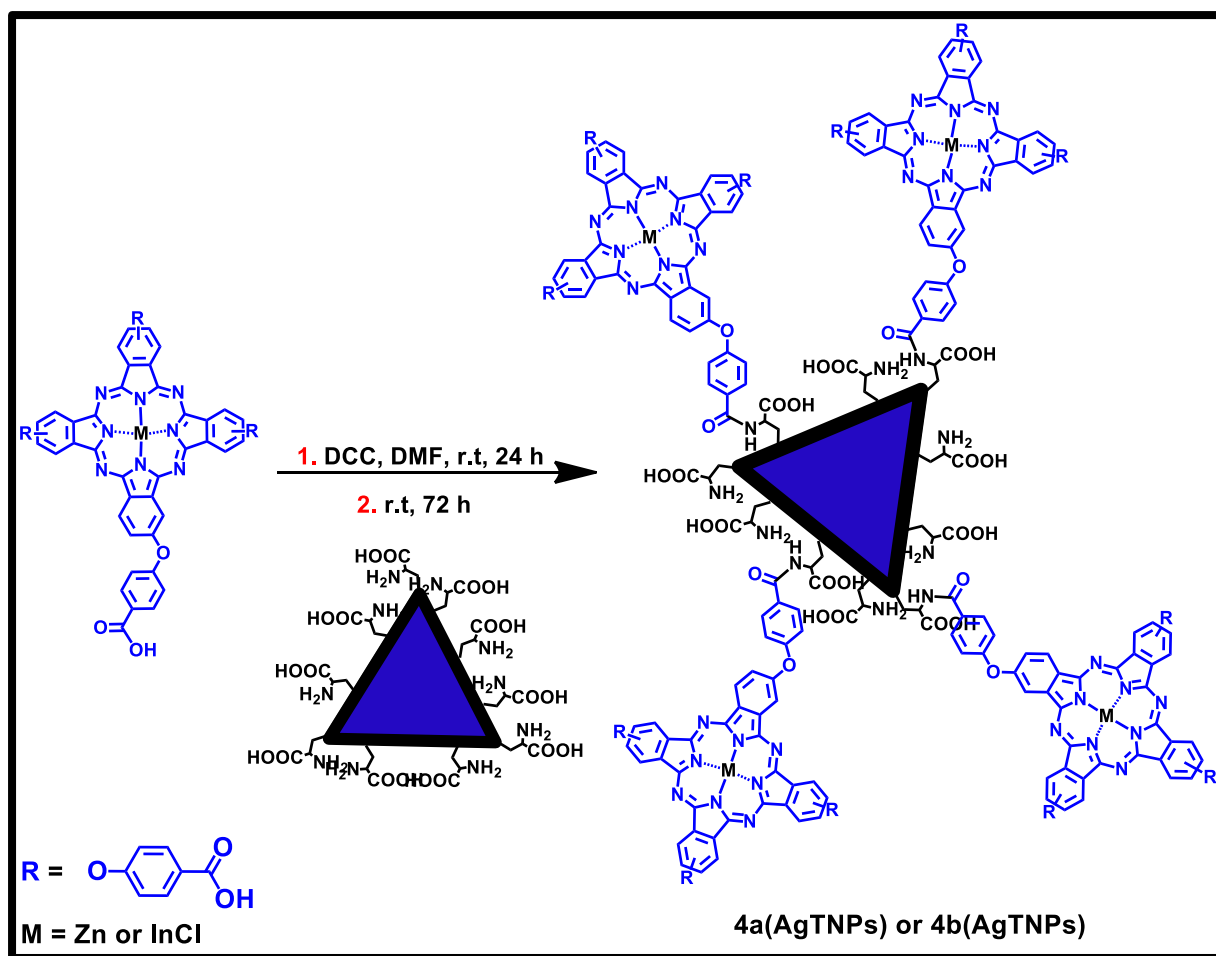
### 3.2.2. Silver triangular nanoprisms (AgTNPs) and MPc conjugates

#### 3.2.2.1. Synthesis

AgTNPs were synthesized using the method reported by Métraux and Mirkin [120], but with some modifications (**Scheme 3.5**). The synthesized AgTNPs gave a blue solution in water which corresponded to relatively large triangular nanoparticles [155]. **Scheme 3.6** shows a representation of the formation of the MPc(AgTNPs) conjugates through amide bonding. Although linkage to one  $-\text{COOH}$  group of the MPcs is shown in **Scheme 3.6**, it is possible that more than one  $-\text{COOH}$  group on the MPc is involved in the linking, depending on orientation.



**Scheme 3.5:** Synthetic route for GSH capped AgTNPs.



**Scheme 3.6:** Synthetic route for **4a**(AgTNPs) and **4b**(AgTNPs).

### 3.2.2.2. TEM

TEM (**Fig. 3.13**) confirms the nanoparticle shape to be triangular nanoprisms with average edge length of about 26 nm. Some relatively circular shaped nanoparticles (possibly spheres or discs) are also observed as a small fraction. The observation of rod-like structures corresponding to edge-view of the AgTNPs confirms the flat plate-like nature of the particles. The TEM images of the nanoconjugates **4a**(AgTNPs) and **4b**(AgTNPs) (**Fig. 3.13**), show that they retained the triangular shape with average sizes (edge length) of 28 nm (**4a**(AgTNPs)) and 27 nm (**4b**(AgTNPs)). These values are not too different compared to AgTNPs alone at 26 nm (**Table 3.2**), hence showing

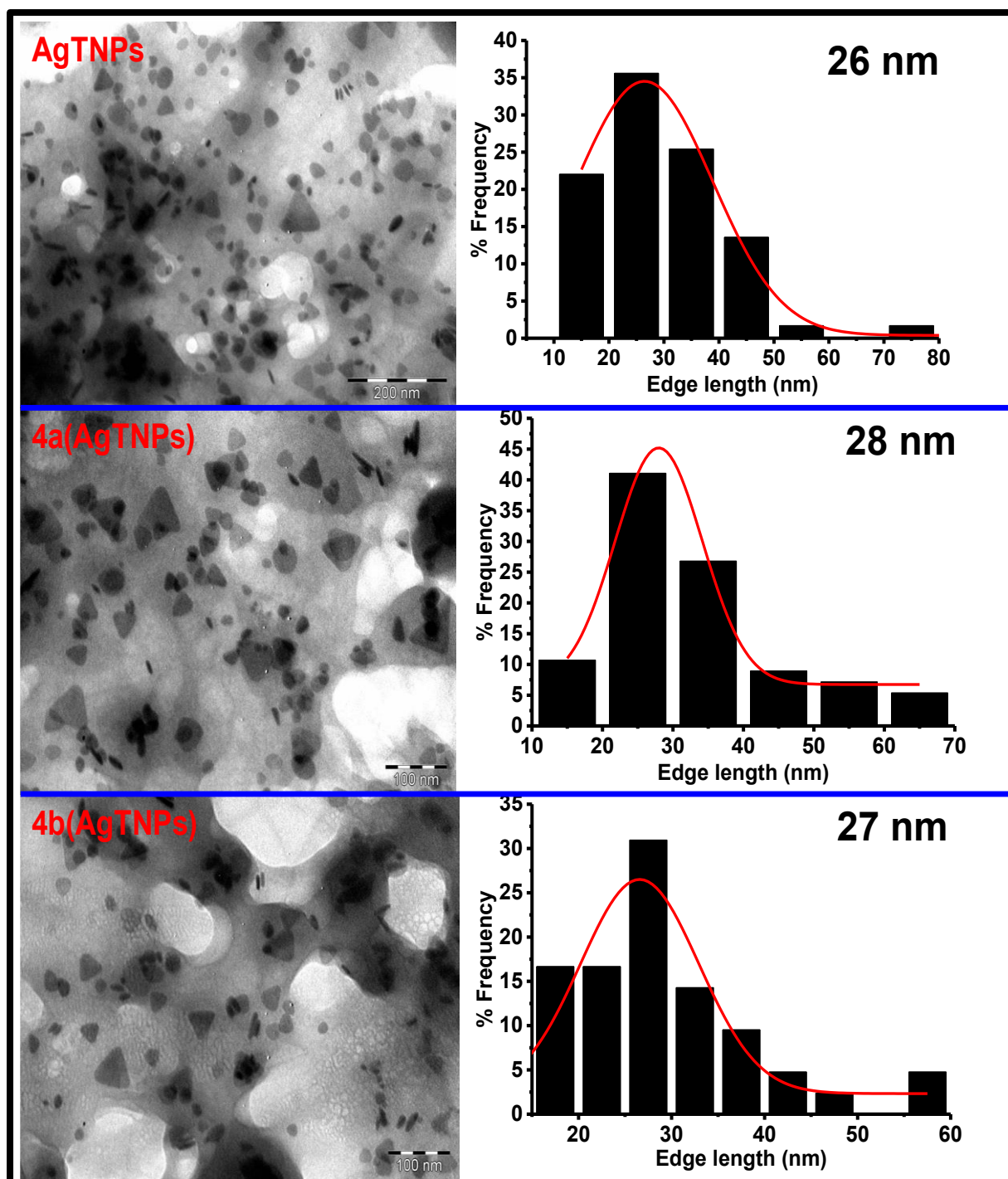


**Fig. 3.13:** TEM micrographs and size distribution histograms for AgTNPs, **4a**(AgTNPs) and **4b**(AgTNPs).

no aggregation. Both AgTNPs and the nanoconjugates were monodispersed (**Fig. 3.13**), Even though there is a larger loading for **4b**(AgTNPs) (discussed below)

compared to **4a**(AgTNPs) (**Table 3.2**), they both show about the same edge length. This can be attributed to the possibility that most of the conjugation would be on the flat faces of AgTNPs and would have little or no observable contribution to edge length increase after conjugation.

### 3.2.2.3. EDS

The presence of sulphur, nitrogen and oxygen in the EDS spectrum of AgTNPs (**Fig. 3.14**), in addition to silver suggests successful capping with glutathione (GSH). The EDS spectra for the conjugates shown in **Fig. 3.14**, verifies the inclusion of indium and chlorine, and zinc, in the elemental compositions of the corresponding nanoconjugates, which suggests successful incorporation of the MPcs in the AgTNPs structure.

### 3.2.2.4. FT-IR

Success in capping with GSH is also proven in the FT-IR spectrum (**Fig. 3.15**) by the observation of the C=O ( $1678\text{ cm}^{-1}$ ), -SH ( $2660\text{ cm}^{-1}$ ), -OH ( $3248\text{ cm}^{-1}$ ), and -NH<sub>2</sub> ( $3447\text{ cm}^{-1}$ ) stretching vibrations for AgTNPs, which are attributed to the GSH capping. It is also important to note that the other -NH<sub>2</sub> stretching vibration peak overlaps with the -OH peak and is not distinctly observed. Since both **4a**(AgTNPs) and **4b**(AgTNPs) possess the same functional groups, the FT-IR spectra of the two conjugates and their precursors were almost identical, hence only complex **4b** and its conjugate are used as examples in **Fig. 3.15**. Observation of the disappearance of the -NH<sub>2</sub> stretching vibration at  $3447\text{ cm}^{-1}$  in AgTNPs and shifting of the C=O stretching vibration to  $1708\text{ cm}^{-1}$  in **4b**(AgTNPs) from  $1701\text{ cm}^{-1}$  of the MPc alone, upon conjugation suggests a successful conjugation.



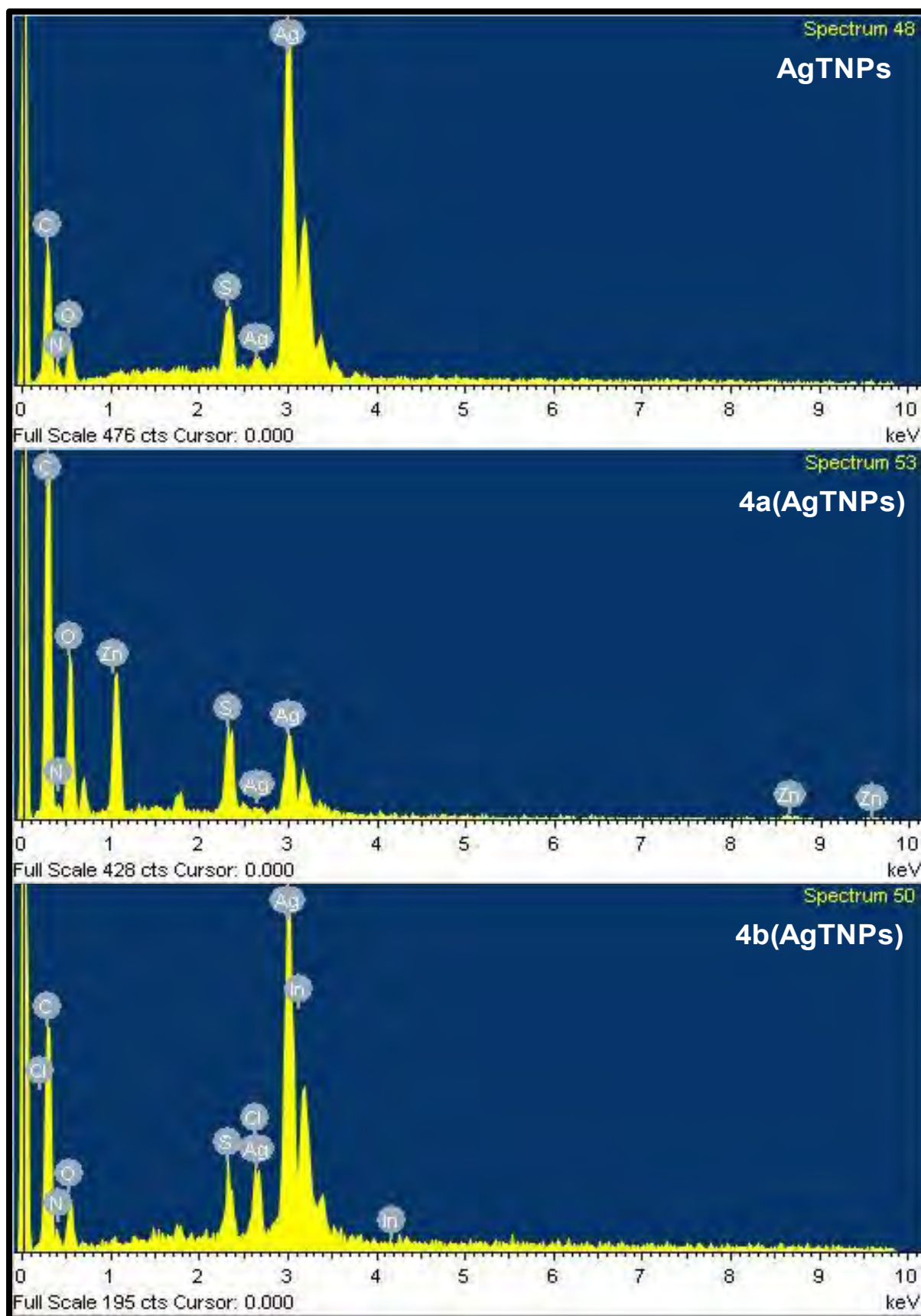


**Fig. 3.14:** EDS spectra for AgTNPs, **4a**(AgTNPs) and **4b**(AgTNPs).

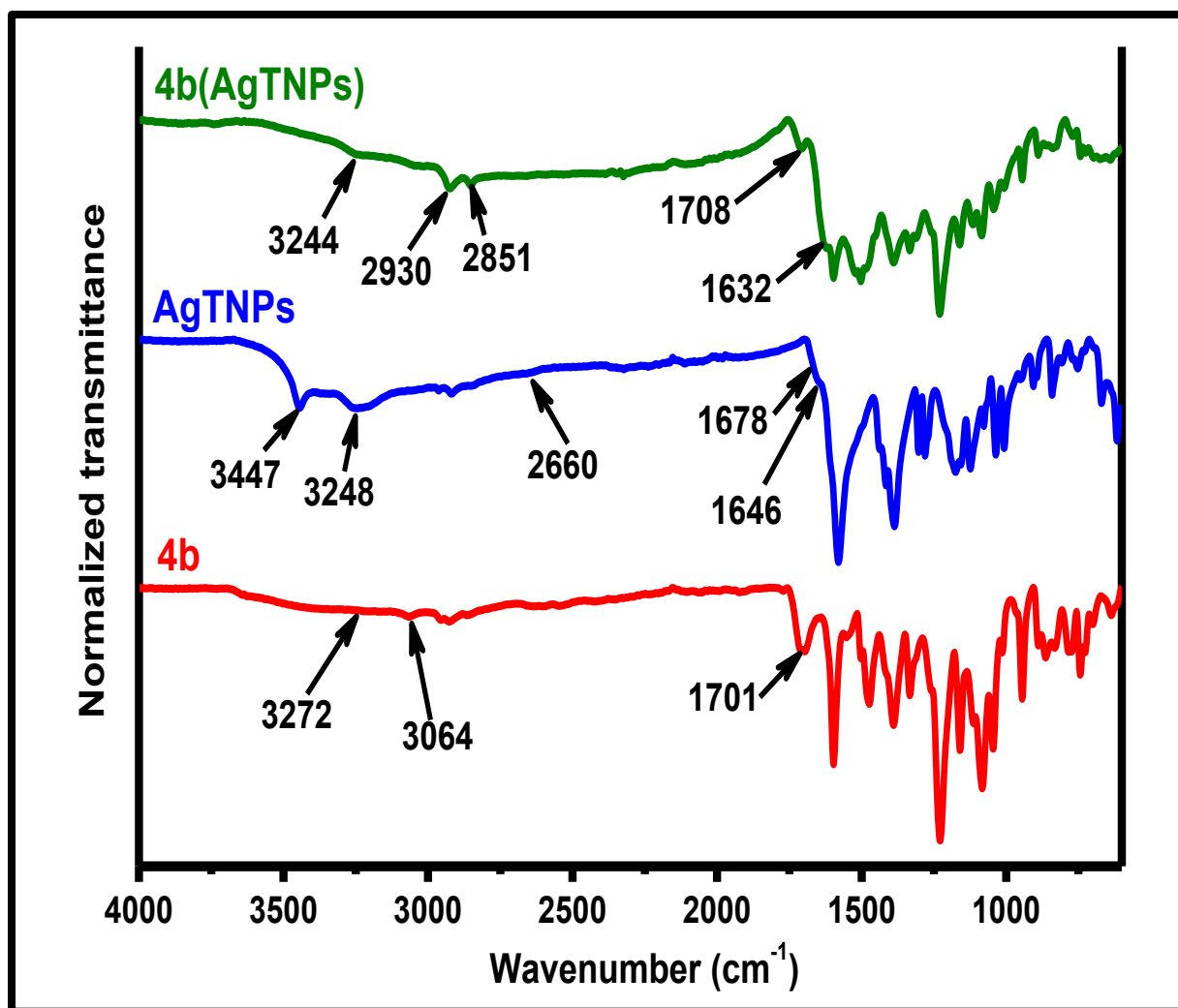
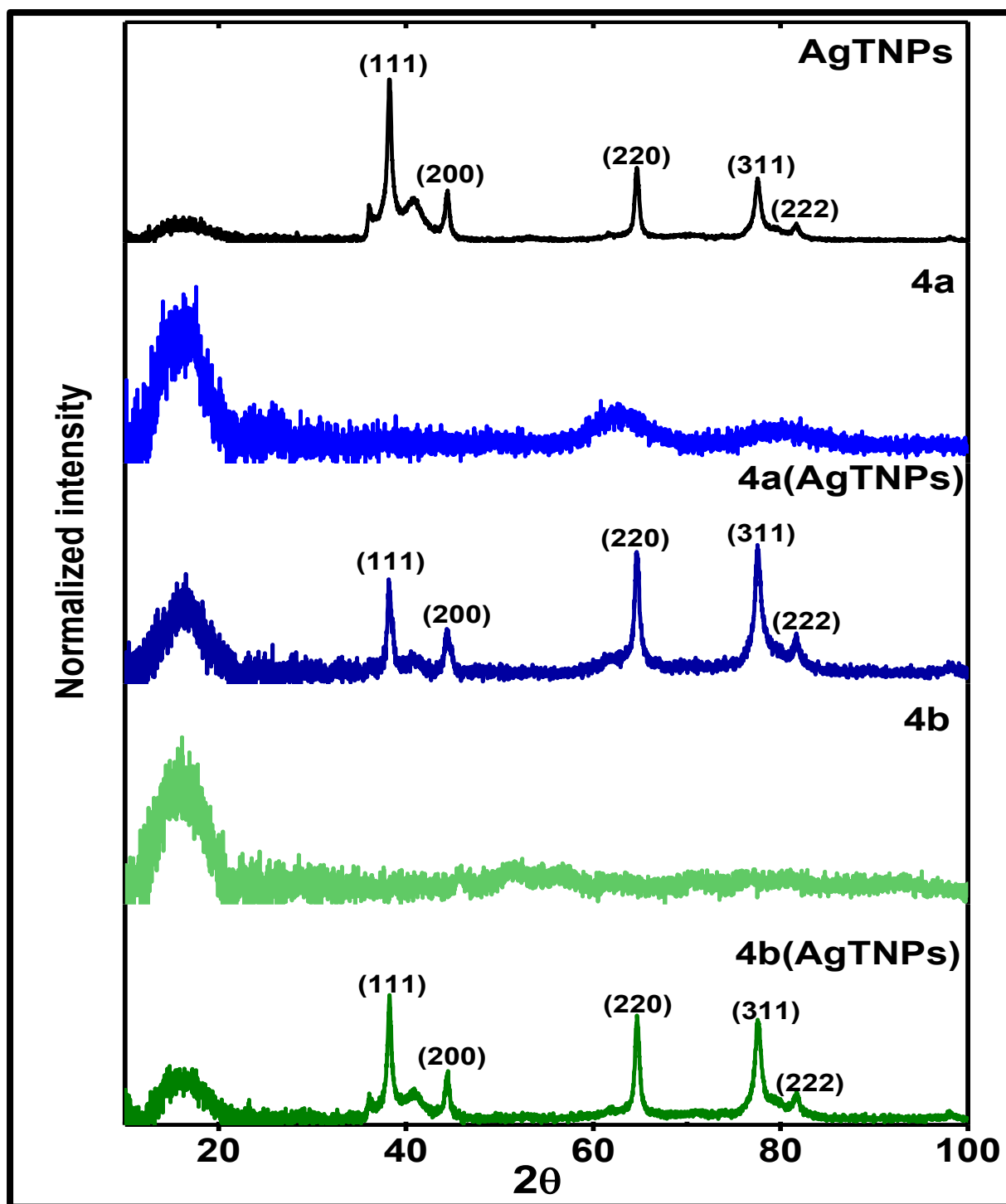


Fig. 3.15: FT-IR spectra for complex **4b**, AgTNPs and **4b**(AgTNPs).

### 3.2.2.5. XRD

The XRD diffractogram (Fig. 3.16) shows AgTNPs to have a face-centred cubic crystalline structure with {111} facet basal lattice planes similar to previous reports [117,120,122,155]. Relatively broad peaks are also observed between  $2\theta = 16$  and  $30^\circ$ , which may be attributed to relative amorphous character introduced by capping with GSH. The diffractograms of the nanoconjugates (Fig. 3.16) show the combined amorphous character of the MPcs [156], as evidenced by broad peaks around  $2\theta = 16^\circ$ , and the crystalline character of the nanoparticles exhibited by corresponding



**Fig. 3.16:** Powder-XRD diffractograms for AgTNPs, **4a**, **4a(AgTNPs)**, **4b** and **4b(AgTNPs)**.

sharp peaks at  $2\theta = 38, 44, 65, 78$ , and  $84^\circ$  assigned to 111, 200, 220, 311, and 222 planes respectively. The differences in the balance between amorphous and

crystalline character (broad and sharp peak intensities) of **4a**(AgTNPs) and **4b**(AgTNPs) is attributed to the differences in MPc loading and MPc orientation in the conjugates.

### 3.2.2.6. UV-Vis

The ground-state UV-Vis absorption spectrum for AgTNPs (**Fig. 3.17**) shows the expected surface plasmon resonance (SPR) band due to in-plane resonance at 702 nm, which is red shifted with comparison to that of the nanospheres around 400 nm [122]. The relative band broadness is attributed to the wide nanoparticle size distribution (as shown by TEM histograms, **Fig. 3.13**). UV-Vis confirmation of the synthesis of AgTNPs is also made by observation of a band accompanying the main SPR band, at 330 nm due to out-of-plane dipole resonance [122]. The SPR band due

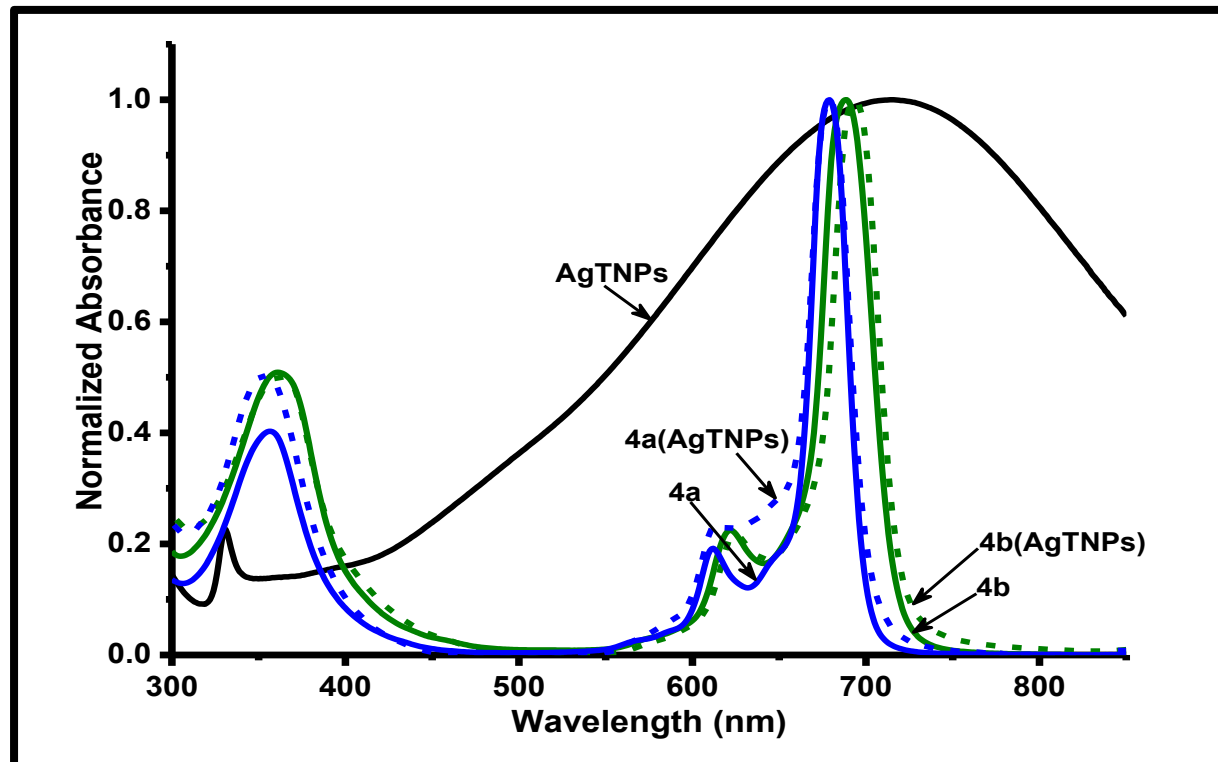


**Fig. 3.17:** UV-Vis spectra for complexes **4a** and **4b**, **4a**(AgTNPs) and **4b**(AgTNPs) in DMSO, and AgTNPs in water.

to in-plane quadrupole resonance of the nanoplates is observed around 500 nm as a gentle shoulder.

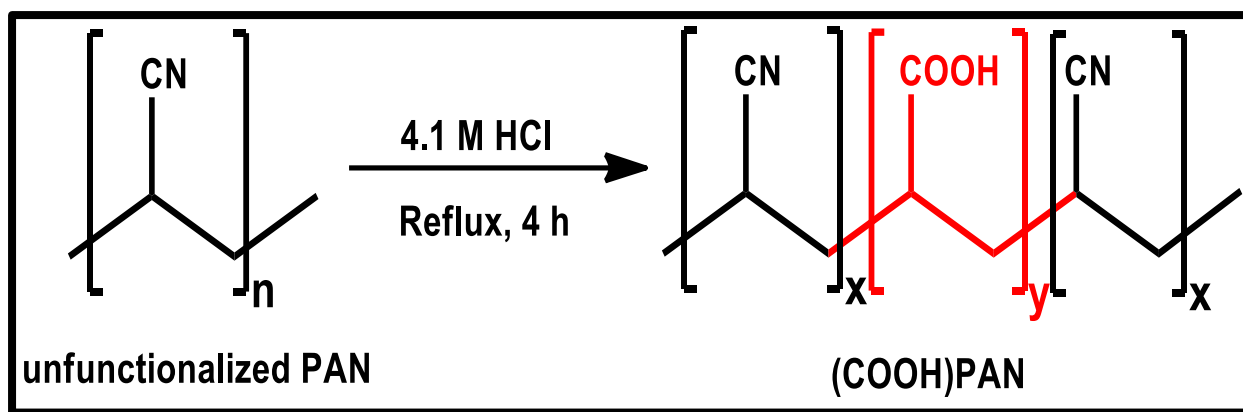
The spectrum for **4a**(AgTNPs) shown in **Fig. 3.17** is slightly modified in the region of the vibronic band due to the presence of the nanoparticles and there is no shift in the Q band of **4a** after conjugation (**Table 3.1**). On the other hand, the spectrum for **4b**(AgTNPs) is generally similar to that of **4b**, but slightly red-shifted (**Fig. 3.17**). Absorption of AgTNPs is relatively suppressed in the spectra of **4a**(AgTNPs) and **4b**(AgTNPs), and this is attributed to the difference in extinction coefficients of the MPcs and AgTNPs in DMSO (solvent in which spectra were obtained), where AgTNPs has low solubility while complexes **4a** and **4b** are highly soluble.

Since the UV-Vis absorption spectra for complexes **4a** and **4b** overlap with that of AgTNPs unlike those for the MPc(GQDs) conjugates, the loading of MPc complexes onto the nanoparticles was investigated following a thermogravimetric analysis (TGA) based method reported in literature [157]. The method involves comparing the thermal decomposition of the MPc in the conjugate with that of the initial MPc before the conjugation, with reference to the thermal decomposition of the nanoparticle using TGA. The loading values are: **4a**(AgTNPs) = 0.35 mg MPc/ mg MPc(AgTNPs) and **4b**(AgTNPs) = 0.59 mg MPc/ mg MPc(AgTNPs), **Table 3.2**.

### 3.3. Functionalization of polymers

#### 3.3.1. (COOH)PAN

(COOH)PAN was synthesized to enable linking of complex **1** for comparison with (COOH)PS, in the identification of the most suitable polymer to work with. Synthesis was achieved by partial acid hydrolysis of the nitrile groups of PAN, achieved by refluxing the polymer in dilute HCl (**Scheme 3.7**). The extent of conversion needed to



**Scheme 3.7:** Synthetic route for (COOH)PAN.

be achieved such that it would be enough to allow subsequent appreciable conjugation of MPcs, while also restricting close proximity of the  $\text{-COOH}$  functional groups to limit the subsequent possibilities of MPc multiple attachments and aggregation in the **1**-PAN conjugate. The balance was achieved by restricting the reflux period to 4 h, since longer reaction times gave rise to polymers which resulted in the formation of insoluble **1**-PAN conjugates, while shorter periods did not show significant functional group conversion. The period of 4 h was found to be an optimal time by monitoring the reaction hourly until the FT-IR spectra showed the presence of carbonyl and hydroxyl vibration signals.

**Fig. 3.18** shows the FT-IR spectra of PAN and (COOH)PAN. The emergence of a stretching vibration peak at  $3258 \text{ cm}^{-1}$  which is characteristic of a carboxylic  $\text{-OH}$  group, and a stretching vibration at  $1699 \text{ cm}^{-1}$  which is characteristic of a carboxylic  $\text{C=O}$  group, in the spectrum of (COOH)PAN confirms the carboxylic functionalization of the polymer. The nitrile vibration at  $2243 \text{ cm}^{-1}$  is also present in the spectrum of (COOH)PAN with only a slight decrease in intensity, thus confirming partial conversion of nitrile to carboxylic groups.

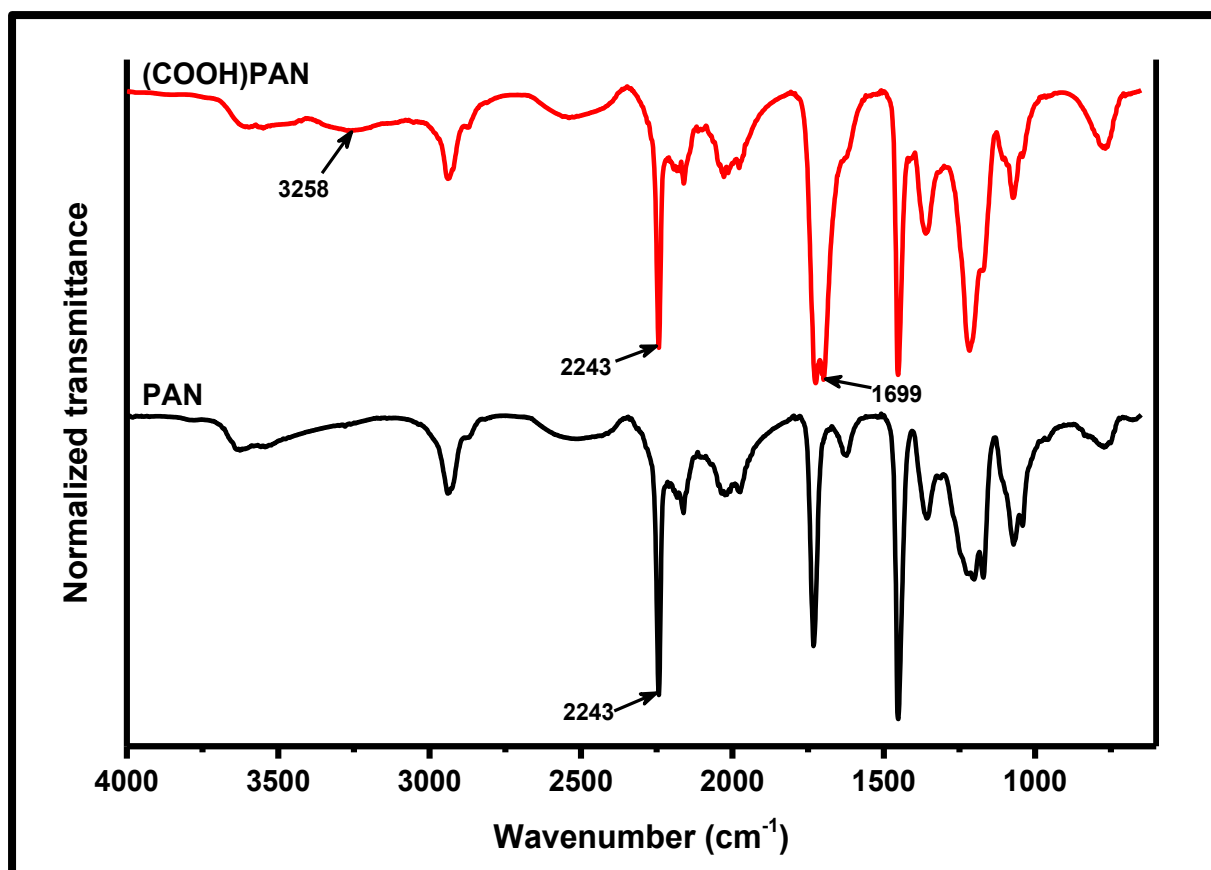
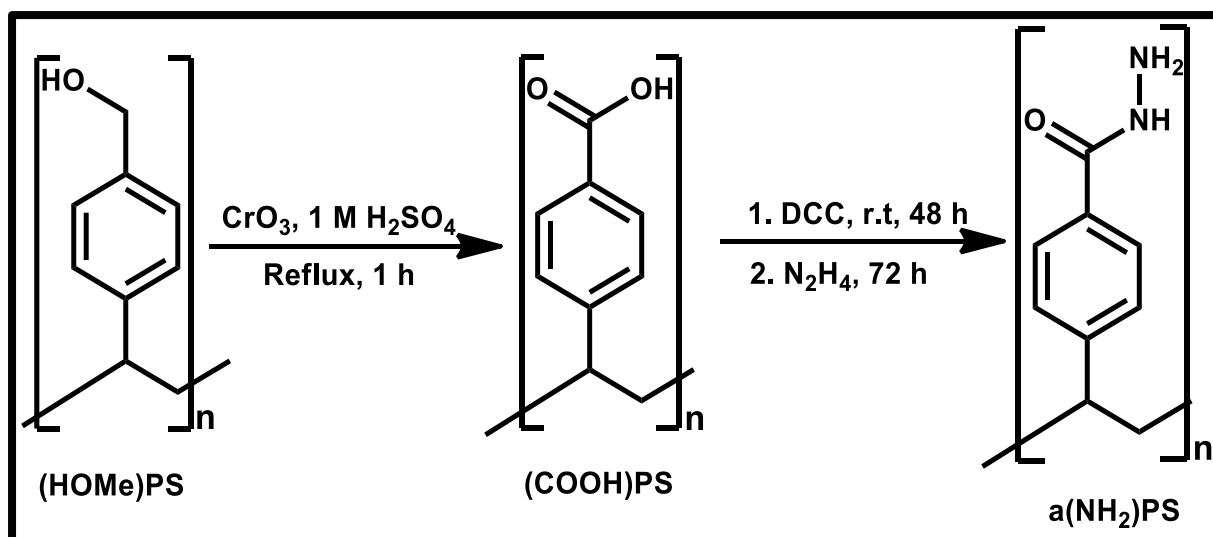


Fig. 3.18: FT-IR spectra of PAN and (COOH)PAN.

### 3.3.2. (COOH)PS and a(NH<sub>2</sub>)PS

As stated already, two types of (NH<sub>2</sub>)PS were synthesized (a(NH<sub>2</sub>)PS and b(NH<sub>2</sub>)PS) (discussed below), due to availability of reagents. (COOH)PS was to be linked to complex **1**, **2π**(GQDs), **3π**(GQDs) and **3**(GQDs) through the –NH<sub>2</sub> groups of complex **1** and the GQDs, while a(NH<sub>2</sub>)PS was to be linked to complexes **3**, **4a** and **4b**, and to the conjugates **4a**(AgTNPs) and **4b**(AgTNPs) through the –COOH of the MPcs (**Table 3.3**). (COOH)PS was synthesized by oxidation of the –OH of commercially available hydroxymethyl-polystyrene ((HOMe)PS) to –COOH using Jones reagent (CrO<sub>3</sub> in aqueous H<sub>2</sub>SO<sub>4</sub>). a(NH<sub>2</sub>)PS was then formed from (COOH)PS by amide linkage of



**Scheme 3.8:** Synthetic route for (COOH)PS and a(NH<sub>2</sub>)PS.

hydrazine to it (**Scheme 3.8**). A functional group interchange is confirmed in the FT-IR spectra in **Fig. 3.19** where the shift of the  $\text{-OH}$  stretching vibration peak from  $3413\text{ cm}^{-1}$  in (HOMe)PS to  $3228\text{ cm}^{-1}$  in (COOH)PS is observed together with the emergence of the carboxylic carbonyl stretching vibration signal at  $1704\text{ cm}^{-1}$ . In the formation of a(NH<sub>2</sub>)PS, use of excess hydrazine limited the possibility of (COOH)PS crosslinking, thus resulting in a PS polymer with available  $\text{-NH}_2$  groups (a(NH<sub>2</sub>)PS). The FT-IR spectrum of a(NH<sub>2</sub>)PS (**Fig. 3.19**) confirms its successful formation where the carbonyl stretching vibration peak of the  $\text{-COOH}$  group in (COOH)PS at  $1704\text{ cm}^{-1}$  is shifted to that of an amide  $\text{C=O}$  stretching vibration at  $1667\text{ cm}^{-1}$ , while observing the emergence of the overlapped bending vibrations for the amine (scissoring) and the amide at  $1643\text{ cm}^{-1}$ . Also, the shift of the stretching vibration at  $3228\text{ cm}^{-1}$  in (COOH)PS to the vibrations at  $3386$  and  $3647\text{ cm}^{-1}$  in a(NH<sub>2</sub>)PS, confirmed the formation of a(NH<sub>2</sub>)PS. The vibration at  $3386\text{ cm}^{-1}$  is significantly more intense than that at  $3647\text{ cm}^{-1}$  because it consists of overlapped amine and amide  $\text{-NH}$  stretching vibrations.



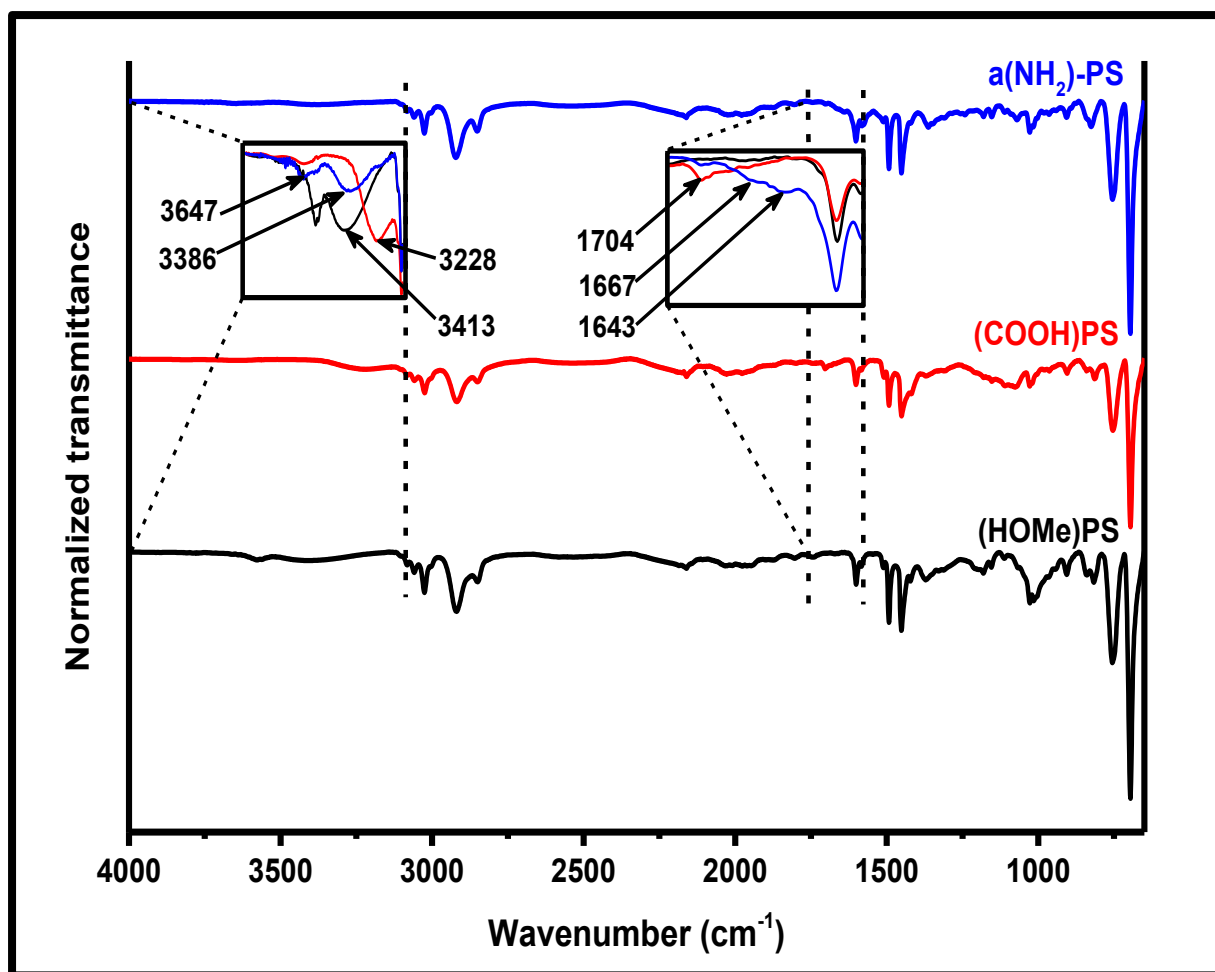
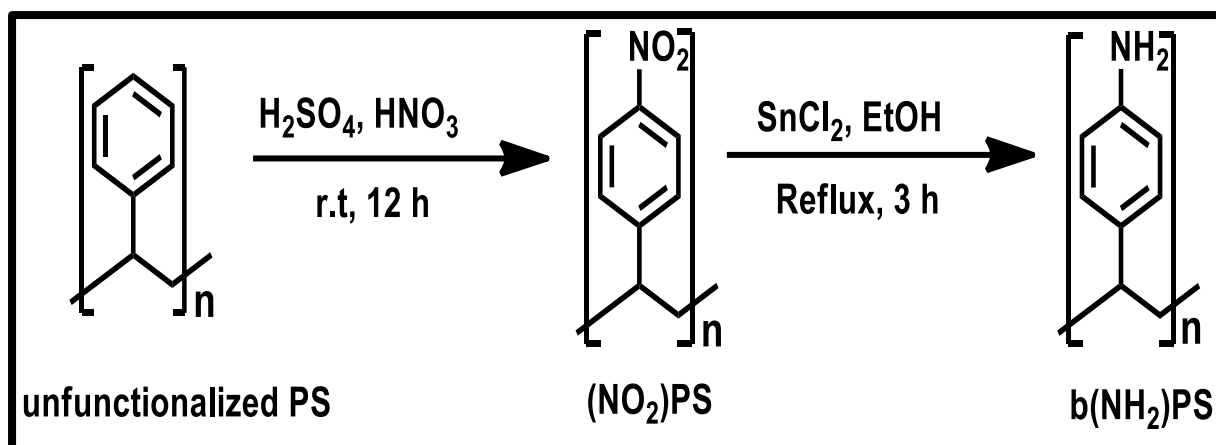


**Fig. 3.19:** FT-IR spectra for (HOMe)PS, (COOH)PS and a(NH<sub>2</sub>)PS.

### 3.3.3. b(NH<sub>2</sub>)PS

Commercially available unfunctionalized PS was functionalized with –NH<sub>2</sub> groups through nitration and reduction steps (**Scheme 3.9**) after an initial fluffing step to convert the compact PS beads to a low-density powder with greater surface area for efficient distribution of functional groups. **Fig. 3.20** shows the FT-IR spectra for the various stages in the preparation of b(NH<sub>2</sub>)PS. After the nitration step, (NO<sub>2</sub>)PS was formed and the characteristic –NO<sub>2</sub> bending vibrations are observed at 1345 and 1519 cm<sup>-1</sup> in **Fig. 3.20**, thus confirming introduction of the functional group. The dilution of



**Scheme 3.9:** Synthetic route for b(NH<sub>2</sub>)PS.

the nitrating acid mixture moderated the nitrating power of the mixture and hence gave rise to a partially functionalized polymer. This is evident in the FT-IR spectrum where the spectrum of (NO<sub>2</sub>)PS is almost identical to the precursor polymer with the exception of the –NO<sub>2</sub> vibration peaks at 1345 and 1519 cm<sup>-1</sup>. Successful reduction of (NO<sub>2</sub>)PS to b(NH<sub>2</sub>)PS is observed in the FT-IR spectrum (**Fig. 3.20**) where the –NO<sub>2</sub> peaks disappeared while the –NH<sub>2</sub> stretching vibrations appeared at 3214 and 3318 cm<sup>-1</sup>. The peaks are broad and overlap each other possibly due to the polymeric environment of the functional group.

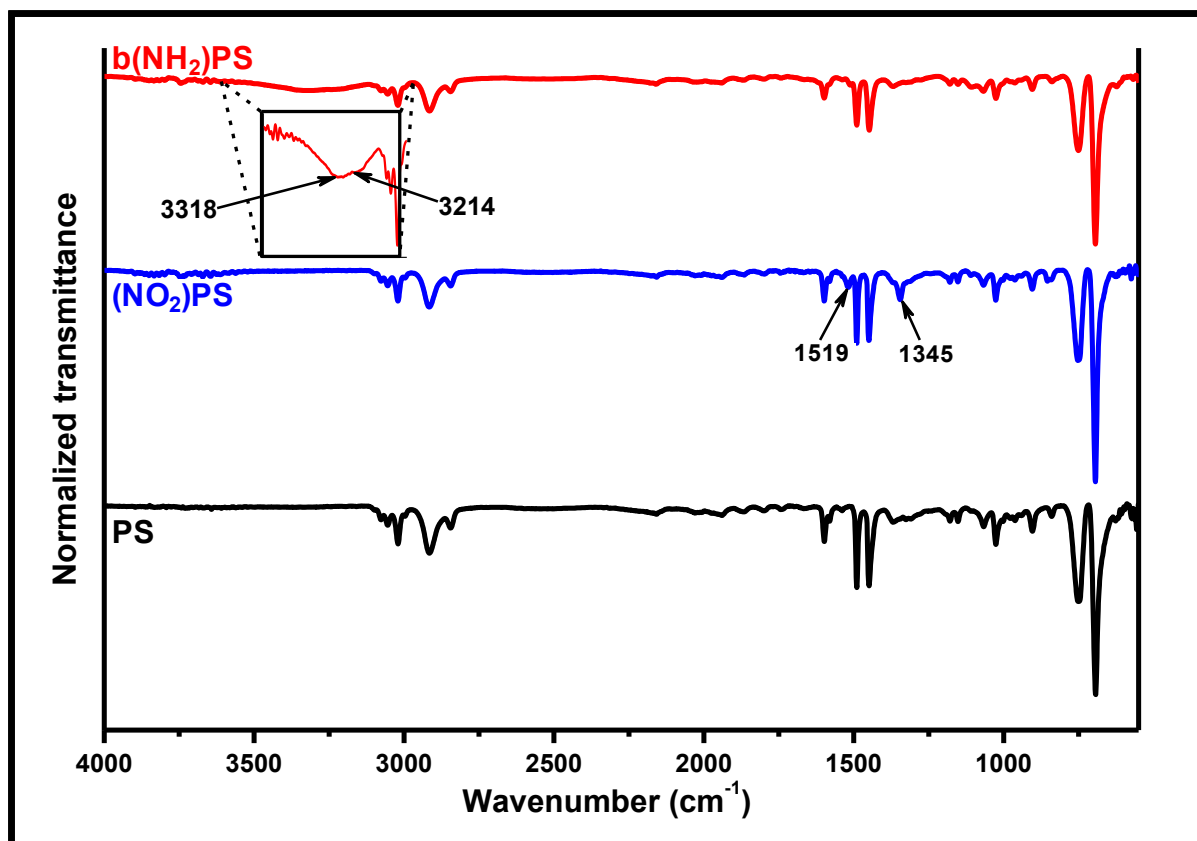


Fig. 3.20: FT-IR spectra for PS, (NO<sub>2</sub>)PS and b(NH<sub>2</sub>)PS.

### 3.4. Photosensitizer-polymer conjugates

Photosensitizers were only linked to polymer anchors to allow casting into functionalized membranes without the photosensitizers leaching out. With the exception of **10**-PS, all photosensitizers (MPcs and MPc(NPs)) were covalently conjugated to appropriately functionalized polymers via amide bonding. Synthesis and characterization of these photosensitizer-polymer conjugates is discussed below. **Table 3.3** summarizes the synthesized photosensitizer-polymer conjugates formed from functionalized polymers, and the subsequently prepared functionalized polymer membranes.

**Table 3.3:** Summary of Photosensitizer-Polymer conjugates formed from functionalized polymers, and the subsequently prepared membranes.

Photosensitizer-Polymer conjugate	Functionalized polymer	Functionalized membrane
1-PAN	(COOH)PAN	1-PAN-memb
1-PS	(COOH)PS	1-PS-memb
2 $\pi$ (GQDs)-PS	(COOH)PS	2 $\pi$ (GQDs)-memb
3-PS	a(NH <sub>2</sub> )PS	3-memb
3 $\pi$ (GQDs)-PS	(COOH)PS	3 $\pi$ (GQDs)-memb
3(GQDs)-PS	(COOH)PS	3(GQDs)-memb
4a-PS	a(NH <sub>2</sub> )PS	4a-memb
4a(AgTNP <sub>s</sub> )-PS	a(NH <sub>2</sub> )PS	4a(AgTNP <sub>s</sub> )-memb
4b-PS	a(NH <sub>2</sub> )PS	4b-memb
4b(AgTNP <sub>s</sub> )-PS	a(NH <sub>2</sub> )PS	4b(AgTNP <sub>s</sub> )-memb
5-PS	b(NH <sub>2</sub> )PS	5-memb
6-PS	b(NH <sub>2</sub> )PS	6-memb
10-PS	b(NH <sub>2</sub> )PS	10-memb

### 3.4.1. Amide conjugates

#### 3.4.1.1. 1-PAN and 1-PS

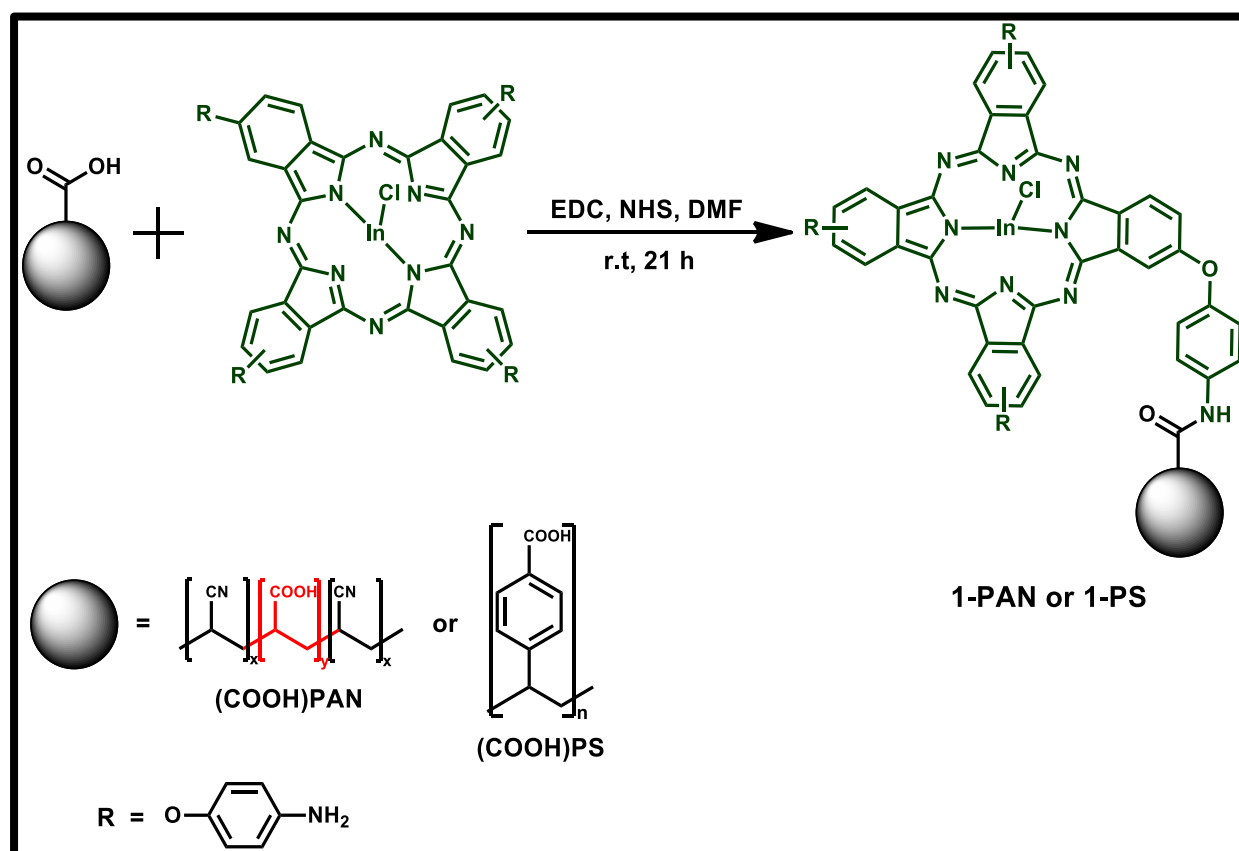
1-PAN and 1-PS were synthesized by amide linkage of the  $\text{-COOH}$  groups of (COOH)PAN and (COOH)PS, with the  $\text{-NH}_2$  groups of complex **1**. Only complex **1** has  $\text{-NH}_2$  groups of the MPcs used in this work, for linking to (COOH)PAN and (COOH)PS, hence it was used in the selection of the better polymer for membrane fabrication and further studies. Since complex **1** is tetra-substituted, its conjugation to functionalized polymers can potentially lead to polymer crosslinking and insolubility of the conjugate. In the formation of 1-PAN the following strategies were employed to avoid polymer crosslinking:

- i. Limiting the number of  $\text{-COOH}$  groups in (COOH)PAN using reaction time discussed above.
- ii. The use of a dilute solution of (COOH)PAN for linking to complex **1**. This was done by using 10 mL of dry DMF for 0.50 g of (COOH)PAN. Less than 10 mL DMF for this amount of (COOH)PAN, resulted in the formation of the insoluble conjugate that precipitated out of the reaction.
- iii. Limiting the amounts of coupling reagents (EDC and NHS) and their dropwise addition to the solution of (COOH)PAN. When EDC and NHS were added in a single dose, the resulting 1-PAN conjugate precipitated out of the reaction mixture, suggesting formation of an insoluble conjugate. Addition of larger amounts of EDC and NHS than stated in the experimental section contributed to the formation of the insoluble conjugate.
- iv. Dropwise addition of complex **1** to the activated (COOH)PAN. In earlier attempts where the addition of complex **1** was done in a single dose each, the conjugate precipitated out.

After these precautions, the observed dispersion of the conjugate in DMF solution confirmed a relative limitation of multiple attachments of complex **1** to (COOH)PAN. On the other hand, the relatively low –OH loading in (HOMe)PS (1.1 mmol/ g as given by manufacturer) significantly restricted multiple attachments of complex **1** to (COOH)PS. As a result, less precautions were needed for the synthesis of **1**-PS.

**Scheme 3.10** shows the synthesis of **1**-PAN and **1**-PS.

For both conjugates, successful preparation was expected to be deduced in the FT-IR spectra (not shown) mostly from the vibrational peak activity in the 3000 - 3600  $\text{cm}^{-1}$  region corresponding to –OH and –NH<sub>2</sub> groups, and the 1600 - 1700  $\text{cm}^{-1}$  corresponding to the amide and carboxylic C=O groups. However, relatively intense vibration activity in the spectrum of complex **1** due to the four –NH<sub>2</sub> groups per



**Scheme 3.10:** Synthetic route for **1**-PAN and **1**-PS.

molecule, masked any major activity in the conjugate spectrum, and no precise conclusion about conjugate formation could be made based on FT-IR alone. XPS was thus employed to confirm the formation of an amide bond.

**Fig. 3.21** shows the high-resolution N 1s XPS spectral data for (COOH)PAN, complex 1, 1-PAN and 1-PS. (COOH)PS is not shown since it does not contain nitrogen. The spectra were corrected using adventitious carbon C–C at 285 eV. In **Fig. 3.21**, a new N 1s component is observed at 401.4 eV and 401.5 eV for 1-PAN and 1-PS,

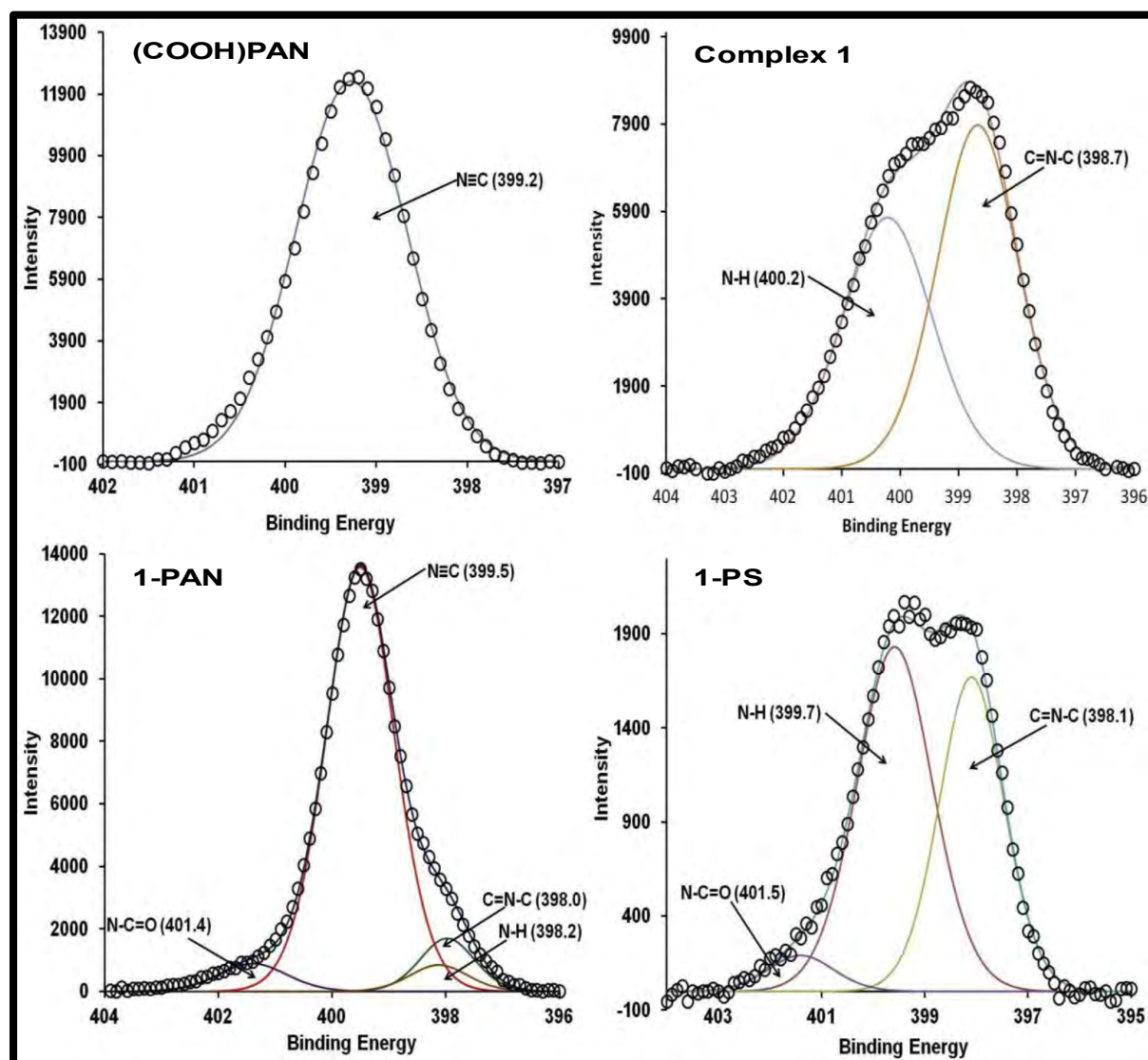


**Fig. 3.21:** High resolution N1s XPS spectra for (COOH)PAN, complex 1, 1-PAN and 1-PS.

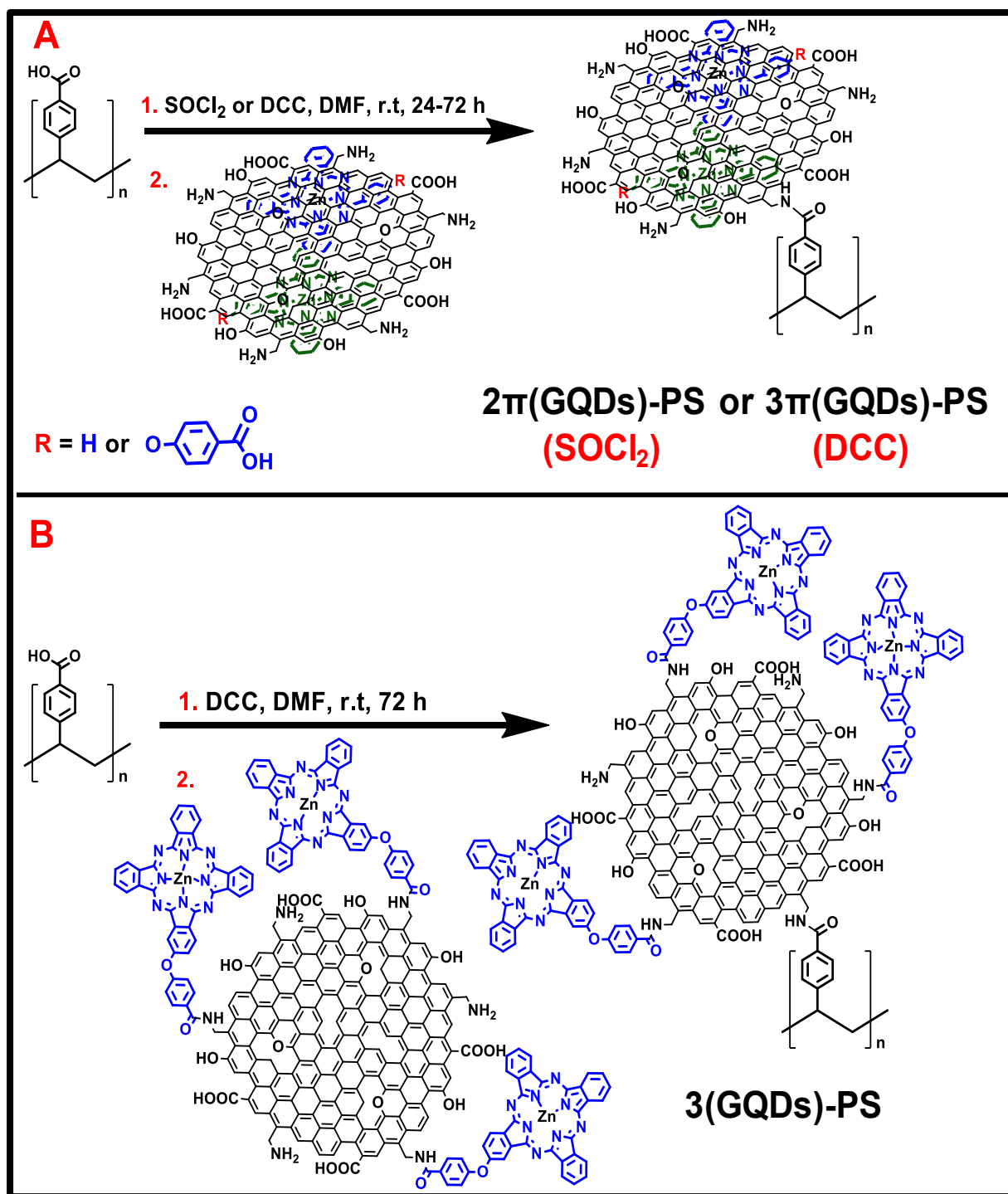
respectively which is not present in (COOH)PAN, (COOH)PS (not shown) and in complex **1** alone. The peak corresponds to the N 1s high resolution XPS peak for the N–C=O group previously reported [158–160] which shows the formation of an amide linkage, hence confirming successful conjugation of **1** to (COOH)PAN and (COOH)PS.

### 3.4.1.2. MPc(GQDs)-PS conjugates ( $2\pi$ (GQDs)-PS, $3\pi$ (GQDs)-PS and $3$ (GQDs)-PS)

The GQDs used in this work were synthesized from citric acid and polyethyleneimine where the polyethyleneimine introduced nitrogen into the GQDs and most importantly, introduced –NH<sub>2</sub> groups in the structure. Synthesis of the MPc(GQDs)-PS conjugates was achieved by the amide coupling of the GQDs' –NH<sub>2</sub> groups with the –COOH of (COOH)PS. For  $2\pi$ (GQDs)-PS coupling was facilitated by thionyl chloride via acyl-chloride activation (**Scheme 3.11 (A)**), while for  $3\pi$ (GQDs)-PS (**Scheme 3.11 (A)**) and  $3$ (GQDs)-PS (**Scheme 3.11 (B)**) the coupling was facilitated by DCC. Confirmation of formation and characterization of the conjugates  $2\pi$ (GQDs)-PS,  $3\pi$ (GQDs)-PS and  $3$ (GQDs)-PS was achieved using FT-IR and XPS. Since in all these conjugates the formation essentially involved the reaction of the same material (GQDs and (COOH)PS), the FT-IR and XPS spectral changes were similar hence only the data for  $2\pi$ (GQDs)-PS is discussed here as a representative.

The FT-IR spectra of  $2\pi$ (GQDs)-PS and its components ( $2\pi$ (GQDs) and (COOH)PS) are shown in **Fig. 3.22**. The C=O carbonyl stretching vibration peak at 1698 cm<sup>-1</sup> in  $2\pi$ (GQDs) is broader in  $2\pi$ (GQDs)-PS (at 1701 cm<sup>-1</sup>) due to the presence of (COOH)PS. There are hence two sources of –COOH groups (C=O vibrations at 1698 cm<sup>-1</sup> for  $2\pi$ (GQDs) and 1704 cm<sup>-1</sup> for (COOH)PS). The FT-IR spectrum of  $2\pi$ (GQDs)-PS also exhibits an amide C=O carbonyl stretching vibration as a shoulder at 1667 cm<sup>-1</sup> which suggests successful coupling of  $2\pi$ (GQDs) and (COOH)PS. The fingerprint





**Scheme 3.11:** Synthetic routes for  $2\pi(\text{GQDs})\text{-PS}$ ,  $3\pi(\text{GQDs})\text{-PS}$  and  $3(\text{GQDs})\text{-PS}$ .

region of the spectrum of  $2\pi(\text{GQDs})\text{-PS}$  shows significant differences from the spectra of  $2\pi(\text{GQDs})$  and  $(\text{COOH})\text{PS}$  which is attributed to the integration of the vibrations

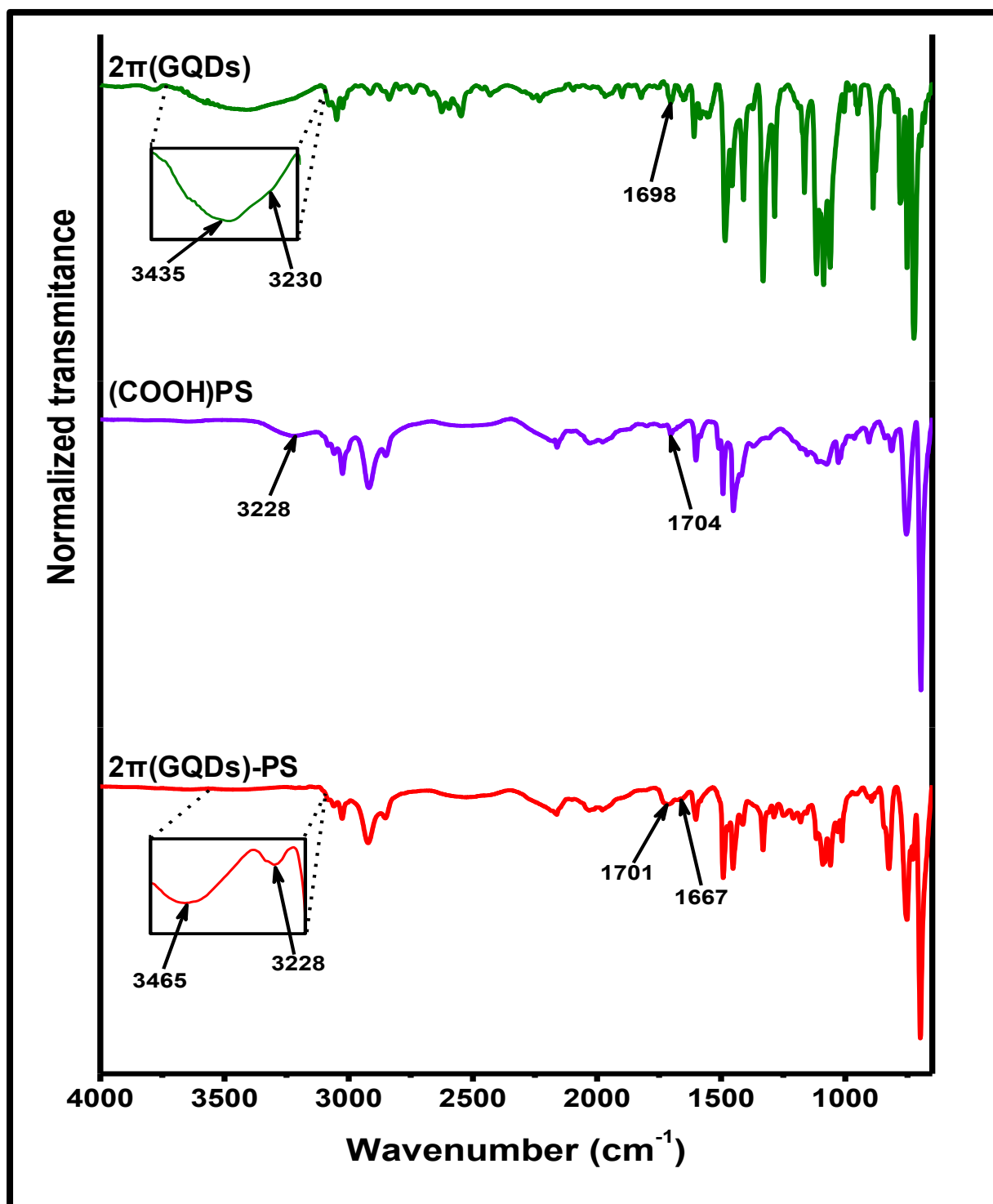


Fig. 3.22: FT-IR spectra for  $(\text{COOH})\text{PS}$ ,  $2\pi(\text{GQDs})$  and  $2\pi(\text{GQDs})\text{-PS}$ .

from both  $2\pi(\text{GQDs})$  and  $(\text{COOH})\text{PS}$ . The significant presence of both  $-\text{NH}_2$  and  $-\text{COOH}$  groups in the product conjugate resulted in the masking of the amide stretching vibrations above  $3000\text{ cm}^{-1}$ .

Fig. 3.23 shows the deconvoluted high resolution N1s spectra of  $2\pi$ (GQDs) and  $2\pi$ (GQDs)-PS. The peaks at 399.6 and 397.8 eV for  $2\pi$ (GQDs) and 400.2 and 398.5 eV for  $2\pi$ (GQDs)-PS are attributed to  $-\text{NH}_2$  and  $-\text{NH}$  groups, respectively, in the

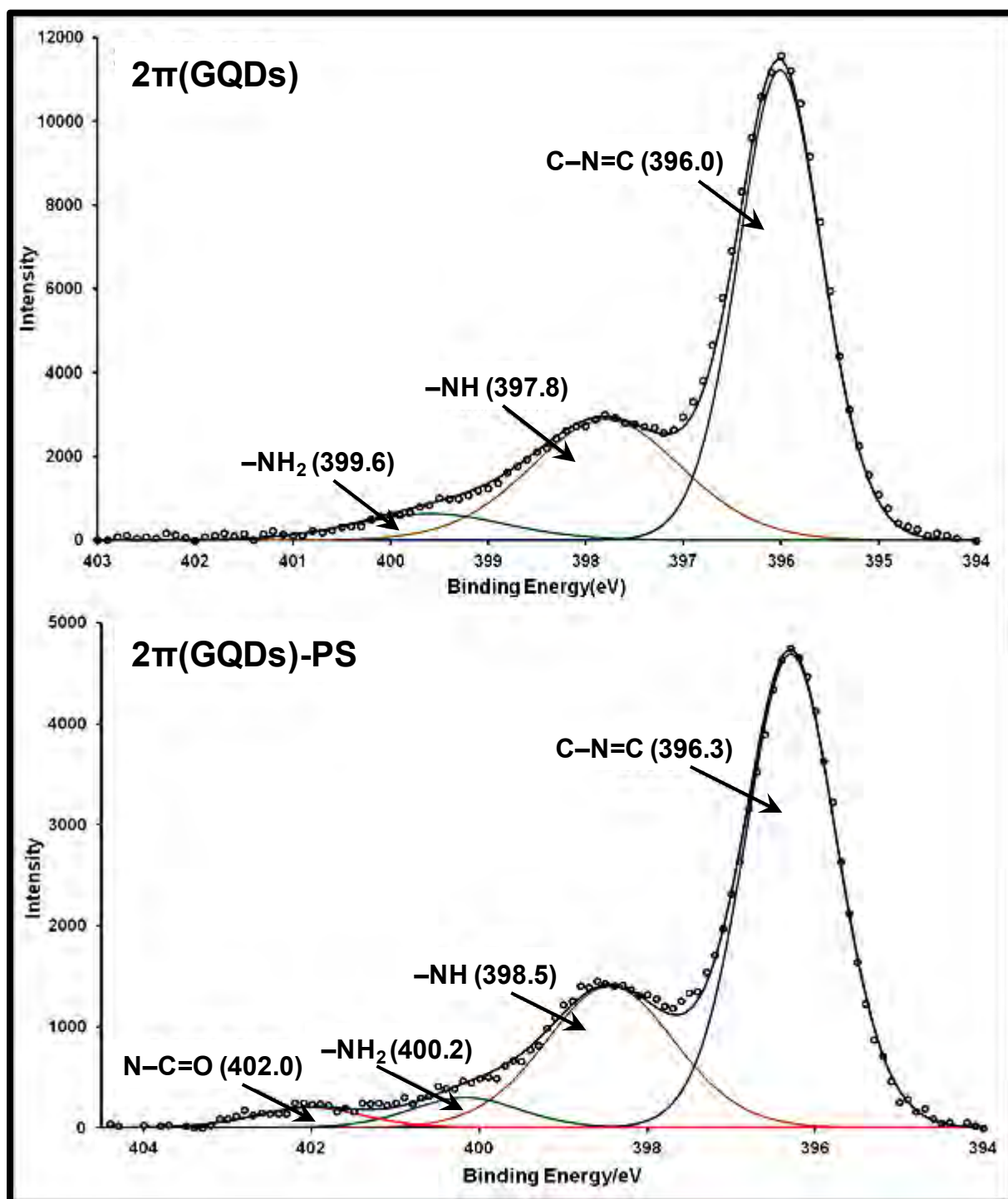


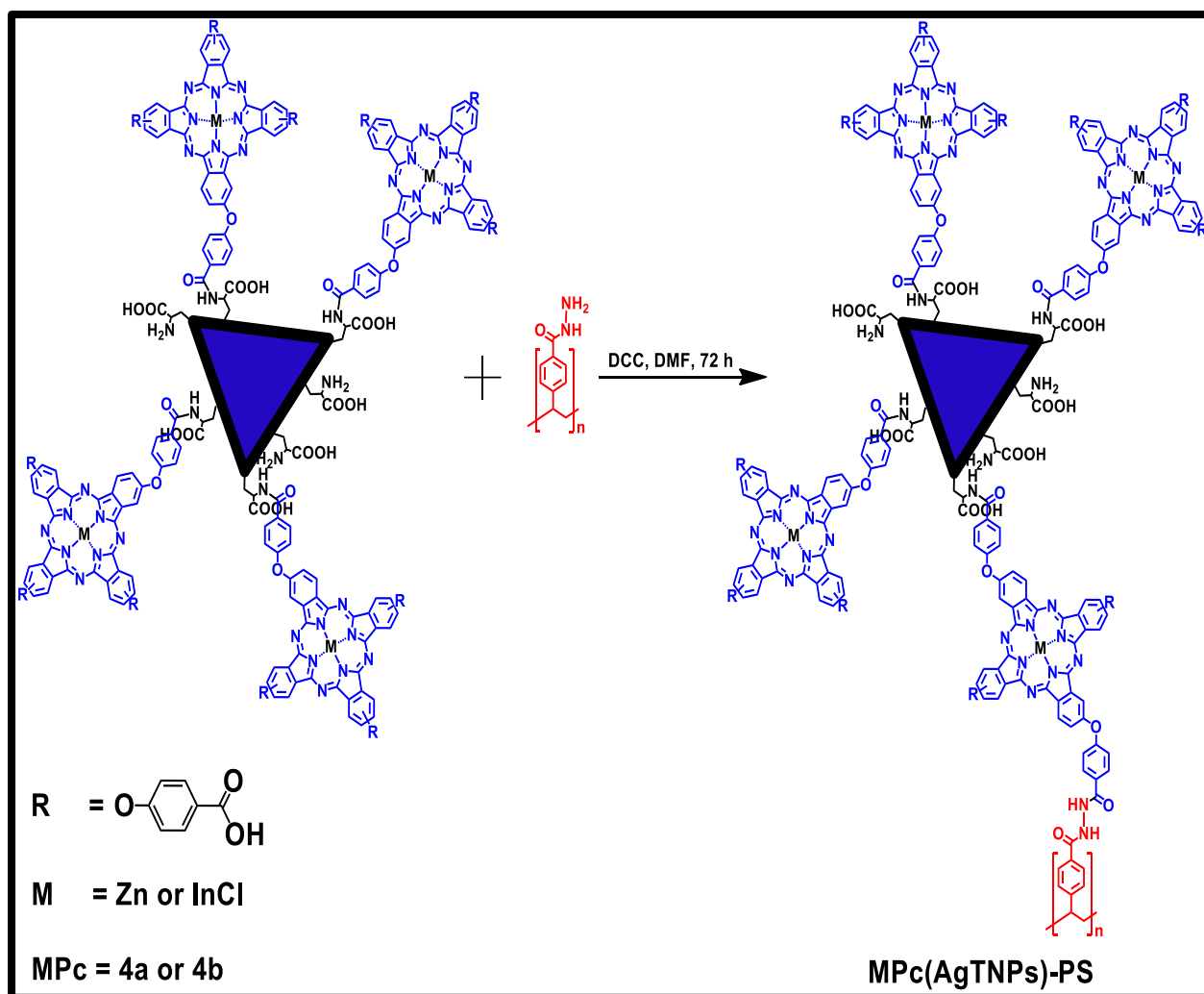
Fig. 3.23: High resolution N1s spectra of  $2\pi$ (GQDs) and  $2\pi$ (GQDs)-Ps.

GQDs component of the material. Similar groups have been reported before at 399.8 eV and 398.7 for  $\text{-NH}_2$  and  $\text{-NH}$ , respectively [128]. The observed shifts in values may be attributed to interaction of the GQDs with complex **2** and further interaction with (COOH)PS. The peak at 396.0 eV for  $2\pi(\text{GQDs})$  and 396.3 eV for  $2\pi(\text{GQDs})\text{-PS}$  is attributed to  $\text{C-N=C}$  in complex **2** [161,162]. The extra peak at 402 eV in  $2\pi(\text{GQDs})\text{-PS}$  is attributed to the amide bond nitrogen [158,160], thus confirming conjugation of  $2\pi(\text{GQDs})$  to (COOH)-PS and formation of  $2\pi(\text{GQDs})\text{-PS}$ .

### 3.4.1.3. $\text{a}(\text{NH}_2)\text{PS}$ and $\text{b}(\text{NH}_2)\text{PS}$ conjugates (**3-PS**, **4a-PS**, **4a(AgTNPs)-PS**, **4b-PS**, **4b(AgTNPs)-PS**, **5-PS** and **6-PS**)

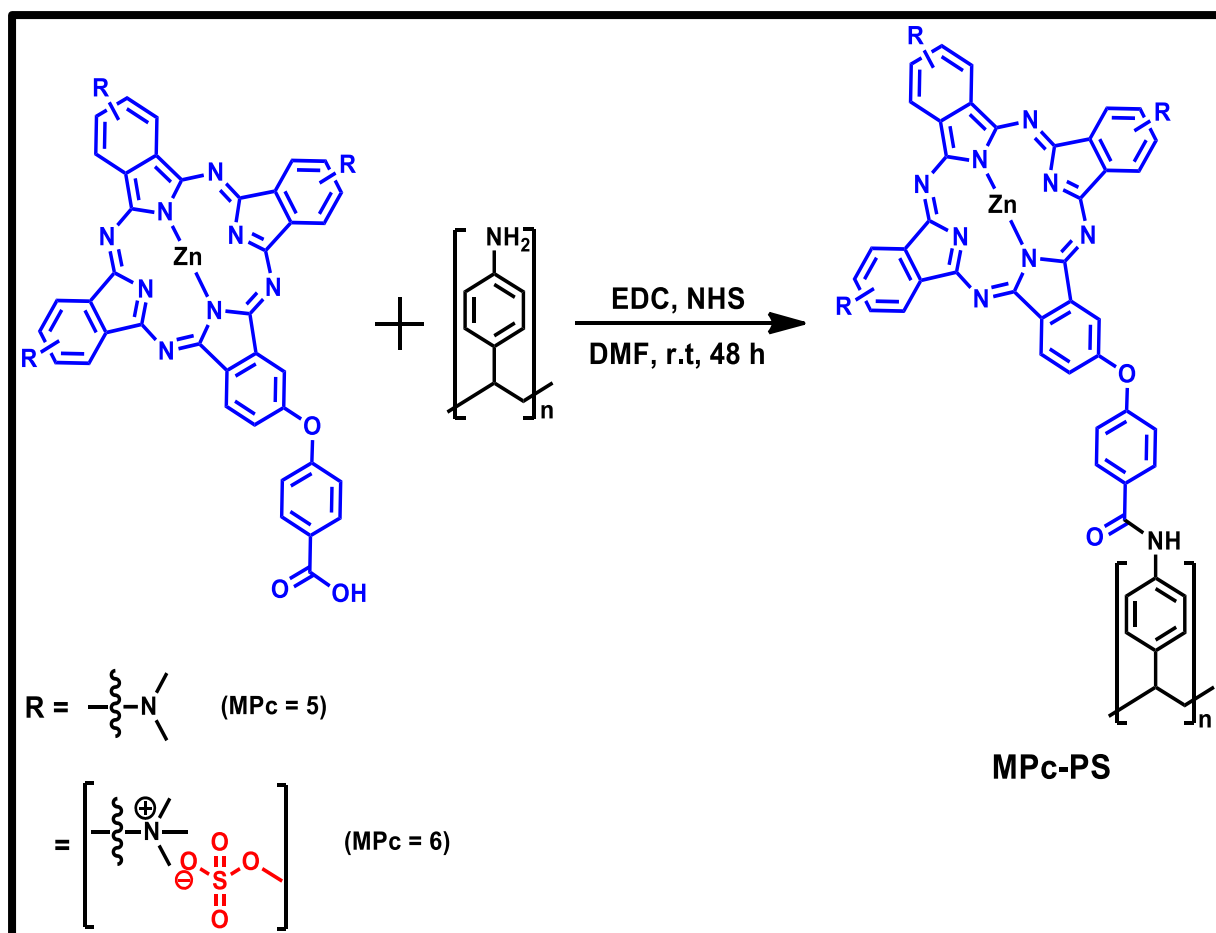
The synthesis of **3-PS**, **4a-PS**, **4a(AgTNPs)-PS**, **4b-PS** and **4b(AgTNPs)-PS** from the corresponding photosensitizer and  $\text{a}(\text{NH}_2)\text{PS}$  was facilitated by DCC. Since  $\text{a}(\text{NH}_2)\text{PS}$  was formed from (COOH)PS, no extra precautions were taken to avoid crosslinking conjugation in the synthesis of **4a-PS**, **4a(AgTNPs)-PS**, **4b-PS** and **4b(AgTNPs)-PS**, as was done for **1-PS**. **Scheme 3.12** shows the synthesis of **4a(AgTNPs)-PS** and **4b(AgTNPs)-PS** as examples for the synthesis of these conjugates. These conjugates were characterized using FT-IR (not shown). Since an amide bond already existed in the polymer ( $\text{a}(\text{NH}_2)\text{PS}$ ), slight changes in the FT-IR spectra in the regions of the  $\text{C=O}$  and  $\text{-OH/ -NH}_2$  stretching vibrations were used to suggest possible success in conjugate formation. Also, integration of the FT-IR spectrum of the  $\text{a}(\text{NH}_2)\text{PS}$  polymer with those of the photosensitizers confirmed the presence of all precursors in the product possibly as a conjugate.

Synthesis of **5-PS** and **6-PS** conjugates from complexes **5** and **6**, and  $\text{b}(\text{NH}_2)\text{PS}$  was facilitated by the EDC-NHS coupling agent pair (**Scheme 3.13**). EDC-NHS coupling agent pair was used instead of DCC because it gave better results and it also simplified



**Scheme 3.12:** Synthetic route for **4a**(AgTNPs)-PS and **4b**(AgTNPs)-PS.

the purification processes. **Fig. 3.24** shows the FT-IR spectra of the **6**-PS conjugate and its components (complex **6** and b(NH<sub>2</sub>)PS) as examples. Upon conjugation, there is a significant reduction in the –NH<sub>2</sub> stretching vibrations of b(NH<sub>2</sub>)PS at 3214 and 3318 cm<sup>-1</sup>, to a broad peak at 3253 cm<sup>-1</sup> attributed mostly to the amide –NH stretching vibration. This is also coupled with the appearance of a small shoulder at 1665 cm<sup>-1</sup>. The absence of complex **6**'s carboxylic –OH stretching vibration peak (at 3395 cm<sup>-1</sup> in the complex) in the FT-IR spectrum of **6**-PS (**Fig. 3.24**), suggests successful conjugation of the complex to b(NH<sub>2</sub>)PS. The shoulder at 1665 cm<sup>-1</sup> is attributed to the



**Scheme 3.13:** Synthetic route for **5-PS** and **6-PS**.

amide carbonyl stretching vibration obtained following conversion of the MPc's carboxylic acid group to the amide. Similar changes were observed in **5-PS**. Due to the small amount of MPc conjugated to b(NH<sub>2</sub>)PS, most of the MPc characteristic peaks were of very low intensity and were masked by the polymer peaks.

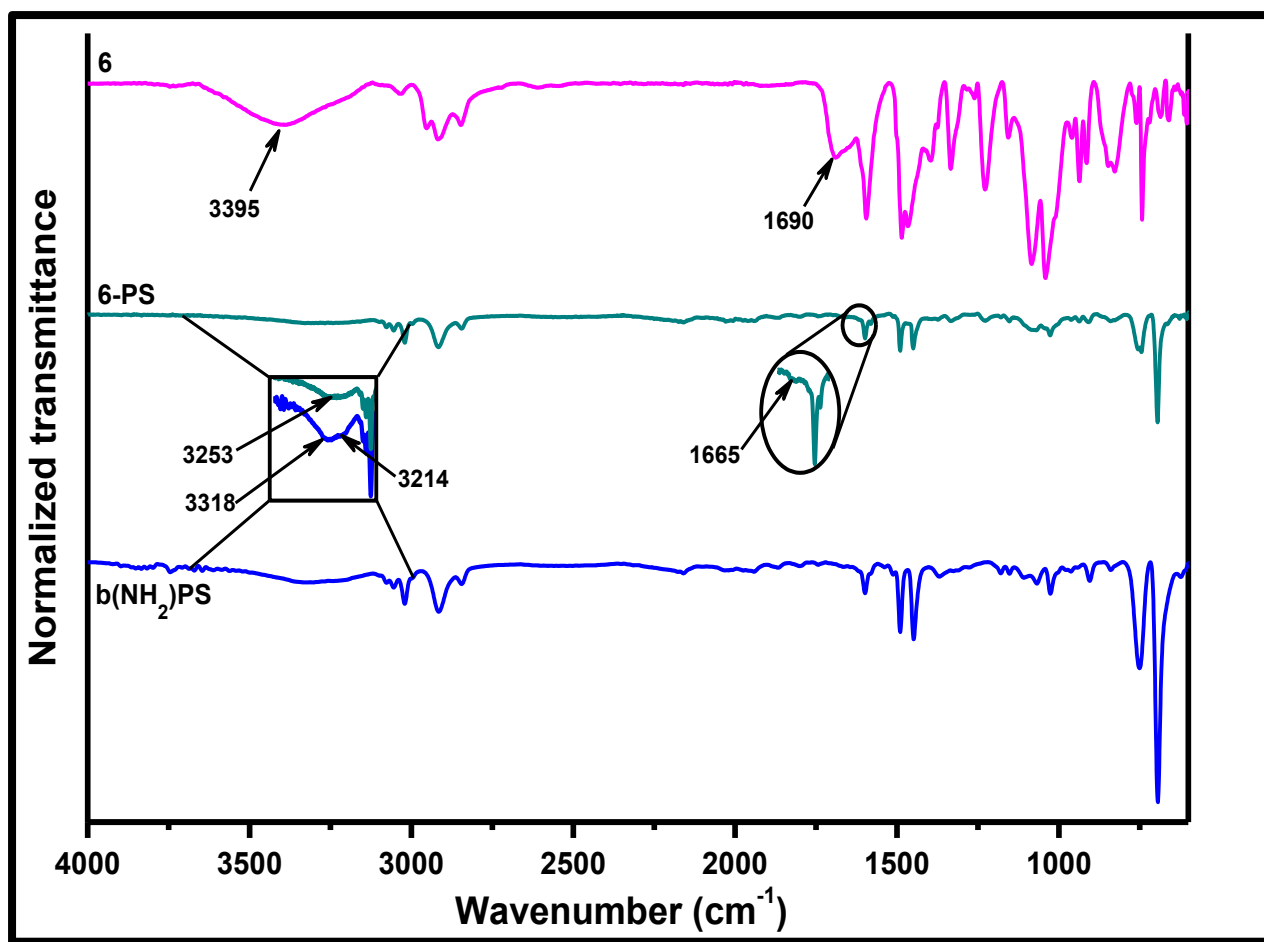
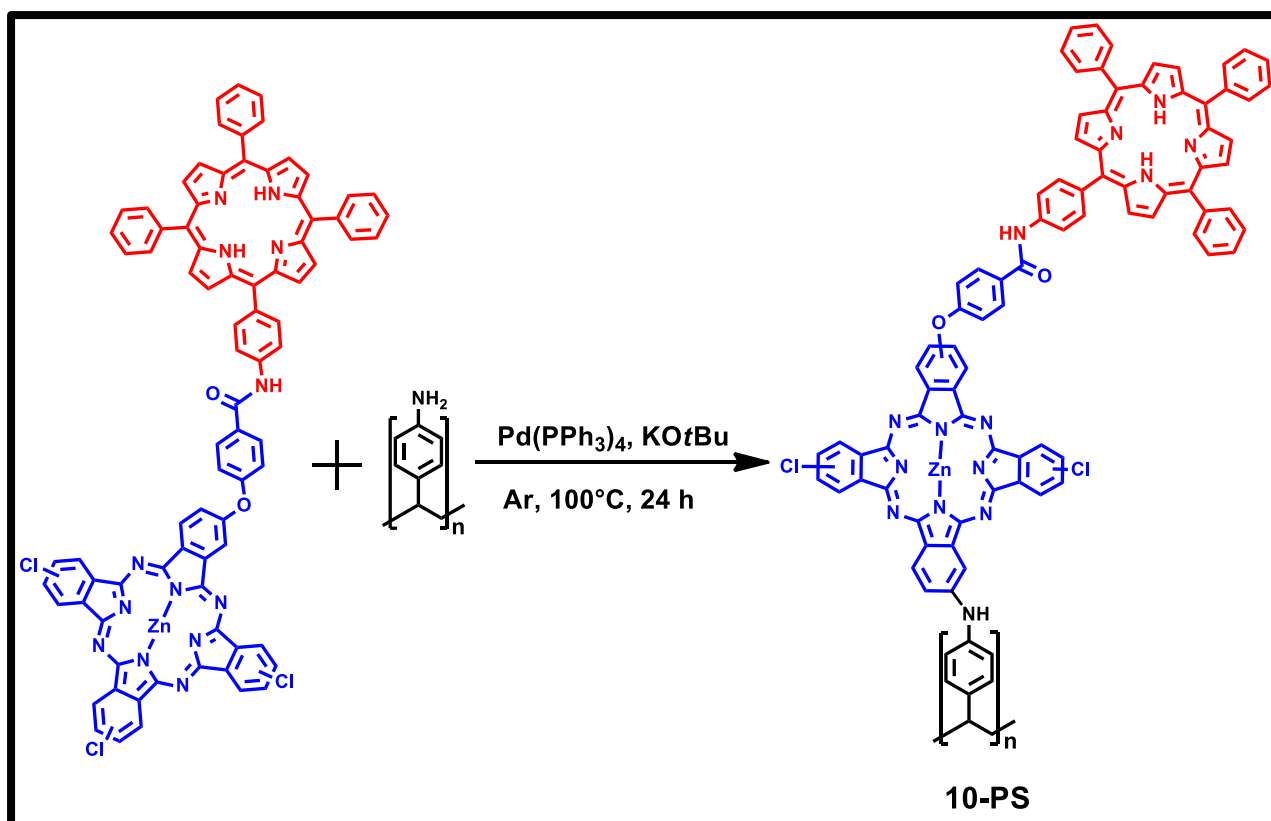


Fig. 3.24: FT-IR spectra for complex **6**, b(NH<sub>2</sub>)PS and **6-PS**.

### 3.4.2. 10-PS (Buchwald-Hartwig coupling)

Complex **10** was designed such that it would have available Cl groups to allow its subsequent conjugation to b(NH<sub>2</sub>)PS. Conjugation was achieved by Buchwald-Hartwig cross coupling of complex **10** and b(NH<sub>2</sub>)PS (**Scheme 3.14**). Complex **10** has three Cl groups on the MPc moiety, which would suggest possibility of multiple linkage by one molecule of complex **10** to b(NH<sub>2</sub>)PS. However, the general bulkiness of complex **10** and b(NH<sub>2</sub>)PS (since the latter is a polymer) was expected to restrict further interaction of the available –Cl and –NH<sub>2</sub> groups, hence avoiding multiple linkage. Also due to the small (catalytic) amount of the catalyst used in the reaction,



**Scheme 3.14:** Synthetic route for **10-PS**.

only one  $-\text{Cl}$  group per molecule of complex **10** could participate in the conjugation reaction at a time.

The FT-IR spectrum of **10-PS** (**Fig. 3.25**) exhibits differences to that of  $\text{b(NH}_2\text{)PS}$  especially in the fingerprint region (highlighted in **Fig. 3.25**), which is attributed to the presence of complex **10**. However due to the small amount of complex **10** conjugated to  $\text{b(NH}_2\text{)PS}$ , most of the photosensitizer's characteristic vibration peaks are of low intensity and are masked by the polymer vibration peaks. Taking into consideration the extensive washing of the conjugate, the presence of complex **10** suggests successful conjugation. Of notable importance, is the shoulder at  $1656\text{ cm}^{-1}$  in **10-PS** which is attributed to the amide  $\text{C=O}$  carbonyl stretching vibration of the conjugated



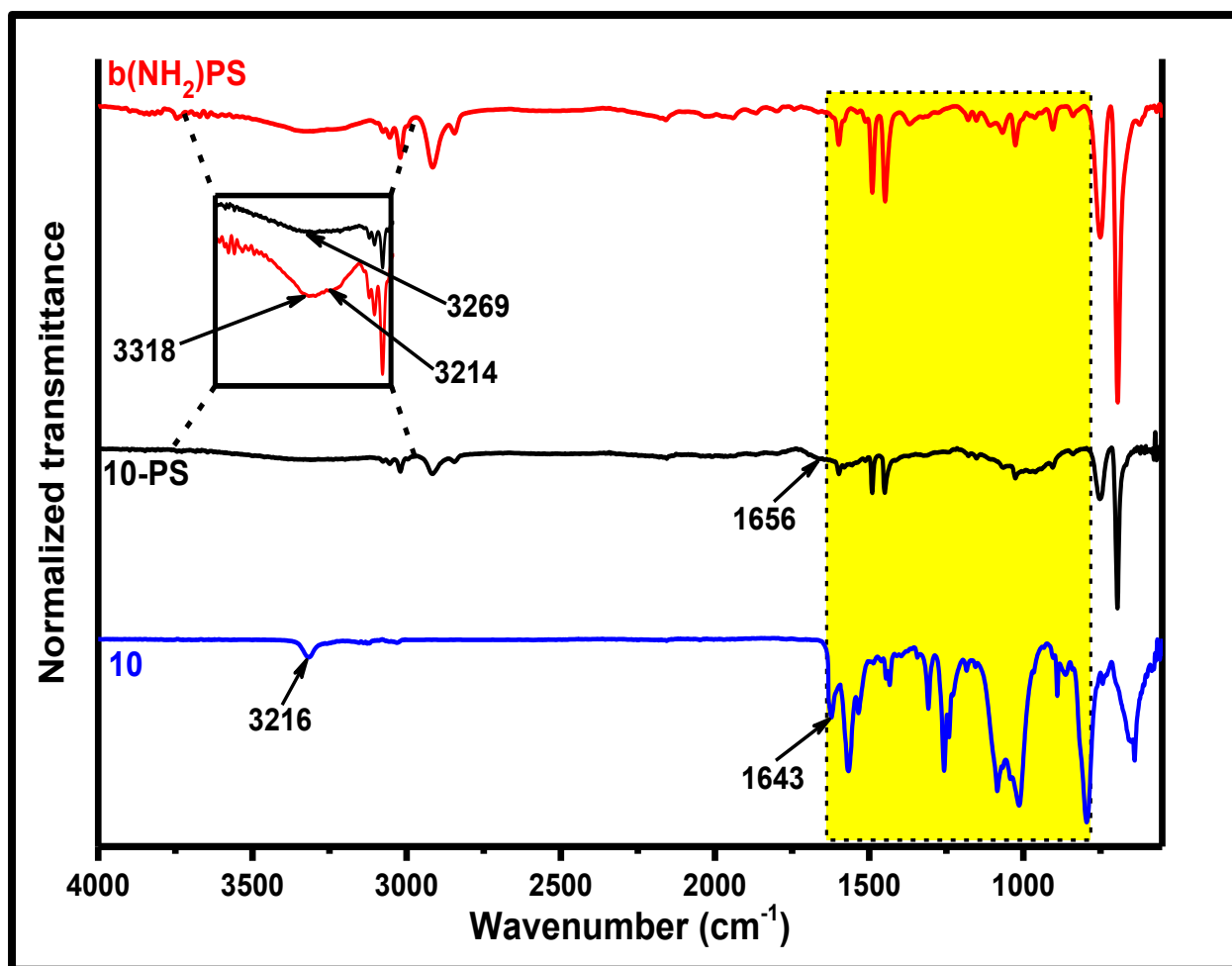


**Fig. 3.25:** FT-IR spectra for complex **10**, b(NH<sub>2</sub>)PS and **10**-PS.

complex **10**. The shift from 1643 cm<sup>-1</sup> in the free complex to 1656 cm<sup>-1</sup> in the conjugate suggests some change in the state or environment of the molecule which is attributed to successful conjugation to b(NH<sub>2</sub>)PS. The shift in the N–H stretching vibration from 3318 cm<sup>-1</sup> in b(NH<sub>2</sub>)PS to 3269 cm<sup>-1</sup> in **10**-PS is attributed to conversion of some of the b(NH<sub>2</sub>)PS primary amine N–H stretching vibrations to secondary amine stretching vibrations. These vibration peaks also overlap with the complex **10** amide N–H stretching vibration to give the observed broad peak. Although not completely conclusive, this observation also suggests successful conjugation.

### 3.4.3. MPc loading

The MPc loading in the photosensitizer-polymer conjugates was obtained using the TGA method [157] used for determining the MPc loading for **4a**(AgTNPs) and **4b**(AgTNPs). **Fig. 3.26** shows the TGA thermograms for the determination of the loading of complexes **5** and **6** onto b(NH<sub>2</sub>)PS as examples. **Table 3.4** summarizes the loading values. Significant variation in loading values is attributed to variations in reacted photosensitizer amounts, coupling method and conditions used, functional group loading of the functionalized polymers used and symmetry of the MPc complexes.

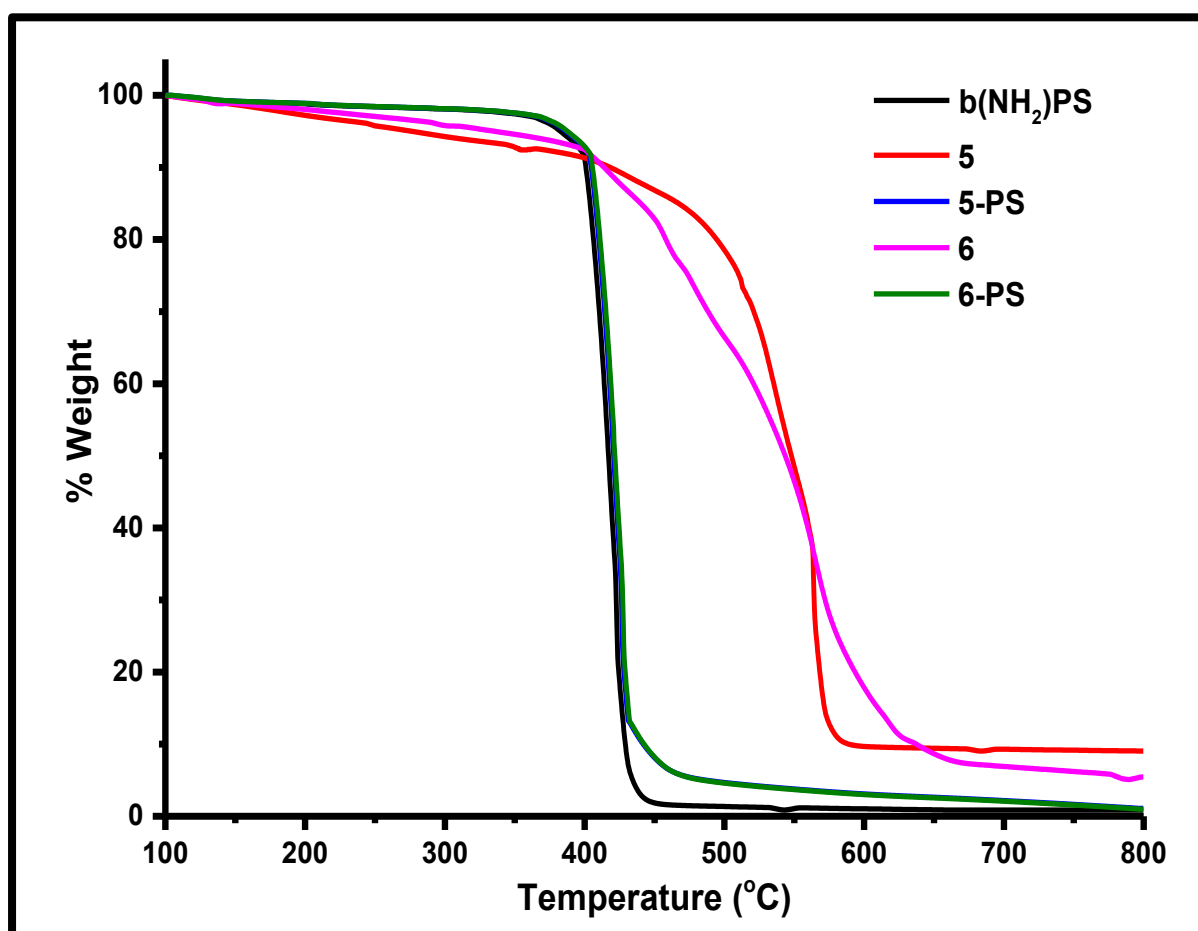


**Fig. 3.26:** TGA profiles of b(NH<sub>2</sub>)PS, complex **5**, 5-PS, complex **6** and 6-PS.

**Table 3.4:** Summary of the MPc loading in photosensitizer-polymer conjugates.

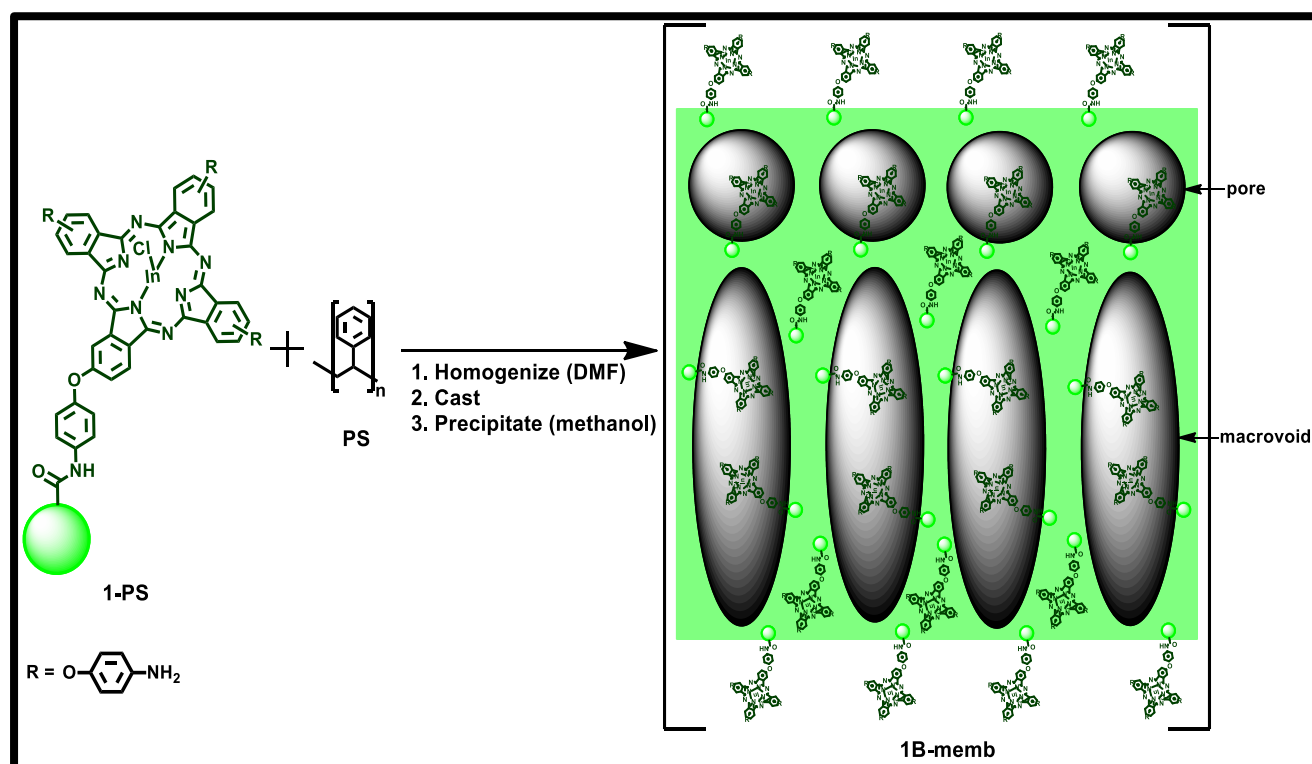
Sample	Loading (mg MPc/ g conjugate)	Loading ( $\mu\text{mol}$ MPc/ g conjugate)
<b>1-PAN</b>	5.4	4.93
<b>1-PS</b>	6.6	6.09
<b>2<math>\pi</math>(GQDs)-PS</b>	3.6	6.15
<b>3-PS</b>	3.4	4.8
<b>3<math>\pi</math>(GQDs)-PS</b>	9.8	13.7
<b>3(GQDs)-PS</b>	7.3	10.2
<b>4a-PS</b>	27.0	24.1
<b>4a(AgTNPs)-PS</b>	5.9	5.3
<b>4b-PS</b>	34.0	28.2
<b>4b(AgTNPs)-PS</b>	11.3	9.4
<b>5-PS</b>	28.0	33.3
<b>6-PS</b>	29.2	22.4
<b>10-PS</b>	24.6	17.2

### 3.5. Polymer membranes

Asymmetric polymer membranes were targeted in this work due to their desirable application related properties [19]. Polyacrylonitrile (PAN) and polystyrene (PS) were used as candidate polymers for use in the study. After the preliminary experiments using both PAN and PS with complex **1**, only polystyrene was used for the subsequent membrane preparations, since the PS membranes had a more structured porosity which would enable easy identification of variations between different functionalized membranes.

Membrane formation was achieved by doping the unfunctionalized polymer solution with a corresponding polymer-anchored photosensitizer prior to membrane casting,

**Table 3.3. Scheme 3.15** shows a schematic representation of functionalized polymer membrane formation using **1**-PS-memb as an example. The illustration of the



**Scheme 3.15:** Synthetic route for **1**-PS-memb.

functionalized membrane indicates the three possible final locations of the photosensitizer in the membrane. These are; the membrane surfaces (top and bottom), lining the surfaces of the pores and entrapped in the polymer matrix. Photosensitizer-free membranes doped with functional group modified polymers were also prepared as controls PAN-memb (PAN membrane) and PS-memb (PS membrane).

### 3.5.1. Physical appearance

**Fig. 3.27** shows the physical appearance of **1**-PAN-memb and **1**-PS-memb as examples of the prepared functionalized membranes with comparison to the control membranes. The membranes were faintly coloured green corresponding to complex **1**'s colour. The colour distribution on both membrane surfaces was evenly spread which suggests homogeneous photosensitizer dispersion. However, the top for **1**-PS-memb (bottom for **1**-PAN-memb) surface colour was less intense than the bottom (top for **1**-PAN-memb) due to the formation of a dense porous skin. This hypothesis is also supported by the observation of indistinguishable colour intensities of the top and bottom surfaces of **10**-memb (not shown) where the surface pore sizes, and distribution between the top and bottom did not differ much.

All functionalized membranes were respectively coloured according to the photosensitizers used (either green or blue), while the control membranes were white. This suggested successful immobilization of the photosensitizers. The colour intensities of the functionalised membranes corresponded to the photosensitizer loading in the photosensitizer-polymer conjugates. Also, in general the top and bottom surfaces of the membranes were distinguished by the relatively shiny appearance of the top while the bottom surfaces were relatively dull.

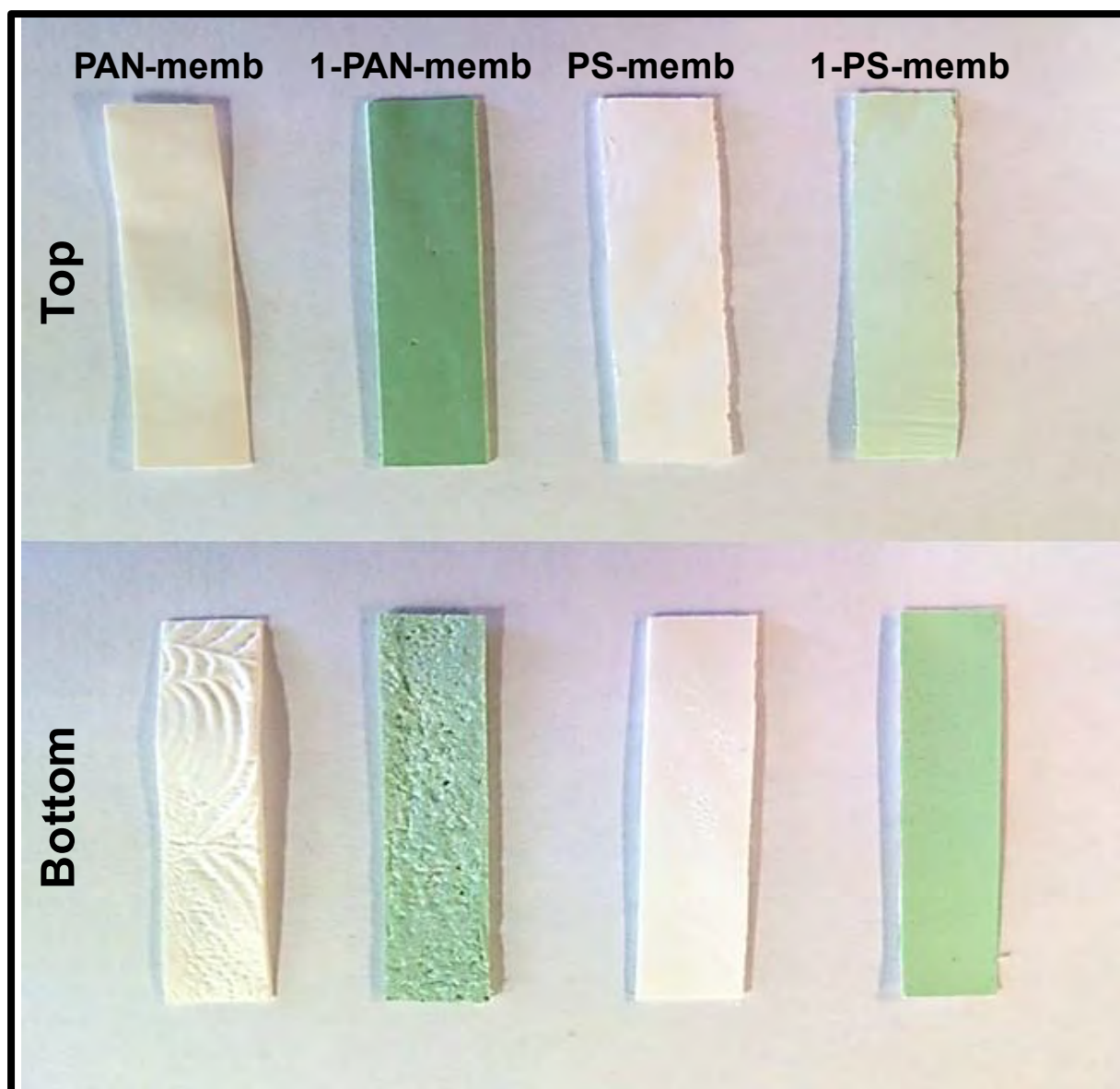


**Fig. 3.27:** Photos of PAN-memb, 1-PAN-memb, PS-memb and 1-PS-memb when viewed from the top or bottom.

### 3.5.2. SEM analysis

All the prepared polymer membranes exhibited the characteristic cross-section of asymmetric polymer membranes, consisting of a thin densely porous skin and a less dense porous supporting bulk. **Fig. 3.28** shows the SEM micrographs of 1-PAN-memb and 1-PS-memb as examples for all prepared membranes. The edge micrograph of



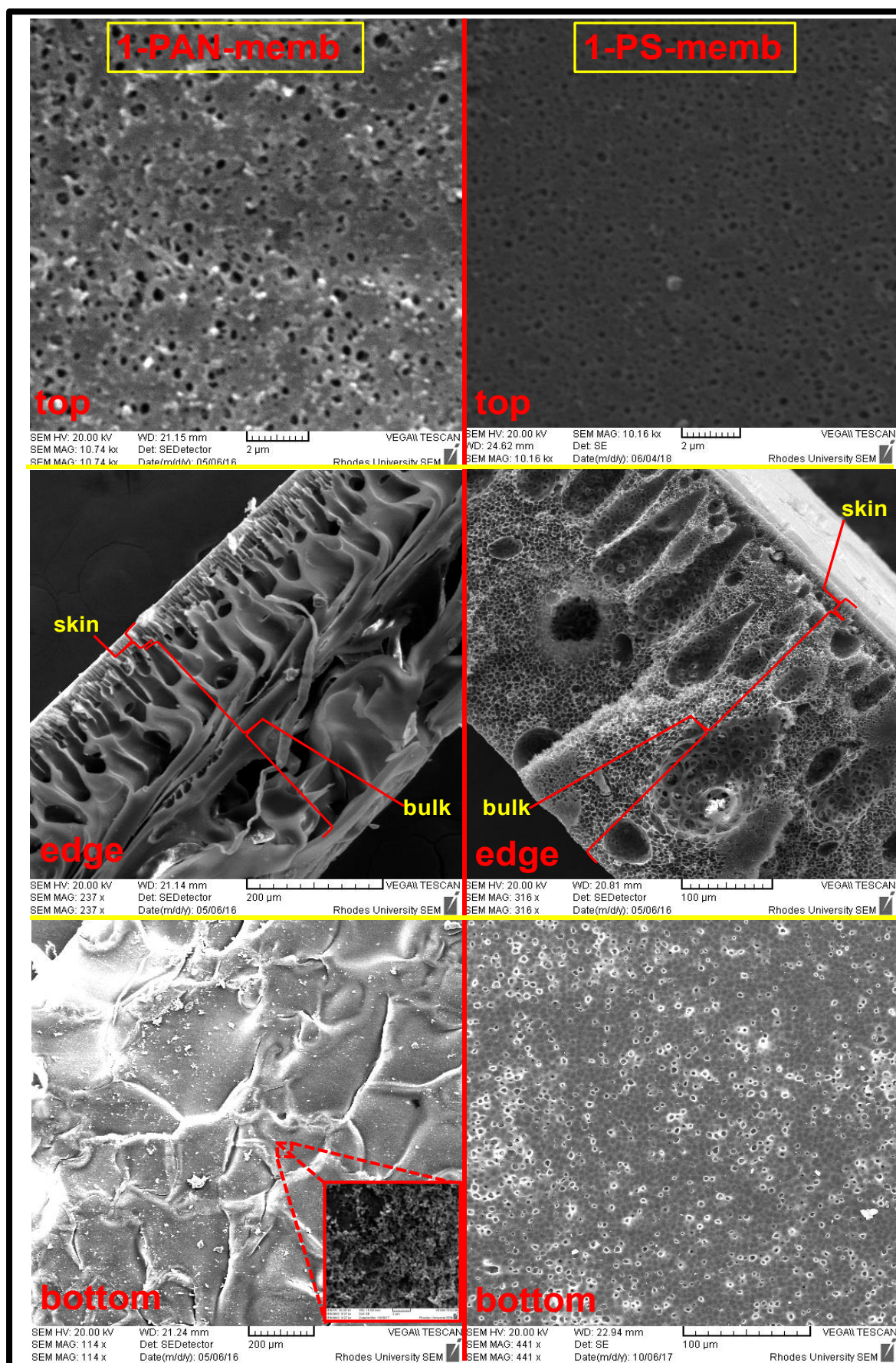


Fig. 3.28: SEM micrographs of 1-PAN-memb and 1-PS-memb.

**1**-PAN-memb shows the membrane bulk to consist of structureless macrovoids with shapes that cannot be easily defined. On the other hand, the edge micrograph of **1**-PS-memb shows a more structured bulk consisting of longitudinal macrovoids spanning the thickness of the membrane within a loose sponge-like matrix. All prepared PS membranes had a similar structure to **1**-PS-memb, but with variations in dimensions of surface pore diameters, and skin and bulk thickness. **Table 3.5** summarizes the dimensions of all prepared membranes as average estimates obtained from SEM micrographs within the limits of the image resolutions.

Focusing on the PS membranes, **Table 3.5** shows that no straightforward general trend in variations in membrane structure can be made and this is attributed to the simultaneous effect of multiple contributing factors. These include; polymer solution concentration, functionalized polymer conjugate amounts, photosensitizer functionality and loading on polymer conjugates, presence and nature of nanoparticles, and nonsolvent composition. As an example, **Fig. 3.29** shows the membrane skin and bottom surface porosity of **5**-memb and **6**-memb where the structures of complexes **5** and **6** are related, complex loading is almost the same and all other preparation parameters were identical, yet there is a distinct difference in the porosity especially on the bottom surfaces, in addition to the relative differences shown in **Table 3.5**. For the skin, the pore structure is relatively different where the skin of **5**-memb consists of a more compact network as compared to **6**-memb. Also, of particular note in **Table 3.5**, is the distinct effect of nano particle presence, especially on the thickness of the membrane bulk where GQDs influenced formation of a thicker membrane bulk while AgTNPs resulted in thinner bulks, all relative to membranes functionalized with corresponding MPcs in the absence of the NPs.



**Table 3.5:** Summary of the average dimensions of prepared membranes.

Membrane	Top pore diameter ( $\mu\text{m}$ )	Bottom pore diameter ( $\mu\text{m}$ )	Membrane skin thickness ( $\mu\text{m}$ )	Membrane bulk thickness ( $\mu\text{m}$ )
PAN-memb	<0.5	- <sup>a</sup>	17	424
1-PAN-memb	<0.5	<0.5 <sup>a</sup>	26	406
PS-memb	<0.5	2.6	17	354
1-PS-memb	<0.5	5.6	18	393
2 $\pi$ (GQDs)-memb	<0.5	4.1	18	323
3-memb	<0.5	2.8	11	358
3 $\pi$ (GQDs)-memb	<0.5	3.7	28	524
3(GQDs)-memb	<0.5	3.2	19	509
4a-memb	<0.5	3.0	20	398
4a(AgTNPs)-memb	1.6	3.9	13	191
4b-memb	<0.5	2.8	22	346
4b(AgTNPs)-memb	<0.5	3.1	18	238
5-memb	<0.5	9.7	47	517
6-memb	0.9	11.6	36	398
10-memb	2.9	5.5	17	336

<sup>a</sup> Pores in the form of slits.

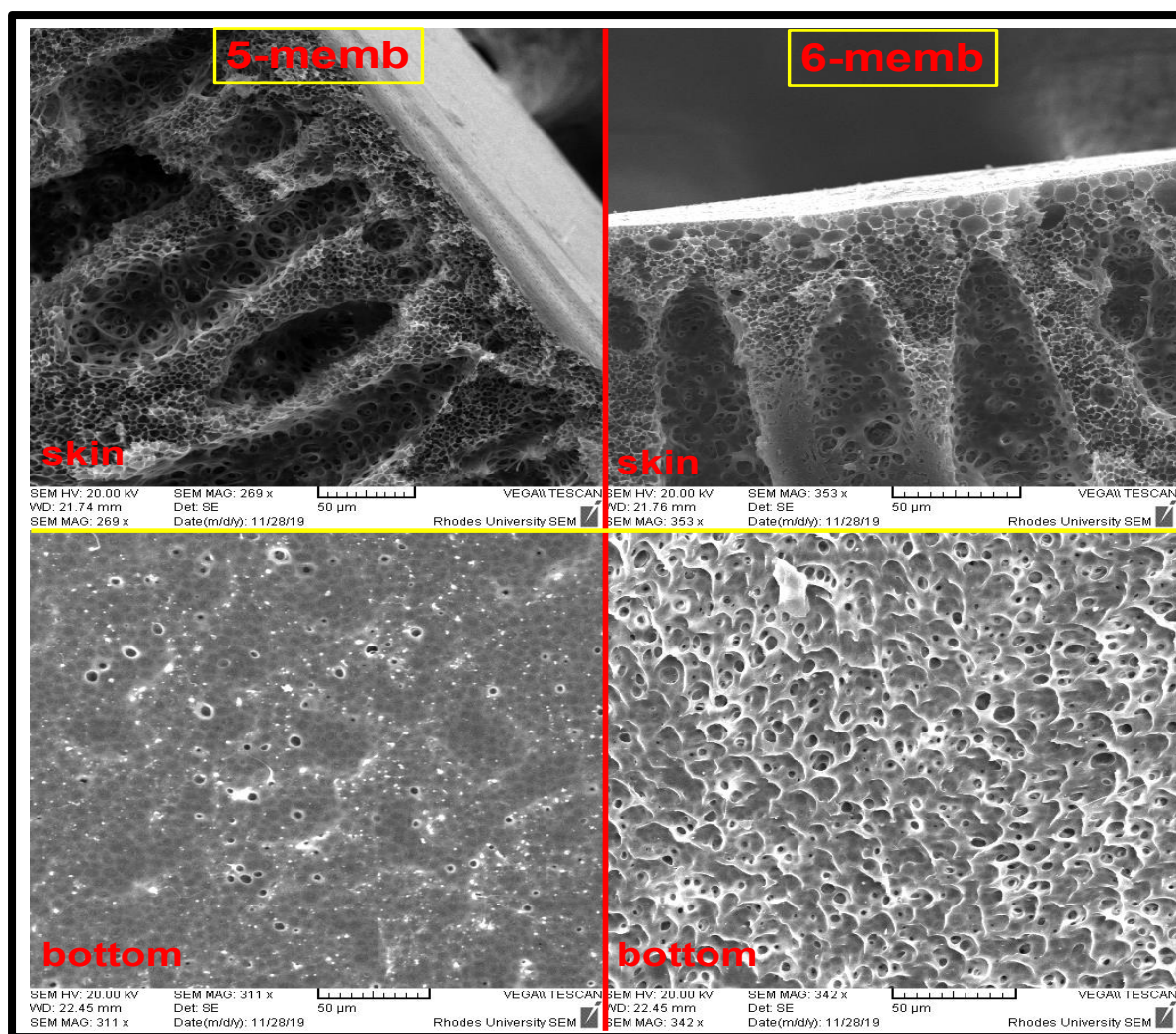


**Fig. 3.29:** SEM micrographs of the skin and bottom surface of **5-memb** and **6-memb**.

### 3.5.3. Solid-state UV-Vis analysis

The solid-state UV-Vis spectra for the functionalized membranes are exemplified by those of **1-PAN-memb** and **1-PS-memb** (top for both) shown in **Fig. 3.30**. Spectra for membranes without photosensitizers did not show any characteristic bands and are hence not presented here. The spectra show the characteristic Q and B-band absorptions of complex **1**, which are broad due to aggregation of the complex in the

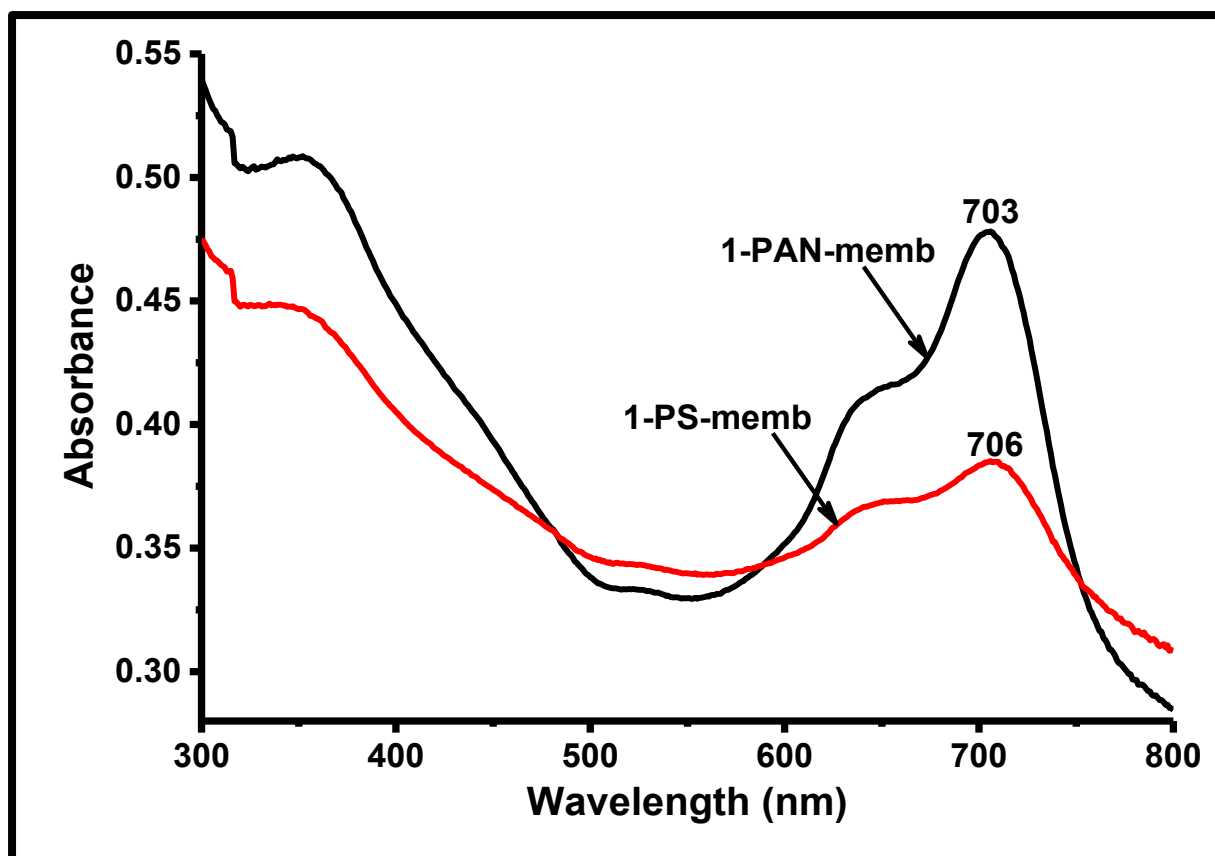


**Fig. 3.30:** Solid-state UV-Vis spectra for 1-PAN-memb and 1-PS-memb.

solid state [163]. Solid state spectra of MPcs is usually explained using the theory of exciton coupling, which is based on the interaction between adjacent MPc molecules [153]. In a cofacial alignment of the MPc molecules, a broad blue shifted Q absorption is expected in the solid-state spectrum, while for the non-cofacial (edge-to-edge) alignment, the exciton theory suggests red-shifting in the Q band. The spectra of **4a**-memb and **4b**-memb (**Fig. 3.31 (A)**), **5**-memb and **6**-memb (not shown) also show similar features. On the other hand, the spectra of MPc(GQDs)-membs (**Fig. 3.31 (B)**) and the **4b**(AgTNP)s-membs (**Fig. 3.31 (A)**) show more resolved spectra where the MPc monomer Q-bands are dominant and the vibronic bands are observed. This observation suggests that introduction of the MPcs as conjugates to nanoparticles improves photosensitizer dispersion, thus reducing aggregation in the solid state.

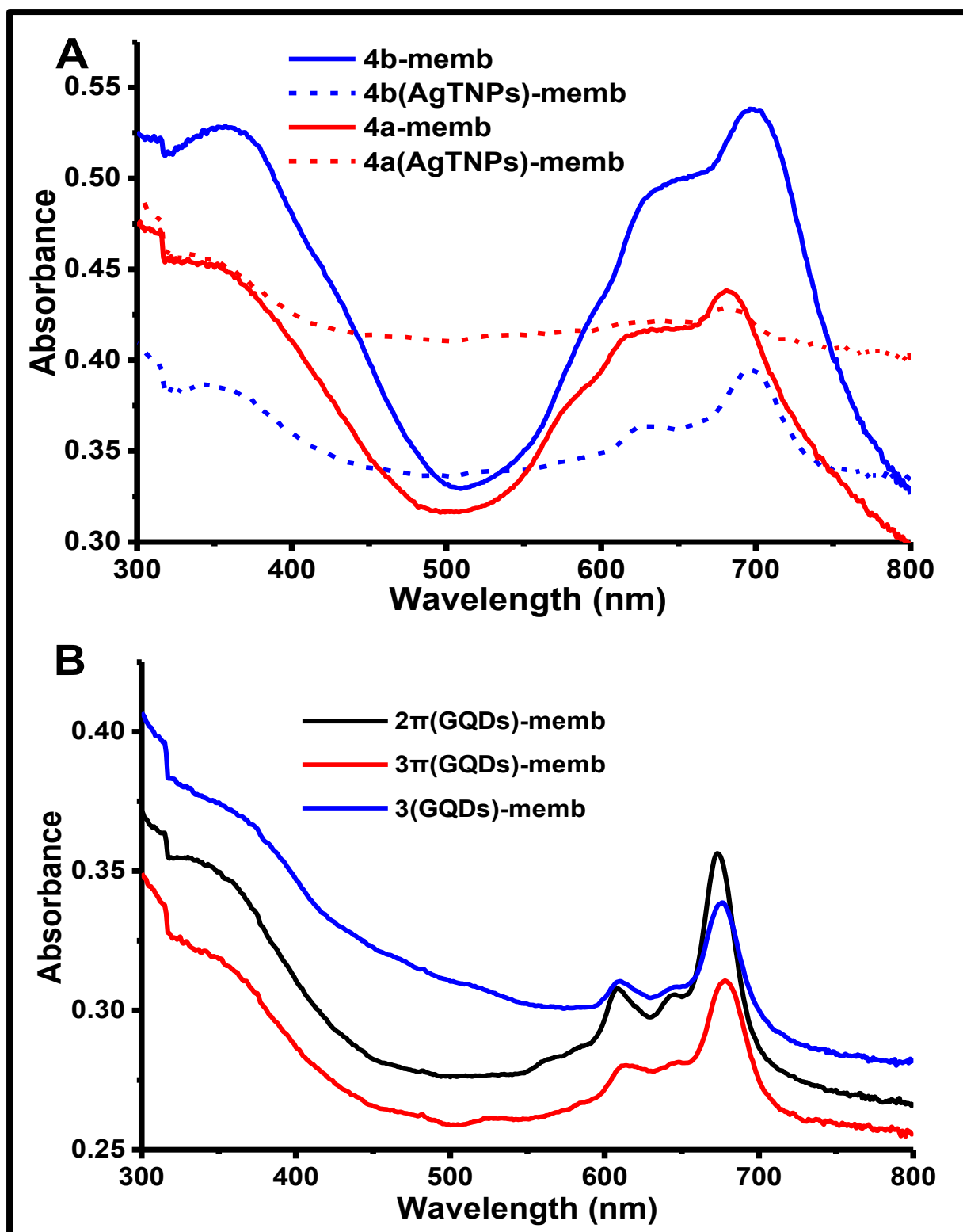


**Fig. 3.31:** Solid-state UV-Vis spectra for (A) **4a**-memb, **4a**(AgTNPs)-memb, **4b**-memb and **4b**(AgTNPs)-memb, and (B) **2 $\pi$** (GQDs)-memb, **3 $\pi$** (GQDs)-memb and **3**(GQDs)-memb.

The normalised solid-state UV-Vis spectrum for **10**-memb is shown in **Fig. 3.32** together with the spectrum for **10**-PS for reference. The spectrum for **10**-memb consists of five visible bands at 423 (Soret), 484 and 529 nm (Q) attributed to the porphyrin component of complex **10**, and bands at 652 and 685 nm (Q) attributed to the MPc component. The MPc band at 652 nm may be attributed to the splitting of the MPc Q-band (due to aggregation) in the solid state which has been reported before [163].

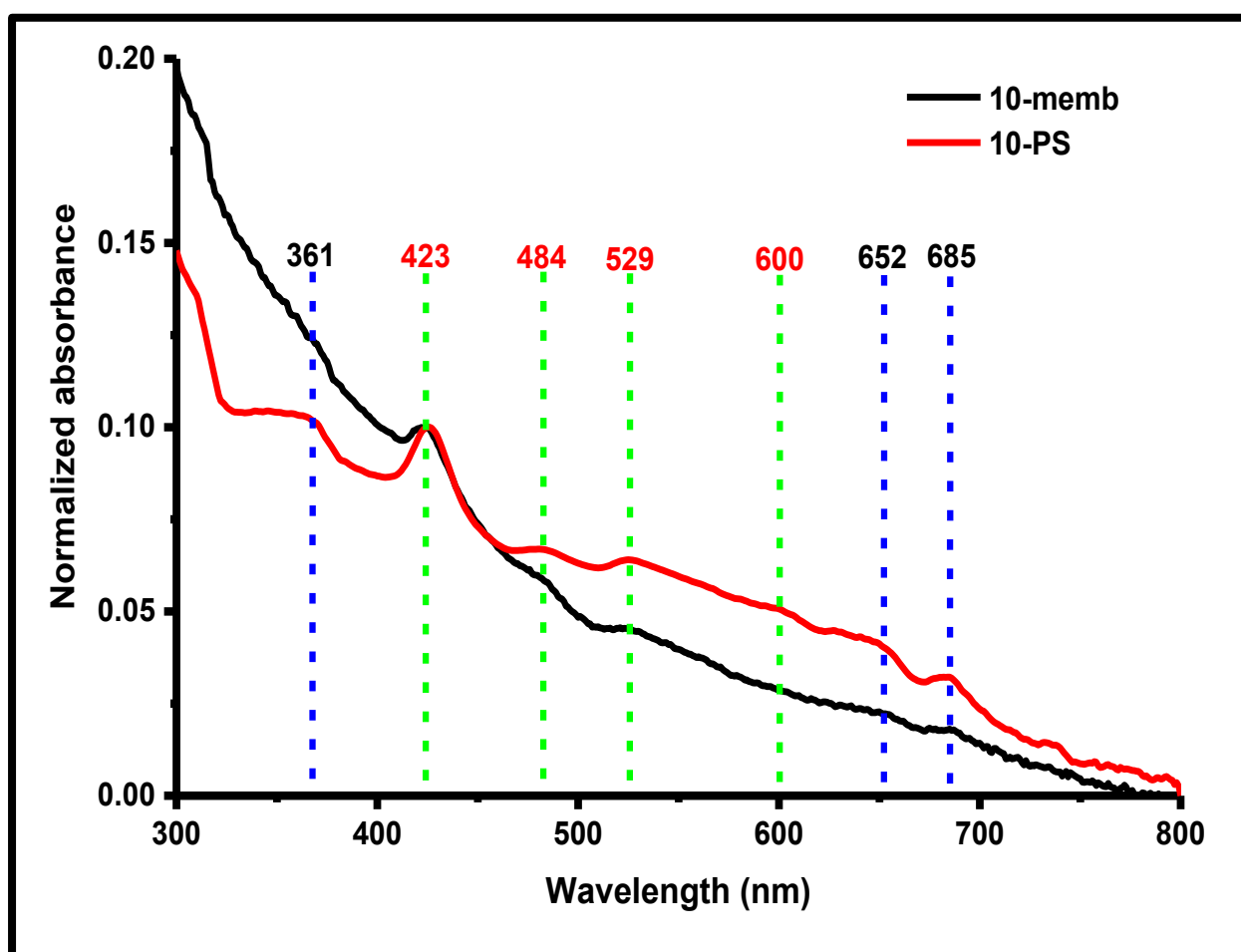


**Fig. 3.32:** Normalised solid-state UV-Vis spectrum for **10**-memb and **10**-PS.

### 3.6. Summary of chapter

Complexes **4b**, **5**, **6**, **8**, **9** and **10** were successfully synthesized and characterized using mass spectrometry, UV-Vis, FT-IR, NMR spectroscopy and elemental analysis. UV-Vis spectra of the MPc complexes **4b**, **5**, **6**, **9** and **10** in DMSO proved the complexes to be metalated with little to no signs of aggregation while the porphyrin complex **8** was a free-base. The elemental analysis FT-IR, NMR and mass spectra confirmed the structure, composition and functionality of the target complexes. GQDs and AgTNPs were also successfully synthesized and conjugated to complexes **2** and **3**, and complexes **4a** and **4b** respectively to form corresponding nanoconjugate photosensitizers. The size and shapes of the nanoparticles and their corresponding MPc nanoconjugates were elucidated using TEM. UV-Vis spectra corresponded to the expected nanoparticles while the spectra of the conjugates mostly resembled those of the corresponding MPcs. Both  $\pi$ - $\pi$  stacking and covalent conjugation proved to be viable means of formation of MPc-GQDs nanoconjugates and hence confirmed possible application of non-covalently conjugatable MPcs in polymer membrane functionalization. Complexes **1-6** and **10**, together with the nanoconjugate photosensitizers were anchored on either PAN or PS polymers before successful preparation of corresponding photosensitizer functionalized asymmetric polymer membranes. Successful anchoring of photosensitizers to polymers was confirmed by FT-IR, and XPS for some conjugates. SEM of the membranes confirmed them to be porous and asymmetric with pores in the micron range, while their solid-state UV-Vis spectra confirmed photosensitizer immobilization.

# CHAPTER 4

## 4. Photophysical and Photochemical Properties

This chapter discusses the photophysical and photochemical properties of the complexes and soluble conjugates used in this thesis. The singlet oxygen generation properties of the prepared photoactive polymer membranes are also discussed in this chapter.

### 4.1. Photophysical and photochemical parameters

#### 4.1.1. Fluorescence quantum yield ( $\Phi_F$ ) and lifetime ( $\tau_F$ )

Fluorescence quantum yield is the ratio of the number of photons emitted via fluorescence to those absorbed [164]. Fluorescence quantum yields of all fluorophore were determined using the comparative method as described in literature [164] according to Eqn (4.1):

$$\Phi_F^{\text{sample}} = \Phi_F^{\text{Std}} \frac{F^{\text{sample}} A^{\text{Std}} (n^{\text{sample}})^2}{F^{\text{Std}} A^{\text{sample}} (n^{\text{Std}})^2} \quad (4.1)$$

where  $\Phi_F^{\text{Std}}$  is the fluorescence quantum yield of the standard,  $A^{\text{sample}}$  and  $A^{\text{Std}}$  are the absorbances of the sample and the standard,  $F^{\text{sample}}$  and  $F^{\text{Std}}$  are the areas under the fluorescence curves of the sample and the standard, and  $n^{\text{sample}}$  and  $n^{\text{Std}}$  are the refractive indices of the solvents used for the sample and standard respectively. ZnPc in DMSO ( $\Phi_F = 0.20$  [145]), quinine sulphate in 0.1 M  $\text{H}_2\text{SO}_4$  ( $\Phi_F = 0.52$  [165]) and ZnTPP ( $\Phi_F = 0.033$  [166]) in DMSO were used as standards for the different fluorophores studied.

Fluorescence lifetimes ( $\tau_F$ , average time the electron stays in an excited state before photon emission) were obtained from the TCSPC setup described earlier.



#### 4.1.2. Förster resonance energy transfer (FRET)

FRET is a non-radiative energy transfer process which occurs between a photoexcited donor fluorophore upon absorption of higher energy photons, and an acceptor molecule near the donor fluorophore [167]. The FRET efficiency ( $Eff$ ) was determined experimentally from the fluorescence quantum yield of the donor in the absence ( $\Phi_{F(donor)}$ ) and presence ( $\Phi_{F(donor)}^{conjugate}$ ) of the acceptor using Eqn (4.2) [167]:

$$Eff = 1 - \frac{\Phi_{F(donor)}^{conjugate}}{\Phi_{F(donor)}} \quad (4.2)$$

The fluorescence quantum yield of the donor in the presence of the acceptor ( $\Phi_{F(donor)}^{conjugate}$ ) was obtained using Eqn (4.3) [168]:

$$\Phi_{F(donor)}^{conjugate} = \Phi_{F(donor)} \frac{F_{donor}^{conjugate}}{F_{donor}} \quad (4.3)$$

where  $\Phi_{F(donor)}$  is the fluorescence quantum yield(s) of donor alone,  $F_{donor}$  is the fluorescence intensity of donor alone and  $F_{donor}^{conjugate}$  is the fluorescence intensity of the donor upon conjugation. The donor–acceptor distance  $r$  (Å) was extrapolated from Eqn (4.4) [169]:

$$Eff = \frac{R_0^6}{R_0^6 + r^6} \quad (4.4)$$

where  $R_0$  (Förster distance) is the critical distance between the donor and the acceptor molecules for which efficiency of the energy transfer is 50% and depends on the quantum yield of the donor Eqn (4.5), [170]

$$R_0^6 = 8.8 \times 10^{23} k^2 n^{-4} \Phi_{F(donor)} J \quad (4.5)$$

where  $\kappa$  is the dipole orientation factor (the value in liquid medium is given as 2/3),  $n$  is the solvent's refractive index,  $\Phi_{F(\text{donor})}$  is the donor quantum yield and  $J$  ( $\text{cm}^6$ ) is the Förster overlap integral [167,170,171]. PhotochemCAD software was then used to compute the FRET parameters [169].

#### 4.1.3. Triplet quantum yield ( $\Phi_T$ ) and lifetime ( $\tau_T$ )

Triplet quantum yield is the fraction of molecules that cross over from the singlet to the triplet state following photoexcitation. The triplet quantum yields were determined using a comparative method from the decay kinetic curves of the triplet absorptions obtained using the laser flash photolysis set-up described earlier. The sample and standard solution absorptions were adjusted to approximately 1.5 and their cross-over wavelength noted. The solutions were then bubbled with argon to remove dissolved oxygen before taking readings after exciting at the cross-over wavelength. ZnPc in DMSO was used as a standard ( $\Phi_T = 0.65$  [172]) and  $\Phi_T$  values were calculated using Eqn (4.6):

$$\Phi_T^{\text{sample}} = \Phi_T^{\text{Std}} \frac{\Delta A_T^{\text{sample}} \epsilon_T^{\text{Std}}}{\Delta A_T^{\text{Std}} \epsilon_T^{\text{sample}}} \quad (4.6)$$

where  $\Phi_T^{\text{Std}}$  the triplet quantum yield for the standard,  $\Delta A_T^{\text{sample}}$  and  $\Delta A_T^{\text{Std}}$  are the changes in the triplet state absorbances of the sample and standard, and  $\epsilon_T^{\text{sample}}$  and  $\epsilon_T^{\text{Std}}$  are the triplet state molar extinction coefficients for the sample and the standard, respectively.  $\epsilon_T^{\text{sample}}$  and  $\epsilon_T^{\text{Std}}$  are determined using the Eqn (4.7) and (4.8):

$$\epsilon_T^{\text{sample}} = \epsilon_S^{\text{sample}} \frac{\Delta A_T^{\text{sample}}}{\Delta A_S^{\text{sample}}} \quad (4.7)$$

$$\epsilon_T^{\text{Std}} = \epsilon_S^{\text{Std}} \frac{\Delta A_T^{\text{Std}}}{\Delta A_S^{\text{Std}}} \quad (4.8)$$

where  $\varepsilon_S^{\text{sample}}$  and  $\varepsilon_S^{\text{Std}}$  are the respective ground state molar extinction coefficients,  $\Delta A_S^{\text{sample}}$  and  $\Delta A_S^{\text{Std}}$  are the changes in absorbances of the ground singlet states, and  $\Delta A_T^{\text{sample}}$  and  $\Delta A_T^{\text{Std}}$  are the changes in the triplet state absorptions.

The average time the electron stays in the triplet excited state before returning to the ground state is called the triplet lifetime ( $\tau_T$ ). The triplet lifetimes for the synthesized compounds and soluble conjugates were determined by exponential fitting of the triplet absorption decay kinetic curves using ORIGIN 8 software.

#### 4.1.4. Singlet oxygen quantum yield ( $\Phi_\Delta$ )

Singlet oxygen quantum yield is the amount of singlet oxygen ( $^1\text{O}_2$  molecules) generated per photon absorbed by a photosensitizer. In this work,  $\Phi_\Delta$  for solutions of soluble photosensitizers was determined using a comparative method reported before in literature [145,173] using unsubstituted ZnPc ( $\Phi_\Delta = 0.67$  [174]) and Rose Bengal ( $\Phi_\Delta = 0.76$  [175]) in DMSO, and ClAlPcSmix in aqueous media ( $\Phi_\Delta = 0.42$  [176]) as standards. DPBF and DMA in DMSO, and ADMA in aqueous media were used as corresponding singlet oxygen quenchers.

In the experiments, equal volumes of the photosensitizer solution (sample or standard with an absorbance of approximately 1.5) and quencher solution (absorbance of approximately 1.8) were mixed in the dark, and the mixtures irradiated by light of a wavelength corresponding to the sample and standard cross-over wavelength. Degradation of the quencher after successive irradiation cycles was then monitored by UV-Vis spectroscopy and the  $\Phi_\Delta$  calculated using Eqn (4.9):

$$\Phi_\Delta^{\text{sample}} = \Phi_\Delta^{\text{Std}} \frac{R^{\text{sample}} I_{\text{abs}}^{\text{Std}}}{R^{\text{Std}} I_{\text{abs}}^{\text{sample}}} \quad (4.9)$$

where  $\Phi_{\Delta}^{\text{Std}}$  is the singlet oxygen quantum yield of a known standard,  $R^{\text{sample}}$  and  $R^{\text{Std}}$  are the singlet oxygen quencher photobleaching rates in the presence of the corresponding photosensitizer.  $I_{\text{abs}}^{\text{sample}}$  and  $I_{\text{abs}}^{\text{Std}}$  are the rates of light absorption by the sample and the standards, respectively and  $I_{\text{abs}}$  for the corresponding photosensitizers and standards is defined by Eqn (4.10):

$$I_{\text{abs}} = \frac{\alpha A I}{N_A} \quad (4.10)$$

where  $\alpha = 1 - 10^{-A(\lambda)}$ ,  $A(\lambda)$  is the absorbance of the sensitizer at the irradiation wavelength,  $A$  is irradiated area,  $I$  is the intensity of light and  $N_A$  is Avogadro's constant.

For the functionalized membranes an absolute method described in literature [173] was employed with DPBF (in ethanol) and ADMA (in water) as quenchers (Q) for the determination of  $\Phi_{\Delta}$ . The functionalized membranes were suspended in quencher solutions with an absorbance of approximately 1.0 and irradiated at the photosensitizer absorption wavelength for a constant time interval while monitoring the quencher degradation using UV-Vis spectroscopy. To account for adsorption of singlet oxygen quenchers onto the polymer membranes, similar precautions to those taken in the membrane photodegradation studies experimental procedure were applied. The singlet oxygen quantum yield values were then calculated using Eqn (4.11) [173]:

$$\frac{1}{\Phi_Q} = \frac{1}{\Phi_{\Delta}} + \frac{1}{\Phi_{\Delta}} \cdot \frac{K_d}{K_a} \cdot \frac{1}{[Q]} \quad (4.11)$$

where  $\Phi_Q$  is the quantum yield of the quencher,  $K_d$  is the decay constant of singlet oxygen,  $K_a$  is the rate constant for the reaction of the quencher (Q) with singlet oxygen and  $[Q]$  is the molar concentration of the quencher. The intercept obtained from the plot of  $1/\Phi_Q$  versus  $1/[Q]$  gave  $\Phi_{\Delta}$ .

$\Phi_Q$  was calculated using Eqn (4.12) [173] and the extinction coefficient of the quencher (ADMA in water,  $\epsilon = 12589$  at 380 nm [177] or DPBF in ethanol,  $\epsilon = 24547$  at 417 nm [178]).

$$\Phi_Q = \frac{(C_O - C_t)V_R}{I_{abs} \cdot t} \quad (4.12)$$

where  $C_O$  and  $C_t$  are the quencher concentrations prior to and after irradiation, respectively;  $V_R$  is the solution volume;  $t$  is the irradiation time per cycle and  $I_{abs}$  is as defined above. The absorbance used for determination of  $I_{abs}$  was that of the photosensitizer on the membrane at the irradiation wavelength. The light measured refers to the light reaching the spectrophotometer cell, and it was expected that some of the light may be scattered, hence the values for the photosensitizer in the membranes are estimates.

## 4.2. Fluorescence properties

### 4.2.1. Fluorescence excitation and emission spectra

The overlay of the absorption, excitation and emission spectra for complex **9** and **4a**(AgTNPs) as examples are shown in Fig. 4.1. The absorption and excitation spectra for complex **9** are similar with almost identical Q-band maxima, which suggests that the nuclear configurations of the ground state and excited states are similar. This also suggests that the configurations of the states are not affected by excitation in the solvent (DMSO) and the complex is not aggregated in DMSO. On the other hand, the emission spectrum is a mirror image of the absorption and excitation spectra with a Stokes shift of about 12 nm. The excitation and emission spectra for **4a**(AgTNPs) are mirror images of each other like those for complex **9**, but the absorption and excitation spectra are slightly different. The difference in the absorption and excitation spectra

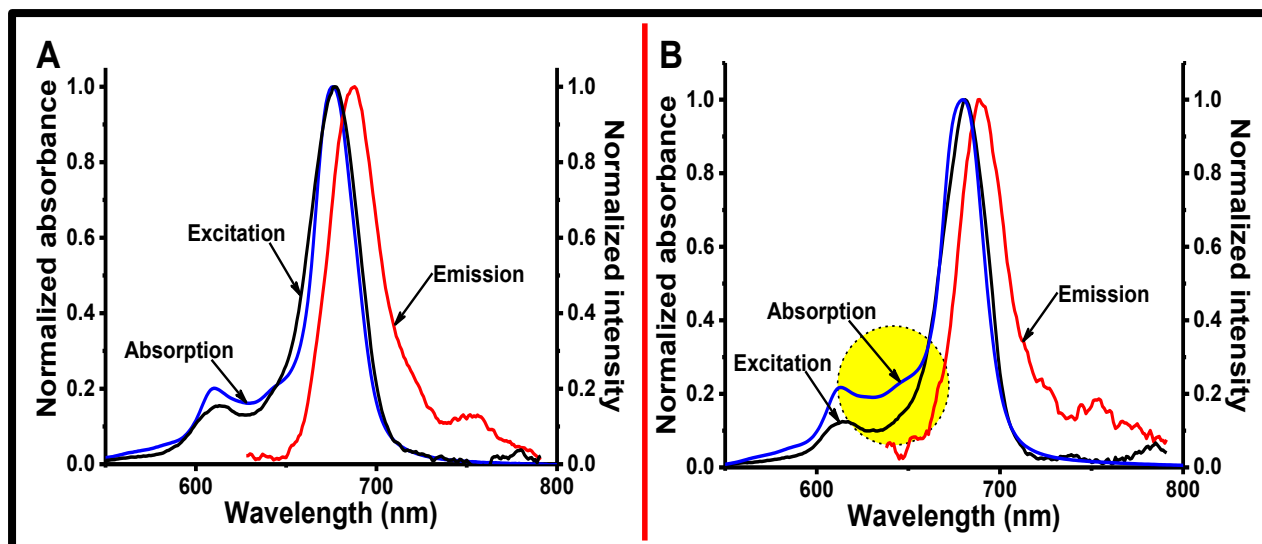


**Fig. 4.1:** Absorption, excitation and emission spectra for (A) complex **9** and (B) **4a**(AgTNPs) in DMSO.

(highlighted in yellow in **Fig. 4.1** (B)) is attributed to the absorption due to the AgTNPs in the conjugate, which also absorb in the same region as the Q-band of complex **4a** also observed in **Fig. 3.17**. A similar feature may also be observed in MPcs as a result of aggregation of the complexes. Except for complexes **1**, **4b** and **5**, **4a**(AgTNPs) and **4b**(AgTNPs), all MPc based photosensitizers studied exhibited fluorescence spectra behaviour similar to complex **9**. On the other hand, the emission signals for complexes **1**, **4b** and **5**, and **4b**(AgTNPs) were of significantly low intensity and not clearly defined.

#### 4.2.2. Fluorescence quantum yield ( $\Phi_F$ ) and lifetime ( $\tau_F$ )

The fluorescence quantum yields ( $\Phi_F$ ) were determined using a comparative method and equations described above, while the fluorescence lifetimes ( $\tau_F$ ) were obtained using the time correlated single photon counting (TCSPC) method. **Fig. 4.2** shows the fluorescence decay curve for complex **9** from which the  $\tau_F$  value was determined, as a typical representative spectrum for all photosensitizers studied. The  $\Phi_F$  and  $\tau_F$

values for the photosensitizers studied are summarized in **Table 4.1**. The complexes exhibited mono-exponential decay, as should be expected in the absence of aggregates and fluorescent impurities [179]. On the other hand, the MPc(NPs) conjugate photosensitizers exhibited bi-exponential decays (two lifetimes) which may be attributed to different orientations of the MPc complexes on the NPs. Bi-exponential decays may also be attributed to the presence of monomeric unconjugated MPc in the conjugate solution [180]. The fluorescence properties of MPc photosensitizers are influenced by intrinsic factors which include the nature of the central metal, substituents, symmetry and conjugation to nanoparticles [94,95,145,181–183], which were briefly studied and are discussed here in this thesis.

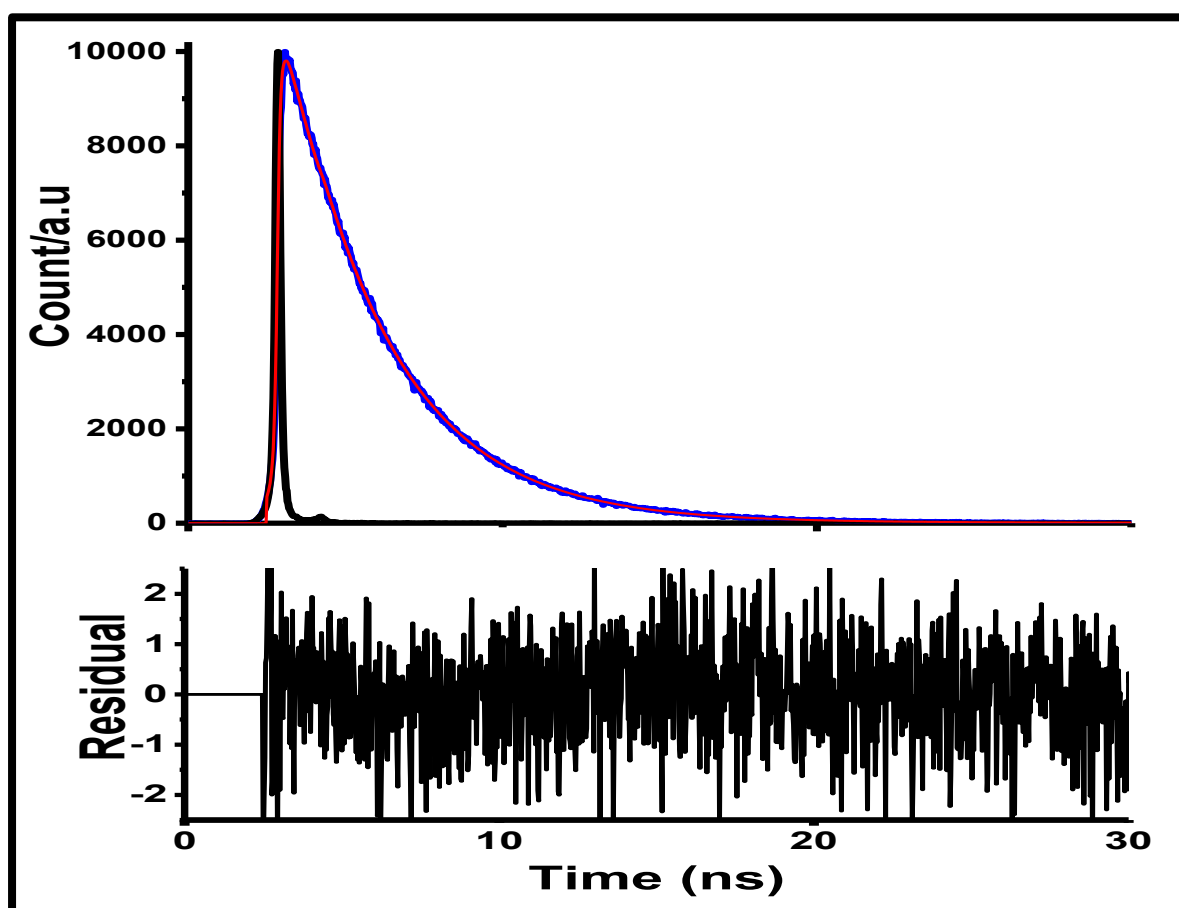


**Fig. 4.2:** Fluorescence decay (blue),  $x^2$  fitting (red) and IRF (black) curves for complex **9** in DMSO.

**Table 4.1:** Fluorescence quantum yields and lifetimes for MPcs and respective conjugates in DMSO.

Sample	$\Phi_F (\pm 0.02)$	Mean $\tau_F$ (ns) ( $\pm 0.03$ )
1	<0.01 [96]	0.29 [96]
2	0.20 [184]	2.80 [185]
GQDs	0.22	4.80
2 $\pi$ (GQDs)	0.20 (0.01)	3.40 (0.14)
3	0.16 [186]	3.14 [186]
GQDs	0.16	3.59
3 $\pi$ (GQDs)	0.18 (0.04)	3.14 (0.79)
3(GQDs)	0.19 (0.02)	3.13 (0.41)
4a	0.27 [58]	2.89
4a(AgTNPs)	0.15	2.78
4b	0.02	0.29
4b(AgTNPs)	0.01	0.29
5	0.03	1.08
6	0.13	2.70
8	0.02	10.7
9	0.15	2.79



10	<0.01 <sup>a</sup>	2.29 <sup>a</sup>
	0.17	2.82

Note: Values in round brackets are for exciting where GQDs absorb otherwise the values are where MPcs absorbs. Values for the GQDs conjugated to complex **2** and complex **3** are different because the particles were prepared in different batches. <sup>a</sup> Values when excited where the only porphyrin absorbs. References are given in square brackets.

#### i. Effects of central metal

Complexes **4a** and **4b** have the same carboxyphenoxy- $\beta$ -substituted Pc macrocycle. Metalation with the heavier indium metal in complex **4b** with comparison to zinc in complex **4a** enhances intersystem crossing (ISC) to the triplet excited state through spin orbit coupling [95] at the expense of fluorescence. This thus gave rise to the lower fluorescence quantum yield and lifetime in **4b** ( $\Phi_F = 0.02$ ;  $\tau_F = 0.29$  ns) compared to **4a** ( $\Phi_F = 0.27$ ;  $\tau_F = 2.89$  ns).

#### ii. Effects of substituents

Comparison of  $\Phi_F$  and  $\tau_F$  for complexes **1** and **4b** (symmetric phenoxy  $\beta$ -substituted indium chloride complexes); and complexes **5** and **6** (asymmetric  $\beta$ -amine derivative zinc complexes) shows that for structurally similar complexes, electron withdrawing groups give rise to higher  $\Phi_F$  and  $\tau_F$ , while electron donating groups appeared to have a quenching effect. The small difference in the  $\Phi_F$  and no difference in  $\tau_F$  between complexes **1** and **4b** (Table 4.1) is attributed to the oxo-bridge in the complexes which dampens the effects of the different peripheral functional groups of the substituents,

on the fluorescence properties of the complexes. The generally low fluorescence of these complexes is attributed to the heavy atom effect of the indium central metal as previously discussed.

Quaternization of the dimethyl amino substituents of complex **5** ( $\Phi_F = 0.03$ ;  $\tau_F = 1.08$  ns) to give complex **6** ( $\Phi_F = 0.13$ ;  $\tau_F = 2.70$  ns) converted the electron donating substituents in complex **5** to the cationic electron withdrawing substituents in complex **6**. The chloro- substituents in complex **9** introduced heavier atoms (chlorine compared to nitrogen in complexes **5** and **6**), in addition to their simultaneous antagonistic resonance donor and inductive acceptor properties. These factors together make prediction of chloro- substituents' effects on the photophysical properties of complex **9** relatively complicated and hence difficult to conclusively compare with complexes **5** and **6**. However, the fluorescence properties of complex **9** ( $\Phi_F = 0.15$ ;  $\tau_F = 2.79$  ns) are relatively comparable to those of complex **3** ( $\Phi_F = 0.16$ ;  $\tau_F = 3.14$  ns) which suggests that the opposing resonance donor and inductive acceptor properties together with the heavy atom effect of the chloro- substituents, may relatively cancel each other out.

Comparison of the  $\Phi_F$  and  $\tau_F$  for complexes **2**, **3** and **4a** to elucidate the effects of the number of substituents does not give a simple trend and this is attributed to the simultaneous effects of other intrinsic factors such as the symmetry of the complexes. On the other hand, higher fluorescence values for complex **4a** ( $\Phi_F = 0.27$ ;  $\tau_F = 2.89$  ns) with comparison to complex **2** ( $\Phi_F = 0.20$ ;  $\tau_F = 2.80$  ns), suggest that the carboxyphenoxy substituents in complex **4a** generally enhance the fluorescence properties of MPc complexes.

### iii. Effects of symmetry

The symmetry of MPcs has been reported before to play a significant role in the photophysical properties of the complexes [182]. The symmetrical MPcs complexes **2** ( $\Phi_F = 0.20$ ;  $\tau_F = 2.80$  ns) and **4a** ( $\Phi_F = 0.27$ ;  $\tau_F = 2.89$  ns) can be related to the asymmetric molecule complex **3** ( $\Phi_F = 0.16$ ;  $\tau_F = 3.14$  ns). Comparison of the fluorescence properties of the three complexes shows a lower  $\Phi_F$  for the asymmetric complex **3** coupled with the highest  $\tau_F$  amongst the three complexes. As stated above, the carboxyphenoxy substituent enhances the fluorescence properties of MPc complexes compared to the unsubstituted complexes. The observation of the lower  $\Phi_F$  for complex **3** coupled with the highest  $\tau_F$  (especially with comparison to complex **2**), thus suggests that the fluorescence properties of complex **3** are the resultant of the effect of multiple factors with the symmetry factor being dominant especially for  $\Phi_F$  determination.

Investigation of the effect of symmetry using complexes **5**, **6** and **9**, was considered futile (based only on MPcs used in this study) due to the possible overwhelming effect of the majority substituents in the complexes which may obscure the effect of symmetry and rendered the analysis inconclusive, although they all showed lower  $\Phi_F$  and  $\tau_F$  values (**Table 4.1**) than both complex **2** and **4a**.

### iv. Effects of conjugation to nanoparticles

MPc complexes were conjugated to two different types of nanoparticles namely GQDs (conjugated to complexes **2** and **3**) and AgTNPs (conjugated to complexes **4a** and **4b**). Conjugation of MPcs to GQDs generally showed slight enhancement in fluorescence properties of the MPcs coupled with a significant decrease in  $\Phi_F$  and  $\tau_F$

of the GQDs in the conjugates thus suggesting the possibility of Förster resonance energy transfer (FRET) occurring.

On the other hand, conjugation to AgTNPs proved to generally give rise to lower  $\Phi_F$  and  $\tau_F$  attributed to enhancement of ISC to the triplet excited state due to spin orbit coupling induced by the silver nanoparticles [187,188], although there was no change in  $\tau_F$  for **4b**. A lower MPc loading in the AgTNPs conjugates showed the most significant effect on the  $\Phi_F$  and  $\tau_F$ , where **4a**(AgTNPs) (loading of 0.35 mg MPc/ mg conjugate, **Table 3.2**) showed a greater decrease in values than **4b**(AgTNPs) (loading of 0.59 mg MPc/ mg conjugate, **Table 3.2**) with comparison to the values for their corresponding free complexes (**Table 4.1**). Higher loading may also result in aggregation.

### 4.2.3. Förster resonance energy transfer (FRET)

The formation of the photosensitizers **2 $\pi$** (GQDs), **3 $\pi$** (GQDs), **3**(GQDs) and complex **10** involved the conjugation of MPcs to fluorescent materials and hence the potential occurrence of Förster resonance energy transfer (FRET) processes [167,171]. **Fig. 4.3** shows the UV-Vis absorption spectra for complexes **2** and **3** (as examples for the GQDs conjugates), and complex **9** together with the emission spectral for GQDs and complex **8** respectively, where the shaded areas represent the spectral overlaps. The observed spectral overlaps confirm the possibility of FRET processes [167,171]. The emission spectrum for complex **10** when excited where only the porphyrin absorbs (**Fig. 4.3 (C)**) confirms the energy transfer between the components of the complex, where the emission of the MPc is observed at the expense of the significantly reduced porphyrin emission.

**Table 4.2** presents the obtained FRET parameter values for **2** $\pi$ (GQDs), **3** $\pi$ (GQDs), **3**(GQDs) and complex **10**. The Förster overlap integral ( $J$ ) values support the observed spectral overlaps (complex **2** (**Fig. 4.3 (A)**) has higher overlap than complex **3** (**Fig. 4.3 (B)**)) while the observed Förster distance ( $R_0$ ) and donor–acceptor distance ( $r$ ) values all lie within the 10-100 Å necessary for the possibility of FRET processes [171]. The FRET efficiency ( $Eff$ ) values also supports occurrence of efficient FRET processes. The high  $Eff$  values for the GQDs conjugates despite the less convincing spectral overlaps (**Fig. 4.3 (A)** and **(B)**), can partially be attributed to the relatively high MPc loading values in these conjugates where many MPc molecules accept energy from the same GQDs particle. Since all  $r$  values obtained are greater than 10 Å, Dexter energy transfer (charge transfer) processes may be considered as a less convincing explanation for the quenching of donor fluorescence in these photosensitizers, but instead other non-radiative processes such as internal conversion and changes in surface defects [189], possibly play a significant role in the donor's excited state deactivation and fluorescence quenching.

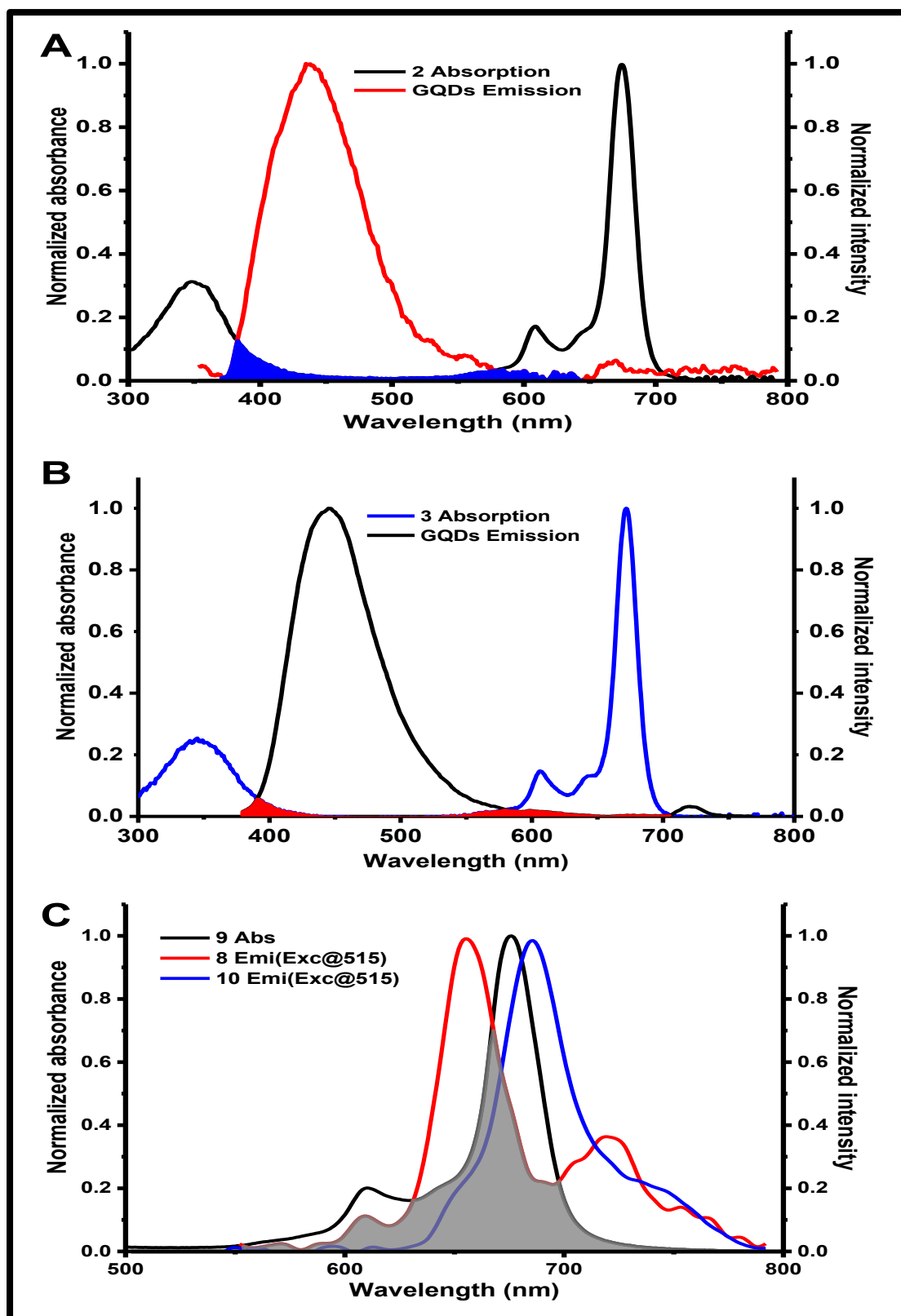


**Fig. 4.3:** UV-Vis spectrum for (A) complex **2** and (B) complex **3**, and fluorescence emission spectrum for corresponding GQDs in DMSO (C) UV-Vis spectrum for complex **9** and fluorescence emission spectrum for complexes **8** and **10** in DMSO.

**Table 4.2:** Summary of FRET parameters for MPc(GQDs) nanoconjugates and complex **10**.

Sample	$J$ (cm <sup>6</sup> )	$R_0$ (Å)	$r$ (Å)	Eff (%)
<b>2<math>\pi</math>(GQDs)</b>	$1.7 \times 10^{-14}$	27.6	16.9	95
<b>3<math>\pi</math>(GQDs)</b>	$1.1 \times 10^{-14}$	24.4	20.3	75
<b>3(GQDs)</b>	$1.1 \times 10^{-14}$	24.4	17.5	88
<b>10</b>	$2.1 \times 10^{-14}$	19.3	15.4	79

### 4.3. Triplet quantum yields ( $\Phi_T$ ) and lifetimes ( $\tau_T$ )

**Fig. 4.4** shows the transient triplet-triplet absorption curve (A) and the corresponding triplet absorption decay curve (B) for complex **9** as a representative for all synthesized complexes. The positive region of the transient absorption spectrum between 384 and 597 nm in **Fig. 4.4 (A)** is attributed to the excited triplet-triplet state absorption ( $T_1 \rightarrow T_n$ ), while the negative regions (323 - 384 nm, and 597 - 707 nm) are attributed to the depletion/ photobleaching of the MPc ground state [190].

The triplet absorption decay curves for all synthesized complexes and soluble conjugates followed second order kinetics which is typical of MPcs at high concentration ( $> 1.0 \times 10^{-5}$  M) due to triplet-triplet recombination [191]. The triplet

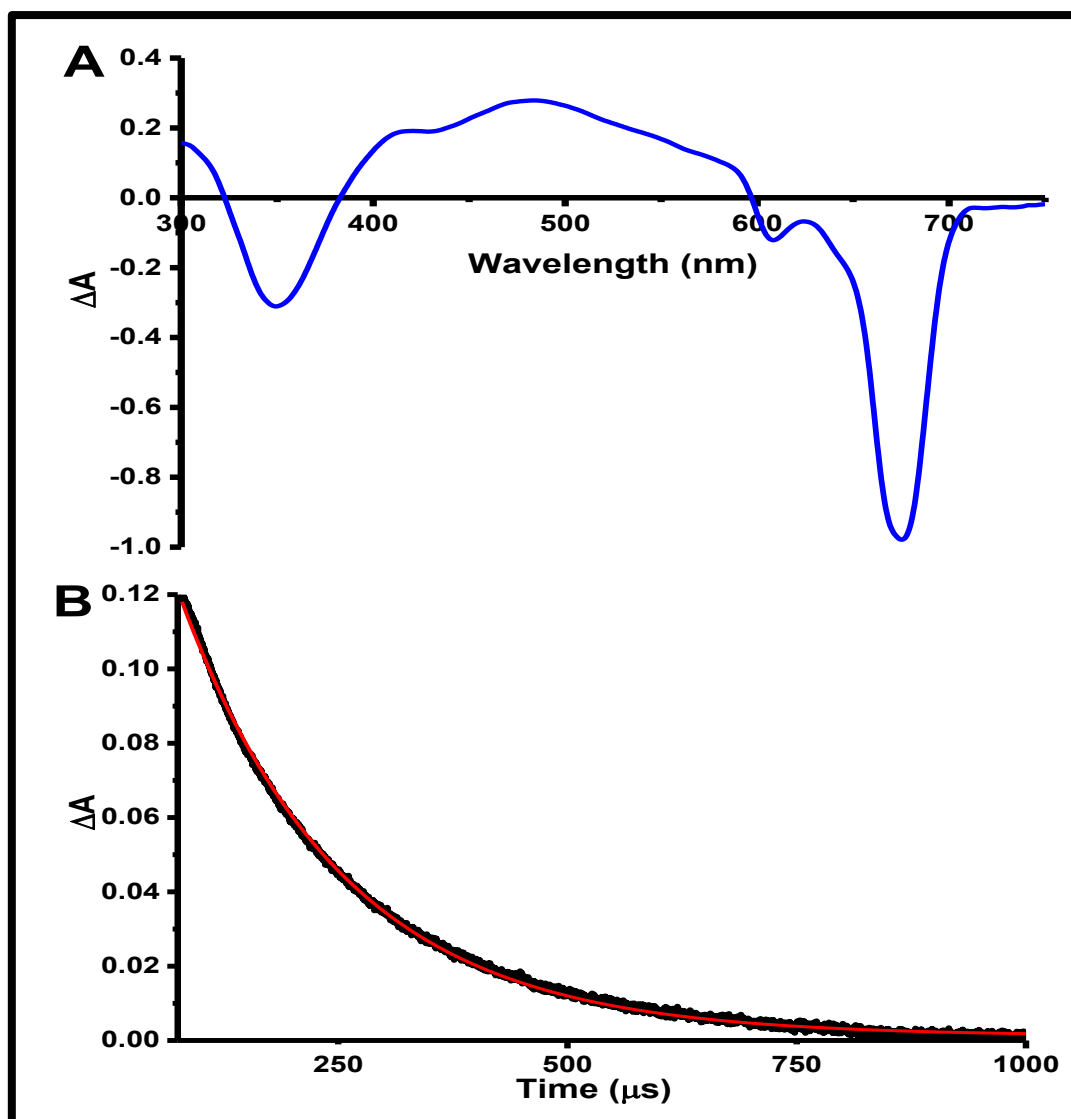


**Fig. 4.4:** (A) Transient curve and (B) Triplet absorption decay curve (black) and fitting (red) for complex **9** in DMSO.

quantum yields ( $\Phi_T$ ) for the complexes and conjugates were determined from the triplet decay curves using a comparative method with reference to a standard, while the triplet lifetimes ( $\tau_T$ ) were obtained from fitting the decay curves at the absorption maximum. **Table 4.3** summarizes the triplet quantum yields and lifetimes for the synthesized complexes and nanoconjugates.



Since fluorescence and ISC to the triplet excited state are competing processes, the previously mentioned intrinsic factors governing the fluorescence properties of MPcs are hence mostly complementarily the determinants for the triplet properties. These intrinsic factors are therefore used here to discuss the triplet properties of the synthesized complexes and nanoconjugates.

### i. Effects of central metal

As previously mentioned, metalation of Pcs with heavier metals such as indium with comparison to zinc enhances ISC to the triplet excited state [95]. This consequently results in higher  $\Phi_T$  as was observed for complex **4b** ( $\Phi_T = 0.70$ ) with comparison to complex **4a** ( $\Phi_T = 0.61$ ), which corresponds to the lower  $\Phi_F$  for complex **4b** since fluorescence and ISC are competing processes. On the other hand, the triplet lifetime for complex **4b** was shorter than that for complex **4a**, as was to be expected [192].

### ii. Effects of substituents

$\Phi_T$  and  $\tau_T$  for complexes **1** ( $\Phi_T = 0.72$ ;  $\tau_T = 52 \mu\text{s}$ ) and **4b** ( $\Phi_T = 0.70$ ;  $\tau_T = 86 \mu\text{s}$ ) show relatively similar values. For the asymmetric complexes **5** and **6**, both  $\Phi_T$  and  $\tau_T$  increased upon quaternization of complex **5** ( $\Phi_T = 0.65$ ;  $\tau_T = 145 \mu\text{s}$ ) to form complex **6** ( $\Phi_T = 0.82$ ;  $\tau_T = 359 \mu\text{s}$ ). Since fluorescence and ISC to the triplet state are competing processes, the observation of a similar trend (an increase) in both  $\Phi_F$  and  $\Phi_T$  from complex **5** to **6** suggests that the lower fluorescence and triplet properties for complex **5** are due to non-radiative processes deactivating the first singlet excited state ( $S_1$ ). The non-radiative deactivation of  $S_1$  is possibly associated with charge transfer processes which are eliminated (disappearance of charge transfer band in spectrum of complex **6** (**Fig. 3.4**)) by the change in electron-donor/ acceptor properties of the complex's substituents upon quaternization. It is interesting to note that, based

on the values for complexes **5** and **6**, fluorescence and triplet properties of MPcs based on the MPc substituents, are not necessarily complementary although fluorescence and triplet are competing processes. For complex **9** ( $\Phi_T = 0.56$ ;  $\tau_T = 218 \mu s$ ), the observed  $\Phi_T$  with reference to the  $\Phi_F$  ( $\Phi_F = 0.15$ ) suggests that there is significant non-radiative deactivation of  $S_1$  (high internal conversion quantum yield ( $\Phi_{IC} = 0.29$ , Eqn (4.13)), thus for the previously mentioned opposing resonance donor and inductive acceptor properties together with the heavy atom effect of the chloro-substituents, the resonance donor effect is possibly dominant.

$$\Phi_{IC} = 1 - (\Phi_F + \Phi_T) \quad (4.13)$$

Comparison of complexes **2** ( $\Phi_T = 0.65$ ;  $\tau_T = 350 \mu s$ ), **3** ( $\Phi_T = 0.70$ ;  $\tau_T = 318 \mu s$ ) and **4a** ( $\Phi_T = 0.61$ ;  $\tau_T = 319 \mu s$ ) to elucidate the effects of the number of substituents shows that the triplet properties of the complexes exhibit a trend that is complimentary to their fluorescence properties (for complex **2**  $\Phi_F = 0.20$ , complex **3**  $\Phi_F = 0.16$ ). Comparison of  $\Phi_T$  for complexes **2** and **4a** confirms the effect of the carboxyphenoxy substituents as fluorescence enhancers at the expense of ISC to the triplet state.

### iii. Effects of symmetry

The greater  $\Phi_T$  value and shorter  $\tau_T$  for complex **3** with comparison to complexes **2** and **4a** suggests that the effect of asymmetry in the complex is a dominant factor. The observed  $\Phi_T$  and  $\tau_T$  values of these three MPc complexes are consistent with the literature which suggests that asymmetric MPcs exhibit better triplet state properties than their corresponding symmetrical analogues [193].

#### iv. Effects of conjugation to nanoparticles

Conjugation of MPcs to nanoparticles resulted in notable changes in the triplet quantum yields and lifetimes depending on the nature and type of nanoparticles. Conjugation to GQDs generally lowered the MPc triplet quantum yields, with the mode of conjugation and loading of MPcs on to the GQDs playing pivotal roles (**Table 4.3**). Compared to complex **2** ( $\Phi_T = 0.65$ ), **2** $\pi$ (GQDs) ( $\Phi_T = 0.57$ ) exhibited reduction in  $\Phi_T$ . No change was observed for **3** $\pi$ (GQDs) ( $\Phi_T = 0.70$ ) compared to complex **3** ( $\Phi_T = 0.70$ ). This difference in triplet generation efficiency may be attributed to the difference in MPc loading, where high loading which may also constitute some MPc aggregates, appears to lower the efficiency. On the other hand, the significantly lower  $\Phi_T$  for **3**(GQDs) ( $\Phi_T = 0.49$ ) compared to **3** $\pi$ (GQDs) ( $\Phi_T = 0.70$ ), despite a lower loading suggests that the mode of conjugation is a superior determination factor. The lower  $\Phi_T$  for **3**(GQDs) may be attributed to intramolecular rotations of complex **3** in the conjugate as a result of the relative rotational flexibility [194–197], when compared to **3** $\pi$ (GQDs). For complexes **2** and **3**,  $\tau_T$  became shorter following conjugation to GQDs (**Table 4.3**).

Conjugation to AgTNPs on the other hand, enhanced the  $\Phi_T$  of both **4a** and **4b** in the conjugates (**Table 4.3**). The enhancement is attributed to the heavy atom effect of silver atoms [187,188] previously mentioned. The  $\tau_T$  also correspondingly became shorter (**Table 4.3**) following conjugate formation. The changes in both  $\Phi_T$  and  $\tau_T$  were greatest in **4a**(AgTNPs) (loading = 0.35 mg MPc/ mg MPc(AgTNPs)) which may be attributed to a lower MPc loading in the conjugate with comparison to **4b**(AgTNPs) (loading = 0.59 mg MPc/ mg MPc(AgTNPs)).

#### 4.4. Singlet oxygen quantum yields ( $\Phi_{\Delta}$ )

The potential of a complex as a good photosensitizer for application in polymer membrane functionalization depends on its ability to generate singlet oxygen, which is quantified by its singlet oxygen quantum yield ( $\Phi_{\Delta}$ ). As mentioned earlier in this thesis, singlet oxygen generation is dependent on the efficiency of generation of the excited triplet state and subsequent energy transfer to ground-state molecular oxygen [54]. **Table 4.3** thus summarizes the  $\Phi_{\Delta}$  values of all complexes and their conjugates used in this study, together with the values of the corresponding functionalized polymer membranes with reference to the  $\Phi_T$  of the photosensitizers. The efficiency of energy transfer from the triplet excited state to molecular oxygen ( $S_{\Delta}$ , Eqn (4.14)) is also presented in the table.

$$S_{\Delta} = \frac{\Phi_{\Delta}}{\Phi_T} \quad (4.14)$$

##### 4.4.1. Singlet oxygen quantum yields in solution

Singlet oxygen quantum yield values in solution were determined in DMSO to allow for direct relation of values to those for  $\Phi_F$  and  $\Phi_T$ , and better understanding of the dissipation of excitation energy. In this study singlet oxygen quantum yields were determined using the photochemical method and **Fig. 4.5** shows the degradation profiles for DPBF and DMA (singlet oxygen quenchers) for complexes **4b** and **10** respectively, as representatives for all synthesized complexes. In all degradation profiles, the photosensitizer absorption bands did not change while those of the quenchers decreased as shown in **Fig. 4.5**. This thus suggests that all the photosensitizers used were stable under the irradiation conditions.

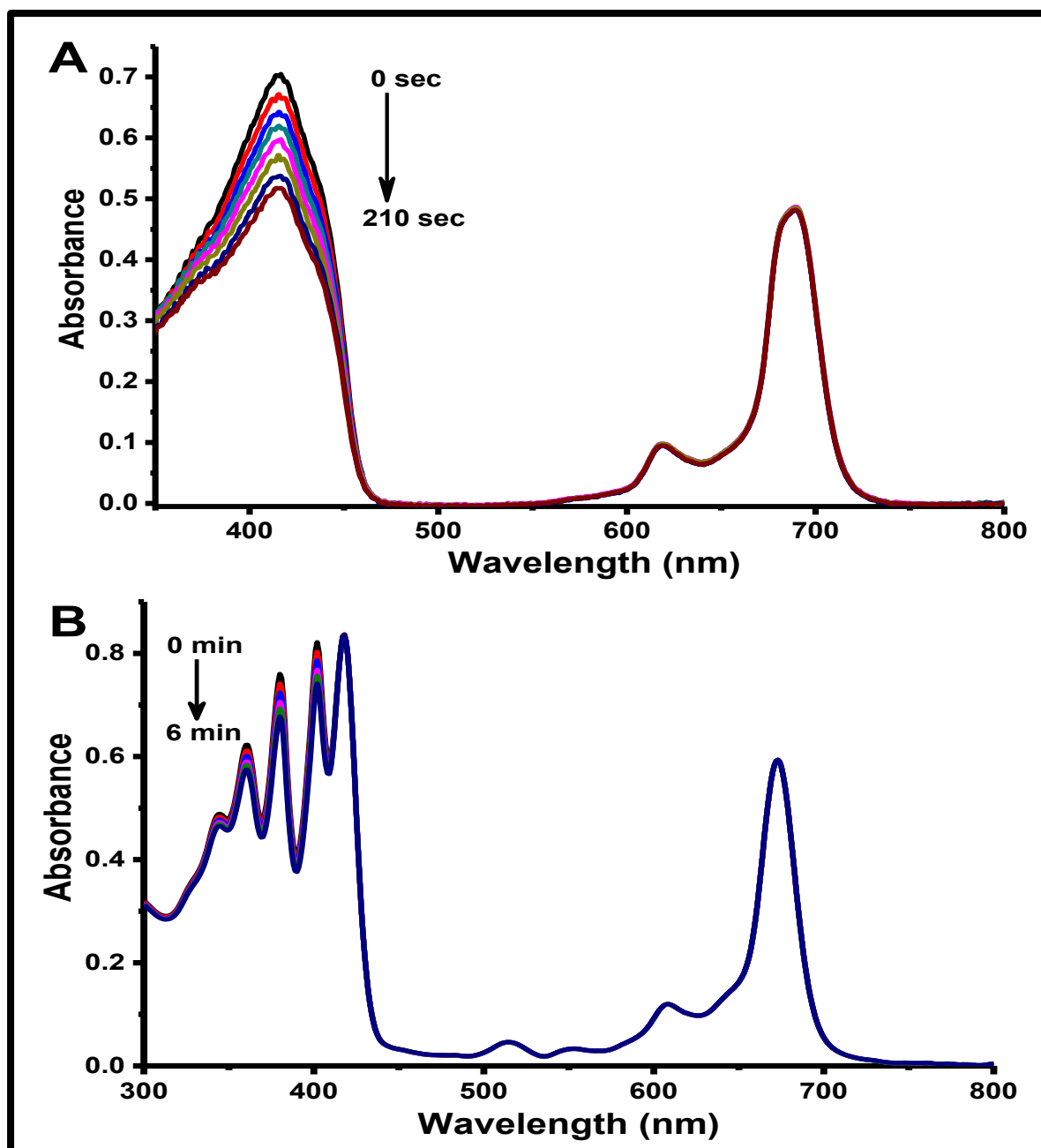


**Fig. 4.5:** (A) DPBF degradation profile by complex **4b** and (B) DMA degradation profile by complex **10** in DMSO.

All  $\Phi_{\Delta}$  values for the photosensitizers followed the same trends as those for  $\Phi_T$ , with the exception of the MPc(GQDs) conjugates **Table 4.3**. This deviation from the trend is observed in the values for complex **3**, **3 $\pi$ (GQDs)** and **3(GQDs)**, where despite **3**

and **3** $\pi$ (GQDs) having the same  $\Phi_T$ , there is a decrease in the  $\Phi_\Delta$  upon conjugate formation. Furthermore, despite **3**(GQDs) having a lower  $\Phi_T$  value than **3** $\pi$ (GQDs), it has a greater ability to generate singlet oxygen. These observations are attributed to the screening effect in **3** $\pi$ (GQDs) which restricts the conjugated complex **3**'s access to molecular oxygen, hence the reduction in singlet oxygen generation efficiency [198].

Conjugation to AgTNPs in **4a**(AgTNPs) and **4b**(AgTNPs) improves singlet oxygen generation ( $\Phi_\Delta$ ) of the corresponding MPc complexes **Table 4.3**. Also, important to note is the improved energy transfer efficiency ( $S_\Delta$ ) in complex **4b** with comparison to **4a** attributed to the indium metal centre in place of zinc; and complex **4b** with comparison to **1**, and complex **6** with comparison to **5**, both attributed to electron withdrawing substituents ( $-\text{COOH}$  and the  $[-\text{N}(\text{CH}_3)_3]^+$  groups) compared to electron donating substituents ( $-\text{NH}_2$  and  $-\text{N}(\text{CH}_3)_2$  groups). An attempt to determine the  $\Phi_\Delta$  for complexes **4a** and **4b** in 2 % DMSO in PBS solution (solvent used in PACT studies) was not successful since only complex **4a** ( $\Phi_\Delta = 0.04$ ) was stable when irradiated. However, the MPc(AgTNPs) conjugates were stable and their values followed the same trend of their values in DMSO (**Table 4.3**).

**Table 4.3:** Triplet quantum yield and lifetime, and singlet oxygen quantum yields of the MPcs and respective nanoconjugates in DMSO unless specified.

Sample	$\Phi_T (\pm 0.03)$	$\tau_T (\mu s) (\pm 15)$	$\Phi_\Delta (\pm 0.03)$	$S_\Delta$
<b>1</b>	0.72 [96]	52 [96]	0.43	0.60
<b>2</b>	0.65 [176]	350 [176]	0.67 [174]	1.03
<b>2<math>\pi</math>(GQDs)</b> (0.67)	0.57	292	0.49	0.86
<b>3</b>	0.70	318	0.56 [186]	0.80
<b>3<math>\pi</math>(GQDs)</b> (0.40)	0.70	299	0.33	0.47
<b>3(GQDs)</b> (0.14)	0.49	289	0.44	0.90
<b>4a</b>	0.61 [58]	319 [58]	0.32 [58] 0.04 <sup>a</sup>	0.52
<b>4a(AgTNPs)</b> (0.35)	0.68	277	0.41 0.12 <sup>a</sup>	0.60
<b>4b</b>	0.70	86	0.46 -	0.66
<b>4b(AgTNPs)</b> (0.59)	0.73	78	0.48 0.17 <sup>a</sup>	0.66
<b>5</b>	0.65	145	0.53	0.82

<b>6</b>	0.82	359	0.76	0.93
<b>8</b>	-	-	0.39 <sup>b</sup>	-
<b>9</b>	0.56	218	0.48	0.86
<b>10</b>	-	-	0.67 <sup>b</sup>	-
	0.58	211	0.51	0.88

<sup>a</sup> Values in 2% DMSO in PBS. <sup>b</sup> Values when excited where the only porphyrin absorbs. MPc loading in mg MPc/ mg conjugate are given in round brackets with conjugate name. References are given in square brackets. “-“ Values not determined for reasons given in text.

#### 4.4.2. Singlet oxygen quantum yields of membranes

Determination of the  $\Phi_{\Delta}$  for the functionalized membranes was achieved using an absolute method [173] in batch experimental setups either in aqueous solution or in ethanol. Water and ethanol were used since the ultimate application of the membranes is in aqueous media, and ethanol is an organic solvent that does not damage the membranes. **Fig. 4.6** shows the DPBF and ADMA degradation profiles by  $2\pi(\text{GQDs})\text{-memb}$  as representatives for all the prepared membranes. In the profiles, absence of photosensitizer absorption bands suggests that degradation of the quenchers was due to membrane bound photosensitizers not those in suspension. Also, all functionalized membranes proved to be photostable despite some complexes (**4b**, **5** and **6**) showing signs of degradation in aqueous solution. The  $\Phi_{\Delta}$  values for the membranes with reference to those for their corresponding unbound photosensitizer in DMSO are summarised in **Table 4.4**. For the membranes of complexes **1** and **3**,  $\Phi_{\Delta}$  was



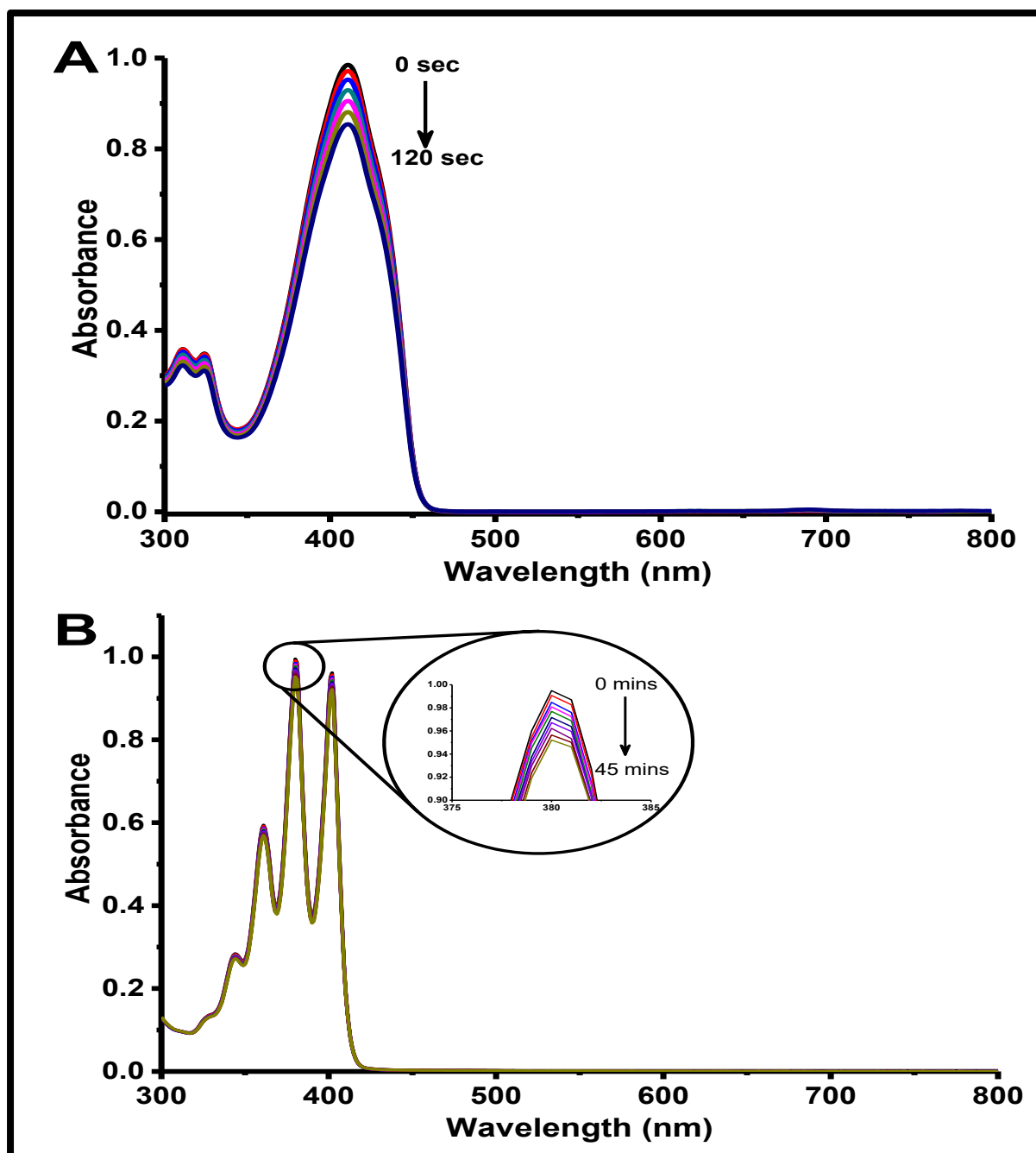


**Fig. 4.6:** (A) DPBF in ethanol and (B) ADMA in water, degradation profiles by  $2\pi(\text{GQDs})\text{-memb.}$

determined as a proof of concept and were only obtained in ethanol, while for the rest values were determined in water as a reference for the aqueous media used in the photodegradation and PACT studies.

**Table 4.4:** Summary of the singlet oxygen quantum yields of the functionalized membranes in water or ethanol with reference to the corresponding photosensitizers in DMSO.

Sample	Photosensitizer $\Phi_{\Delta(\text{DMSO})}$ ( $\pm 0.03$ )	$\Phi_{\Delta(\text{Water})}$ ( $\pm 0.02$ )	$\Phi_{\Delta(\text{Ethanol})}$ ( $\pm 0.03$ )
1-PAN-memb	0.43	-	0.35
1-PS-memb	0.43	-	0.51
2 $\pi$ (GQDs)-memb	0.49	0.37	0.43
3-memb	0.56	-	0.13
3 $\pi$ (GQDs)-memb	0.33	-	0.16
3(GQDs)-memb	0.44	-	0.29
4a-memb	0.32	0.19	0.24
4a(AgTNPs)-memb	0.41	0.30	0.46
4b-memb	0.46	0.06	0.15
4b(AgTNPs)-memb	0.48	0.13	0.30
5-memb	0.53	0.24	-
6-memb	0.76	0.27	-
10-memb	0.67 <sup>a</sup>	0.29 <sup>a</sup>	-
	0.51	0.23	-

“-“ Values not determined for reasons given in text. <sup>a</sup> Values when excited where the only porphyrin absorbs. References are given in square brackets.

$\Phi_{\Delta}$  values for all the membranes in aqueous solution were lower than those of the free photosensitizers in DMSO due to aggregation of MPcs in the solid state and the quenching effects of water [95]. It is important to note that in the experiments, light may be scattered and limitations of batch experiments (explained in chapter 5), together may have resulted in the observed lower  $\Phi_{\Delta}$  values, thus obtained values are estimates. The  $\Phi_{\Delta}$  values observed in ethanol are also lower than for the free photosensitizers despite the difference in solvents. However, no overall general trend in the  $\Phi_{\Delta}$  values can be observed, and this is attributed to the simultaneous variations in the factors that determine the efficiency of the singlet oxygen-quencher (DPBF or ADMA) reaction. These factors include cumulative effects of differences in photosensitizer loading, orientation and extent of aggregation in the different membranes, in addition to the differences in the intrinsic properties of the photosensitizers.

### 4.5. Summary of chapter

The photophysical and photochemical properties of the synthesized complexes and nanoconjugate photosensitizers, and the singlet oxygen generating properties of their corresponding polymer membranes were studied. All the complexes and conjugates exhibited relative properties that were attributed to intrinsic properties of the photosensitizers such as the nature of the central metal, substituents, symmetry and conjugation to nanoparticles.

Heavier central metals (exemplified by indium compared to zinc) as was expected, proved to induce superior singlet oxygen generation as a result of high  $\Phi_T$  due to spin

orbit coupling enhanced intersystem crossing to the triplet excited state at the expense of fluorescence. Asymmetry in the MPc complexes gave rise to higher  $\Phi_T$  and  $\Phi_\Delta$  also at the expense of fluorescence properties. Complexes with electron withdrawing substituents exhibited higher quantum yields ( $\Phi_F$ ,  $\Phi_T$  and  $\Phi_\Delta$ ) especially where the electron withdrawing groups are directly linked to the MPc macrocycle as exemplified by comparison complex **5** and its quaternized derivative complex **6**.

Conjugation of MPc complexes to GQDs slightly enhanced either the  $\Phi_F$  or the  $\tau_F$ . On the other hand, the  $\Phi_T$  and  $\Phi_\Delta$  values proved to be significantly affected by the means of conjugation, where  $\pi$ – $\pi$  stacking results in lower  $S_\Delta$  values due to significantly lowered  $\Phi_\Delta$  as a result of the screening effect. Conjugation of MPc complexes to AgTNPs lowered the  $\Phi_F$  of the conjugates, while  $\Phi_T$ ,  $\Phi_\Delta$  and  $S_\Delta$  increased. Although no specific trend in membrane  $\Phi_\Delta$  values could be identified, all photosensitizer-functionalized polymer membranes proved to be photoactive and photostable with potential for application in photocatalytic degradation of pollutants in water and PACT.

# CHAPTER 5

## 5. Photodegradation and Photodynamic Antimicrobial Chemotherapy (PACT)

In this section of the thesis, the potential application of phthalocyanine functionalized polymer membrane technology towards minimizing biological fouling and photocatalytic degradation of organic pollutants in water is investigated. Since the objective of this section is concept evaluation, only polystyrene polymer membranes, *S.aureus* (model microorganisms) and 4-CP (model organic pollutant) were used, but concepts are potentially applicable with other polymers, microorganisms and organic pollutants. Motivation for the specific choices of model microorganism and organic pollutant have been given in chapter 1 of this thesis.

### 5.1. Photocatalytic degradation of 4-chlorophenol (4-CP)

In this application, two functionalized polymer membranes ( $2\pi$ (GQDs)-memb and **10**-memb) were employed. Using  $2\pi$ (GQDs)-memb, the potential practical application of functional group deficient phthalocyanines in functionalized polymer membranes is assessed, while **10**-memb was used to assess the potential application of porphyrin-phthalocyanine heterodyad functionalized polymer membranes in efficient solar radiation driven photocatalytic reactions. The 4-CP degradation kinetic parameters for each membrane are also discussed. The photocatalytic studies using the membranes were carried out using batch experiments hence the obtained values are estimates due to unavoidable kinetic limitations associated with application of the membranes in batch processes.

#### 5.1.1. UV-Vis spectral studies

Photodegradation of 4-CP by Pc-based catalysts has been reported before [199–201]. In the reported studies experiments were carried out in pH 11 buffer to optimise singlet

oxygen oxidation of the 4-CP. In this work pH 11 buffer (with  $2\pi(\text{GQDs})\text{-memb}$ ) and deionized water (with **10**-memb) were used, where deionized water was used as a relatively neutral media to avoid environment based enhanced activity of the catalyst. The 4-CP characteristic bands under pH 11 conditions were observed at 244 and 298 nm, while under neutral conditions the bands were observed at 225 nm and 280 nm as has been reported before [79,202]. **Fig. 5.1** shows the UV-Vis spectra degradation profile for 4-CP by **10**-memb under neutral conditions as an example and similar spectra were also observed with  $2\pi(\text{GQDs})\text{-memb}$  at pH 11, but spectral bands were red shifted in the latter.

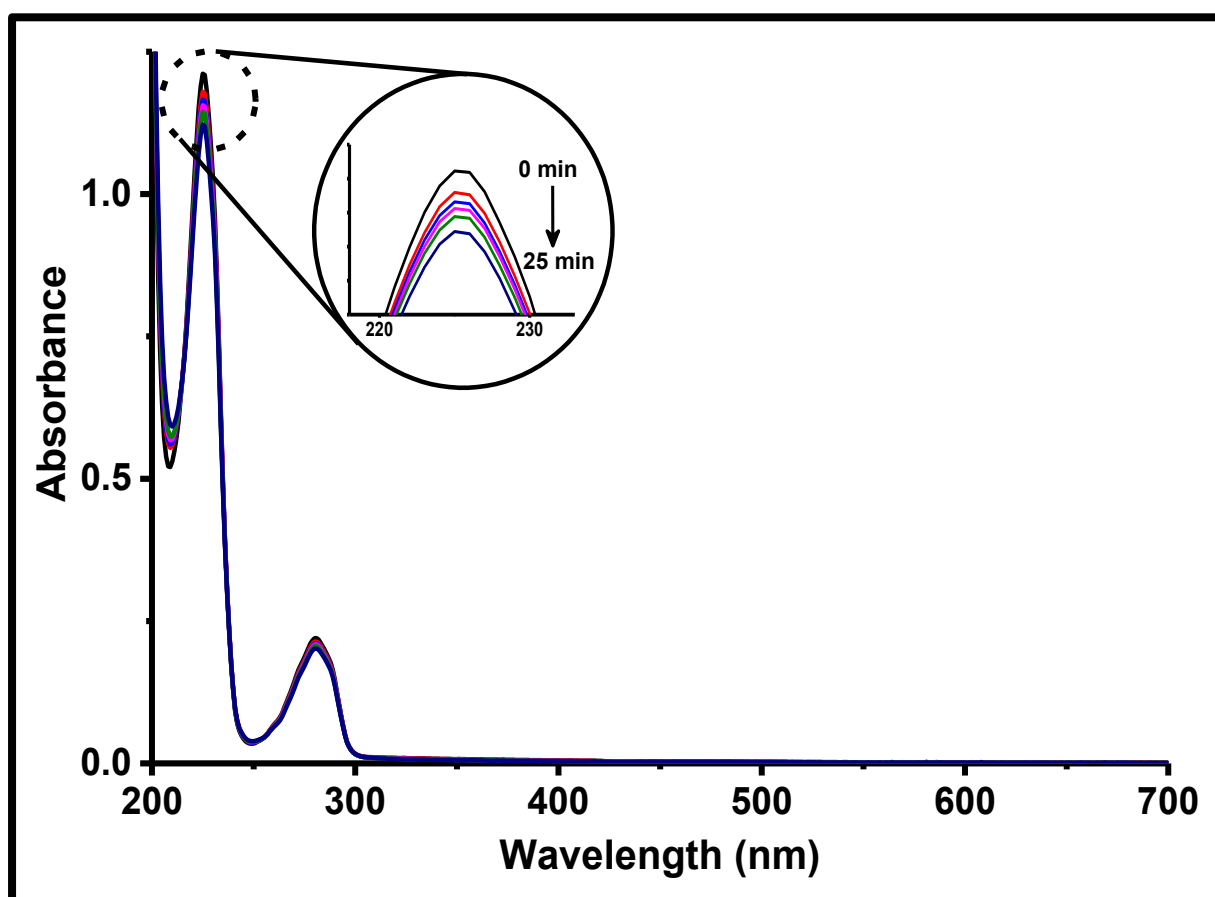


**Fig. 5.1:** Degradation profile of 4-CP ( $1.02 \times 10^{-5} \text{ molL}^{-1}$ ) by **10**-memb under 515 nm laser irradiation in neutral water.

Relatively short irradiation periods (5 min for **10**-memb and 1 min for **2 $\pi$** (GQDs)-memb) in comparison to some previously reported in literature [66,201,203] were targeted to limit possible experimental error that may be associated with batch experiments when using a bulk heterogenous catalyst. Slow changes in the UV-Vis spectra (**Fig. 5.1**) were observed during light irradiation for both **2 $\pi$** (GQDs)-memb and **10**-memb, especially for **10**-memb which is consistent with the reported limited degradation rates for 4-CP under neutral to low pH conditions [199,200]. The mechanism of 4-CP degradation using MPc-based catalysts has been studied before where the degradation products of the reaction were identified as hydroquinone (from type I oxidation mechanisms) and benzoquinone (from type II oxidation mechanisms) [79,201], hence in this work such studies were not explored. Benzoquinone with absorption at 244 nm in water [204], was observed as the main product thus the singlet oxygen dependant type II mechanism is the main degradation pathway. Due to the limited irradiation periods and slow UV-Vis spectral changes, the phototransformation of 4-CP to hydroquinone (absorption at 222 and 296 nm [204]) and benzoquinone is not distinctly observed in **Fig. 5.1**.

The relative stability of the functionalized membranes was also briefly accessed using solid-state UV-Vis spectroscopy and SEM shown in **Fig. 5.2** for **2 $\pi$** (GQDs)-memb as an example. The solid-state UV-Vis spectra before and after photocatalysis experiments (**Fig. 5.2 (A)**) show no significant differences which suggests that the photosensitizer was stable during irradiation. SEM micrograms of the top surface (irradiated surface) and the edge view of the skin before and after application of the membrane in photocatalysis experiments (**Fig. 5.2 (B)**) shows no visible change in the membrane structure thus experimental conditions especially light irradiation, had no



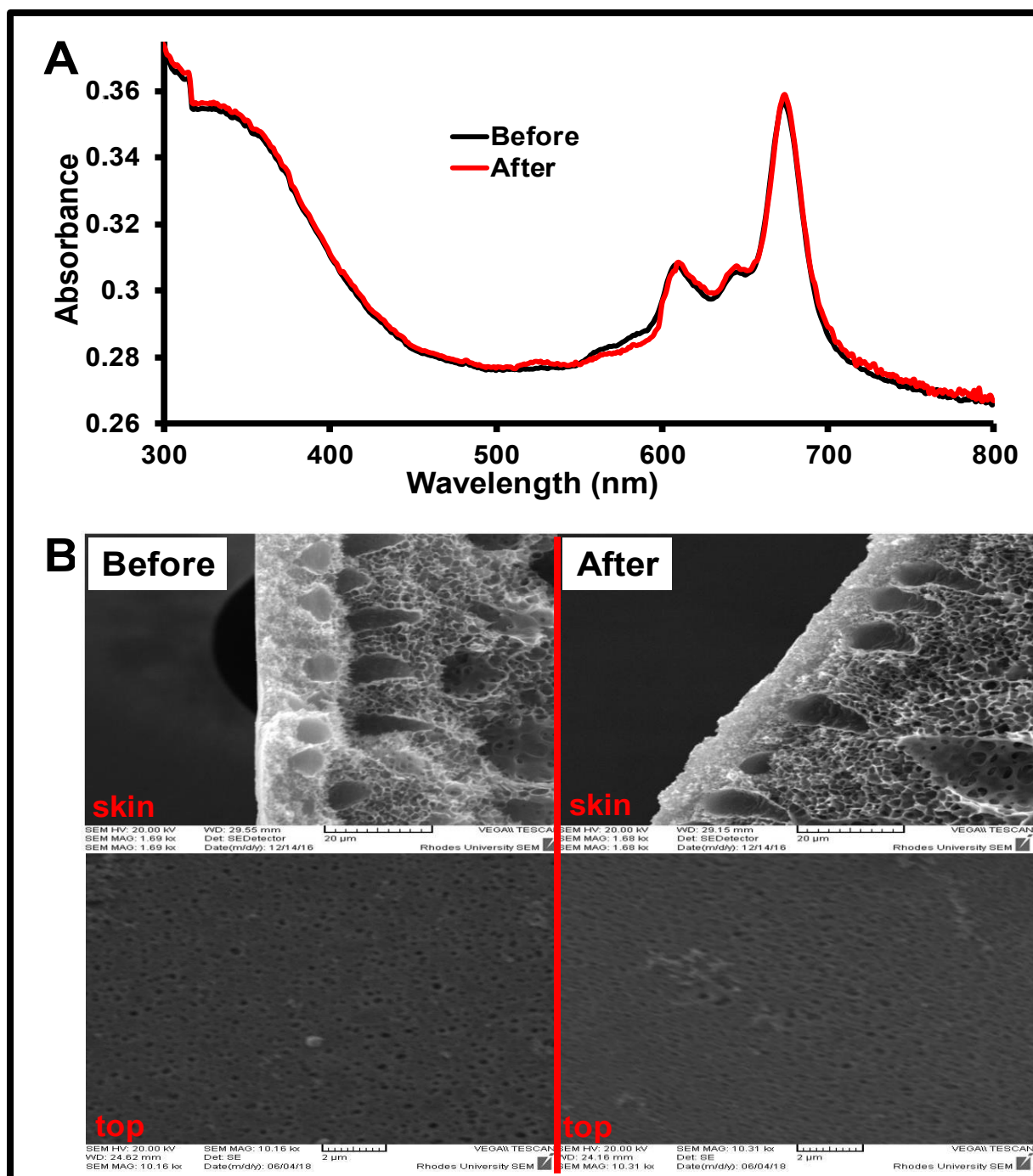


**Fig. 5.2:** (A) Solid state UV-Vis spectra and (B) SEM (skin and top) micrographs of  $2\pi(\text{GQDs})\text{-memb}$  before and after use in photocatalysis experiments.

physical effect on the membranes. Similar observations were also observed for **10-memb** after photocatalysis experiments. The stability of the membranes suggests the possibility of reuse.

### 5.1.2. Kinetics of 4-chlorophenol photooxidative degradation

The reaction kinetics of 4-CP photocatalytic degradation by **10**-memb were studied at the two complementary absorption wavelengths used to study the photophysical parameters (515 and 690 nm). On the other hand, for **2 $\pi$** (GQDs)-memb studies were carried out under 680 nm light irradiation. Relatively high 4-CP concentrations (high UV-Vis absorbances) were used to minimize the effects of membrane confinement, hence obtained values are relative estimates. Data obtained from the experiments was fitted into the first and second order kinetic models. For **2 $\pi$** (GQDs)-memb data gave best fitting for second order kinetics, while **10**-memb gave best fitting for the pseudo-first order kinetic model at both studied wavelengths, based on regression analysis. **Fig. 5.3** shows the kinetic plots for the photocatalytic degradation of 4-CP by **2 $\pi$** (GQDs)-memb (second order) and **10**-memb (pseudo-first order for 515 nm data as an example) for the concentrations studied. Both first and second order kinetics are known for heterogenous photocatalysis reaction systems [205–209]. **Table 5.1** summarizes the second order kinetic parameters for **2 $\pi$** (GQDs)-memb, while **Table 5.2** summarizes the pseudo-first order kinetic parameters for **10**-memb from the kinetic study experiments. For both **2 $\pi$** (GQDs)-memb and **10**-memb (at both studied wavelengths for the latter), similar trends in kinetic model parameters were observed where the rate constants ( $k_{obs}$ ) and initial rates ( $r_0$ ) were directly proportional to the initial 4-CP concentration while the half-lives ( $t_{1/2}$ ) were inversely proportional.

For **10**-memb, the observed trends in variations in pseudo-first order half-life and rate constant values with initial concentration contradict the trends observed by other researchers in photocatalytic degradation studies [22,57,58,210,211]. These contradictions were attributed to the bulk state of the photocatalyst (**10**-memb) where

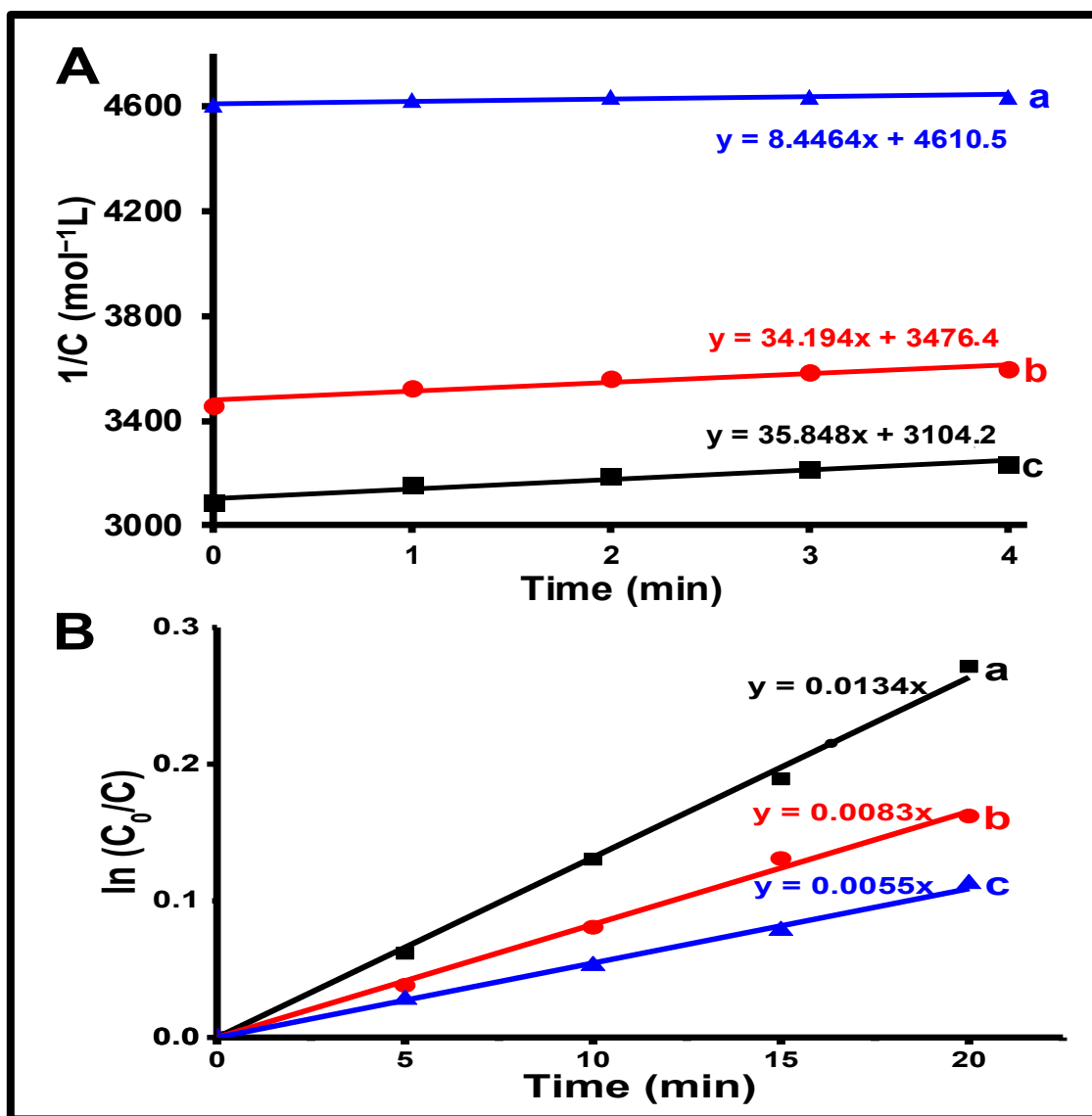


**Fig. 5.3:** Kinetic plots for the photocatalytic degradation of 4-CP, (A) second order at (a)  $2.17 \times 10^{-4} \text{ molL}^{-1}$ , (b)  $2.89 \times 10^{-4} \text{ molL}^{-1}$  and (c)  $3.24 \times 10^{-4} \text{ molL}^{-1}$  by  $2\pi(\text{GQDs})\text{-memb}$ , and (B) pseudo-first order at (a)  $1.02 \times 10^{-4} \text{ molL}^{-1}$ , (b)  $6.74 \times 10^{-5} \text{ molL}^{-1}$  and (c)  $3.10 \times 10^{-5} \text{ molL}^{-1}$  by **10-memb** under 515 nm light irradiation.

the photocatalysts in reported studies were in powder or granular form. Divided catalysts (powders and granules) can be well dispersed in the reaction solution during experiments and can mix together with the target for degradation, thus maintaining the reaction mixture homogeneity and diffusion distances at a minimum.

**Table 5.1:** Second order kinetic parameters for the degradation of 4-CP by 2 $\pi$ (GQDs)-memb at the various initial concentrations studied.

[4-CP] <sub>0</sub> (molL <sup>-1</sup> )	<i>k</i> <sub>obs</sub> (Lmol <sup>-1</sup> min <sup>-1</sup> ) (± 2.1)	<i>r</i> <sub>0</sub> (molL <sup>-1</sup> min <sup>-1</sup> ) (± 1.22 × 10 <sup>-7</sup> )	<i>t</i> <sub>1/2</sub> (min) (± 7)
3.24 × 10 <sup>-4</sup>	35.8	3.77 × 10 <sup>-6</sup>	86
2.89 × 10 <sup>-4</sup>	34.2	2.86 × 10 <sup>-6</sup>	101
2.17 × 10 <sup>-4</sup>	8.45	3.99 × 10 <sup>-7</sup>	545

**Table 5.2:** Pseudo-first order kinetic parameters for the degradation of 4-CP by 10-memb at the various initial concentrations studied.

Irradiation wavelength (nm)	[4-CP] <sub>0</sub> (molL <sup>-1</sup> )	<i>k</i> <sub>obs</sub> (min <sup>-1</sup> ) (± 0.0004)	<i>r</i> <sub>0</sub> (molL <sup>-1</sup> min <sup>-1</sup> ) (± 9.20 × 10 <sup>-8</sup> )	<i>t</i> <sub>1/2</sub> (min) (± 4)
515	1.02 × 10 <sup>-4</sup>	0.0134	1.36 × 10 <sup>-6</sup>	52
	6.74 × 10 <sup>-5</sup>	0.0083	5.59 × 10 <sup>-7</sup>	84
	3.10 × 10 <sup>-5</sup>	0.0055	1.70 × 10 <sup>-7</sup>	126
690	1.02 × 10 <sup>-4</sup>	0.0073	7.43 × 10 <sup>-7</sup>	95
	6.74 × 10 <sup>-5</sup>	0.0047	3.17 × 10 <sup>-7</sup>	147
	3,10 × 10 <sup>-5</sup>	0.0036	1.12 × 10 <sup>-7</sup>	193

However, in batch experiments with bulk catalysts such as in the work in this thesis, only the degradation target is capable of diffusion and hence an overall solution concentration gradient is established and maintained during light irradiation as shown in **Fig. 5.4**. In such a setup, low concentrations of the degradation target mean longer

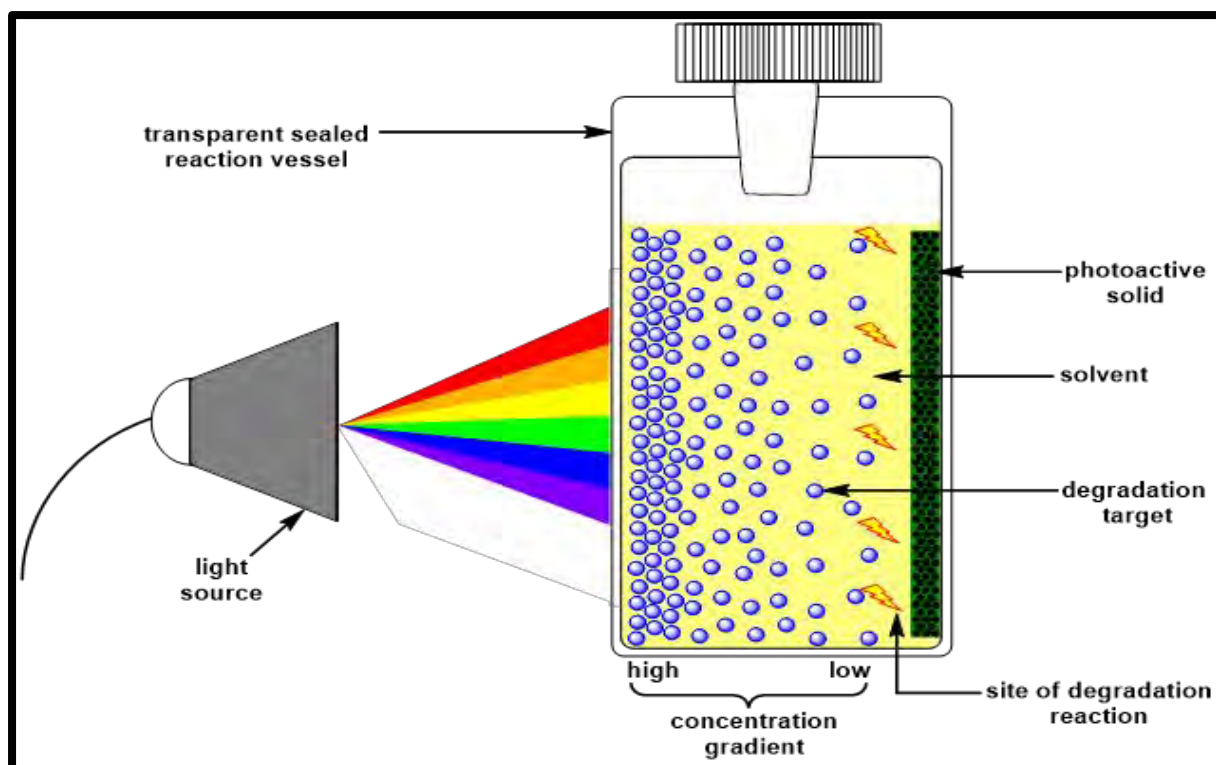


**Fig. 5.4:** Schematic illustration of solution concentration gradient formation in membrane photocatalyzed batch experiments.

diffusion distances and slower rate of reactive specie-target interaction resulting in lower effective usage of generated reactive oxygen species due to their short lifetime and general quenching by water [54]. On the other hand, with higher concentrations diffusion distances are shorter and the established concentration gradient is steeper which favours faster diffusion hence the observed trends in this work.

It is also important at this point to note that, since the degradation experiments in this work were dependent on rate and efficiency of diffusion of 4-CP, the studies were temperature sensitive hence this was maintained by conducting all the experiments in an air-conditioned room set at 20°C. With dispersed catalyst systems such as those in literature mentioned above, the low degradation target concentration simply means less to be degraded with virtually no significant change in diffusion distances for

effective reactive species-target interactions. This thus results in increasingly shorter periods required to degrade the target using the same amount of catalyst as the initial target concentration is decreased, hence the rate constant and half-life trends observed in the references above.

### 5.1.3. Light harvesting studies of 10-memb

Light harvesting studies were carried out by separately irradiating **10**-memb with light ranges of the same intensity from different regions of the electromagnetic spectrum, in the presence of 4-CP. **Fig. 5.5** shows the UV-Vis spectrum for complex **10** with reference to the UV-Vis spectra of its components (complexes **8** and **9**) and the transmittance spectra of the light filters used. The three filters essentially divided the

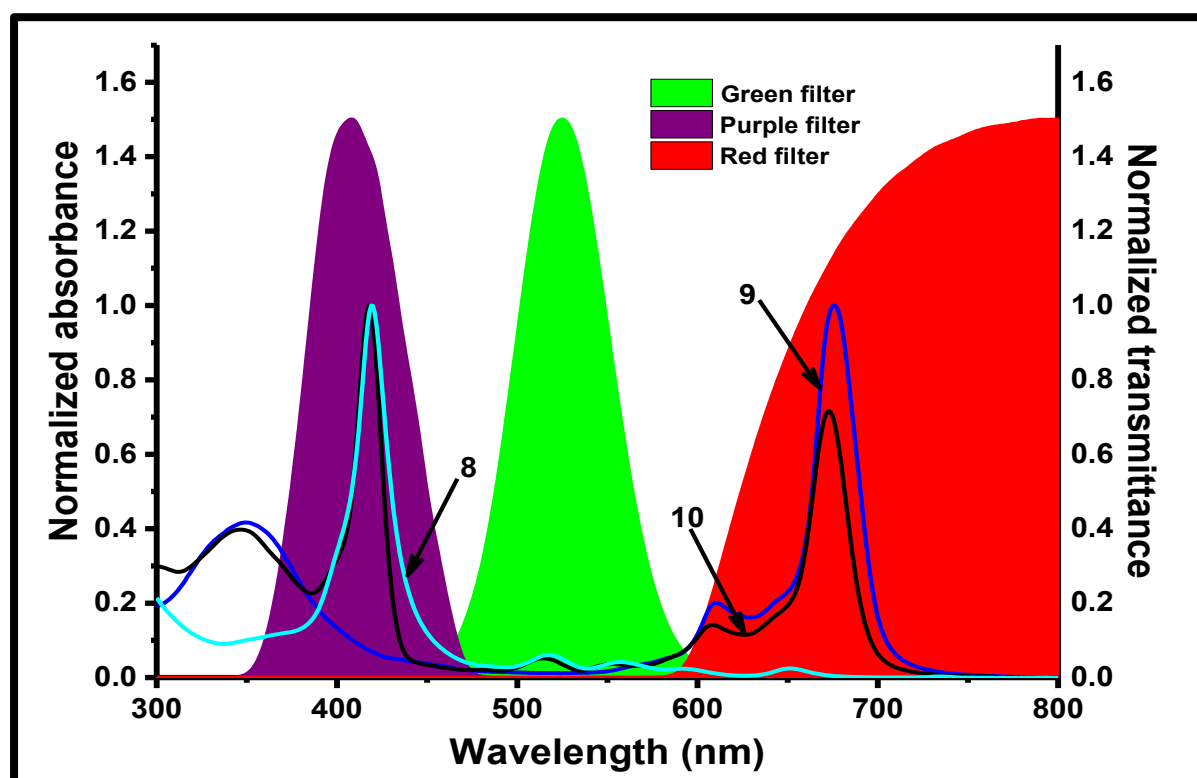


**Fig. 5.5:** Normalized UV-Vis ground state absorption spectra for complexes **8**, **9** and **10** in DMSO and the normalized transmittance spectra for the green, purple and red light filters used in this work.

irradiated light into ranges that separately irradiated the porphyrin Soret band (purple filter), porphyrin Q-bands (green filter) and the MPc Q-band (red filter).

Change in 4-CP concentration (monitored using UV-Vis spectroscopy) after light irradiation in all three wavelength ranges studied confirmed the photocatalytic activity of the functionalized membrane in these wavelength ranges. The activity of the membrane was dependant on two important factors apart from the photosensitizer's singlet oxygen generation capability namely, the energy corresponding to the wavelength of irradiated light and absorption intensity of the membrane at the different wavelength ranges. The observed relative activities of the membrane under the different irradiation lights (**Fig. 5.6**) where activity was in the order purple > green > red, suggests that the energy of irradiation light is the most important activity determining factor.

A significantly higher degradation activity following green light treatment was observed with comparison to red light treatment despite a lower photosensitizer absorption intensity in the green light absorption region. This observation fortifies the idea of photosensitizer absorption range expansion since a membrane only functionalized with the MPc would not have had good activity in this region due to low to no light absorption. It is important to note that the wavelength range of green light absorption is of great interest since it corresponds to the greatest solar radiation intensity [212]. Also, the observed FRET processes in complex **10** discussed in chapter 4, serve as a high energy (short wavelength light) loss prevention mechanisms and could be responsible for the observed higher photocatalytic activity of the green filter. On the other hand, under red light irradiation energy loss due to fluorescence is not recycled and is of low magnitude (long wavelength light). A similar concept would also be

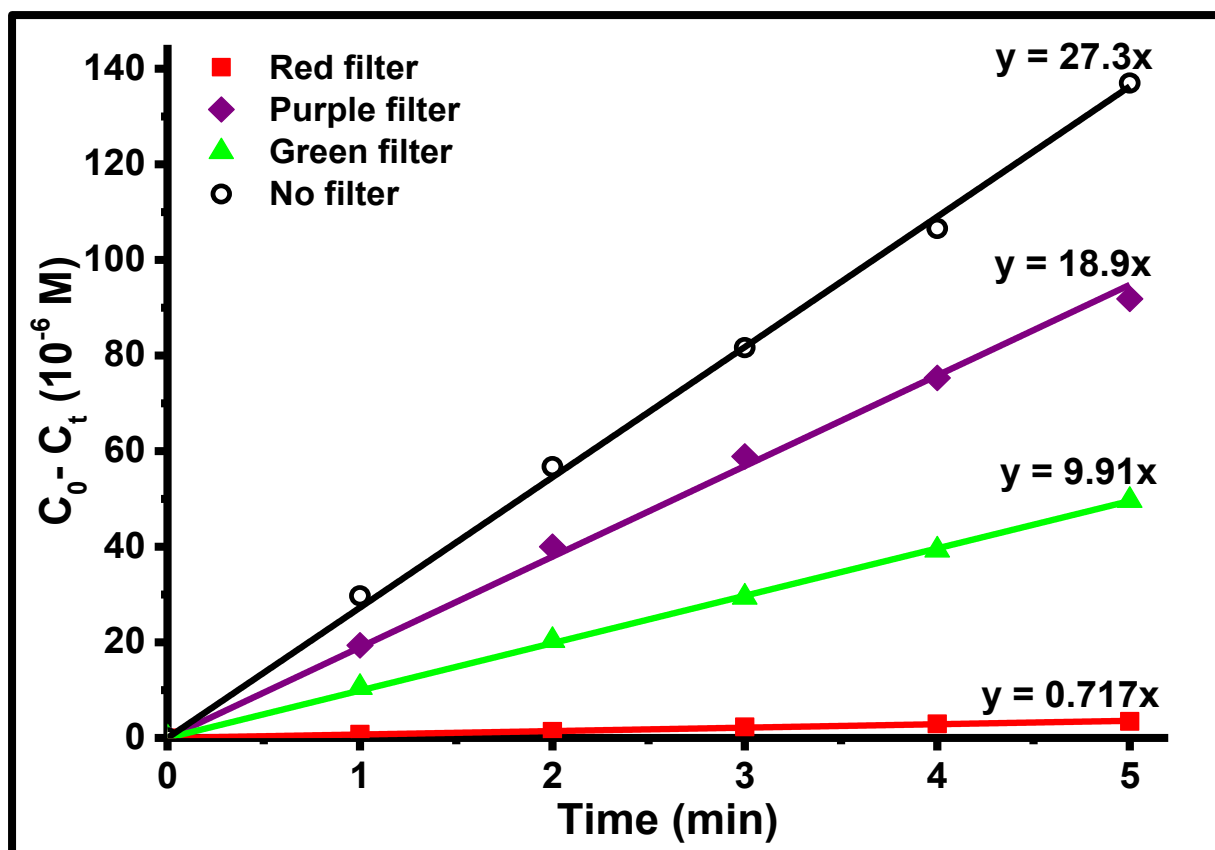


**Fig. 5.6:** Comparison of rates of 4-CP degradation by **10-memb** under irradiation by light of different wavelength ranges.

expected to explain the highest activity under purple light irradiation although the photosensitizer absorption intensity is relatively high in this region (**Fig. 5.5**).

The maximum photocatalytic activity by **10-memb** was observed under white light irradiation which can be observed to reasonably approximate the combined activity of all three different light irradiations. This observed higher photocatalytic activity under white light irradiation confirms the anticipated enhanced light harvesting capability of porphyrin-phthalocyanine hybrid photosensitizers. Such photosensitizers are hence promising efficient solar energy harvesters for potential practical applications in membrane technology.



### 5.2. Photodynamic Antimicrobial Chemotherapy (PACT)

Preliminary control experiments confirmed that DMSO (2%) had no effect on the bacteria, hence all bacterial studies with photosensitizers in solution in this work were carried out in 2 % DMSO in PBS solution to aid the dispersion of the aqueous insoluble photosensitizers.

#### 5.2.1. Application of AgTNPs for enhanced PACT

The PACT activity of complex **4a** and **4b** as examples in solution were studied and quantified with comparison to their corresponding AgTNPs nanoconjugates. The PACT activity of the MPc and MPc(AgTNPs) conjugate functionalized polymer membranes (**4a**-memb, **4a**(AgTNPs)-memb, **4b**-memb and **4b**(AgTNPs)-memb) was also studied and is discussed here.

##### 5.2.1.1. Dark toxicity studies

The dark toxicity study outcomes for complexes **4a** and **4b** at various concentrations are shown in **Fig. 5.7 (A)**. Both complexes proved to have some dark toxicity which gradually increased with complex concentration. Complex **4a** (approximately 72 % bacteria viability) shows more dark toxicity than complex **4b** (approximately 78 % bacteria viability at 40  $\mu$ M). Considering the structural similarities of complexes **4a** and **4b**, and the observed variation of dark toxicity with complex concentration, the toxicity may be related to the functionality on the complexes. On the other hand, the higher toxicity of complex **4a** is attributed to its observed better solubility in the buffer solution used, compared to complex **4b**. The lower dark toxicity of complex **4b** may also be related to the degradation of the complex when irradiated in the 2 % DMSO in PBS solution.

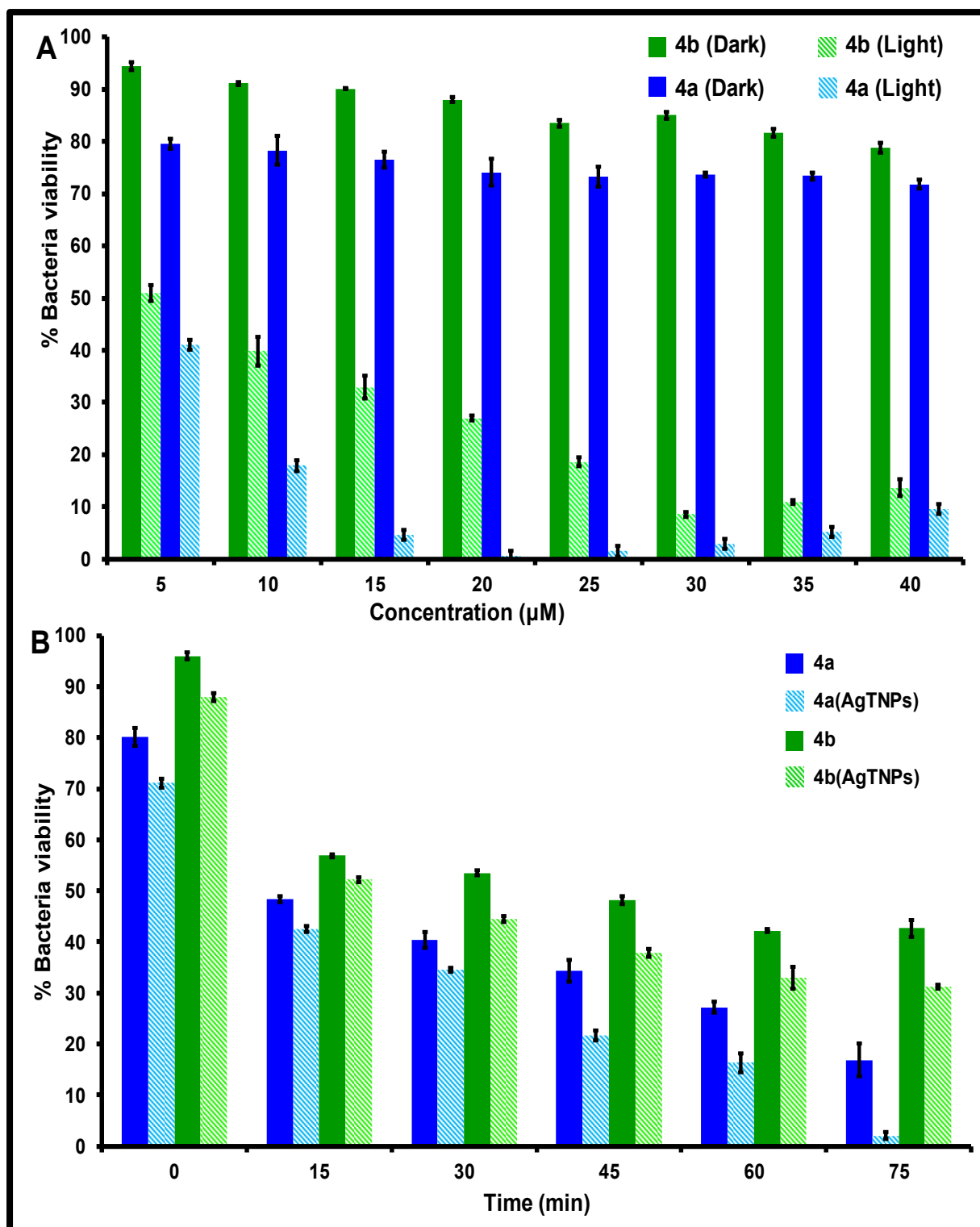


**Fig. 5.7:** (A) PACT activity (against *S. aureus*) with changing concentration of **4a** and **4b** at 30 min irradiation. (B) PACT activity time study of **4a**, **4a(AgTNPs)**, **4b**, and **4b(AgTNPs)**, at 5  $\mu\text{M}$  MPc concentration.

### 5.2.1.2. PACT activity

**Fig. 5.7 (A)** shows the PACT activity for complexes **4a** and **4b** at the different concentrations studied. Both complexes after 30 min of irradiation at a wavelength of 680 nm, gave bacterial viability reductions > 50 % at all concentrations with complex **4a** being more active despite having a lower  $\Phi_{\Delta}$ . The greater activity of complex **4a** may partially be attributed to the observed higher dark toxicity and the previously mentioned (chapter 4) tendency of complex **4b** to degrade when irradiated in aqueous solution. The activity of the MPcs increased with increase in concentration but at higher concentrations, the activity gradually decreases with further increase in concentration (**Fig. 5.7 (A)**), which could possibly be due to aggregation of the complexes at these higher concentrations in aqueous media.

Optimization of the MPc concentration to use in the time-correlated study (**Fig. 5.7 (A)**) showed that 5  $\mu$ M for both MPcs would be most suitable to allow for comparison of the complexes since they exhibited the least dark toxicity at this concentration. Corresponding conjugate solutions (**4a**(AgTNPs) and **4b**(AgTNPs)) of 5  $\mu$ M complex concentrations were also studied. **Fig. 5.7 (B)** shows that for both sets of compounds, the MPc(AgTNPs) conjugates had greater activity than the corresponding MPcs complex. For both conjugates, enhanced activity was attributed to enhanced  $\Phi_{\Delta}$  generation (**Table 4.3**) and possible independent activity of the AgTNPs. The observed larger activity of **4a**(AgTNPs) compared to **4b**(AgTNPs) may also be attributed to the possible degradation of the latter within the conjugates since as stated above, complex **4b** degraded in aqueous media.

### 5.2.1.3. Antimicrobial activity of AgTNPs

To validate the above proposed activity contribution by AgTNPs, the antibacterial activity of the nanoparticles was studied at two concentrations (0.010 and 0.004

mg/mL) corresponding to the nanoparticle content of the 5  $\mu$ M MPc, conjugate solutions. The 0.010 mg/mL AgTNPs concentration corresponds to the nanoparticle content in the **4a**(AgTNPs) solution. The activity of the AgTNPs alone was observed to be relatively constant at various irradiation dosages both in the light and dark (**Fig. 5.8**) which suggests that the nanoparticle antibacterial activity was independent of light irradiation. The difference in AgTNPs activity in **Fig. 5.8** also suggests that, a larger amount of AgTNPs per volume of solvent, gives greater antibacterial activity. This hence confirms that the greater antimicrobial activity of **4a**(AgTNPs) was also due to a greater non-PACT activity of AgTNPs.

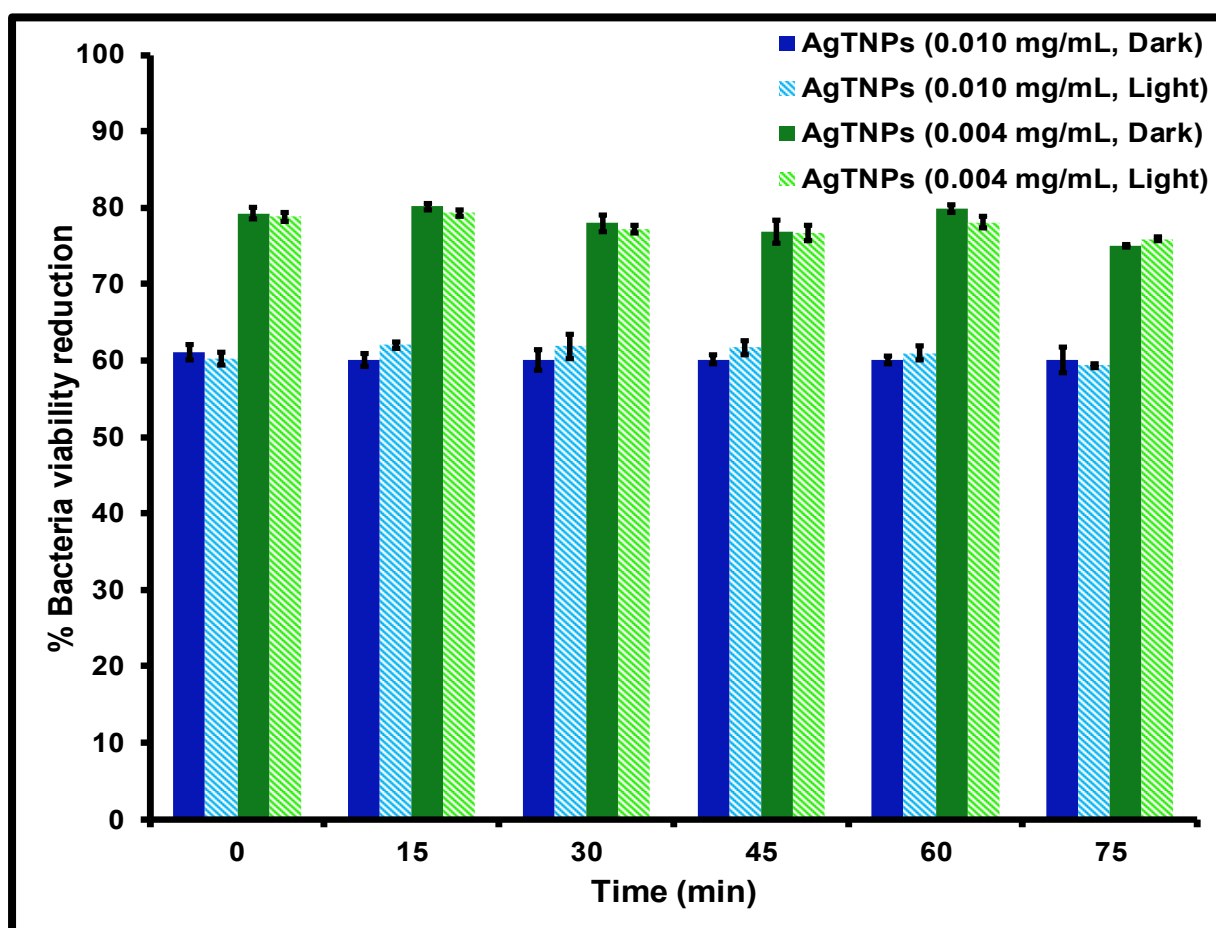


**Fig. 5.8:** PACT activity of AgTNPs with time at 0.004 mg/ mL and 0.010 mg/ mL dosages.

#### 5.2.1.4. Antibacterial studies of photosensitizer functionalized polymer membranes

**Fig. 5.9** shows agar plates with samples of the membranes functionalized with the studied photosensitizers, after one hour of dark treatment (**Fig. 5.9 (B)**) and irradiation at 680 nm (**Fig. 5.9 (C)**). All functionalized membranes decreased bacterial growth on their surface while bacteria grew on the control (unfunctionalized membrane) (**Fig. 5.9 (C)**). Bacterial growth can be seen in the blank (unfunctionalized membrane) in **Fig. 5.9 (C)** section b, where there was bacterial growth on the membrane (encircled in blue). However, the functionalized membranes show no bacterial growth (**Fig. 5.9 (C)**, section e, (encircled in red) for **4b**(AgTNPs) as an example). In **Fig. 5.9 (A)**, the corresponding photos of the membranes are encircled. In the dark, the membranes cannot be easily seen (**Fig. 5.9 (B)**) since the bacteria has grown all over them. Hence suggesting that the AgTNPs activity alone in the membrane was not enough to protect

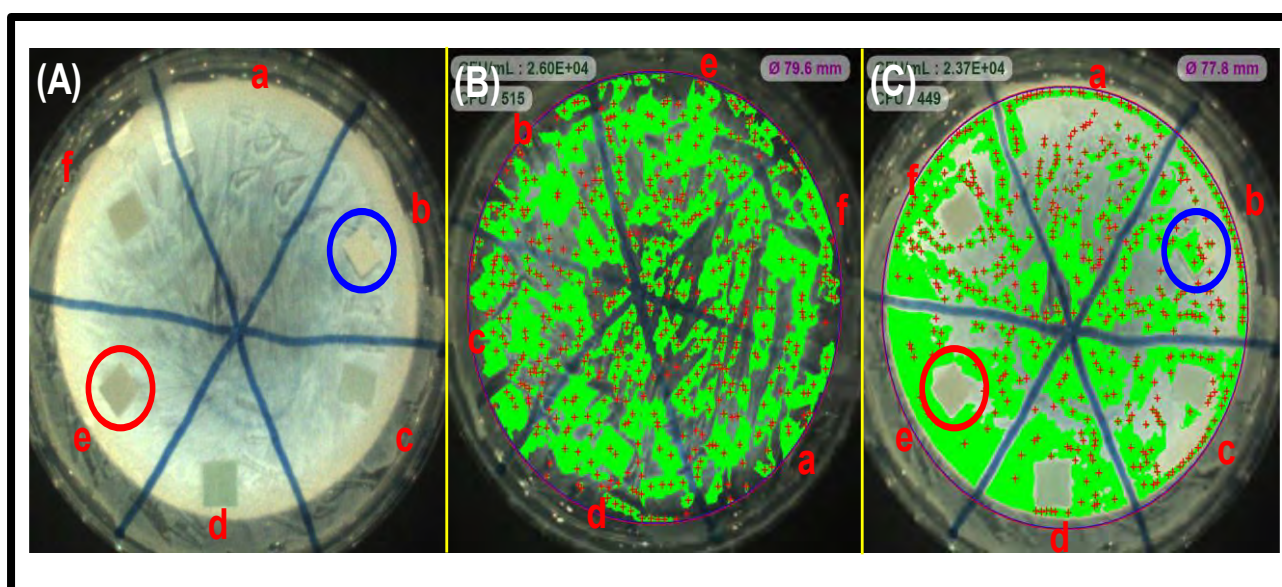


**Fig. 5.9:** Agar plates with (a) blank (no membrane), (b) control (unfunctionalized membrane), (c) **4a**-memb, (d) **4b**-memb, (e) **4b**(AgTNPs)-memb and (f) **4a**(AgTNPs)-memb. (A) Photo showing the position of the membranes, and colony counts (B) after dark treatment and (C) after light treatment (PACT).

the membranes from bacterial growth, while also confirming that the observed activity in **Fig. 5.9 (C)** was due to PACT activity. This shows that regardless of the differences in the membrane MPc loading, the PACT activity of the membranes was sufficient to decrease bacterial growth.

### 5.2.2. Quaternization of MPcs for enhanced PACT activity

The PACT activity of complex **5** and its quaternized derivative complex **6** in solution were studied and quantified as references for the activities of the corresponding functionalized polymer membranes (**5-memb** and **6-memb**). The activity of the functionalized membranes was then observed by comparison of extent of bacteria inhibition without light irradiation and with light irradiation after various exposure periods.

#### 5.2.2.1. Dark toxicity studies

Complex **5** showed almost no dark toxicity at all concentrations studied, but complex **6** showed a drastic fall in bacteria viability up to 0 % at the highest concentration studied, **Fig. 5.10 (A)**. The observed dark toxicity for **6** could be attributed to the charges on the molecules. The neutral to negative charge of complex **5** possibly resulted in challenges of the complex binding to and localizing in the bacterial cells due to repulsion by the general negative cell surface charge, coupled with low solubility of the complex in aqueous media. On the other hand, the positive charge nature of complex **6** enabled its solubility in aqueous media and facilitated binding to and localization of the complex in the bacterial cells [213–215], enhancing dark toxicity. Based on the results observed in **Fig. 5.10 (A)**, a concentration of 1  $\mu\text{M}$  was selected for the time-correlated studies for both complexes to allow for their comparison since

both complexes showed the least dark toxicity (> 90 % bacteria viability) at this concentration.

### 5.2.2.2. PACT activity

The PACT activity of the two ZnPc derivatives (complexes **5** and **6**) against *S. aureus* at various concentrations in solution, is displayed in **Fig. 5.10 (A)**. There was an increase in PACT activity with increase in concentration. Both MPcs showed activity after 60 min of light irradiation, with complex **5** reaching a maximum activity of 14.3 % bacteria viability (log reduction of 0.71) at the highest concentration studied (16  $\mu$ M), while complex **6** achieved 0 % bacteria viability (log reduction of 9.4) at all concentrations. The complete elimination of the bacteria by complex **6** in the presence of light with comparison to complex **5** also supports the idea of better localization of complex **6** resulting in dark toxicity.

**Fig. 5.10 (B)** shows the graphical summary of the PACT activity of complexes **5** and **6** (concentration = 1  $\mu$ M) in solution after various irradiation periods from 0 to 60 min. Complex **5** only achieved a maximum activity of 80.3 % bacteria viability after 60 min while complex **6** achieved 0 % bacteria viability within 15 min. The results represent log reductions of 0.08 ( $p < 0.05$ ) for complex **5** and 9.4 ( $p < 0.05$ ) for complex **6**. The dark toxicity did not vary with irradiation time and was observed to be above 80 % bacteria viability for complex **6** and above 90 % for complex **5** throughout the study. The MPc complexes were stable under light irradiation during singlet oxygen determination studies, so stability was also expected during PACT studies. The log reduction reported here for complex **6** in solution is higher than those reported for *S. aureus* using an InPc [216] at log 8.3, a fluorine based asymmetric ZnPc at log 7 [217] and a quaternized symmetric ZnPc at log 4 [218]. This shows the importance of both quaternization and asymmetry.



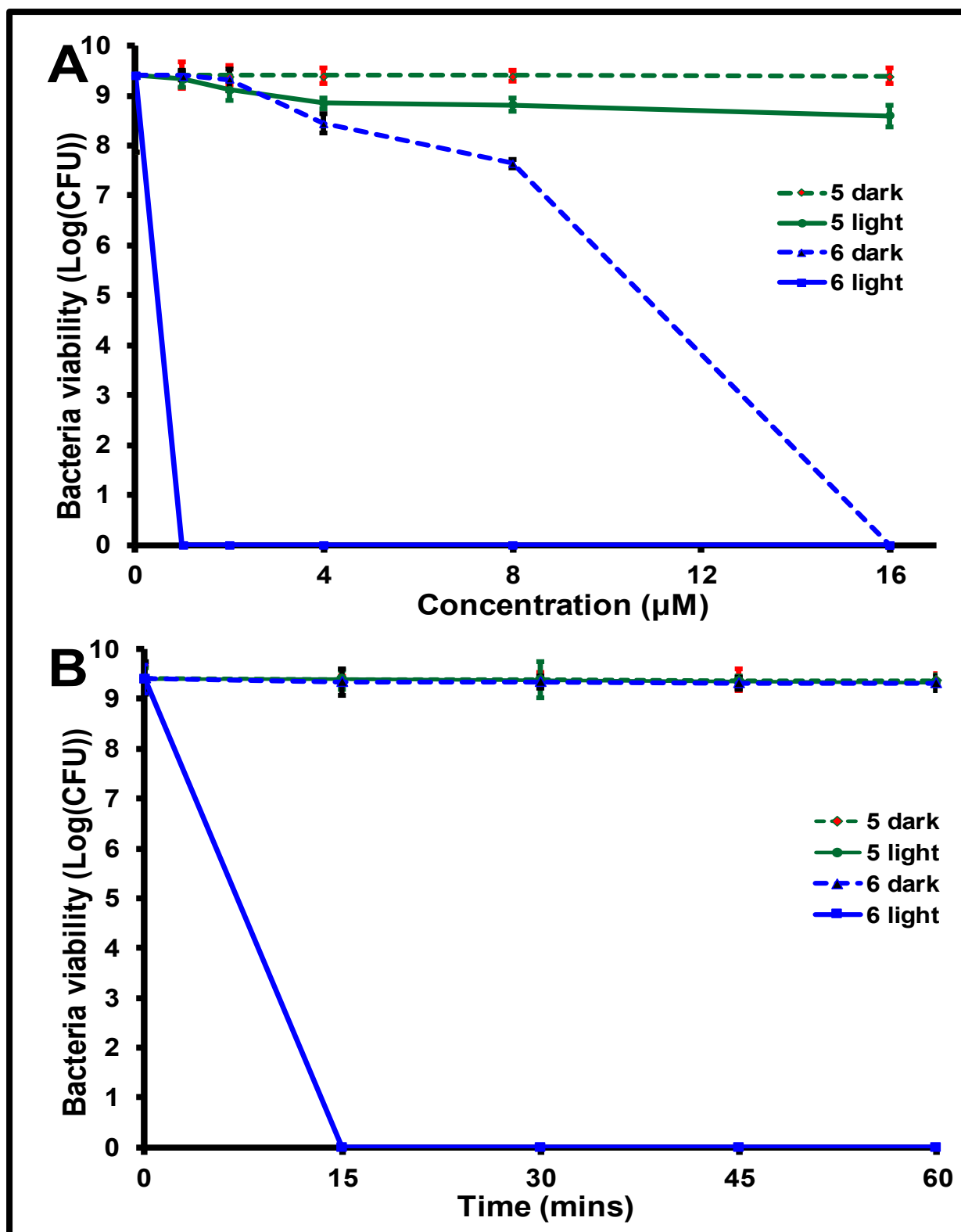


**Fig. 5.10:** (A) PACT activity (against *S. aureus*) at different concentrations of complexes **5** and **6** after 60 min irradiation. (B) PACT activity time study of complexes **5** and **6** at 1  $\mu\text{M}$  MPc concentration.



### 5.2.2.3. Antibacterial studies of MPC functionalized polymer membranes

**Fig. 5.11** shows images of the results of the PACT studies using functionalized polymer membranes. These were comparative studies between the two functionalized membranes where activity of the membranes was based on area of bacteria clearance as a function of irradiation time. As mentioned above, unfunctionalized PS membranes have no antimicrobial activity, hence results of these membranes are not shown. The observed results at 0 min (**Fig. 5.11**) irradiation confirmed that in the absence of light, the membranes do not show any notable or relevant antimicrobial activity. Similar results were observed after 15 min (**Fig. 5.11**) and 30 min (**Fig. 5.11**) of light irradiation. After 45 min of irradiation **6-memb** showed notable signs of activity (**Fig. 5.11**, white arrows show areas of clearing) although the clearance was not complete. After 60 min the activity of **6-memb** became more pronounced (**Fig. 5.11**), with all triplicate samples showing distinct bacterial clearance. On the other hand, **5-memb** only began to show signs of bacterial clearance after 60 min of light irradiation (**Fig. 5.11**). The distinct difference in activity between the solution and membrane studies especially for complex **6** and **6-memb** suggests that, indeed the excellent activity of complex **6** was mainly due to efficient localization in the bacteria, since activity appears to significantly be reduced when the complex is immobilized on the membranes. It is important to note that this is an estimated comparison since concentration difference is a factor for consideration although it was in favour of **6-memb**.

The mechanism of traditional membrane antimicrobial activity is to repel or discourage microorganism adherence and proliferation on the membrane surface, by establishing a hydrophilic negative surface charge [219]. Although the positive surface charge on **6-memb** of the membranes in this work contradicts the traditional mechanism, the

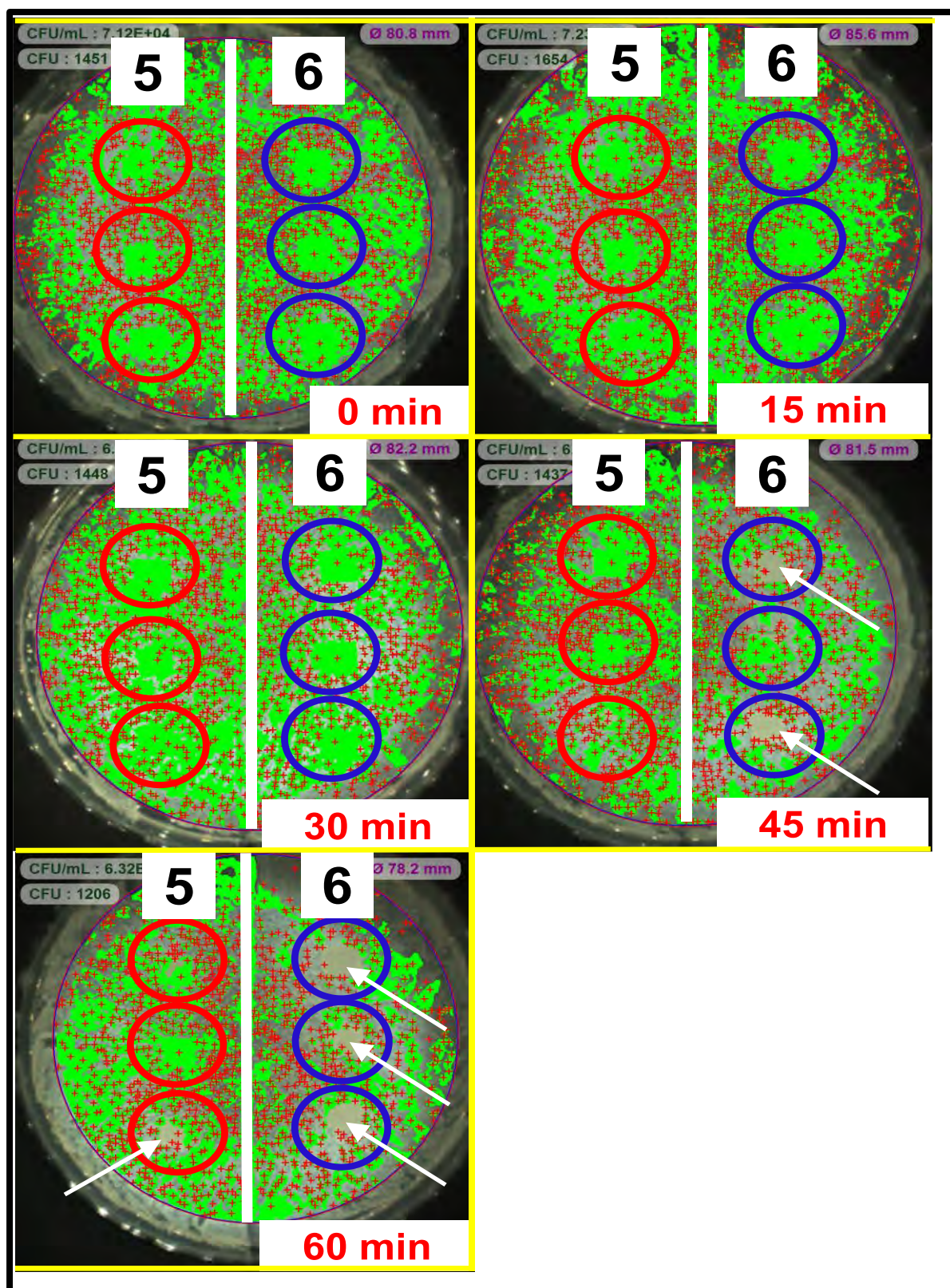


**Fig. 5.11:** Agar plates with triplicates of 5-memb and 6-memb (represented as just 5 and 6, respectively) after PACT against *S. aureus* for different periods of light irradiation.

membranes show enhanced antimicrobial activity with comparison to its non-positively charged analogue **5-memb**. This observed enhanced activity is attributed to the favourable requirements for PACT based antimicrobial activity, of which the most important is efficient destructive interaction of microorganism with the generated singlet oxygen. The positive surface charge of **6-memb** facilitated and enhanced bacterial adherence to the membrane surface as opposed to repulsion. This in turn significantly reduced the distance between the source of singlet oxygen generation (MPcs) and the site of action (bacteria), thus resulting in efficient destructive interaction of the bacteria and the generated singlet oxygen. Lack of such enhanced adherence with **5-memb** may have resulted in the observed lower activity. The molar loading values (based on the MPc and using the loading in mg MPc/g MPc-PS presented in chapter 3) for the MPc-PS conjugates were observed to be 0.033 mM MPc/ g MPc-PS for **5-PS** and 0.024 mM MPc/ g MPc-PS for **6-PS**, thus suggesting **5-memb** was at an advantage based on dye concentration hence ruling out effects of concentration as an explanation for observed antimicrobial activity.

### 5.3. Summary of chapter

The singlet oxygen generation capability of MPc-functionalized polymer membranes renders them photocatalytic with the potential to degrade organic pollutants. The potential of MPc functionalized polymer membranes in photocatalytic degradation of organic pollutants (exemplified by 4-CP) in water was studied using **2 $\pi$** (GQDs)-membs and **10-memb** as sample membranes. Also, the potential photocatalytically induced biological fouling resistance through PACT was studied using **4a-memb**, **4a**(AgTNPs)-membs, **4b-memb**, **4b**(AgTNPs)-memb, **5-memb** and **6-memb** as

sample membranes, with reference to the PACT activity of the parent photosensitizers in solution.

The successful degradation of 4-CP in both first and second order kinetic reactions while the membranes' functionalization remained unchanged confirmed the potential for application of phthalocyanines in the formation of stable photoactive polymer membranes. Successful application of complex **2** (unsubstituted ZnPc) functionalized polymer membranes in the photodegradation of 4-CP, substantiated the possibility of application of any MPc regardless of the functional groups present. On the other hand, functionalization of polymer membranes with hybrid MPc photosensitizers such as the porphyrin-phthalocyanine heterodiyad complex **10** proved to give rise to catalytic membranes with a greater activation wavelength range and potentially exceptional solar radiation utilization efficiency.

Functionalization of polymer membranes with MPcs such as in **4a**-memb and **4b**-memb, induced photoactivated antimicrobial properties of the membranes, while functionalization using MPc-silver nanoparticle conjugates (**4a**(AgTNPs) and **4b**(AgTNPs)) gave rise to membranes with antimicrobial activity both in the presence and absence of light, as exemplified by activity against *S.aureus*. Also, an overall positive MPc charge (such as that presented by quaternization), hence the surface charge of the resultant membrane proved to give rise to exceptional antibacterial properties despite that a negative membrane surface charge has traditionally been used to induce microbial resistance in membrane technology. The enhanced activity of positively charged membranes is however limited to photoactive polymer membranes due to the mechanism bringing about the antimicrobial activity.

# CHAPTER 6



### 6. Conclusions and Recommendations

#### 6.1. General conclusions

The simplified lab-scale fabrication and photocatalytic evaluation of microporous asymmetric polystyrene polymer membranes functionalized with metallophthalocyanine (MPc) based photosensitizers, as a potential advanced water treatment technology have been discussed and presented as the focus of this thesis.

Photosensitizer functionalized asymmetric polymer membranes were successfully prepared using the phase inversion technique and as a proof of concept, all the prepared membranes were evaluated for photoactivity by their ability to generate singlet oxygen. However, stable functionalization was only possible when the photosensitizers were covalently anchored to a polymer, thus limiting the scope of phthalocyanine photosensitizers that could be employed. The application of the concept of  $\pi$ - $\pi$  stacking interaction capability of MPcs to graphene quantum dots (GQDs) was hence investigated and proved to be a promising strategy for enabling the potential application of non-covalently conjugatable MPc complexes in the preparation of stable photoactive polymer membranes. However, application of  $\pi$ - $\pi$  stacking also implies some reduction in singlet oxygen generation capability from the triplet excited state of the MPc photosensitizers due to the screening effect.

Singlet oxygen generation properties of the functionalized polymer membranes rendered them photocatalytic, thus enabling them to degrade 4-CP as a model organic pollutant in a reaction whose kinetics depend on the 4-CP concentration and photocatalyst loading in the membrane when considering batch experiments. Singlet oxygen generation also renders the membranes potentially antimicrobial with evidence in this study of antibacterial activity of the functionalized membranes. Also,

despite the traditional negative membrane surface charge strategy for preserving polymer membranes against biological fouling, a positive membrane surface charge proved to be incredibly active if the membrane is photocatalytic. On the other hand, application of antimicrobial nanoparticles such as silver nanoprisms in the formation of photosensitizer conjugates for membrane functionalization has the potential to improve MPc distribution in the membrane and singlet oxygen generation, but most importantly, it introduces light independent antimicrobial properties, thus providing uninterrupted protection against biological fouling.

For polystyrene polymer membranes, the established synthesis parameters gave membranes of the same general cross section where variations in MPc identity and loading mainly affected surface pore sizes and distribution. In addition to the reported compounds complexes **1**, **3** and **4a**, the novel compounds complexes **4b**, **5**, **6**, **8**, **9** and **10** were successfully synthesized, characterized and their potential applications in polymer membrane functionalization investigated for the first time. Application of porphyrin-phthalocyanine heterodyad complexes such as complex **10** presented here, and possibly higher arrays in polymer membrane functionalization, is envisaged to gives membranes with an expanded scope for light absorption and good access to the 400 - 700 nm wavelength light, thus making them potentially efficient solar radiation activated material.

As a general conclusion, MPc functionalized polymer membranes have been reported here for the first time and various aspects related to their potential applications in water treatment investigated. The functionalized membranes show great potential in organic pollutant photocatalytic degradation and biological fouling resistance, with potential expansion of the concept to application of other organic photocatalytic compounds.

### 6.2. Recommendations

For future work and direction, it would be interesting to evaluate MPc functionalized polymer membrane photocatalytic degradation activity and antimicrobial properties in a continuous flow water treatment system. Also, in line with this, optimization of photosensitizer loading to enable applicable pollutant elimination from real samples would be of significant interest.

In photoactive membranes, only the surface exposed photosensitizers are available for light absorption photoactivity. This hence means that preparation of functionalized membranes using functionalized polymer results in photosensitizer wastage since most of it is embedded in the polymer and shielded from irradiated light, thus exploration into post-cast membrane surface functionalization for efficient photocatalyst use may be of significant interest. It would also be interesting to explore the application of higher porphyrin-phthalocyanine multinuclei arrays in polymer membrane functionalization as a further step towards efficient solar radiation application in membrane photocatalysis.

The photocatalytic properties of MPc functionalized polymer membranes in the current work were restricted to only activity towards 4-CP and *S.aureus*, hence further investigation into photoactivity towards other classes of water pollutants, and antimicrobial properties against gram (-) bacteria, and other microorganisms such as fungi and protozoans may be necessary.



## REFERENCES

- [1] Y. Yang, X. Jian, D. Yang, S. Zhang, L. Zou, Poly(phthalazinone ether sulfone ketone) (PPESK) hollow fiber asymmetric nanofiltration membranes: Preparation, morphologies and properties, *J. Memb. Sci.* 270 (2006) 1–12. doi:10.1016/j.memsci.2005.06.036.
- [2] P. Radovanovic, S.W. Thiel, S.T. Hwang, Formation of asymmetric polysulfone membranes by immersion precipitation. Part II. The effects of casting solution and gelation bath compositions on membrane structure and skin formation, *J. Memb. Sci.* 65 (1992) 231–246. doi:10.1016/0376-7388(92)87025-S.
- [3] S. Ying, J. Yang, Morphological Structure of Membranes for Gas Separation Prepared By Phase, *AUTEX Res. J.* 2 (2002) 100–108.
- [4] K. Guerra, J. Pellegrino, Development of a Techno-Economic Model to Compare Ceramic and Polymeric Membranes, *Sep. Sci. Technol.* 48 (2013) 51–65. doi:10.1080/01496395.2012.690808.
- [5] WHO, Guidelines for drinking-water quality, 4th ed., WHO Press, Geneva, 2011. doi:10.1016/S1462-0758(00)00006-6.
- [6] A. Mansourizadeh, A.F. Ismail, Effect of additives on the structure and performance of polysulfone hollow fiber membranes for CO<sub>2</sub> absorption, *J. Memb. Sci.* 348 (2010) 260–267. doi:10.1016/j.memsci.2009.11.010.
- [7] M. Sadrzadeh, S. Bhattacharjee, Rational design of phase inversion membranes by tailoring thermodynamics and kinetics of casting solution using polymer additives, *J. Memb. Sci.* 441 (2013) 31–44. doi:10.1016/j.memsci.2013.04.009.
- [8] G.R. Guillen, Y. Pan, M. Li, E.M. V Hoek, Preparation and characterization of membranes formed by nonsolvent induced phase separation: A review, *Ind. Eng. Chem. Res.* 50 (2011) 3798–3817. doi:10.1021/ie101928r.
- [9] S. Loeb, S. Sourirajan, Sea water demineralization by means of an osmotic membrane, in: R.F. Gould (Ed.), *Adv. Chem. Saline Water Conversion-II*, American Chemical Society, Washington DC, 1963: pp. 117–132. doi:10.1021/ba-1963-0038.
- [10] X. Tan, D. Rodrigue, A Review on Porous Polymeric Membrane Preparation. Part I: Production Techniques with Polysulfone and Poly (Vinylidene Fluoride), *Polymers (Basel)*. 11 (2019) 1160. doi:10.3390/polym11071160.
- [11] D.S. Dlamini, B.B. Mamba, J. Li, The role of nanoparticles in the performance of nano-enabled composite membranes – A critical scientific perspective, *Sci. Total Environ.* 656 (2019) 723–731. doi:10.1016/j.scitotenv.2018.11.421.
- [12] A. Ammar, A.M. Al-Enizi, M.A. AlMaadeed, A. Karim, Influence of graphene oxide on mechanical, morphological, barrier, and electrical properties of polymer membranes, *Arab. J. Chem.* 9 (2016) 274–286. doi:10.1016/j.arabjc.2015.07.006.
- [13] M.N. Subramaniam, P.-S. Goh, W.-J. Lau, B.-C. Ng, A.F. Ismail, Development

- of nanomaterial-based photocatalytic membrane for organic pollutants removal, in: W.-J. Lau, A.F. Ismail, A. Isloor, A. Al-Ahmed (Eds.), *Adv. Nanomater. Membr. Synth. Its Appl.*, Elsevier Inc., 2019: pp. 45–67. doi:10.1016/b978-0-12-814503-6.00003-3.
- [14] M. Ghanbari, D. Emadzadeh, W.J. Lau, S.O. Lai, T. Matsuura, A.F. Ismail, Synthesis and characterization of novel thin film nanocomposite (TFN) membranes embedded with halloysite nanotubes (HNTs) for water desalination, *Desalination*. 358 (2015) 33–41. doi:10.1016/j.desal.2014.11.035.
- [15] L.F. Padilha, C.P. Borges, Pvc Membranes Prepared Via Non-Solvent Induced Phase Separation Process, *Brazilian J. Chem. Eng.* 36 (2019) 497–509. doi:10.1590/0104-6632.20190361s20170132.
- [16] D.M. Koenhen, M.H.V. Mulder, C.A. Smolders, Phase separation phenomena during the formation of asymmetric membranes, *J. Appl. Polym. Sci.* 21 (1977) 199–215. doi:10.1002/app.1977.070210118.
- [17] I.M. Wienk, R.M. Boom, M.A.M. Beerlage, A.M.W. Bulte, C.A. Smolders, H. Strathmann, Recent advances in the formation of phase inversion membranes made from amorphous or semi-crystalline polymers, *J. Memb. Sci.* 113 (1996) 361–371. doi:10.1016/0376-7388(95)00256-1.
- [18] W.Y. Chuang, T.H. Young, W.Y. Chiu, C.Y. Lin, The effect of polymeric additives on the structure and permeability of poly(vinyl alcohol) asymmetric membranes, *Polymer (Guildf)*. 41 (2000) 5633–5641. doi:10.1016/S0032-3861(99)00818-6.
- [19] K.C. Khulbe, *Synthetic Membranes for Membrane Processes*, in: S. Laboratory (Ed.), *Synth. Polym. Membr.*, Springer, Berlin, Heidelberg, 2008: pp. 5–18.
- [20] S. Mozia, D. Darowna, K. Szymański, S. Grondzewska, K. Borchert, R. Wróbel, A.W. Morawski, Performance of two photocatalytic membrane reactors for treatment of primary and secondary effluents, *Catal. Today*. 236 (2014) 135–145. doi:10.1016/j.cattod.2013.12.049.
- [21] C.S. Ong, W.J. Lau, P.S. Goh, B.C. Ng, A.F. Ismail, C.M. Choo, The impacts of various operating conditions on submerged membrane photocatalytic reactors (SMPR) for organic pollutant separation and degradation: A review, *RSC Adv.* 5 (2015) 97335–97348. doi:10.1039/c5ra17357d.
- [22] R.A. Damodar, S.J. You, Performance of an integrated membrane photocatalytic reactor for the removal of Reactive Black 5, *Sep. Purif. Technol.* 71 (2010) 44–49. doi:10.1016/j.seppur.2009.10.025.
- [23] A. Rachel, M. Subrahmanyam, P. Boule, Comparison of photocatalytic efficiencies of TiO<sub>2</sub> in suspended and immobilised form for the photocatalytic degradation of nitrobenzenesulfonic acids, *Appl. Catal. B Environ.* 37 (2002) 301–308. doi:10.1016/S0926-3373(02)00007-3.
- [24] P. Argurio, E. Fontananova, R. Molinari, E. Drioli, Photocatalytic membranes in photocatalytic membrane reactors, *Processes*. 6 (2018) 162. doi:10.3390/pr6090162.
- [25] R. Bergamasco, P.F. Coldebella, F.P. Camacho, D. Rezende, N.U.

- Yamaguchi, M.R.F. Klen, C.J.M. Tavares, M.T.S.P. Amorim, Self-assembly modification of polyamide membrane by coating titanium dioxide nanoparticles for water treatment applications, *Rev. Ambient. e Agua*. 14 (2019) 2297. doi:10.4136/ambi-agua.2297.
- [26] S.S. Chin, K. Chiang, A.G. Fane, The stability of polymeric membranes in a TiO<sub>2</sub> photocatalysis process, *J. Memb. Sci.* 275 (2006) 202–211. doi:10.1016/j.memsci.2005.09.033.
- [27] D. Zioui, H. Salazar, L. Aoudjit, P.M. Martins, S. Lanceros-Mendez, Photocatalytic polymeric nanocomposite membrane towards oily wastewater, *Preprints*. 2019 (2019) 2019040060. doi:10.20944/preprints201904.0060.v1.
- [28] U.N. Rusli, N.H. Alias, M.Z. Shahrudin, N.H. Othman, Photocatalytic degradation of oil using polyvinylidene fluoride/titanium dioxide composite membrane for oily wastewater treatment, *MATEC Web Conf.* 69 (2016) 05003. doi:10.1051/mateconf/20166905003.
- [29] M.N. Subramaniam, P.S. Goh, W.J. Lau, B.C. Ng, A.F. Ismail, AT-POME colour removal through photocatalytic submerged filtration using antifouling PVDF-TNT nanocomposite membrane, *Sep. Purif. Technol.* 191 (2018) 266–275. doi:10.1016/j.seppur.2017.09.042.
- [30] A. Pugin, Phthalocyanine Pigments, US3296008A, 1967. doi:10.1074/JBC.274.42.30033.(51).
- [31] J. Alzeer, P.J.C. Roth, N.W. Luedtke, An efficient two-step synthesis of metal-free phthalocyanines using a Zn(II) template, *Chem. Commun. (Camb)*. 15 (2009) 1970–1971. doi:10.1039/b822985f.
- [32] H.S. Nalwa, The effect of central metal atom on the electrical properties of phthalocyanine macromolecule, *J. Electron. Mater.* 17 (1988) 291–295. doi:10.1007/BF02652108.
- [33] A. Ogunsipe, T. Nyokong, Effects of central metal on the photophysical and photochemical properties of non-transition metal sulfophthalocyanine, *J. Porphyr. Phthalocyanines*. 9 (2005) 121–129. doi:10.1142/S1088424605000186.
- [34] M. Grobosch, C. Schmidt, R. Kraus, M. Knupfer, Electronic properties of transition metal phthalocyanines: The impact of the central metal atom ( $d^5$  -  $d^{10}$ ), *Org. Electron. Physics, Mater. Appl.* 11 (2010) 1483–1488. doi:10.1016/j.orgel.2010.06.006.
- [35] M. Gouterman, Optical Spectra and Electronic Structure of Porphyrins and Related Rings, in: D. Dolphin (Ed.), *The Porphyrins*, Academic Press, Inc., New York, 1978: pp. 1–165. doi:10.1016/b978-0-12-220103-5.50008-8.
- [36] L. Edwards, M. Gouterman, Porphyrins XV. Vapor Absorption Spectra and Stability: Phthalocyanines, *J. Mol. Spectrosc.* 33 (1970) 292–310.
- [37] B.I. Kharisov, U.O. Mendez, A.J.L. Garza, A.J.R. Rodriguez, Synthesis of non-substituted phthalocyanines by standard and non-standard techniques. Influence of solvent nature in phthalocyanine preparation at low temperature by UV-treatment of the reaction system, *New J. Chem.* 29 (2005) 686–692.

- [38] V.N. Nemykin, S. V. Dudkin, F. Dumoulin, C. Hirel, A.G. Gürek, V. Ahsen, Synthetic approaches to asymmetric phthalocyanines and their analogues, *Arkivoc.* 2014 (2014) 142–204. doi:10.3998/ark.5550190.p008.412.
- [39] R. Giovannetti, The use of spectrophotometry UV-Vis for the study of porphyrins, in: J. Uddin (Ed.), *Macro To Nano Spectrosc.*, InTech, 2012: pp. 87–108.
- [40] C.G. Claessens, U. Hahn, T. Torres, Phthalocyanines: From outstanding electronic properties to emerging applications, *Chem. Rec.* 8 (2008) 75–97. doi:10.1002/tcr.20139.
- [41] R. Jacobs, K. Stranius, E. Maligaspe, H. Lemmetyinen, N. V Tkachenko, M.E. Zandler, F.D. Souza, Syntheses and excitation transfer studies of near-orthogonal free-base porphyrin-ruthenium phthalocyanined dyads and pentad, *Inorg. Chem.* 51 (2012) 3656–3665.
- [42] J.P.C. Tomé, A.M.V.M. Pereira, C.M.A. Alonso, M.G.P.M.S. Neves, A.C. Tomé, A.M.S. Silva, J.A.S. Cavaleiro, M.V. Martínez-Díaz, T. Torres, G.M.A. Rahman, J. Ramey, D.M. Guldi, Synthesis and photophysical studies of new porphyrin-phthalocyanine dyads with hindered rotation, *European J. Org. Chem.* 2006 (2006) 257–267. doi:10.1002/ejoc.200500558.
- [43] J. Follana-Berná, S. Seetharaman, L. Martín-Gomis, G. Charalambidis, A. Trapali, P.A. Karr, A.G. Coutsolelos, F. Fernández-Lázaro, F. D'Souza, Á. Sastre-Santos, Supramolecular complex of a fused zinc phthalocyanine-zinc porphyrin dyad assembled by two imidazole-C<sub>60</sub> units: ultrafast energy transfer followed by electron transfer, *Phys. Chem. Chem. Phys.* 20 (2018) 7798–7807. doi:10.1039/C8CP00382C.
- [44] S.I. Yang, J. Li, H.S. Cho, D. Kim, D.F. Bocian, D. Holten, J.S. Lindsey, Synthesis and excited-state photodynamics of phenylethyne-linked porphyrin-phthalocyanine dyad, *J. Mater. Chem.* 10 (2000) 283–296.
- [45] T.H. Tran-Thi, Assemblies of phthalocyanines with porphyrins and porphyrazines : ground and excited state optical properties, *Coord. Chem. Rev.* 160 (1997) 53–91. doi:10.1016/S0010-8545(96)01341-0.
- [46] Z. Zhao, K.I. Ozoemena, D.M. Maree, T. Nyokong, Synthesis and electrochemical studies of a covalently linked cobalt(II) phthalocyanine-cobalt(II) porphyrin conjugate, *Dalt. Trans.* (2005) 1241–1248. doi:10.1039/b418611g.
- [47] P.C. Lo, X. Leng, D.K.P. Ng, Hetero-arrays of porphyrins and phthalocyanines, *Coord. Chem. Rev.* 251 (2007) 2334–2353. doi:10.1016/j.ccr.2007.03.007.
- [48] J.S. Lindsey, I.C. Schreiman, H.C. Hsu, P.C. Kearney, A.M. Marguerettaz, Rothemund and Adler-Longo reactions revisited: Synthesis of tetraphenylporphyrins under equilibrium conditions, *J. Org. Chem.* 52 (1987) 827–836.
- [49] M.J.F. Calvete, J.P.C. Tomé, J.A.S. Cavaleiro, Synthesis and characterization of new cross-like porphyrin– naphthalocyanine and porphyrin–phthalocyanine pentads, *J. Heterocycl. Chem.* 51 (2014) 202–208. doi:10.1002/jhet.

- [50] C.S. Foote, E.L. Clennan, Properties and reactions of singlet oxygen, in: C.S. Foote, J.S. Valentine, A. Greenberg, J.F. Liebman (Eds.), *Act. Oxyg. Chem.*, First Edit, Blackie Academic and Professional, London, 1995: pp. 105–141.
- [51] B. Halliwell, J.M.C. Gutteridge, *Free radicals in biology and medicine*, Fifth Edit, Oxford University Press, New York, 2015.
- [52] S.C. Ameta, P.B. Punjabi, C.S. Chobisa, N. Mangal, R. Bhardwaj, Singlet molecular oxygen, *Asian J Chem Rev.* 1 (1990) 106–124.
- [53] Y. V Savin, L.V. Goryachev, Y.A. Adamenkov, T. V Rakhimova, Y.A. Mankelevich, N.A. Popov, A.A. Adamenkov, V. V Egorov, S.P. Ilyin, Y. V Kolobyanin, E.A. Kudryashov, G.S. Rogozhnikov, B.A. Vyskubenko, Singlet oxygen production and quenching mechanisms in travelling microwave discharges, *J. Phys. D. Appl. Phys.* 37 (2004) 3121–3128. doi:10.1088/0022-3727/37/22/010.
- [54] P. Douglas, R.C. Evans, H.D. Burrows, The photochemical laboratory, in: R.C. Evans, P. Douglas, H.D. Burrows (Eds.), *Appl. Photochem.*, Springer, New York, London, 2013: pp. 467–531. doi:10.1007/978-3-319-31671-0.
- [55] İ. Altın, M. Sökmen, Z. Bıyıklioğlu, Quaternized zinc(II) phthalocyanine-sensitized TiO<sub>2</sub>: surfactant-modified sol–gel synthesis, characterization and photocatalytic applications, *Desalin. Water Treat.* 57 (2016) 16196–16207. doi:10.1080/19443994.2015.1084535.
- [56] A.E. Pirbazari, Photocatalytical Treatment of Synthetic Wastewater Containing Chlorophenols by TiO<sub>2</sub> Nanoparticles Sensitized with Cobalt Phthalocyanine Under Visible Light, *J. Chem. Eng. Process Technol.* 8 (2017) 1000333. doi:10.4172/2157-7048.1000333.
- [57] M.A. Zanjanchi, A. Ebrahimian, M. Arvand, Sulphonated cobalt phthalocyanine-MCM-41: An active photocatalyst for degradation of 2,4-dichlorophenol, *J. Hazard. Mater.* 175 (2010) 992–1000. doi:10.1016/j.jhazmat.2009.10.108.
- [58] M. Ledwaba, N. Masilela, T. Nyokong, E. Antunes, Surface modification of silica-coated gadolinium oxide nanoparticles with zinc tetracarboxyphenoxy phthalocyanine for the photodegradation of Orange G, *J. Mol. Catal. A Chem.* 403 (2015) 64–76. doi:10.1016/j.molcata.2015.03.023.
- [59] Z. Chen, Y. Zhang, D. Wang, L. Li, S. Zhou, J.H. Huang, J. Chen, P. Hu, M. Huang, Photodynamic antimicrobial chemotherapy using zinc phthalocyanine derivatives in treatment of bacterial skin infection, *J. Biomed. Opt.* 21 (2016) 18001. doi:10.1117/1.jbo.21.1.018001.
- [60] J. Chen, Z. Chen, Y. Zheng, S. Zhou, J. Wang, N. Chen, J. Huang, F. Yan, M. Huang, Substituted zinc phthalocyanine as an antimicrobial photosensitizer for periodontitis treatment, *J. Porphyr. Phthalocyanines.* 15 (2011) 293–299. doi:10.1142/S1088424611003276.
- [61] Z. Xiong, Y. Xu, L. Zhu, J. Zhao, Photosensitized oxidation of substituted phenols on aluminum phthalocyanine-intercalated organoclay, *Environ. Sci. Technol.* 39 (2005) 651–657. doi:10.1021/es0487630.



- [62] J.L.N. Bastos, M. Nitschke, N.A. Parizotto, Analysis of photodynamic antimicrobial chemotherapy (PACT) action with Chloro-Aluminum Phthalocyanine (Pc-ClAl) on *Pseudomonas aeruginosa* (Gram -) and *Staphylococcus aureus* (Gram +) microorganisms., *Rev. Bras. Eng. Biomed.* 29 (2013) 175–183. doi:10.4322/rbeb.2013.017.
- [63] R.M. Mohamed, M.M. Mohamed, Copper (II) phthalocyanines immobilized on alumina and encapsulated inside zeolite-X and their applications in photocatalytic degradation of cyanide: A comparative study, *Appl. Catal. A Gen.* 340 (2008) 16–24. doi:10.1016/j.apcata.2008.01.029.
- [64] M. Silva, M.J.F. Calvete, N.P.F. Gonçalves, H.D. Burrows, M. Sarakha, A. Fernandes, M.F. Ribeiro, M.E. Azenha, M.M. Pereira, Zinc(II) phthalocyanines immobilized in mesoporous silica Al-MCM-41 and their applications in photocatalytic degradation of pesticides, *J. Hazard. Mater.* 233–234 (2012) 79–88. doi:10.1016/j.jhazmat.2012.06.059.
- [65] S.L. Wang, Y.F. Fang, Y. Yang, J.Z. Liu, A.P. Deng, X.R. Zhao, Y.P. Huang, Catalysis of organic pollutant photodegradation by metal phthalocyanines immobilized on TiO<sub>2</sub>@SiO<sub>2</sub>, *Chinese Sci. Bull.* 56 (2011) 969–976. doi:10.1007/s11434-010-4280-3.
- [66] S. Mapukata, N. Kobayashi, M. Kimura, T. Nyokong, Asymmetrical and symmetrical zinc phthalocyanine-cobalt ferrite conjugates embedded in electrospun fibers for dual photocatalytic degradation of azo dyes: Methyl Orange and Orange G, *J. Photochem. Photobiol. A Chem.* 379 (2019) 112–122. doi:10.1016/j.jphotochem.2019.04.048.
- [67] A. Magadla, D.O. Oluwole, M. Managa, T. Nyokong, Physicochemical and antimicrobial photodynamic chemotherapy (against *E. coli*) by indium phthalocyanines in the presence of silver–iron bimetallic nanoparticles, *Polyhedron.* 162 (2019) 30–38. doi:10.1016/j.poly.2019.01.032.
- [68] N. Masilela, P. Kleyi, Z. Tshentu, G. Priniotakis, P. Westbroek, T. Nyokong, Photodynamic inactivation of *Staphylococcus aureus* using low symmetrically substituted phthalocyanines supported on a polystyrene polymer fiber, *Dye. Pigment.* 96 (2013) 500–508. doi:10.1016/j.dyepig.2012.10.001.
- [69] M. Beran, R. Korinkova, H. Polaskova, J. Drahorad, O. Vltavsky, Antimicrobial polyhydroxybutyrate submicron fiber mat loaded with zinc phthalocyanine derivative, *J. Sci. Eng. Res.* 6 (2019) 44–56.
- [70] O.L. Osifeko, T. Nyokong, Applications of lead phthalocyanines embedded in electrospun fibers for the photoinactivation of *Escherichia coli* in water, *Dye. Pigment.* 111 (2014) 8–15. doi:10.1016/j.dyepig.2014.05.010.
- [71] S. Mapukata, A.S. Hainer, A.E. Lanterna, J.C. Scaiano, T. Nyokong, Decorated titania fibers as photocatalysts for hydrogen generation and organic matter degradation, *J. Photochem. Photobiol. A Chem.* 388 (2020) 112185. doi:10.1016/j.jphotochem.2019.112185.
- [72] S. Tombe, E. Antunes, T. Nyokong, Electrospun fibers functionalized with phthalocyanine-gold nanoparticle conjugates for photocatalytic applications, *J. Mol. Catal. A Chem.* 371 (2013) 125–134. doi:10.1016/j.molcata.2013.01.033.

- [73] H.D. Burrows, M.L. Canle, J.A. Santaballa, S. Steenken, Reaction pathways and mechanisms of photodegradation of pesticides, *J. Photochem. Photobiol. B Biol.* 67 (2002) 71–108.
- [74] H.D. Burrows, L.S. Ernestova, T.J. Kemp, Y.I. Skurlatov, A.P. Purmal, A.N. Yermakov, Kinetics and mechanism of photodegradation of chlorophenols, *Prog. React. Kinet.* 23 (1998) 145–207.
- [75] M.I. Silva, H.D. Burrows, M.G. Miguel, S.J. Formosinho, Tris-2,2'-Bipyridylruthenium ( II ) peroxydisulphate as a photosensitizer in the oxidative degradation of 4-chlorophenol, *Ber. Bunsenges. Phys. Chem.* 100 (1996) 138–143.
- [76] A.A. Oluwasanu, Fate and Toxicity of Chlorinated Phenols of Environmental Implications: A Review, *Med. Anal. Chem. Int. J.* 2 (2018) 000126. doi:10.23880/macij-16000126.
- [77] U.G. Ahlborg, T.M. Thunberg, H.C. Spencer, Chlorinated phenols: Occurrence, toxicity, metabolism, and environmental impact, *Crit. Rev. Toxicol.* 7 (1980) 1–35. doi:10.3109/10408448009017934.
- [78] E.O. Igbinosa, E.E. Odjadjare, V.N. Chigor, I.H. Igbinosa, A.O. Emoghene, F.O. Ekhaize, N.O. Igiehon, O.G. Idemudia, Toxicological profile of chlorophenols and their derivatives in the environment: The public health perspective, *Sci. World J.* 2013 (2013) 460215. doi:10.1084/jem.184.2.585.
- [79] E. Silva, M.M. Pereira, H.D. Burrows, M.E. Azenha, M. Sarakha, M. Bolte, Photooxidation of 4-chlorophenol sensitised by iron meso -tetrakis (2, 6-dichloro-3-sulfophenyl ) porphyrin in aqueous solution †, *Photochem Photobiol Sci.* 3 (2004) 200–204. doi:10.1039/b308975d 2.
- [80] P. Khoza, T. Nyokong, Photocatalytic behavior of phthalocyanine-silver nanoparticle conjugates supported on polystyrene fibers, *J. Mol. Catal. A Chem.* 395 (2014) 34–41. doi:10.1016/j.molcata.2014.07.031.
- [81] L. Fernández, V.I. Esteves, Â. Cunha, R.J. Schneider, Photodegradation of organic pollutants in water by immobilized porphyrins and phthalocyanines, *J. Porphyr. Phthalocyanines.* 20 (2016) 1–17. doi:10.1142/S108842461630007X.
- [82] M. Wainwright, Photodynamic antimicrobial chemotherapy (PACT), *J. Antimicrob. Chemother.* 42 (1998) 13–28. doi:10.1002/9783527676132.ch10.
- [83] M.E. Stryjewski, G.R. Corey, Methicillin-resistant *Staphylococcus aureus*: An evolving pathogen, *Clin. Infect. Dis.* 58 (2014) 10–19. doi:10.1093/cid/cit613.
- [84] N. Malachowa, F.R. DeLeo, Mobile genetic elements of *Staphylococcus aureus*, *Cell. Mol. Life Sci.* 67 (2010) 3057–3071. doi:10.1007/s00018-010-0389-4.
- [85] M. Kasha, H.R. Rawls, M.A. El-Bayoumi, The Exciton Model In Molecular Spectroscopy, *Pure Appl. Chem.* 11 (1965) 371–392. doi:10.1351/pac196511030371.
- [86] Z. Malik, H. Ladan, Y. Nitzan, Photodynamic inactivation of Gram-negative bacteria: problems and possible solutions, *J. Photochem. Photobiol. B Biol. Photobiol B.* 14 (1992) 262–266.

- [87] Y. Nitzan, Z. Malik, B. Eherenberg, Photosensitization of microbial cells, in: E. Riklis (Ed.), *Photobiol. Sci. Its Appl.*, Plenum Press, New York, 1991: pp. 815–820.
- [88] H. Nikaido, Permability of the lipid domains of bacterial membranes, in: R. Aloia, C. Curatin, L. Gordon (Eds.), *Membr. Transp. Inf. Storage*, Liss, Alan R, New York, 1990: pp. 165–190.
- [89] Y. Nitzan, H.M. Wexler, S.M. Finegold, Inactivation of anaerobic bacteria by various photosensitized porphyrins or by hemin, *Curr. Microbiol.* 29 (1994) 125–131.
- [90] S.Y.C. Tong, J.S. Davis, E. Eichenberger, T.L. Holland, V.G. Fowler, *Staphylococcus aureus* infections: Epidemiology, pathophysiology, clinical manifestations, and management, *Clin. Microbiol. Rev.* 28 (2015) 603–661. doi:10.1128/CMR.00134-14.
- [91] B.P. Howden, J.K. Davies, P.D.R. Johnson, T.P. Stinear, M.L. Grayson, Reduced vancomycin susceptibility in *Staphylococcus aureus*, including vancomycin-intermediate and heterogeneous vancomycin-intermediate strains: Resistance mechanisms, laboratory detection, and clinical implications, *Clin. Microbiol. Rev.* 23 (2010) 99–139. doi:10.1128/CMR.00042-09.
- [92] M.A. Kertesz, Riding the sulfur cycle - Metabolism of sulfonates and sulfate esters in Gram-negative bacteria, *FEMS Microbiol. Rev.* 24 (1999) 135–175. doi:10.1016/S0168-6445(99)00033-9.
- [93] M. Wainwright, T. Maisch, S. Nonell, K. Plaetzer, A. Almeida, G.P. Tegos, M.R. Hamblin, Photoantimicrobials? are we afraid of the light?, *Lancet Infect. Dis.* 17 (2017) 49–55. doi:10.1016/S1473-3099(16)30268-7.
- [94] K. Hayashi, M. Nakamura, H. Miki, S. Ozaki, M. Abe, T. Matsumoto, T. Kori, K. Ishimura, Photostable iodinated silica/porphyrin hybrid nanoparticles with heavy-atom effect for wide-field photodynamic/photothermal therapy using single light source, *Adv. Funct. Mater.* 24 (2014) 503–513. doi:10.1002/adfm.201301771.
- [95] A. Gorman, J. Killoran, C. O'Shea, T. Kenna, W.M. Gallagher, D.F. O'Shea, In vitro demonstration of the heavy-atom effect for photodynamic therapy, *J. Am. Chem. Soc.* 126 (2004) 10619–10631. doi:10.1021/ja047649e.
- [96] K. Sanusi, E.K. Amuhaya, T. Nyokong, Enhanced optical limiting behavior of an indium phthalocyanine – single-walled carbon nanotube composite: An investigation of the effects of solvents, *J. Phys. Chem. C.* 118 (2014) 7057–7069. doi:10.1021/jp501469e.
- [97] G. Roncucci, D. Dei, M.P. De Filippis, L. Fantetti, D. Nistri, Metal substituted non centrosymmetrical phthalocyanine analogues, their preparation and use in photodynamic therapy and in vivo diagnostic, CA2441386C, 2002.
- [98] M.R. Ke, J.D. Huang, S.M. Weng, Comparison between non-peripherally and peripherally tetra-substituted zinc (II) phthalocyanines as photosensitizers: Synthesis, spectroscopic, photochemical and photobiological properties, *J. Photochem. Photobiol. A Chem.* 201 (2009) 23–31. doi:10.1016/j.jphotochem.2008.09.011.



- [99] I. Khan, K. Saeed, I. Khan, Nanoparticles: Properties, applications and toxicities, *Arab. J. Chem.* 12 (2019) 908–931. doi:10.1016/j.arabjc.2017.05.011.
- [100] J. Conde, J.T. Dias, V. Grazú, M. Moros, P. V Baptista, J.M. de la Fuente, Revisiting 30 years of Biofunctionalization and Surface Chemistry of Inorganic Nanoparticles for Nanomedicine Revisiting 30 years of biofunctionalization and surface chemistry of inorganic nanoparticles for nanomedicine, *Front. Chem.* 2 (2014) 48. doi:10.3389/fchem.2014.00048.
- [101] J. Zhang, L. Na, Y. Jiang, D. Lou, L. Jin, Graphene quantum dots as a fluorescence-quenching probe for quantitative analysis of Ponceau 4R solution, *Anal. Methods.* 8 (2016) 7242–7246. doi:10.1039/C6AY02203K.
- [102] P.N. Joshi, S. Kundu, S.K. Sanghi, D. Sarkar, Graphene Quantum Dots - From Emergence to Nanotheranostic Applications, in: A.D. Sezer (Ed.), *Smart Drug Deliv. Syst.*, Intech, Croatia, 2016: pp. 159–195. doi:10.5772/61932.
- [103] L. Li, G. Wu, G. Yang, J. Peng, J. Zhao, J.-J. Zhu, Focusing on luminescent graphene quantum dots: current status and future perspectives., *Nanoscale.* 5 (2013) 4015–39. doi:10.1039/c3nr33849e.
- [104] H. Sun, L. Wu, W. Wei, X. Qu, Recent advances in graphene quantum dots for sensing, *Mater. Today.* 16 (2013) 433–442. doi:10.1016/j.mattod.2013.10.020.
- [105] T. Ogi, H. Iwasaki, K. Aishima, F. Iskandar, W.-N. Wang, K. Takimiya, K. Okuyama, Transient nature of graphene quantum dot formation via a hydrothermal reaction, *RSC Adv.* 4 (2014) 55709–55715. doi:10.1039/C4RA09159K.
- [106] O.J. Achadu, I. Uddin, T. Nyokong, Fluorescence behavior of nanoconjugates of graphene quantum dots and zinc phthalocyanines, *J. Photochem. Photobiol. A Chem.* 317 (2016) 12–25. doi:10.1016/j.jphotochem.2015.11.006.
- [107] O.J. Achadu, I. Uddin, T. Nyokong, The interaction between graphene quantum dots grafted with polyethyleneimine and Au@Ag nanoparticles: Application as a fluorescence “turn-on” nanoprobe, *J. Photochem. Photobiol. A Chem.* 324 (2016) 96–105. doi:http://dx.doi.org/10.1016/j.jphotochem.2016.03.016.
- [108] L. Li, G. Wu, T. Hong, Z. Yin, D. Sun, E.S. Abdel-Halim, J.J. Zhu, Graphene quantum dots as fluorescence probes for turn-off sensing of melamine in the presence of Hg<sup>2+</sup>, *ACS Appl. Mater. Interfaces.* 6 (2014) 2858–2864. doi:10.1021/am405305r.
- [109] O.J. Achadu, M. Managa, T. Nyokong, Fluorescence behaviour of supramolecular hybrids containing graphene quantum dots and pyrene-derivatized phthalocyanines and porphyrins, *J. Photochem. Photobiol. A Chem.* 333 (2017) 174–185. doi:10.1016/j.jphotochem.2016.10.029.
- [110] J. Deng, Q. Lu, H. Li, Y. Zhang, S. Yao, Large scale preparation of graphene quantum dots from graphite oxide in pure water via one-step electrochemical tailoring, *RSC Adv.* 5 (2015) 29704–29707. doi:10.1039/C4RA16805D.
- [111] H. Shen, L. Zhang, M. Liu, Z. Zhang, Biomedical applications of graphene,

- Theranostics. 2 (2012) 283–294. doi:10.7150/thno.3642.
- [112] A. Kalluri, D. Debnath, B. Dharmadhikari, P. Patra, Graphene Quantum Dots: Synthesis and Applications, *Methods Enzymol.* 609 (2018) 335–354. doi:10.1016/bs.mie.2018.07.002.
- [113] W. Chen, G. Lv, W. Hu, D. Li, S. Chen, Z. Dai, Synthesis and applications of graphene quantum dots: A review, *Nanotechnol. Rev.* 7 (2018) 157–185. doi:10.1515/ntrev-2017-0199.
- [114] O.M. Bankole, O.J. Achadu, T. Nyokong, Nonlinear interactions of zinc phthalocyanine-graphene quantum dots nanocomposites : Investigation of effects of surface functionalization with heteroatoms, *J. Fluoresc.* 2 (2017) 755–766. doi:10.1007/s10895-016-2008-8.
- [115] N. Nwahara, J. Britton, T. Nyokong, Improving singlet oxygen generating abilities of phthalocyanines : Aluminum tetrasulfonated phthalocyanine in the presence of graphene quantum dots and folic acid, *J. Coord. Chem.* 70 (2017) 1601–1616. doi:10.1080/00958972.2017.1313975.
- [116] N. Nwahara, O.J. Achadu, T. Nyokong, In-situ synthesis of gold nanoparticles on graphene quantum dots-phthalocyanine nanoplateforms: First description of the photophysical and surface enhanced Raman scattering behaviour, *J. Photochem. Photobiol. A Chem.* 359 (2018) 131–144. doi:10.1016/j.jphotochem.2018.04.011.
- [117] N. Bakar, J.G. Shapter, M.M. Salleh, A.A. Umar, Self-assembly of high density of triangular silver nanoplate films promoted by 3-aminopropyltrimethoxysilane, *Appl. Sci.* 5 (2015) 209–221. doi:10.3390/app5030209.
- [118] P.M. Ajayan, L.D. Marks, Quasimelting and Phases of Small Particles P., *Phys. Rev. Lett.* 60 (1988) 585–587.
- [119] D.W. Hatchett, H.S. White, Electrochemistry of sulfur adlayers on the low-index faces of silver, *J. Phys. Chem.* 100 (1996) 9854–9859. doi:10.1021/jp953757z.
- [120] G.S. Métraux, C.A. Mirkin, Rapid thermal synthesis of silver nanoprisms with chemically tailorable thickness, *Adv. Mater.* 17 (2005) 412–415. doi:10.1002/adma.200401086.
- [121] R. Jin, Y. Cao, C.A. Mirkin, K.L. Kelly, G.C. Schatz, J.G. Zheng, Photoinduced conversion of silver nanospheres to nanoprisms, *Science.* 294 (2001) 1901–1903. doi:10.1126/science.1066541.
- [122] P. Van Dong, C. Ha, L. Binh, J. Kasbohm, Chemical synthesis and antibacterial activity of novel-shaped silver nanoparticles, *Int. Nano Lett.* 2 (2012) 1–9. doi:10.1186/2228-5326-2-9.
- [123] M. Ambroz, A. Beeby, A.J. MacRobert, M.S.C. Simpson, R.K. Svensen, D. Phillips, Preparative, analytical and fluorescence spectroscopic studies of sulphonated aluminium phthalocyanine photosensitizers, *J. Photochem. Photobiol. B Biol.* 9 (1991) 87–95. doi:10.1007/978-3-642-33350-7-18.
- [124] H. Kliesch, A. Weitemeyer, S. Müller, D. Wöhrle, Synthesis of phthalocyanines with one sulfonic acid, carboxylic acid, or amino group, *Liebigs Ann.* 1995

- (1995) 1269–1273. doi:10.1002/jlac.1995199507168.
- [125] S.A. Mikhaleenko, V.M. Derkacheva, E.A. Luk'yanets, Phthalocyanines and related compounds. XIX. Tetra- and octaamino-substituted phthalocyanines, *J. Gen. Chem. USSR*. 51 (1981) 1405–1411. doi:10.1002/chin.198152337.
- [126] C.S. Keenan, S.S. Murphree, Rapid and convenient conversion of nitroarenes to anilines under microwave conditions using nonprecious metals in mildly acidic medium, *Synth. Commun.* 47 (2017) 1085–1089. doi:10.1080/00397911.2017.1310897.
- [127] E.M. Antunes, T. Nyokong, Synthesis and Photophysical Properties of Tetra- and Octasubstituted Phosphorous Oxide Triazatetrabenzcorrole, *Met. Based. Drugs*. 2008 (2008) 498916. doi:10.1155/2008/498916.
- [128] C. Wang, Z. Xu, C. Zhang, Polyethyleneimine-functionalized fluorescent carbon dots: Water stability, pH sensing, and cellular imaging, *ChemNanoMat*. 1 (2015) 122–127. doi:10.1002/cnma.201500009.
- [129] N. Kunjuzwa, L.N. Nthunya, E.N. Nxumalo, S.D. Mhlanga, The use of nanomaterials in the synthesis of nanofiber membranes and their application in water treatment, in: *Adv. Nanomater. Membr. Synth. Its Appl.*, Elsevier Inc., 2019: pp. 101–125. doi:10.1016/b978-0-12-814503-6.00005-7.
- [130] M. Ulbricht, Advanced functional polymer membranes, *Polymer (Guildf)*. 47 (2006) 2217–2262. doi:10.1016/j.polymer.2006.01.084.
- [131] Y. Zhang, S. Wei, Y. Hu, S. Sun, Membrane technology in wastewater treatment enhanced by functional nanomaterials, *J. Clean. Prod.* 197 (2018) 339–348. doi:10.1016/j.jclepro.2018.06.211.
- [132] E. Gürel, M. Pişkin, S. Altun, Z. Odabaş, M. Durmuş, Synthesis, characterization and investigation of the photophysical and photochemical properties of highly soluble novel metal-free, zinc(II), and indium(III) phthalocyanines substituted with 2,3,6-trimethylphenoxy moieties, *Dalt. Trans.* 44 (2015) 6202–6211. doi:10.1039/c5dt00304k.
- [133] M. Nappa, J.S. Valentine, The Influence of axial ligands on metalloporphyrin visible absorption spectra . Complexes of tetraphenylporphinatozinc, *J. Am. Chem. Soc.* 100 (1978) 5075–5080.
- [134] H. Li, T.J. Jensen, F.R. Fronczek, M.G.H. Vicente, Syntheses and Properties of a Series of Cationic Water-Soluble Phthalocyanines, *J. Med. Chem.* 51 (2008) 501–511.
- [135] G. Gümrükçü, G.K. Karaoğlu, A. Erdoğan, A. Gül, U. Avcıata, Photophysical, photochemical, and BQ quenching properties of zinc phthalocyanines with fused or interrupted extended conjugation, *J. Chem.* 2014 (2014) 1–11. doi:10.1155/2014/435834.
- [136] G.K. Karaoğlu, G. Gümrükçü, A. Koca, A. Gül, U. Avcata, Synthesis and characterization of novel soluble phthalocyanines with fused conjugated unsaturated groups, *Dye. Pigment.* 90 (2011) 11–20. doi:10.1016/j.dyepig.2010.10.002.
- [137] J. Morley, M.H. Charlton, Theoretical Investigation of the Structure and

- Spectra of Zinc Phthalocyanines, *J. Phys. Chem.* 99 (1995) 1928–1934.
- [138] A. Lyubimtsev, Z. Iqbal, G. Crucius, S. Syrbu, E.S. Taraymovich, T. Ziegler, M. Hanack, Aggregation behavior and UV-vis spectra of tetra- and octaglycosylated zinc phthalocyanines, *J. Porphyr. Phthalocyanines*. 15 (2011) 39–46. doi:10.1142/S1088424611002891.
- [139] K. Palewska, J. Sworakowski, J. Lipiński, Molecular aggregation in soluble phthalocyanines - Chemical interactions vs.  $\pi$ -stacking, *Opt. Mater. (Amst)*. 34 (2012) 1717–1724. doi:10.1016/j.optmat.2012.02.009.
- [140] V. Theodorou, G. Paraskevopoulos, K. Skobridis, A mild alkaline hydrolysis of *N*- and *N,N*-substituted amides and nitriles, *Arch. Org. Chem.* 2015 (2015) 101–112.
- [141] H. Scheer, J.J. Katz, Nuclear magnetic resonance spectroscopy of porphyrins and metalloporphyrins, in: K.M. Smith (Ed.), *Porphyrins Met. A New Ed. Based Orig. Vol. by J. E. Falk*, Elsevier Scientific Publishing Company, Amsterdam, 1975: pp. 399–514.
- [142] G. de la Torre, M. Nicolau, T. Torres, Phthalocyanines: Synthesis, Supramolecular Organization, and Physical Properties, in: H.S. Nalwa (Ed.), *Supramol. Photosensit. Electroact. Mater.*, Academic Press, San Diego, 2001: pp. 1–111. doi:10.1016/b978-012513904-5/50003-x.
- [143] L.T. Ueno, C.C. Jayme, L.R. Silva, E.B. Pereira, S.M. De Oliveira, A.E.H. MacHado, Photophysics and spectroscopic properties of zinc phthalocyanine revisited using quantum chemistry, *J. Braz. Chem. Soc.* 23 (2012) 2237–2247. doi:10.1590/S0103-50532012001200013.
- [144] J. Obirai, N.P. Rodrigues, F. Bedioui, T. Nyokong, Synthesis, spectral and electrochemical properties of a new family of pyrrole substituted cobalt, iron, manganese, nickel and zinc phthalocyanine complexes, *J. Porphyr. Phthalocyanines*. 7 (2003) 508–520. doi:10.1142/S1088424603000641.
- [145] A. Ogunsipe, J.-Y. Chen, T. Nyokong, Photophysical and photochemical studies of zinc(II) phthalocyanine derivatives-effects of substituents and solvents, *New J. Chem.* 28 (2004) 822–827. doi:10.1002/hlca.200390279.
- [146] C.A. Hunter, J.K.M. Sanders, The nature of  $\pi$ – $\pi$  interactions, *J. Am. Chem. Soc.* 112 (1990) 5525–5534. doi:10.1021/ja00170a016.
- [147] B. Brozek-Płuska, I. Szymczyk, H. Abramczyk, Raman spectroscopy of phthalocyanines and their sulfonated derivatives, *J. Mol. Struct.* 744–747 (2005) 481–485. doi:10.1016/j.molstruc.2004.12.056.
- [148] L.M. Malard, M.A. Pimenta, G. Dresselhaus, M.S. Dresselhaus, Raman spectroscopy in graphene, *Phys. Rep.* 473 (2009) 51–87. doi:10.1016/j.physrep.2009.02.003.
- [149] Z. Sun, A.-R.O. Raji, Y. Zhu, C. Xiang, Z. Yan, C. Kittrell, E.L.G. Samuel, J.M. Tour, Large-Area Bernal-Stacked Bi-, Tri-, and Tetralayer Graphene, *ACS Nano*. 6 (2012) 9790–9796.
- [150] M.M. El-Nahass, H.M. Zeyada, M.S. Aziz, N.A. El-Ghamaz, Structural and optical properties of thermally evaporated zinc phthalocyanine thin films, *Opt.*

- Mater. (Amst). 27 (2004) 491–498. doi:10.1016/j.optmat.2004.04.010.
- [151] M. Samanta, U.K. Ghorai, B. Das, P. Howli, S. Das, D. Sen, K.K. Chattopadhyay, Facile synthesis of ZnPc nanoflakes for cold cathode emission, RSC Adv. 6 (2016) 42739–42744. doi:10.1039/C6RA01968D.
- [152] C. Schünemann, C. Elschner, A.A. Levin, M. Levichkova, K. Leo, M. Riede, Zinc phthalocyanine - Influence of substrate temperature, film thickness, and kind of substrate on the morphology, Thin Solid Films. 519 (2011) 3939–3945. doi:10.1016/j.tsf.2011.01.356.
- [153] M.J. Stillman, T. Nyokong, Phthalocyanines - Properties and Applications, in: A.B.P. Lever, C.C. Leznoff (Eds.), Porphyrin Handb., Volume 1, VCH, New York, 1989: pp. 133–289.
- [154] L. Li, J.-F. Zhao, N. Won, H. Jin, S. Kim, J.-Y. Chen, Quantum Dot - Aluminum phthalocyanine Conjugates perform photodynamic reactions to kill cancer cells via fluorescence resonance energy transfer (FRET), Nanoscale Res. Lett. 7 (2012) 386–393. doi:10.1186/1556-276X-7-386.
- [155] D. Aherne, D.M. Ledwith, M. Gara, J.M. Kelly, Optical properties and growth aspects of silver nanoprisms produced by a highly reproducible and rapid synthesis at room temperature, Adv. Funct. Mater. 18 (2008) 2005–2016. doi:10.1002/adfm.200800233.
- [156] R. Prabakaran, R. Kesavamoorthy, G.L.N. Reddy, F.P. Xavier, Structural investigation of copper phthalocyanine thin films using X-ray diffraction, Raman scattering and optical absorption measurements, Phys. Status Solidi Basic Res. 229 (2002) 1175–1186. doi:10.1002/1521-3951(200202)229:3<1175::AID-PSSB1175>3.0.CO;2-K.
- [157] K. Gulati, M. Sinn Aw, D. Losic, Nanoengineered drug-releasing Ti wires as an alternative for local delivery of chemotherapeutics in the brain, Int. J. Nanomedicine. 7 (2012) 2069–2076. doi:10.2147/IJN.S29917.
- [158] S. Barazzouk, C. Daneault, Amino Acid and Peptide Immobilization on Oxidized Nanocellulose: Spectroscopic Characterization, Nanomaterials. 2 (2012) 187–205. doi:10.3390/nano2020187.
- [159] S. Kundu, W. Xia, W. Busser, M. Becker, D.A. Schmidt, M. Havenith, M. Muhler, The formation of nitrogen-containing functional groups on carbon nanotube surfaces: a quantitative XPS and TPD study, Phys. Chem. Chem. Phys. 12 (2010) 4351–4359. doi:10.1039/c004746p.
- [160] S.J. Xiao, M. Textor, N.D. Spencer, M. Wieland, B. Keller, H. Sigrist, Immobilization of the cell-adhesive peptide Arg-Gly-Asp-Cys (RGDC) on titanium surfaces by covalent chemical attachment, J. Mater. Sci. Mater. Med. 8 (1997) 867–872. doi:10.1023/A:1018501804943.
- [161] L. Lozzi, L. Ottaviano, S. Santucci, High resolution XPS studies on hexadecafluoro-copper-phthalocyanine deposited onto Si(111)7×7 surface, Surf. Sci. 470 (2001) 265–274. doi:http://dx.doi.org/10.1016/S0039-6028(00)00866-9.
- [162] L. Ottaviano, L. Lozzi, F. Ramondo, P. Picozzi, S. Santucci, Copper



- hexadecafluoro phthalocyanine and naphthalocyanine: The role of shake up excitations in the interpretation and electronic distinction of high-resolution X-ray photoelectron spectroscopy measurements, *J. Electron Spectros. Relat. Phenomena*. 105 (1999) 145–154. doi:10.1016/S0368-2048(99)00064-X.
- [163] L. Alagna, A. Capobianchi, M.P. Casaletto, G. Mattocono, A.M. Paoletti, G. Pennesi, G. Rossi, Effect of molecular packing on the solid state spectra of ruthenium phthalocyanine: anomalous behaviour of a monodimensional stacked assembly, *J. Mater. Chem.* 11 (2001) 1928–1935. doi:10.1039/b100041l.
- [164] S. Fery-Forgues, D. Lavabre, Are Fluorescence Quantum Yields So Tricky to Measure? A Demonstration Using Familiar Stationery Products, *J. Chem. Educ.* 76 (1999) 1260–1264. doi:10.1021/ed076p1260.
- [165] A.M. Brouwer, Standards for photoluminescence quantum yield measurements in solution (IUPAC Technical Report), *Pure Appl. Chem.* 83 (2011) 2213–2228. doi:10.1351/PAC-REP-10-09-31.
- [166] P.G. Seybold, M. Gouterman, Porphyrins. XIII: Fluorescence spectra and quantum yields, *J. Mol. Spectrosc.* 31 (1969) 1–13. doi:10.1016/0022-2852(69)90335-X.
- [167] C. Berney, G. Danuser, FRET or no FRET: A quantitative comparison, *Biophys. J.* 84 (2003) 3992–4010. doi:10.1016/S0006-3495(03)75126-1.
- [168] M. Idowu, J.-Y. Chen, T. Nyokong, Photoinduced energy transfer between water-soluble CdTe quantum dots and aluminium tetrasulfonated phthalocyanine, *New J. Chem.* 32 (2008) 290–296. doi:10.1039/b707808k.
- [169] H. Du, R.-C.A. Fuh, J. Li, L.A. Corkan, J.S. Lindsey, PhotochemCAD: A computer-aided design and research tool in photochemistry., *Photochem. Photobiol.* 68 (1998) 141–142. doi:10.1111/j.1751-1097.1998.tb02480.x.
- [170] J.R. Lakowicz, Principles of Fluorescence Spectroscopy Principles of Fluorescence Spectroscopy, in: *Princ. Fluoresc. Spectrosc.*, 3rd ed., Springer, New York, 2007: pp. 443–449. doi:10.1007/978-0-387-46312-4.
- [171] S.A. Hussain, An Introduction to Fluorescence Resonance Energy Transfer (FRET), *Sci. J. Phys.* 2012 (2012) 1–4. doi:10.7237/sjp/268.
- [172] T.H. Tran Thi, C. Desforge, C. Thiec, S. Gaspard, Singlet-singlet and triplet-triplet intramolecular transfer processes in a covalently linked porphyrin-phthalocyanine heterodimer, *J. Phys. Chem.* 93 (1989) 1226–1233. doi:10.1021/j100341a013.
- [173] W. Spiller, H. Kliesch, D. Wöhrle, S. Hackbarth, B. Röder, G. Schnurpfeil, Singlet Oxygen Quantum Yields of Different Photosensitizers in Polar Solvents and Micellar Solutions, *J. Porphyrins Phthalocyanines*. 2 (1998) 145–158. doi:10.1002/(SICI)1099-1409.
- [174] N.A. Kuznetsova, N.S. Gretsova, V.M. Derkacheva, S.A. Mikhaleenko, L.I. Solov'eva, O.A. Yuzhakova, O.L. Kaliya, E.A. Luk'yanets, Generation of singlet oxygen with anionic aluminum phthalocyanines in water, *Russ. J. Gen. Chem.* 72 (2002) 300–306. doi:10.1023/A:1015402524813.

- [175] N. Gandra, A.T. Frank, O. Le Gendre, N. Sawwan, D. Aebisher, J.F. Liebman, K.N. Houk, A. Greer, R. Gao, Possible singlet oxygen generation from the photolysis of indigo dyes in methanol, DMSO, water, and ionic liquid, 1-butyl-3-methylimidazolium tetrafluoroborate, *Tetrahedron*. 62 (2006) 10771–10776. doi:10.1016/j.tet.2006.08.095.
- [176] T. Nyokong, E. Antunes, Photochemical and photophysical properties of metallophthalocyanines, in: K.M. Kadish, K.M. Smith, R. Guillard (Eds.), *Handb. Porphyr. Sci. with Appl. to Chem. Physics, Mater. Sci. Eng. Biol. Med.*, Hackensack, N.J. ; London : World Scientific, Singapore, 2010: pp. 247–349.
- [177] A. Ogunsipe, T. Nyokong, Photophysical and photochemical studies of sulphonated non-transition metal phthalocyanines in aqueous and non-aqueous media, *J. Photochem. Photobiol. A Chem.* 173 (2005) 211–220. doi:10.1016/j.jphotochem.2005.03.001.
- [178] X.F. Zhang, X. Li, The photostability and fluorescence properties of diphenylisobenzofuran, *J. Lumin.* 131 (2011) 2263–2266. doi:10.1016/j.jlumin.2011.05.048.
- [179] J.W. Owens, M. Robins, Phthalocyanine photophysics and photosensitizer efficiency on human embryonic lung fibroblasts, *J. Porphyr. Phthalocyanines*. 5 (2001) 460–464. doi:10.1002/jpp.340.
- [180] Z. Petrášek, D. Phillips, A time-resolved study of concentration quenching of disulfonated aluminium phthalocyanine fluorescence, *Photochem. Photobiol. Sci.* 2 (2003) 236–244. doi:10.1039/b209906c.
- [181] C.C. Byeon, M.M. McKerns, W. Sun, T.M. Nordlund, C.M. Lawson, G.M. Gray, Excited state lifetime and intersystem crossing rate of asymmetric pentaazadentate porphyrin-like metal complexes, *Appl. Phys. Lett.* 84 (2004) 5174–5176. doi:10.1063/1.1763983.
- [182] T. Fukuda, S. Homma, N. Kobayashi, Deformed phthalocyanines: Synthesis and characterization of zinc phthalocyanines bearing phenyl substituents at the 1-, 4-, 8-, 11-, 15-, 18-, 22-, and/or 25-positions, *Chem. - A Eur. J.* 11 (2005) 5205–5216. doi:10.1002/chem.200500176.
- [183] T. Nyokong, Effects of substituents on the photochemical and photophysical properties of main group metal phthalocyanines, *Coord. Chem. Rev.* 251 (2007) 1707–1722. doi:10.1016/j.ccr.2006.11.011.
- [184] A. Ogunsipe, D. Maree, T. Nyokong, Solvent effects on the photochemical and fluorescence properties of zinc phthalocyanine derivatives, *J. Mol. Struct.* 650 (2003) 131–140. doi:10.1016/S0022-2860(03)00155-8.
- [185] J. Savolainen, D. van der Linden, N. Dijkhuizen, J.L. Herek, Characterizing the functional dynamics of zinc phthalocyanine from femtoseconds to nanoseconds, *J. Photochem. Photobiol. A Chem.* 196 (2008) 99–105. doi:10.1016/j.jphotochem.2007.11.018.
- [186] G.G. Matlou, N. Kobayashi, M. Kimura, T. Nyokong, Physicochemical properties of water soluble unsymmetrical phthalocyanine-folic acid conjugates, *Dye. Pigment.* 149 (2018) 393–398. doi:10.1016/j.dyepig.2017.10.030.

- [187] N. Rapulenyane, E. Antunes, T. Nyokong, A study of the photophysics and antimicrobial properties of two zinc phthalocyanine-silver nanoparticle conjugates, *New J. Chem.* 37 (2013) 1216–1223. doi:10.1039/c3nj41107a.
- [188] S.N. Nyamu, L. Ombaka, E. Masika, M. Ng'ang'a, Antimicrobial Photodynamic Activity of Phthalocyanine Derivatives, *Adv. Chem.* 2018 (2018) 1–8. doi:10.1155/2018/2598062.
- [189] K.S. Adarsh, M.K. Singh, M.A. Shivkumar, M.K. Rabinal, B.N. Jagatap, B.G. Mulimani, M.I. Savadatti, S.R. Inamdar, FRET from core and core-shell quantum dots to laser dye: A comparative investigation, *J. Lumin.* 160 (2015) 216–222. doi:10.1016/j.jlumin.2014.12.014.
- [190] Z.N. Erol, P. Atienzar, Y. Arslanoğlu, E. Hamuryudan, H. García, Synthesis and photophysical properties of phthalocyanines having calixpyrrole units, *RSC Adv.* 5 (2015) 55901–55908. doi:10.1039/c5ra05830a.
- [191] M.G. Debacker, O. Deleplanque, B. van Vleirberge, F.X. Sauvage, A laser photolysis study of triplet lifetimes and of triplet-triplet annihilation reactions of phthalocyanines in DMSO solutions, *Laser Chem.* 8 (1988) 1–11. <http://cat.inist.fr/?aModele=afficheN&cpsidt=7651403>.
- [192] J.R. Darwent, P. Douglas, A. Harriman, G. Porter, M.C. Richoux, Metal phthalocyanines and porphyrins as photosensitizers for reduction of water to hydrogen, *Coord. Chem. Rev.* 44 (1982) 83–126. doi:10.1016/S0010-8545(00)80518-4.
- [193] S. Venugopal Rao, P.T. Anusha, L. Giribabu, S.P. Tewari, Picosecond optical nonlinearities in symmetrical and unsymmetrical phthalocyanines studied using the Z-scan technique, *Pramana - J. Phys.* 75 (2010) 1017–1023. doi:10.1007/s12043-010-0157-x.
- [194] Z. Lou, Y. Hou, K. Chen, J. Zhao, S. Ji, F. Zhong, Y. Dede, B. Dick, Different Quenching Effect of Intramolecular Rotation on the Singlet and Triplet Excited States of Bodipy, *J. Phys. Chem. C.* 122 (2018) 185–193. doi:10.1021/acs.jpcc.7b10466.
- [195] H.L. Chen, Y.F. Huang, T.S. Lim, C.H. Su, P.H. Chen, A.C. Su, K.T. Wong, T.C. Chao, S.I. Chan, W. Fann, Excited-State Backbone Twisting of Polyfluorene As Detected from Photothermal After-Effects, *J. Phys. Chem. B.* 113 (2009) 8527–8531. doi:10.1021/jp901556v.
- [196] A.C. Benniston, A. Harriman, P. Li, P. V Patel, C.A. Sams, The effect of torsion angle on the rate of intramolecular triplet energy transfer, *Phys. Chem. Chem. Phys.* 7 (2005) 3677–3679. doi:10.1039/b512307k.
- [197] A.C. Benniston, A. Harriman, P. Li, P. V Patel, J.P. Rostron, C.A. Sams, An Apparent Angle Dependence for the Nonradiative Deactivation of Excited Triplet States of Sterically Constrained, Binuclear Ruthenium (II) Bis (2,2':6',2''-terpyridine) Complexes, *J. Phys. Chem. A.* 110 (2006) 9880–9886. doi:10.1021/jp061059g.
- [198] E.I. Zenkevich, E.I. Sagun, V.N. Knyukshto, A.M. Shulga, C. von Borczyskowski, Extra-ligation and screening effects upon interaction of



- photoinduced excited states of multiporphyrin arrays with molecular oxygen in solutions, in: A.Y. Chikishev, V.A. Orlovich, A.N. Rubinov, A.M. Zheltikov (Eds.), ICONO 2001 Nov. Trends Nonlinear Laser Spectrosc. Opt. Diagnostics Lasers Chem. Biophys. Biomed., SPIE, 2002: pp. 360–369. doi:10.1117/12.468916.
- [199] R. Gerdes, D. Wöhrle, W. Spiller, G. Schneider, G. Schnurpfeil, G. Schulz-Ekloff, Photo-oxidation of phenol and monochlorophenols in oxygen-saturated aqueous solutions by different photosensitizers, *J. Photochem. Photobiol. A Chem.* 111 (1997) 65–74. doi:10.1016/S1010-6030(97)00209-8.
- [200] K. Ozoemena, N. Kuznetsova, T. Nyokong, Photosensitized transformation of 4-chlorophenol in the presence of aggregated and non-aggregated metallophthalocyanines, *J. Photochem. Photobiol. A Chem.* 139 (2001) 217–224. doi:10.1016/S1010-6030(01)00383-5.
- [201] R. Zugle, E. Antunes, S. Khene, T. Nyokong, Photooxidation of 4-chlorophenol sensitized by lutetium tetraphenoxy phthalocyanine anchored on electrospun polystyrene polymer fiber, *Polyhedron*. 33 (2012) 74–81. doi:10.1016/j.poly.2011.11.005.
- [202] P. Kluson, M. Drobek, a. Kalaji, S. Zarubova, J. Krysa, J. Rakusan, Singlet oxygen photogeneration efficiencies of a series of phthalocyanines in well-defined spectral regions, *J. Photochem. Photobiol. A Chem.* 199 (2008) 267–273. doi:10.1016/j.jphotochem.2008.06.003.
- [203] R. Gerdes, O. Bartels, G. Schneider, D. Wöhrle, G. Schulz-Ekloff, Photooxidation of sulfide, thiol, phenols, and cyclopentadiene by artificial light and solar light irradiation, *Int. J. Photoenergy*. 1 (1999) 41–47. doi:10.1155/s1110662x99000082.
- [204] T. Wilke, M. Schneider, K. Kleinermanns, 1, 4-Hydroquinone is a Hydrogen Reservoir for Fuel Cells and Recyclable via Photocatalytic Water Splitting, *Open J. Phys. Chem.* 3 (2013) 97–102.
- [205] K.M. Lee, S.B. Abd Hamid, C.W. Lai, Mechanism and kinetics study for photocatalytic oxidation degradation: A case study for phenoxyacetic acid organic pollutant, *J. Nanomater.* 2015 (2015) 1–10. doi:10.1155/2015/940857.
- [206] V. Loddò, M. Bellardita, G. Camera-Roda, F. Parrino, L. Palmisano, Heterogeneous Photocatalysis: A Promising Advanced Oxidation Process, in: A. Basile, S. Mozia, R. Molinari (Eds.), *Curr. Trends Futur. Dev. Membr. Photocatalytic Membr. Photocatalytic Membr. React.*, 1st ed., Elsevier Inc., Amsterdam, 2018: pp. 1–43. doi:10.1016/B978-0-12-813549-5.00001-3.
- [207] R. Shan, L. Lu, J. Gu, Y. Zhang, H. Yuan, Y. Chen, B. Luo, Photocatalytic degradation of methyl orange by Ag/TiO<sub>2</sub>/biochar composite catalysts in aqueous solutions, *Mater. Sci. Semicond. Process.* 114 (2020) 105088. doi:10.1016/j.mssp.2020.105088.
- [208] Y. Li, X. Li, J. Li, J. Yin, Photocatalytic degradation of methyl orange by TiO<sub>2</sub>-coated activated carbon and kinetic study, *Water Res.* 40 (2006) 1119–1126. doi:10.1016/j.watres.2005.12.042.
- [209] K.Y. Pete, M.M. Sillanpää, M.S. Onyango, O. Aoyi, Analysis of Kinetic Models

- in Heterogeneous Catalysis of Methyl Orange Using TiO<sub>2</sub>/ Silica Composite Photocatalyst, in: *Int. Conf. Chem. Integr. Waste Manag. Environ. Eng.*, Johannesburg, 2014: pp. 169–173.
- [210] M.H. Farzana, S. Meenakshi, Visible light-driven photoactivity of zinc oxide impregnated chitosan beads for the detoxification of textile dyes, *Appl. Catal. A Gen.* 503 (2015) 124–134. doi:10.1016/j.apcata.2014.12.034.
- [211] M.H. Farzana, S. Meenakshi, Exploitation of zinc oxide impregnated chitosan beads for the photocatalytic decolorization of an azo dye, *Int. J. Biol. Macromol.* 72 (2015) 900–910. doi:10.1016/j.ijbiomac.2014.09.038.
- [212] F. Behar-Cohen, G. Baillet, T. de Ayguavives, P.O. Garcia, J. Krutmann, P. Pena-Garcia, C. Reme, J.S. Wolffsohn, Ultraviolet damage to the eye revisited: Eye-sun protection factor (E-SPF®), a new ultraviolet protection label for eyewear, *Clin. Ophthalmol.* 8 (2014) 87–104. doi:http://dx.doi.org/10.2147/OPTH.S46189.
- [213] R.F. Donnelly, P.A. McCarron, M.M. Tunney, Antifungal photodynamic therapy, *Microbiol. Res.* 163 (2008) 1–12. doi:10.1016/j.micres.2007.08.001.
- [214] O.L. Osifeko, M. Durmuş, T. Nyokong, Physicochemical and photodynamic antimicrobial chemotherapy studies of mono- and tetra-pyridyloxy substituted indium(III) phthalocyanines, *J. Photochem. Photobiol. A Chem.* 301 (2015) 47–54. doi:10.1016/j.jphotochem.2014.12.011.
- [215] M.G. Strakhovskaya, Y.N. Antonenko, A.A. Pashkovskaya, E.A. Kotova, V. Kireev, V.G. Zhukhovitsky, N.A. Kuznetsova, O.A. Yuzhakova, V.M. Negrimovsky, A.B. Rubin, Electrostatic binding of substituted metal phthalocyanines to enterobacterial cells: Its role in photodynamic inactivation, *Biochem.* 74 (2009) 1305–1314. doi:10.1134/S0006297909120025.
- [216] A. Sindelo, O.L. Osifeko, T. Nyokong, Synthesis, photophysicochemical and photodynamic antimicrobial chemotherapy studies of indium pyridyl phthalocyanines: Charge versus bridging atom, *Inorganica Chim. Acta.* 476 (2018) 68–76. doi:10.1016/j.ica.2018.02.020.
- [217] M.A. Revuelta-Maza, P. González-Jiménez, C. Hally, M. Agut, S. Nonell, G. de la Torre, T. Torres, Fluorine-substituted tetracationic ABAB-phthalocyanines for efficient photodynamic inactivation of Gram-positive and Gram-negative bacteria, *Eur. J. Med. Chem.* 187 (2020) 111957. doi:10.1016/j.ejmech.2019.111957.
- [218] A. Segalla, C.D. Borsarelli, S.E. Braslavsky, J.D. Spikes, G. Roncucci, D. Dei, G. Chiti, G. Jori, E. Reddi, Photophysical, photochemical and antibacterial photosensitizing properties of a novel octacationic Zn(II)-phthalocyanine, *Photochem. Photobiol. Sci.* 1 (2002) 641–648. doi:10.1039/b202031a.
- [219] M.K. Purkait, M.K. Sinha, P. Mondal, R. Singh, Introduction to Membranes, *Interface Sci. Technol.* 25 (2018) 1–37. doi:10.1016/B978-0-12-813961-5.00001-2.